

2002 SUMMER RESEARCH PROGRAM FOR HIGH SCHOOL JUNIORS

AT THE

UNIVERSITY OF ROCHESTER'S

LABORATORY FOR LASER ENERGETICS

STUDENT RESEARCH REPORTS

PROGRAM COORDINATOR

Dr. R. Stephen Craxton

March 2003

Laboratory Report 329

2002 SUMMER RESEARCH PROGRAM FOR HIGH SCHOOL JUNIORS

AT THE

UNIVERSITY OF ROCHESTER'S

LABORATORY FOR LASER ENERGETICS

STUDENT RESEARCH REPORTS

PROGRAM COORDINATOR

Dr. R. Stephen Craxton

LABORATORY FOR LASER ENERGETICS

University of Rochester

250 East River Road

Rochester, NY 14623-1299

During the summer of 2002, 15 students from Rochester-area high schools participated in the Laboratory for Laser Energetics' Summer High School Research Program. The goal of this program is to excite a group of high school students about careers in the areas of science and technology by exposing them to research in a state-of-the-art environment. Too often, students are exposed to "research" only through classroom laboratories, which have prescribed procedures and predictable results. In LLE's summer program, the students experience many of the trials, tribulations, and

rewards of scientific research. By participating in research in a real environment, the students often become more excited about careers in science and technology. In addition, LLE gains from the contributions of the many highly talented students who are attracted to the program.

The students spent most of their time working on their individual research projects with members of LLE's scientific staff. The projects were related to current research activities at LLE and covered a broad range of areas of interest including laser optics modeling, analysis of OMEGA implosion experiments, hydrodynamics modeling, cryogenic target physics and characterization, liquid crystal chemistry, thin-film deposition, and the development and control of laser fusion diagnostics. The students, their high schools, their LLE supervisors, and their project titles are listed in the table. Their written reports are collected in this volume.

The students attended weekly seminars on technical topics associated with LLE's research. Topics this year included lasers, fusion, holographic optics, hydrodynamic instability, laboratory astrophysics, computer-controlled optics manufacturing, and microcontrollers and their applications. The students also received safety training, learned how to give scientific presentations, and were introduced to LLE's resources, especially the computational facilities.

The program culminated on 28 August with the "High School Student Summer Research Symposium," at which the students presented the results of their research to an audience including parents, teachers, and LLE staff. Each student spoke for approximately ten minutes and answered questions. At the symposium the William D. Ryan Inspirational Teacher award was presented to Mr. James Keefer, a physics and

chemistry teacher at Brockport High School. This annual award honors a teacher, nominated by alumni of the LLE program, who has inspired outstanding students in the areas of science, mathematics, and technology. Mr. Keefer was nominated by Priya Rajasethupathy, a participant in the 2000 Summer Program.

A total of 145 high school students have participated in the program since it began in 1989. The students this year were selected from approximately 50 applicants. Each applicant submitted an essay describing their interests in science and technology, a copy of their transcript, and a letter of recommendation from a science or math teacher.

In the past, several participants of this program have gone on to become semifinalists and finalists in the prestigious, nationwide Intel Science Talent Search. This year, the program was particularly productive, resulting in the selection of three students (Siddhartha Ghosh, Phoebe Rounds, and Joy Yuan) as among the 300 semifinalists nationwide in this competition. Rounds was selected as a finalist in the Talent Search—an honor bestowed upon only 40 of the nearly 1600 participating students.

LLE plans to continue this program in future years. The program is strictly for students from Rochester-area high schools who have just completed their junior year. Applications are generally mailed out in early February with an application deadline near the end of March. For more information about the program or an application form, please contact Dr. R. Stephen Craxton at LLE.

This program was supported by the U.S. Department of Energy Office of Inertial Confinement Fusion under Cooperative Agreement No. DE-FC03-92SF19460.

High School Students and Projects (Summer 2002)

Name	High School	Supervisor	Brief Project Title
Megan Alexander	Honeoye Falls–Lima	J. Zuegel/W. Seka	Picket Pulse Shaping with Phase and Amplitude Modulation in the Frequency Domain
Stefan Astheimer	Honeoye Falls–Lima	P. B. Radha	Estimation of Magnetic Fields in Direct-Drive Implosions
Christine Balonek	Byron–Bergen	K. Marshall	Improvement of Self-Organization and Selective Reflection Quality in Lyotropic Crystalline Polysaccharide Films
David Dingeldine	Churchville–Chili	J. Knauer	Plasma Energy Measurement with an Open-Cell Metal Foam
Sonya Dumanis	Harley School	V. Smalyuk	
Sid Ghosh	Pittsford–Mendon	P. Jaanimagi	Secondary Electrons from X-Ray Photocathodes
Kyle Gibney	Livonia	C. Stoeckl	Computer-Controlled Neutron Diagnostics
Sharon Jin	Victor	S. Craxton	A Ray-Tracing Model for Cryogenic Target Uniformity Characterization
Jue Liao	Brighton	R. Epstein	Rayleigh–Taylor Growth Rates for Arbitrary Density Profiles Calculated with a Variational Method
Christopher Moody	Spencerport	D. Harding	Characterization of the Absorption Spectrum of Deuterium for Infrared Wavelengths
Phoebe Rounds	Irondequoit	S. Craxton	Multiple-Tripler Broad-Bandwidth Frequency Conversion for Laser Fusion
Micah Sanders	Pittsford–Mendon	N. Bassett	Thin Film Characterization of Al ₂ O ₃ Utilizing Reactive Pulsed dc Magnetron Sputtering
Gurshawn Singh	Rush–Henrietta	J. Marozas	2-D Pulsed Laser Beam Modeling Using PROP
Archana Venkataraman	Brighton	F. Marshall	Characterization of Multilayer Diffractors for Framed Monochromatic Imaging
Joy Yuan	Pittsford–Mendon	M. Guardalben	Noncollinear Phase Matching in Optical Parametric Chirped-Pulse Amplification

**Picket Pulse Shaping with Phase and Amplitude
Modulation in the Frequency Domain**

Megan Alexander

Pulse Shaping with Phase and Amplitude Modulation in the Frequency Domain

Megan Alexander

Advisors: Wolf Seka and Jonathan Zuegel

LABORATORY FOR LASER ENERGETICS

University of Rochester

250 East River Road

Rochester, NY, 14623-1299

ABSTRACT:

The conversion of transform-limited short laser pulses to shaped longer pulses with frequency chirp was investigated. A program was created to simulate how transform-limited short input pulse shapes can be converted into output pulses of desired temporal shape and phase. The program models both electric field and spectral intensities of the pulses, conserves energy, and accounts for spectral limitations set by the input pulse and experimental system limitations. This work serves as foundation for further studies of pulse shaping using transform-limited mode-locked input pulse trains.

INTRODUCTION:

Inertial confinement fusion (ICF) laser pulse shapes consist of a long “foot” forerunning the main pulse (Fig. 1). Replacing the low intensity foot pulse with a picket-fence pulse train has been suggested¹ to increase efficiency and power balance of ICF lasers. Therefore, investigating methods to provide arbitrary control of picket pulse shapes is deemed worthwhile.

Current pulse stretching methods employ diffraction gratings, which broaden the pulse, but do not allow arbitrary control of the resulting pulse phase. Pulse shaping through phase and amplitude modulation in the frequency domain would make the results more flexible and can be simulated computationally using such tools as MATLAB, the selected approach for this endeavor. MATLAB has many convenient tools to compute the pulse shape with and without phase chirp, as well as the corresponding spectra.

Specifications for laser pulses relate to ideal ICF conditions. Typical ICF implosion experiments require at least sixty large beams with identical well-defined pulse shapes. To achieve this, a very high degree of control of the laser pulse shapes and laser

amplification process is required. For laser physics reasons it turns out that picket-fence pulses may be preferable to continuous pulses. Hence the present pulse shaping code is a start to study picket-fence pulse shaping. Generally, a pulse with constant intensity can be well approximated by the average of a series of short, appropriately spaced, higher intensity pulses (see Fig. 1). The individual pulses of this series may have various pulse characteristics such a pulse shape or duration and/or time-varying frequency or phase (frequency chirp).

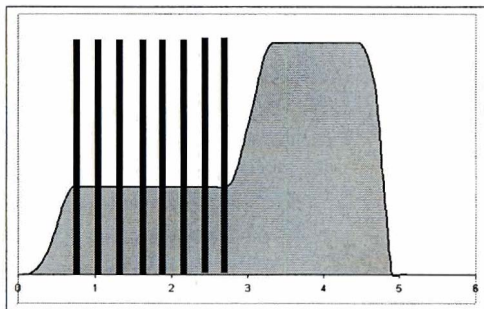


Figure 1: A standard ICF pulse with and without pickets.

The purpose of this project was to determine whether, to what degree, and how mode-locked laser pulses may be stretched through amplitude and phase changes in

the frequency domain. Keeping basic laws of physics in mind, like energy conservation, and allowing for various output pulse characteristics, a MATLAB program was developed to simulate this process. This program, FIREFLY simulates and compares input and output pulses under ideal conditions as well as non-optimal ones. The current version allows for single pulse generation only, though the same concepts apply to more complex scenarios involving pulse trains.

The desired output pulse is defined in the temporal domain both in terms of pulse shape and time-varying phase. For convenience we have chosen output pulses whose center frequencies change linearly during the pulse – also called a frequency chirp – that corresponds

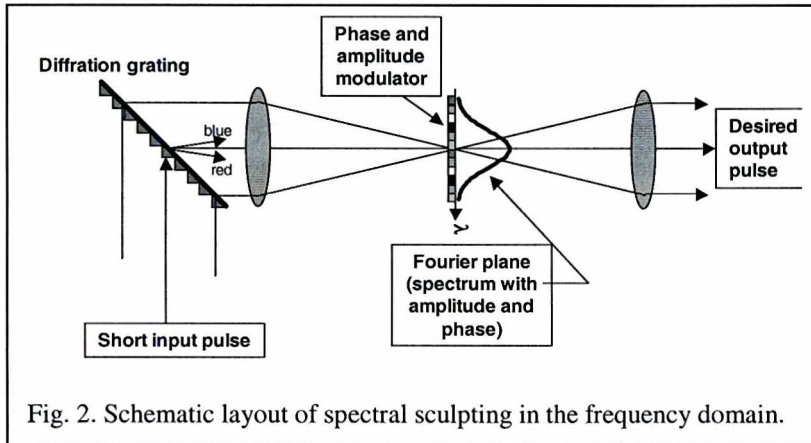


Fig. 2. Schematic layout of spectral sculping in the frequency domain.

to a quadratically changing phase with time. We then transform the input pulse and the desired output pulse mathematically into the spectral domain via Fourier transforms. Comparison of the input and desired output spectra in terms of amplitude *and* phase

then allows the specification of the Fourier amplitude and phase filters (or masks). It also allows the calculation of the efficiency of such devices. Thus, while the simulations impose the phase chirp in the temporal domain the real phase and amplitude modifications would be applied in the frequency domain.

Experimentally, one accesses the frequency domain by propagating the laser pulse through a diffraction grating followed by a converging lens. In the focal plane of this lens the pulse spectrum is dispersed as shown schematically in Fig. 2. This plane is the Fourier plane of the input pulse as well as the output pulse.

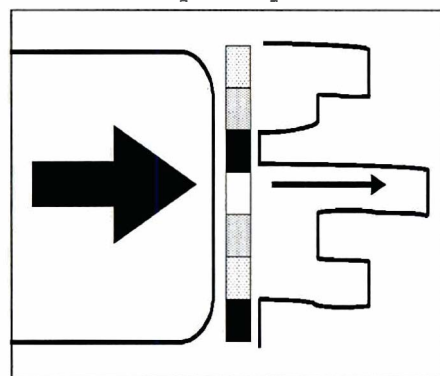


Figure 3: LCDs of varying transmission control the passage of an initially square beam (with frequencies dispersed in the vertical direction) through a sculping device. The output depends on the arrangement of LCDs.

Modifying the intensity or phase of different spectral components of the input laser pulse is then achieved by placing a mask (or masks, also called filters) in this plane as shown in Figures 2 and 3. These masks have spatially varying transmission or indices of refraction. The former changes the spectral pulse shape of the output pulse while the latter changes the optical path of a particular spectral component and thus its phase. These masks are typically linear arrays of liquid crystal devices (LCD) whose transmission or index of refraction depends on the applied voltage. Operating like miniature traffic signals, these cells may change the transmission for different lanes of light, thus sculping the spectrum of the beam (Fig. 3). To convert the output pulse back

into the temporal domain, it is passed through another lens (see Fig. 2).

It is of interest to note that the phase of a particular frequency component is really an angle whose magnitude is determined by the frequency chirp we desire for the

output pulse. While this angle may be computed to be very large, one may add or subtract any multiple of 2π radians (360°) to this angle without affecting the (output) pulse shape. Thus the phase mask only needs to modify the phase of any particular spectral component within 0 and 2π . The exact phase angle change is obtained by adding or subtracting an appropriate multiple of 2π from the phase change computed by the Fourier transform of the desired output pulse. Thus a desired phase change of 370° is equivalent to a phase change of 10° .

Another consequence of the Fourier relationship between time domain and frequency domain can be seen in Fig. 4. A single short pulse has a broad continuous spectrum indicated with the “individual picket” heading. The spectrum of a series (or train) of the same pulses leads to a channeled spectrum with the same envelope as the single pulse spectrum (sidebands). Computationally, the Fourier transform between time domain and frequency domain is obtain using fast Fourier transform algorithms (FFT). A similar algorithm is used for the inverse process (IFFT) that allows transitioning from the frequency domain to the temporal domain.

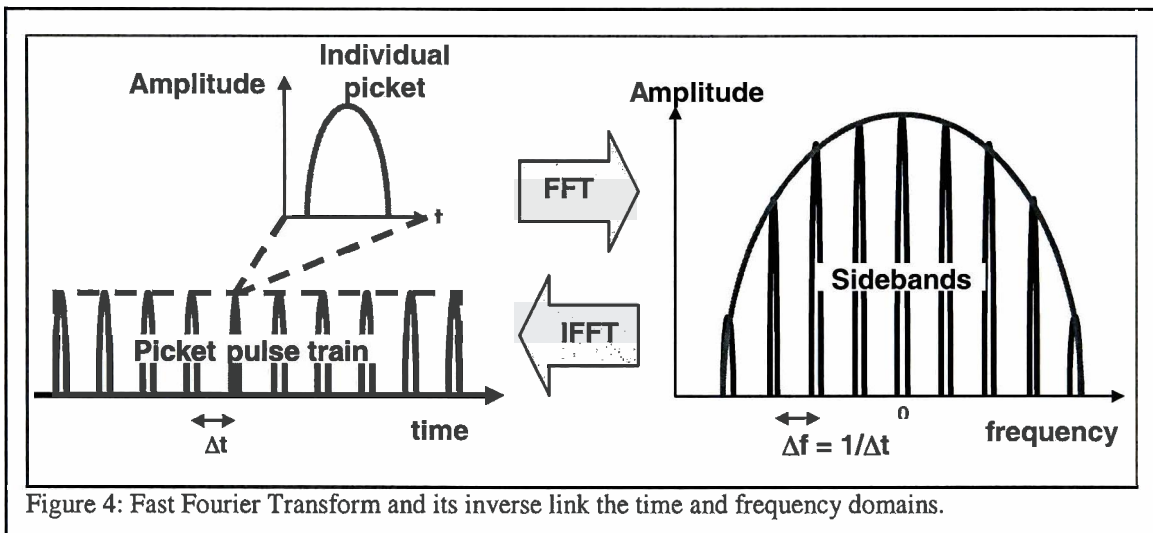


Figure 4: Fast Fourier Transform and its inverse link the time and frequency domains.

METHODS: FIREFLY simulates this experimental process by completing the same sequence of tasks: starting from an electric field for the short input pulse, its spectrum is obtained using a FFT conversion. Similarly, the desired output pulse is transformed to the spectral domain using a FFT conversion. Comparing the input and desired output spectra allows specification of the amplitude transmission and phase masks. In the present project we have restricted ourselves to comparing the input and output spectra in intensity and phase from which we also compute throughput efficiencies. The actual mask characteristics have not been computed explicitly but the spectral mask is obtained from simple ratios of the spectral intensities of the output and input pulses while the phase mask (within modulo 2π) is given by the calculated (desired) output phases (the input phase is constant and can be neglected since we have assumed a transform-limited input pulse shape).

The input to FIREFLY is a short (1-5 ps) laser pulse and its spectrum is calculated via fast Fourier transform simulating the effect of a grating and the lens in Fig. 2. We similarly calculate the spectrum for a specific requested output pulse (Full Width at Half Max [FWHM], pulse shape [Gaussian, super-Gaussian, sech], and phase [corresponding to a frequency chirp]).

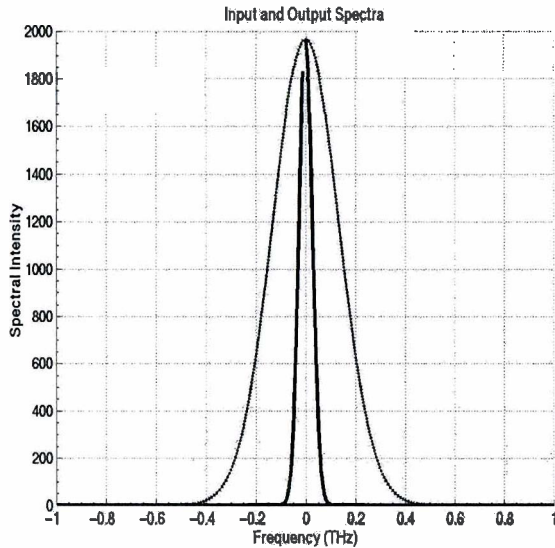


Figure 5: The spectrum of the wider output pulse fits entirely underneath that of the 2ps input pulse.

The short pulse has a corresponding broad spectrum (large bandwidth). The spectrum of the requested output pulse must fit under the envelope of the input pulse (Figure 5).

A transform-limited long output pulse has a much narrower spectrum than the input pulse as shown in Fig. 5. If the desired output pulse has an impressed frequency chirp the corresponding spectrum is wider and can more nearly (or completely) match the input spectrum. When the input and output spectra are identical, a maximum throughput efficiency of 100% can be achieved. Other conditions make sculpting much like the round peg and square hole paradox,

i.e., energy must be thrown away in order to return the desired pulse. This is expected and FIREFLY typically returns several alternatives along with the corresponding throughput efficiencies.

The area under the spectral intensity curves shown in Fig. 5 represents the pulse energy. Since the output spectral intensity must not exceed the input spectrum anywhere, the transform-limited long pulse contains much less energy than the short input pulse, leading to a low throughput efficiency. For desired output pulses with large frequency chirp and correspondingly large bandwidth (spectrum) we may have to take advantage of the extended spectral wings of the input pulse that are not easily visible in linear graphs such as Fig. 5. We must then force the output spectrum to fall

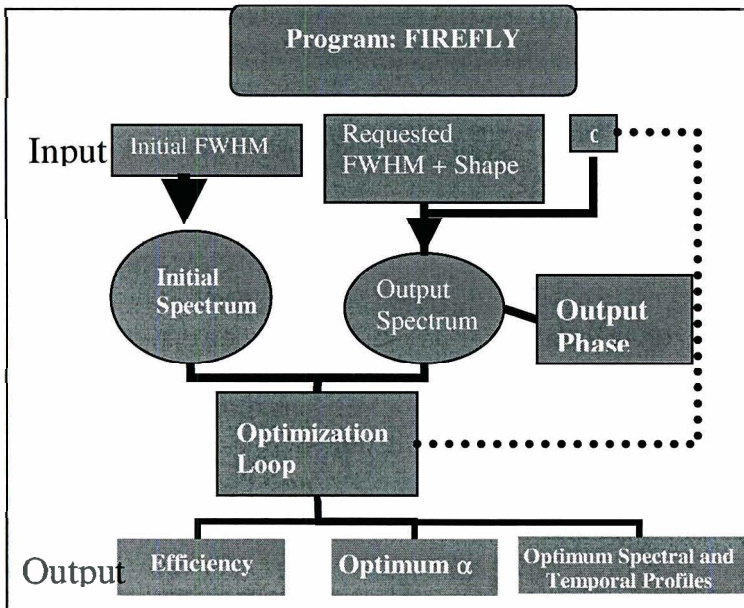


Figure 6: A schematic diagram of the workings of FIREFLY, phase and amplitude modulation program.

Since the output spectral intensity must not exceed the input spectrum anywhere, the transform-limited long pulse contains much less energy than the short input pulse, leading to a low throughput efficiency. For desired output pulses with large frequency chirp and correspondingly large bandwidth (spectrum) we may have to take advantage of the extended spectral wings of the input pulse that are not easily visible in linear graphs such as Fig. 5. We must then force the output spectrum to fall

entirely below the input spectrum (or touching it) everywhere by reducing its spectral amplitude. The consequence of this operation is reduced output energy and reduced throughput efficiency. The name of the process appropriately summarizes this concept: spectral sculpting. Just as a sculptor can never add material to his work, neither can we patch the spectrum. Instead, the desired figure is chipped away from the starting block.

The output spectra for various phase terms (or frequency chirps) are then calculated and fit under the input spectrum from which an optimum output pulse chirp is obtained such that the throughput efficiency reaches a maximum. The more closely the input and output spectra are matched, the greater the throughput efficiency.

FIREFLY furnishes a series of graphs consisting of pulse shapes, spectra, bandwidth, and throughput efficiency as a function of their phase modulation parameters. In addition, phase terms for each of the input, requested output, trial output, and actual output pulses are also provided by FIREFLY. Nested families of comparative pulses and spectra allow for the study of non-optimal alternatives. Figure 6 displays a flow chart of the operation of the program.

There are several potential implementation opportunities for this program. First, an extension to handle pulse trains is trivial. Second, more complex output pulse shapes may be tested easily for efficiency before experimental implementation. Quite generally, most parameters of the input and output pulses are easily modified making for convenient variable manipulation.

To implement these ideas in computer-operable mathematics we first specify numerically the desired output pulse characteristics as a function of time. Making use of the complex electric field notation the slowly varying amplitude of the electric field is multiplied by a slowly varying phase term

$$E = A(t) \cdot e^{i\phi(t)}, \quad (1)$$

where ϕ is defined by our assumed linear frequency chirp as

$$\phi = \alpha \cdot t^2. \quad (2)$$

The high frequency corresponding to the carrier frequency of light (corresponding to the color of the light) has been neglected. For an N'th order Gaussian the slowly varying electric field amplitude is given by

$$E = e^{-\left(\frac{t}{t_0}\right)^N}, \quad (3)$$

where t_0 is related to the FWHM by

$$t_0 = \frac{t_{FWHM}}{2 \cdot \left(\frac{\ln 2}{2}\right)^{\left(\frac{1}{N}\right)}}. \quad (4)$$

For a conventional Gaussian (N=2), $E = e^{-\left(t/t_0\right)^2}$. The intensity is proportional to the square of the electric field,

$$I \propto E^2. \tag{5}$$

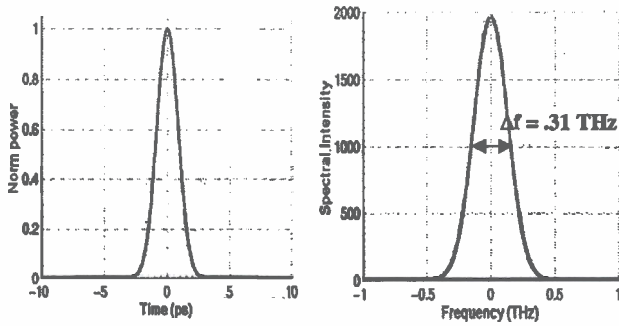


Figure 7: A Gaussian pulse of width 2 ps at FWHM translates to a spectrum of bandwidth 0.31 THz.

In most experiments one measures intensities rather than electric fields, although the field generally contains more detailed information about the phase. The FFT of the field is therefore the useful calculation and reveals the characteristics of the spectrally or temporally varying phase, but the spectral intensity is the useful graph as it represents an easily measured quantity. The square of the magnitude of the

complex Fourier transformed field represents this spectral intensity, just as the square of the electric field in the time domain represents the temporally varying intensity. (Fig.7). Since we have adopted the complex notation of the electric field, the phase angle is given by

$$\phi = \text{Tan}^{-1} \left(\frac{\text{Im}(E)}{\text{Re}(E)} \right)$$

(see Fig. 8), where Im(E) and Re(E) are the imaginary and the real part of the electric field.

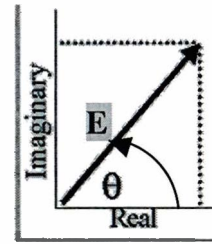


Figure 8: Phase angle is the electric field angle in the complex plane.

RESULTS AND DISCUSSION: The results of a series of runs with FIREFLY are very instructive and lead to some generally applicable conclusions.

Figures 9 to 11 contains sample outputs of the program FIREFLY. Figure 9 contains graphs pertaining to one particular Gaussian (N=2) input pulse of 2 ps FWHM and two Gaussian output pulses of 10 ps FWHM. One of the 10 ps Gaussian output pulses is transform-limited while the other one has an imposed optimal frequency chirp for 100% throughput efficiency. Figure 9a displays the short input pulse and the long output pulse once normalized (heavy line) and then properly scaled to the short pulse intensity (dashed line) for the optimum frequency chirp that leads to 100% throughput efficiency (i.e., no energy loss, see Fig. 9c). The transform-limited 10 ps output pulse has a peak intensity approximately 5 times lower than the dashed pulse shown in Fig 9a with a corresponding throughput efficiency of ~ 20%. Figure 9b displays the spectra for the 2 ps input pulse (~0.3 THz bandwidth) and the transform-limited 10 ps output pulse (heavy line). The spectrum for the optimally chirped 10 ps output pulse is identical to that of the input pulse. The spectral phase variations of the output pulses are shown in Fig. 9d for the transform-limited output pulse (horizontal line =constant phase) and the optimally chirped pulse (parabola). The maximum phase excursion over three times the bandwidth (~1 THz) is ~81 radians. Of course, a typical phase filter would not span the 81 rad but rather cover only the range between 0 and 2π phase shifts with appropriate multiples of 2π subtracted from the phase drawn in Fig. 9d.

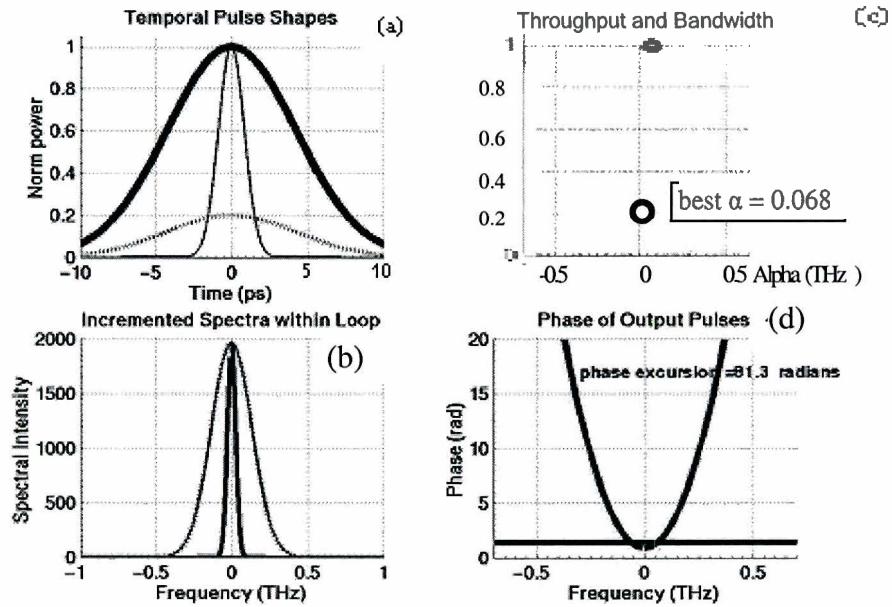


Figure 9: Input (thin), requested output (thick), and actual output (dotted) temporal pulse shapes and spectra, as well as parabolic phase applied to achieve actual output spectrum.

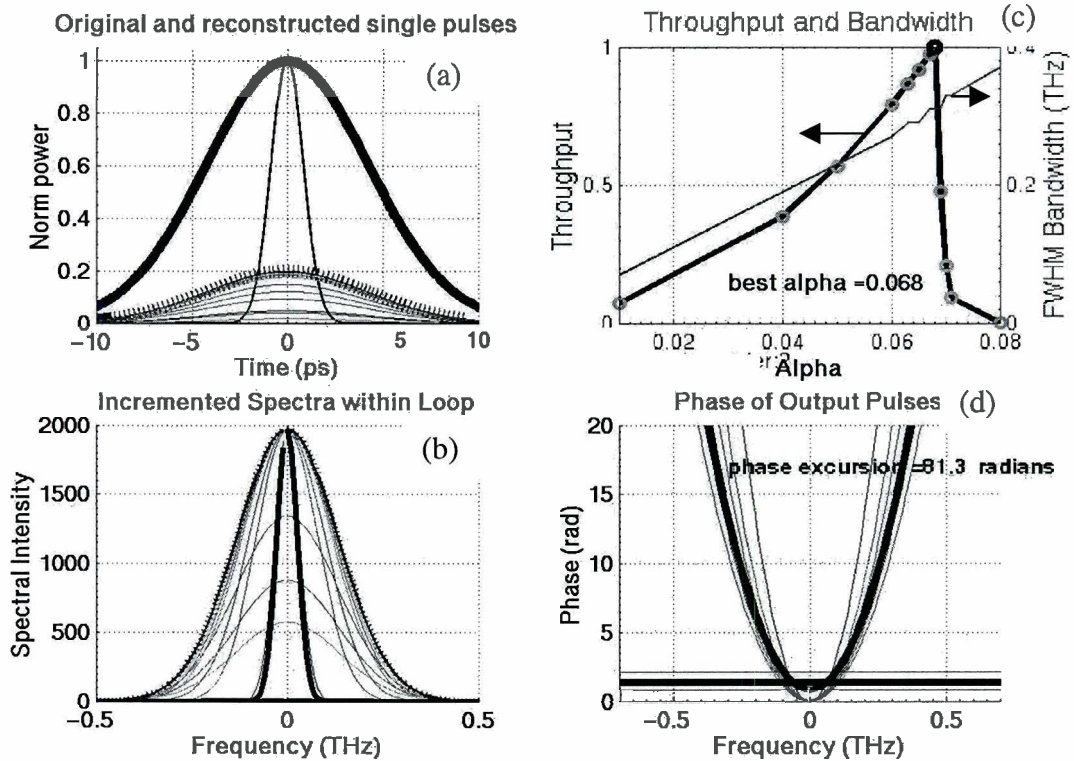


Figure 10: The continuation of the program run from figure 8a shows temporal and frequency domain pulse families, as well as a completed throughput graph for all evaluated α .

Each of the initial pulse shapes have 10 ps FWHM but the highest peak amplitude is reached for the optimally chirped pulse (same as in Fig. 9), while smaller or larger chirps lead to smaller peak amplitudes and correspondingly smaller throughput efficiencies (Fig. 10a-c). The spectra are seen to gradually broaden (Fig. 10c), until the input spectrum is exceeded, at which point the spectral amplitudes must be reduced to fit under the input spectrum. Note that we have arbitrarily chosen a frequency cut-off point at ± 0.75 THz beyond which we did not force the output spectrum to lie below the input spectrum. Since there is no appreciable spectral intensity beyond that point this does not introduce a significant error. However, in the strictest interpretation of the spectral shaping philosophy the throughput efficiency would drop to zero for an arbitrarily small incremental increase in bandwidth beyond the optimum. The throughput efficiency (thick line) and bandwidth (thin line) of the output pulses with varying phase parameter α are shown in Fig. 10b. The throughput gradually increases up to 100% and drops precipitously beyond that while the bandwidth continues to increase monotonically.

From Fig. 10c it is easily seen that beyond the optimum frequency chirp the throughput efficiency drops extremely rapidly and any experimental arrangement would best aim at a bandwidth slightly below the optimum bandwidth in order to avoid potentially devastating losses in throughput efficiency for small increases in bandwidth.

Depending on the laser system to which this pulse shaping scheme is to be applied the optimum chirp from a throughput efficiency point of view may not correspond to that of the laser system. The program FIERFLY allows finding a combined optimum by varying the input pulse shape such that the optimum bandwidth and throughput efficiency are indeed obtained near the optimum for the laser system.

Figure 11 displays the output for a super-Gaussian ($N=4$) output pulse shape. We note that the maximum throughput efficiency (Fig. 11c) is significantly lower than for a standard Gaussian (Fig. 10c), as the shapes dictate certain losses. In general, for output pulse shapes that are different from the input pulse shape the maximum throughput efficiency is less than 100% and depends on the particular input and output pulse characteristics.

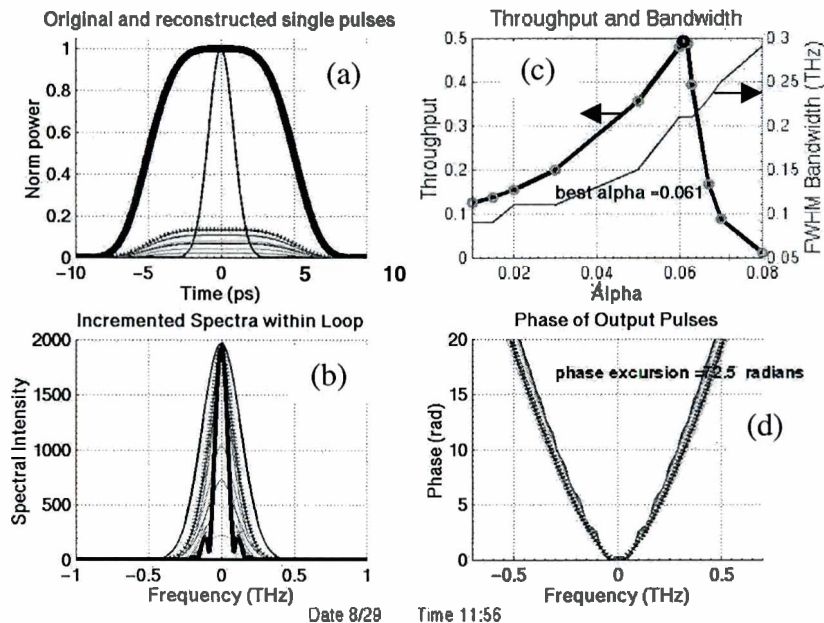
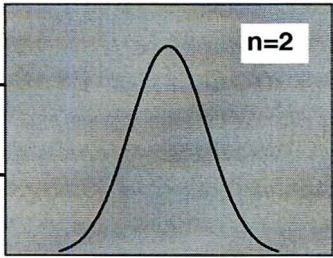
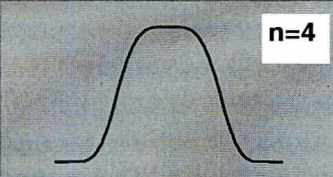



Figure 11: 4th order super-Gaussians are able to be created, with lower throughput and larger phase excursions.

Table 1. is a summary of results given by FIREFLY, evidencing the relationship between input, output, and throughput conditions. As shown in Table 1, wider input pulses yield less bandwidth. Since the object is to match the bandwidth of the input pulse, changing that value essentially allows working backwards and optimizing both throughput and bandwidth to optimally fit the laser system.

	Output Pulse Shape	Input FWHM (ps)	Optimum α	Throughput	Bandwidth (THz)
Gaussian		1	0.138	100%	0.63
		2	0.068	100%	0.31
		3	0.044	100%	0.21
Super-Gaussian		1	0.183	73%	0.69
		2	0.061	49%	0.21
		1	0.172	69%	0.59

There are several advantages to designing the code using the aforementioned methods and functions. First of all, computer simulations allow for convenient testing, whereas laboratory setups are much more time consuming and expensive. Performing all manipulation in the frequency domain parallels experimental methods, which shape in the fourier plane, i.e., in frequency space. Additionally, arbitrary control of pulse shape and duration is a new and intriguing capability that brings versatility to the shaping process.

The current optimization scheme is based on throughput only but other criteria may be just as important or even more so. Refinements of the present simulations and optimization code could quite easily be implemented and allow for more general optimization schemes as well more general phase modulation schemes beyond the simple linear phase chirp assumed in the present work. Overall, the goals of the present project have been met and the simulation code FIREFLY works quickly and yields useful results.

CONCLUSIONS:

Picket pulse shaping through amplitude and phase modulation in the frequency domain has been demonstrated in computer simulations albeit within self-imposed constraints (e.g. linear chirp). In the simulations, transform-limited short laser pulses have been shaped using spectral amplitude and phase control. Gaussian and super-Gaussian pickets have been optimized under hypothetical conditions for energy transfer.

REFERENCES:

1. J.E. Rothenberg, "Ultrafast picket fence pulse trains to enhance frequency conversion of shaped inertial confinement fusion laser pulses," Appl. Opt. 39, 6931-6938 (2000).

ACKNOWLEDGMENTS:

I would like to send out thanks to the motivators and instigators of my summer's work. Thank you, Dr. Craxton for maintaining this program and allowing us all to be here; Dr. Seka, I'm eternally grateful for your infinite patience and expertise you kindly shared with me; Dr. Zuegel, your perspectives and mantras have been invaluable to me and will not be forgotten; Dr. Marozas, thanks for your explanations and mathematical know-how; Dr. Myatt, for your MATLAB advice. To the rest of the lab, this has truly been an unparalleled experience, and I am grateful to you all for providing this environment.

Estimation of Magnetic Fields in Direct-Drive Implosions

Stefan Asheimer

Estimation of Magnetic Fields in Direct Drive Implosions

By Stefan Astheimer

TABLE OF CONTENTS

1.	INTRODUCTION	2
2.	ABOUT THE DRACO SIMULATION	3
	BACKGROUND.....	4
3.	COMPUTATIONAL PROCESSES	4
	NONCOLLINEAR GRADIENT COMPUTATION	4
	CURL CALCULATION.....	5
	FIELD CALCULATION.....	5
	LENGTH SCALE CALCULATIONS.....	7
4.	RESULTS	7
	TRAJECTORY BEND CALCULATIONS	7
	OTHER POSSIBLE ISSUES	8
5.	CONCLUSIONS	9
6.	ACKNOWLEDGMENTS	10
7.	APPENDIX A: EQUATIONS	11
8.	APPENDIX B: FIGURES	14

Abstract

Charged particles are used to infer the extent of compression in implosions on OMEGA. Statistically significant variances in particle yield have been observed at different locations around the target. These variations are unexpected because the fusion reaction that produces the charged particles is isotropic. One possible cause for this deviation could be the existence of magnetic fields in the target. Magnetic fields can result from hydrodynamic instabilities in the implosion. Large fields would be able to bend the trajectories of charged particles significantly, possibly causing this variation in the particle yield. Using results from a two-dimensional hydrodynamic simulation of an implosion, the magnetic field source term and resulting deflection of charged particles have been estimated. The estimated strength of the magnetic field should be regarded as an upper limit as it does not include effects of return currents etc. The calculated deflection is small, but not irrelevant when compared with the slit size of the measurement devices. This suggests that magnetic fields cannot be ruled out as a possible cause for the variation in charged particle yields.

1. Introduction

Direct drive fusion implosions are a very important field of research in today's scientific community. They may hold the keys to unlimited power supply and also offer a laboratory for the study of astrophysical phenomena. Thus, it is important that we understand all that we can about these implosions. Scientists use the distribution of charged particles produced in the fuel core to infer about compression. Since particle production is isotropic, scientists expect a very even distribution of particle yield with

respect to placement of the detector. This should be true even if there are nonuniformities in the target. However, instead, scientists find a distribution that varies greatly in places (see Figure 1). In fact, there is deviation by as much as a factor of two between detectors. There are a variety of possible reasons for this unusual distribution; one possible cause is the presence of magnetic fields, which can be created internally in direct drive implosions.

Density and temperature gradients in inertial confinement fusion implosions result in hydrodynamic instabilities. These instabilities result in non-collinear gradients in the density of charge and electron temperature around the fuel shell and ablation surface of the implosion. These gradients lead to the formation of magnetic fields at the surfaces. These fields can cause particles, even the most energetic, to change trajectories, and deflect as they pass through the field. To determine whether or not internally created magnetic fields are actually responsible for the altered variance, we used a DRACO hydrocode simulation to estimate the magnitude of the fields and the resultant deflection of charged particles. In section II, we will describe the simulation. Section III describes the steps involved in the calculation of the magnetic field. Section IV discusses the results in the context of particle trajectories, and we conclude in section V.

2. About the DRACO Simulation

DRACO is a two dimensional hydrocode that models the conditions of an implosion, similar to those at the LLE. In the simulation considered, DRACO takes into account nonuniformities in the laser. It should be noted that the magnetic field computations we have performed are post-processing computations. Had the magnetic field computations been placed inside of the actual simulation, there would need to be

adjustment for back-current and convection which are formed by the movement of plasma, and which partially counteract the effects of the magnetic fields. Thus, what is estimated is an upper limit on the magnitudes of the magnetic fields.

Background

Nonuniformities in the incident laser light are imprinted on the plastic shell of the core. These imprinted perturbations grow during the ablation phase. Furthermore, through a process known as feedthrough, these perturbations travel through the plastic shell and are imprinted on the fuel surface. During the compression phase, these perturbations grow as Rayleigh-Taylor instabilities, and can give rise to the magnetic fields during the time of peak particle production.

In the absence of fields, since particle production is isotropic, the particles should be evenly incident on different placements of the detector. However, if the magnetic field is significant and nonuniform enough, the trajectories will be altered, and the particles will deflect, leading to an altered distribution.

3. Computational Processes

NonCollinear Gradient Computation

Maxwell's laws were used to compute the strength of the magnetic fields. Maxwell's laws express magnetic field strength as the cross product of the gradients of electron density and temperature (see appendix A). We therefore compute the gradients of electron density and temperature in order to compute the magnitude of the magnetic fields at the time of peak particle production. Figures 2 through 5 show contour plots of

charge density and cell temperature, as well as vector diagrams of their respective gradients. The gradients are computed numerically from the values of a given cell and its neighbors, and the distances between cells. Because the gradients are computed using the neighboring cells, the gradients of the innermost and outermost cells are not calculated. However, by looking at the contour plots of electron density and temperature, it is clear that the values near the origin and very far from the center are very uniform. Thus, the magnetic fields at these places are so trivial as to be irrelevant to further computations.

Curl Calculation

Figure 6 depicts the values of the partial time derivative of the magnetic field at the time of 1.9 ns, which is the time of peak particle production. The values of this partial derivative were computed using the Maxwell equations for magnetic fields. The time derivative is expressed as a function of the cross product of the gradients of electron density and cell temperature at the time step. Notice that there are two places where the derivative is exceptionally high. The closer of the two, located approximately 35 microns from the center, is the fuel shell interface; the farther away of the two is from residual gradients arising from instabilities in the ablation surface earlier in the implosion during the acceleration phase. Finally, notice that the derivative takes both positive and negative values. This shows that the magnetic field assumes both positive and negative directions.

Field Calculation

Figure 7 shows the magnitude of the magnetic field's strength after the implosion has gone on for 1.9 nanoseconds. This time step is of particular interest because this is

the time at which particle production is greatest. Unfortunately, the simulation records its output only once every 20 picoseconds, and the fuel cell surface of the target traverses a distance of almost 4 microns in the 20 picoseconds between measurements at 1.88ns and 1.9 ns, thus, it is almost impossible to create an accurate time integral over even such a small period of time. Instead, the magnetic field strength was computed by multiplying the interpolated values of the field strength gradient by the time interval of 30 picoseconds to obtain an approximate integral value. This time interval was computed by dividing the approximate length of the significant fields (10 microns) by the velocity at which the fluid moves (about 30,000,000 cm/s). This gives a timescale for which the motion of the field is, more or less, reasonable (Appendix A). The magnetic field is greatest, the order of 1 to 10 MegaGauss, at a distance of about 35 microns from the center of the target. The magnitude of the earth's magnetic field is approximately one quarter of a Gauss, and the largest fields ever created in a lab setting are on the order of 1-10 KiloGauss, which is about one thousand times less potent than the implosion's fields. Clearly the magnetic fields in these implosions are immensely powerful. Recall that this distance almost exactly correlates to the boundary of the fuel-shell surface. These instabilities have created noncollinear temperature and density gradients that resulted in the formation of the magnetic field. There is also a smaller field at about 70 microns out, which is a remnant from earlier instabilities that were created at the boundary of the ablation surface during the early parts of the implosion. At all other places, the magnetic fields are only on the order of a few gauss, and thus comparatively negligible. Notice the width of the band of high field strength at the fuel shell interface. It is on the order of 2 to 10 microns, however, it is generally only 2 to 4 microns wide.

Length Scale Calculations

Figures 8 and 9 show the computed scale length with respect to both electron density and cell temperature at the time of peak particle production. These lengths were computed by taking the values of electron density and cell temperature and dividing them by the norms of their respective gradients. The figures show that these fields have lengths of between 2 and 10 microns. Notice that the temperature length scales at the fuel shell surface are much greater than density length scales. This is because at the fuel shell interface, the electron density changes drastically across a very small distance, however, as we have seen in Figures 2 through 5, the temperature changes gradually across a relatively large distance.

4. Results

Trajectory Bend Calculations

Figures 10 and 11 depict the amount of bending that 14.5 MeV protons and 10 MeV deuterons experience as they pass through magnetic fields of varying strength and width. These particles are of interest as they are used to infer compression in fusion implosions. The values for these were computed outside the simulation and the postprocessing code. The Larmor radius and the magnitude of the field were calculated from the postprocessing data, and plotted separately to determine an approximate range of deflection values. The angles by which the particles were deflected were on the order of one tenth of a degree, or one six-hundredth of a radian. Notice that the amount of deflection varies more or less hyperbolically with changes in either field strength or scale length. Also observe that fields of strength of one or more MegaGauss require a

relatively small scale to alter the trajectory of these highly energetic protons and deuterons. These relevant magnitudes are present near the fuel shell interface. In a number of places, the particles may be subjected to such fields for distances of five to ten microns if they are deflected back into the field. These distances are more than enough to cause some very energetic particles like the protons and deuterons to deflect by as much as a third to a half of a millimeter as they travel the distance, about 20 centimeters, between their egress from the significant magnetic fields and their incidence upon the detector. This deflection is significant when compared to the slit width of the detector, so although the angles of deflection are tiny, the distance the particles travel, 20 cm, is large enough compared to the detector's slit width to lead to significant deflection.

Other Possible Issues

Internally created magnetic fields may not be the only things to alter the trajectories of charged particles. The most obvious explanation for the varied distribution may be related to the detectors themselves. One possible error may be a lack of cross calibration. However, the producers of the spectrometer which was used as a detector are reasonably sure that no such faults exist in their devices. Thus, we will not consider the experimental apparatus as a source for such large errors. There are a number of other possible properties of the implosion that may also play a role. First, it has been hypothesized that there exist external magnetic fields that are formed during the implosion. These externally created magnetic fields may have some impact on the paths of the particles, but we have no estimate of their size, and it seems very unlikely that, without the massive gradients of electron density and temperature present at the fuel shell interface, the external fields are large enough to bend the trajectories significantly.

(Recall that the magnetic fields at the fuel shell interface during the time of peak particle production are on the order of a thousand times greater than any ever created in a controlled environment.) Second, it is possible that the laser itself influences the motion of the particles. However, since the laser has been turned off almost one whole nanosecond before the time of peak particle production, the magnitudes of the magnetic fields intrinsic to the laser beams may have decayed to irrelevant trace levels. Thus, the lasers themselves may have little if any effect on the trajectories, especially those of such energetic charged particles. Finally, it is possible that particle production is actually anisotropic with respect to angle. Plasma properties, such as a polarization of the spin of the fusing ions, may result in nonuniformities in particle production. If this were the case the distribution of energetic, charged particles would not be uniform, regardless of the presence of magnetic fields. However, there have been many tests done, showing that the processes involved in the particle production in lower temperature laboratory situations are isotropic. It is logical to extend this generalization to high temperatures and densities. In doing so, we can assume that the contribution from spin polarization is small.

5. Conclusions

It should be noted that the hydrodynamic properties of the plasma are not affected by the magnetic fields very much. The absolute maximum pressure exerted by the magnetic fields is on the order of one million atmospheres, approximately two orders of magnitude lower than the minimum value of the intrinsically created pressure of the plasma. Thus, there is approximately a 1% deviation in hydrodynamic attributes as a result of these magnetic fields. Considering that this is at the time when the magnetic

fields are at some of their greatest values, it is indicative that there will never be much greater than 1% deviation as a result of the magnetic fields.

Clearly, it is possible that the magnitudes of the internally created magnetic fields at the time of peak particle production are large enough to cause the trajectories of highly energetic particles to bend by as much as a few tenths of a millimeter after they travel 20 cm from the field. To accurately determine how large the deflection is and what the effect on the distribution is, two things need to be done. First, there need to be self consistent calculations which take into account back current and convection. Second, there also needs to be a particle trajectory-tracking program that determines the amount of deflection as a function of angle of emission. Furthermore, this program would actually compute the yield for the changing magnetic fields. This work indicates that magnetic fields cannot be ruled out as the cause of this variation in particle yields around an imploding target.

6. Acknowledgments

I would like to thank Dr. R. S. Craxton for running the program, and allowing me to participate in this summer program. I would also like to thank Chris Piro, Matt Fiedler, and everyone else who has helped me with my project and presentation. Most of all, I would like to thank my advisor, Dr. Radha Bahukutumbi for assisting, teaching and mentoring me.

7. Appendix A: Equations

Variables And Constants:

n_e : electron density

e : elementary charge of an electron

E : electric field strength

k : Boltzmann constant

t_e : electron temperature

c : light speed

B : magnetic field strength

v : the velocity of the fluid

l : the length scale for the field

r : the radial coordinates of a cell in the simulation

θ : the polar coordinate of a cell in the simulation

The formula for the electric field in terms of the electron pressure gradient:

$$n_e e E = \nabla(n_e k t_e)$$

Faraday's Law; the law which gives the time dependent partial derivative of magnetic field strength as a function of the curl of electric field strength:

$$\nabla \times E = \frac{-1}{c} \frac{\partial B}{\partial t}$$

The formula used to calculate the time dependent partial derivative of the magnetic field as a function of the cross product of the gradients of electron temperature and density; this formula is a combination of the electrical field formula and Faraday's law:

$$\frac{\partial B}{\partial t} = \frac{ck}{en_e} \nabla n_e \times \nabla t_e$$

These gradients were computed numerically by taking a Taylor series approximation of the differences in values of t_e and n_e over a set of cells, around one cell a , in the radial and polar directions, yielding:

$$\begin{aligned} \frac{\partial t_e}{\partial r}(a) &= \frac{1}{\Delta r_{31} \Delta \theta_{42} - \Delta r_{42} \Delta \theta_{31}} \left((\Delta \theta_{42} t_{e3} + \Delta r_{42} t_{e1}) - (\Delta \theta_{42} t_{e1} + \Delta r_{31} t_{e3}) \right) \\ \frac{\partial t_e}{\partial \theta}(a) &= \frac{1}{\Delta r_{31} \Delta \theta_{42} - \Delta r_{42} \Delta \theta_{31}} \left((\Delta r_{31} t_{e4} + \Delta \theta_{31} t_{e2}) - (\Delta \theta_{42} t_{e2} + \Delta r_{31} t_{e4}) \right) \\ \frac{\partial n_e}{\partial r}(a) &= \frac{1}{\Delta r_{31} \Delta \theta_{42} - \Delta r_{42} \Delta \theta_{31}} \left((\Delta \theta_{42} n_{e3} + \Delta r_{42} n_{e1}) - (\Delta \theta_{42} n_{e1} + \Delta r_{31} n_{e3}) \right) \\ \frac{\partial n_e}{\partial \theta}(a) &= \frac{1}{\Delta r_{31} \Delta \theta_{42} - \Delta r_{42} \Delta \theta_{31}} \left((\Delta r_{31} n_{e4} + \Delta \theta_{31} n_{e2}) - (\Delta \theta_{42} n_{e2} + \Delta r_{31} n_{e4}) \right) \end{aligned}$$

Here the subscripts correspond to the values of r , θ , n_e , and t_e at the four cells neighboring a . From here we can express our gradients in terms of these partial derivatives.

The formula for the time scale of integration (a sensitivity analysis for the scale length was incorporated into the deflection calculation):

$$\frac{l}{v} \approx \frac{10\mu m}{3 \times 10^7 \frac{cm}{s}} = 30 ps$$

Calculations of Trajectory Bending

As long as a moving, charged particle is acted on by a magnetic field it will bend along a circular path. The radius of this circle is given by:

$$r = \frac{mv}{qB}.$$

where m , v , and q are the particle's mass, velocity and charge respectively, and B is the magnetic field's magnitude. We know the values of m , v , and q for different particles, so using trigonometry, we can compute the amount of deflection when the particles reach the detector, which is a distance of 20 cm, as a function of r and d , the distance over which the field acts on the particle.

8. Appendix B: Figures

Figure 1: This graph shows particle yield as a function of the placement of the detector. There are statistically significant differences between yield at different placements; KO-1 and TIM-5 for example.

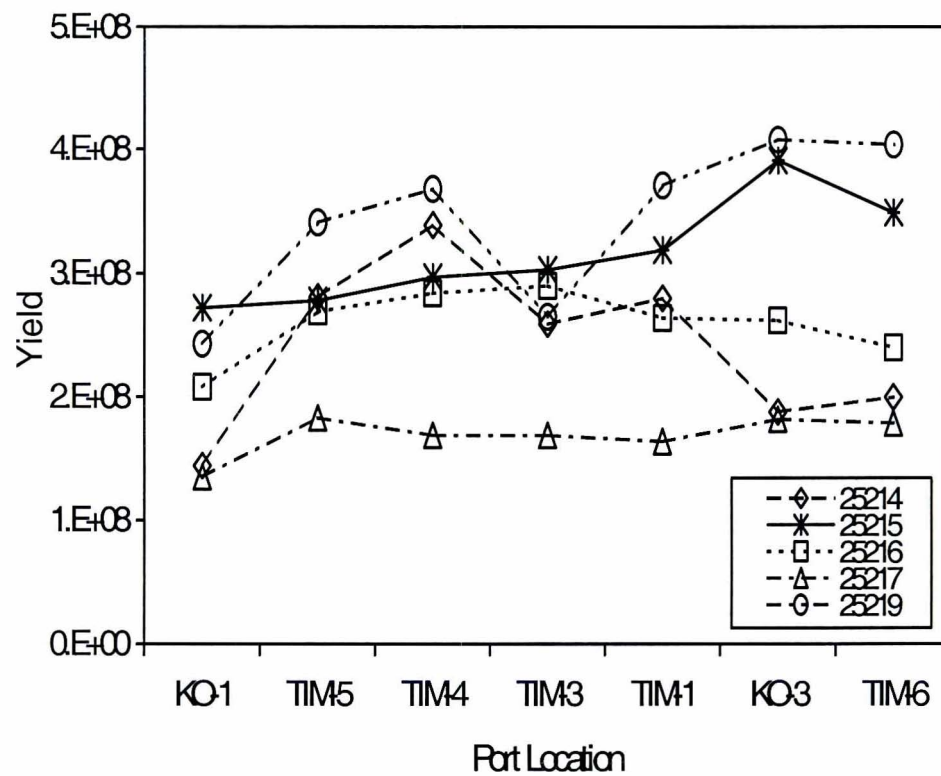


Figure 2: This contour plot shows the electron density in the imploding target at the time of peak particle production (about 1.9 ns). Notice the two “layers” of the graph. The sharp change between these layers represents the fuel shell surface. The irregularities in this interface are caused by the nonuniformities in the laser that are modeled in the DRACO simulation.

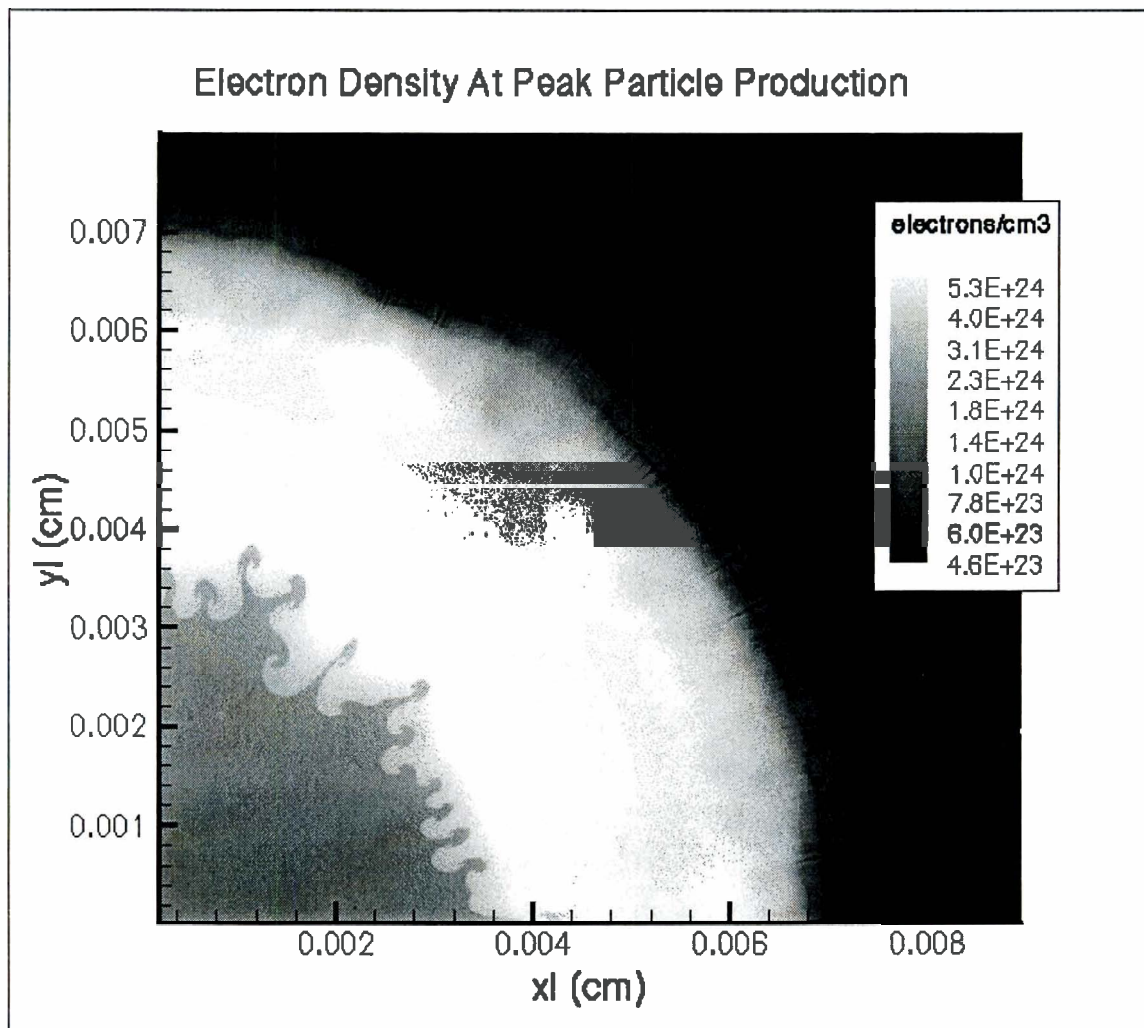


Figure 3: This contour plot shows electron temperatures in the imploding target at the time of peak particle production.

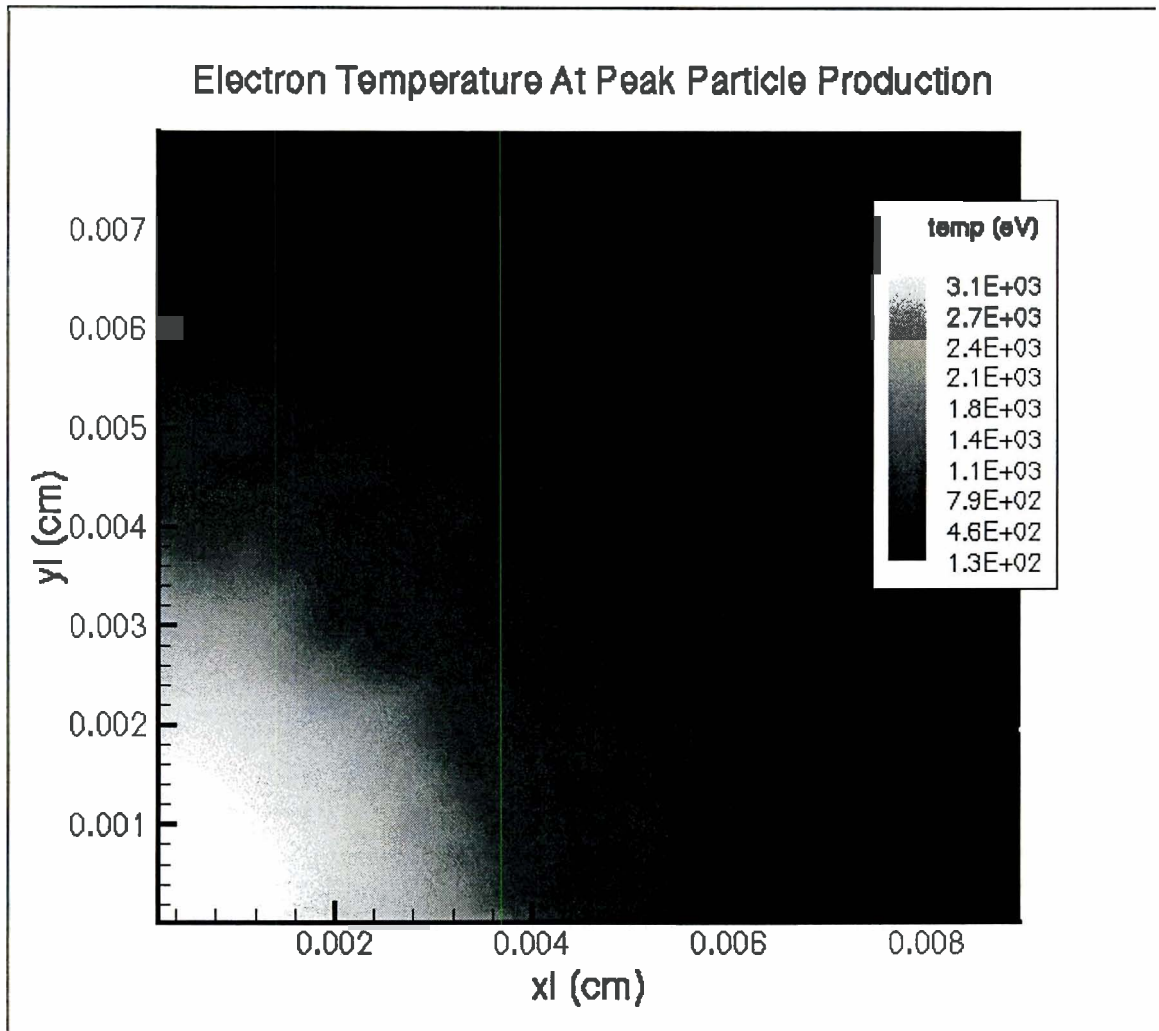


Figure 4: This diagram shows the vector gradients of the electron temperature at the time of peak particle production. Notice that the vectors at the fuel shell surface are orders of magnitude larger than those farther away. Also notice that the nonuniformities imprinted on the surface by the laser have led to gradients which do not follow a nice flow.

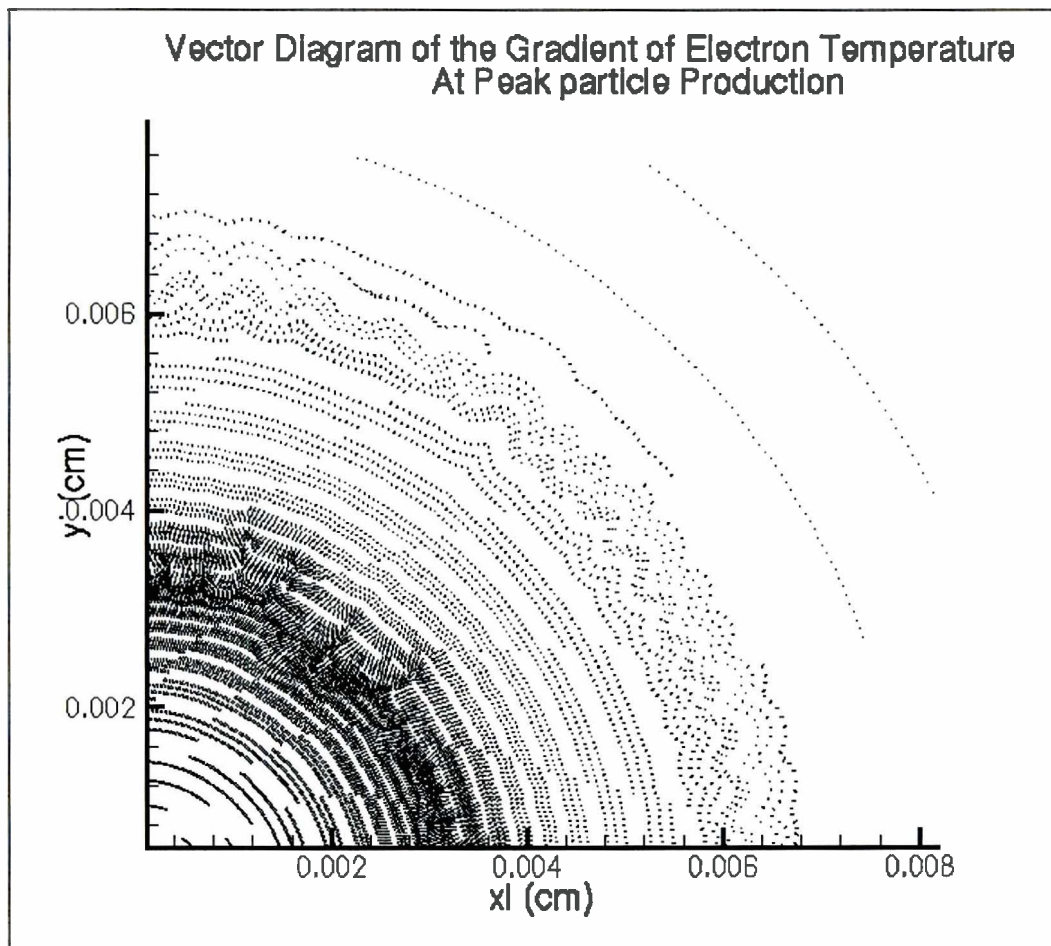


Figure 5: This diagram shows the vector gradients of the electron density at the time of peak particle production. Notice that while the vectors at the fuel shell surface are somewhat larger than those farther away, there is more uniformity here both in magnitude and direction of the vectors.

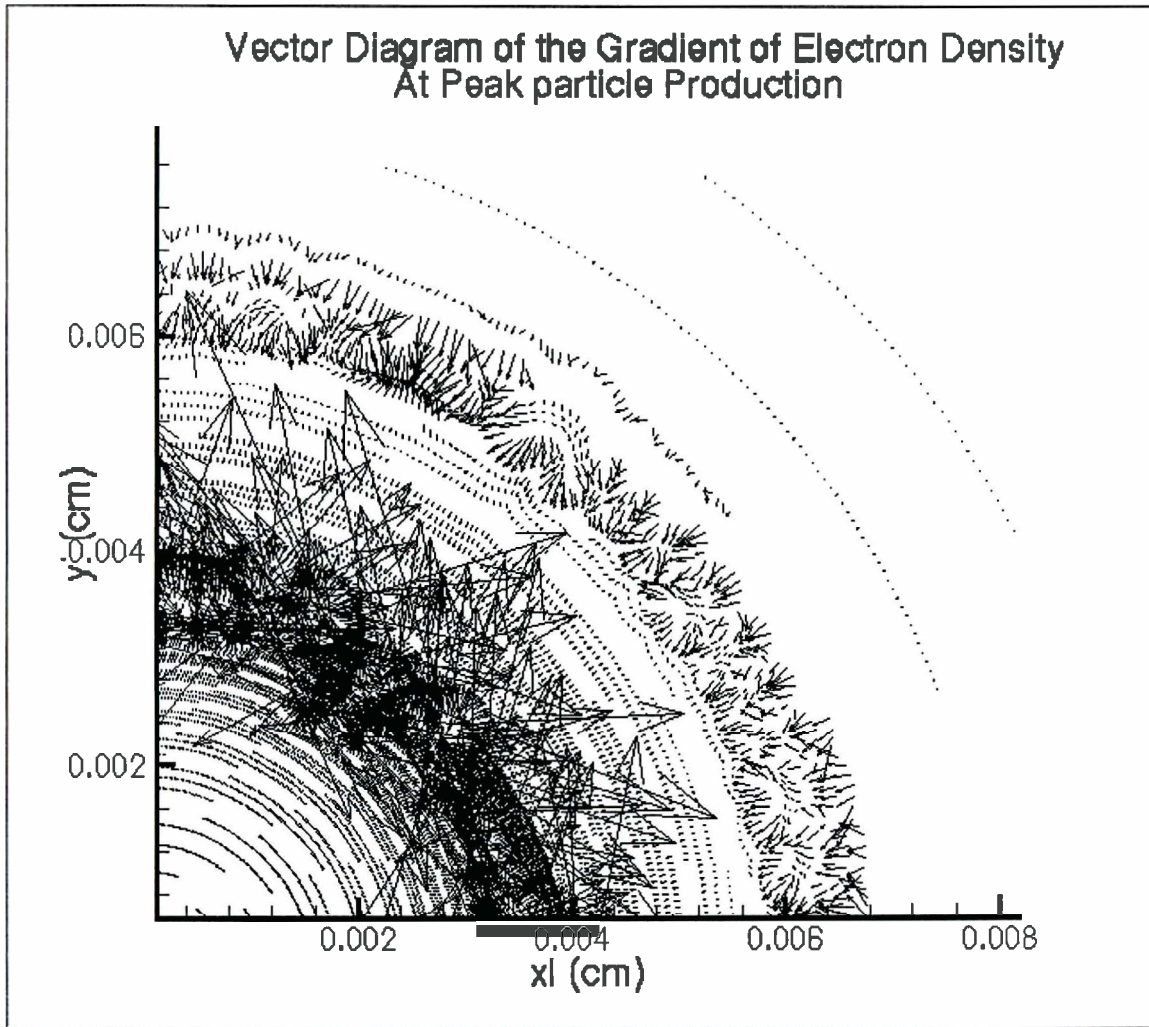


Figure 6: This contour plot shows the partial time derivative of magnetic field strength at the time of peak particle production.

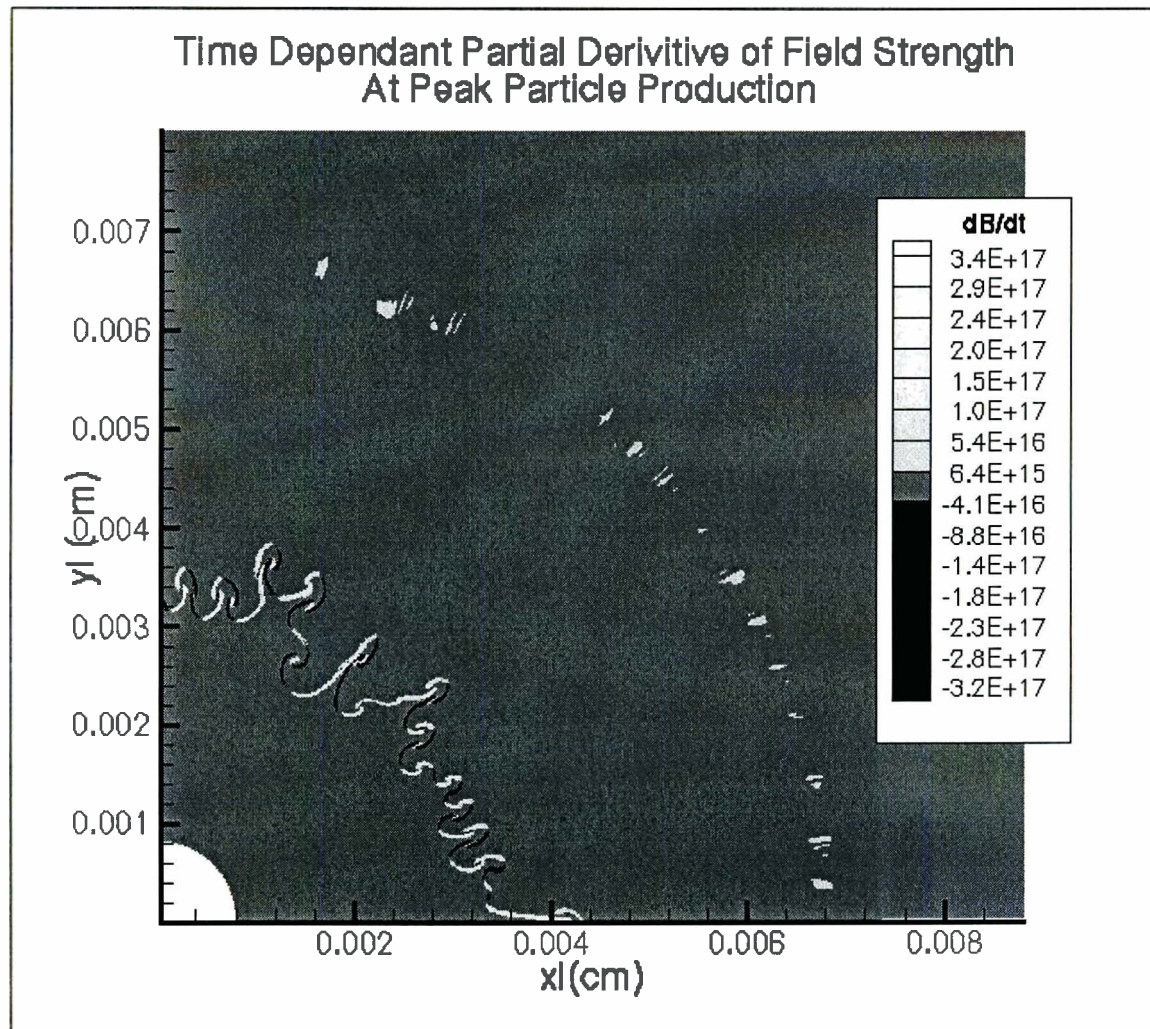


Figure 7: This contour plot shows the value of the magnetic field strength in the target at the time of peak particle production. Notice that the fields are (relatively) small except near the fuel shell interface where they are immense.

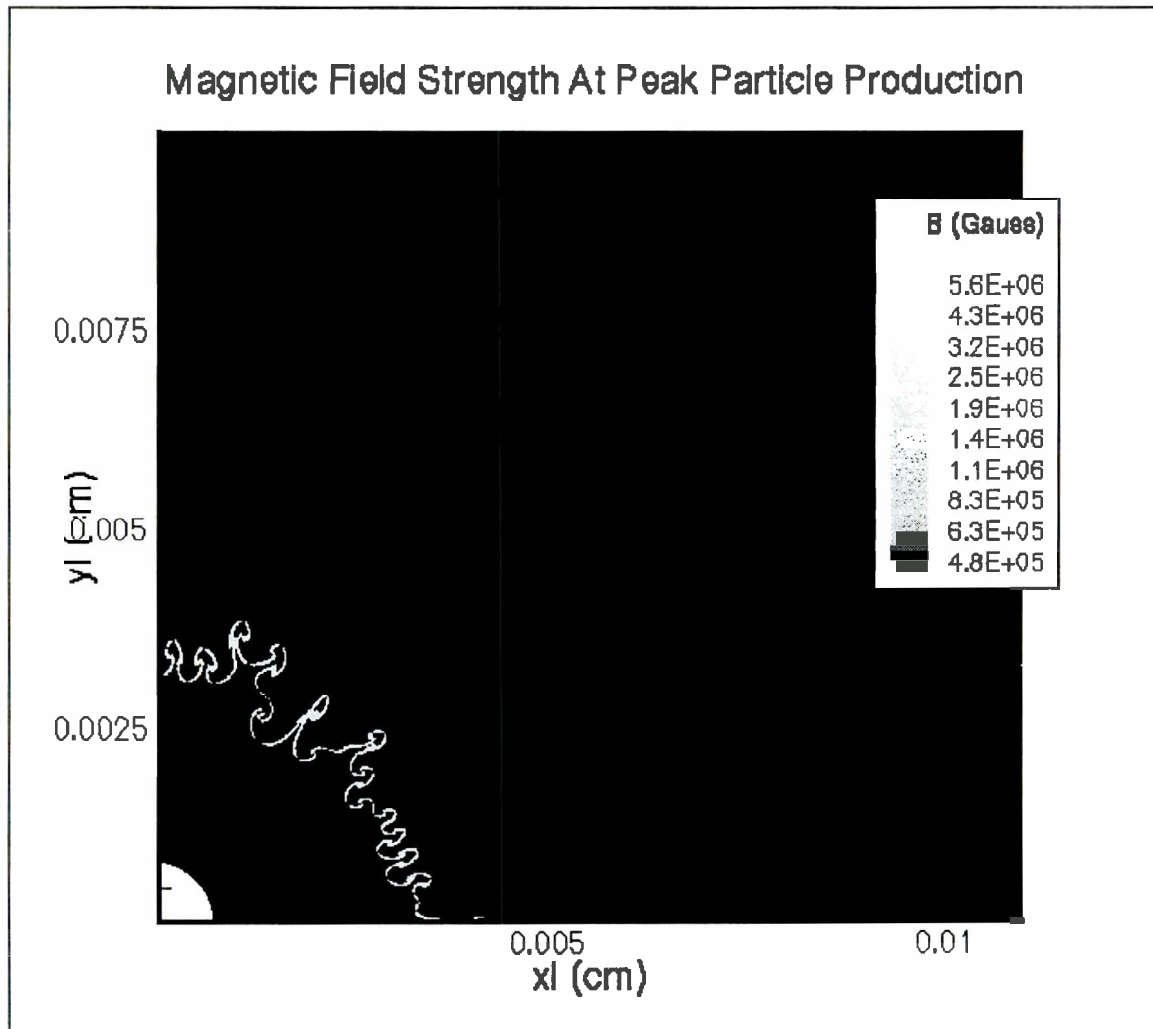


Figure 8: This contour plot shows the “scale length” for density gradients, or the approximate distance over which particles are subjected to magnetic fields caused by density gradients.

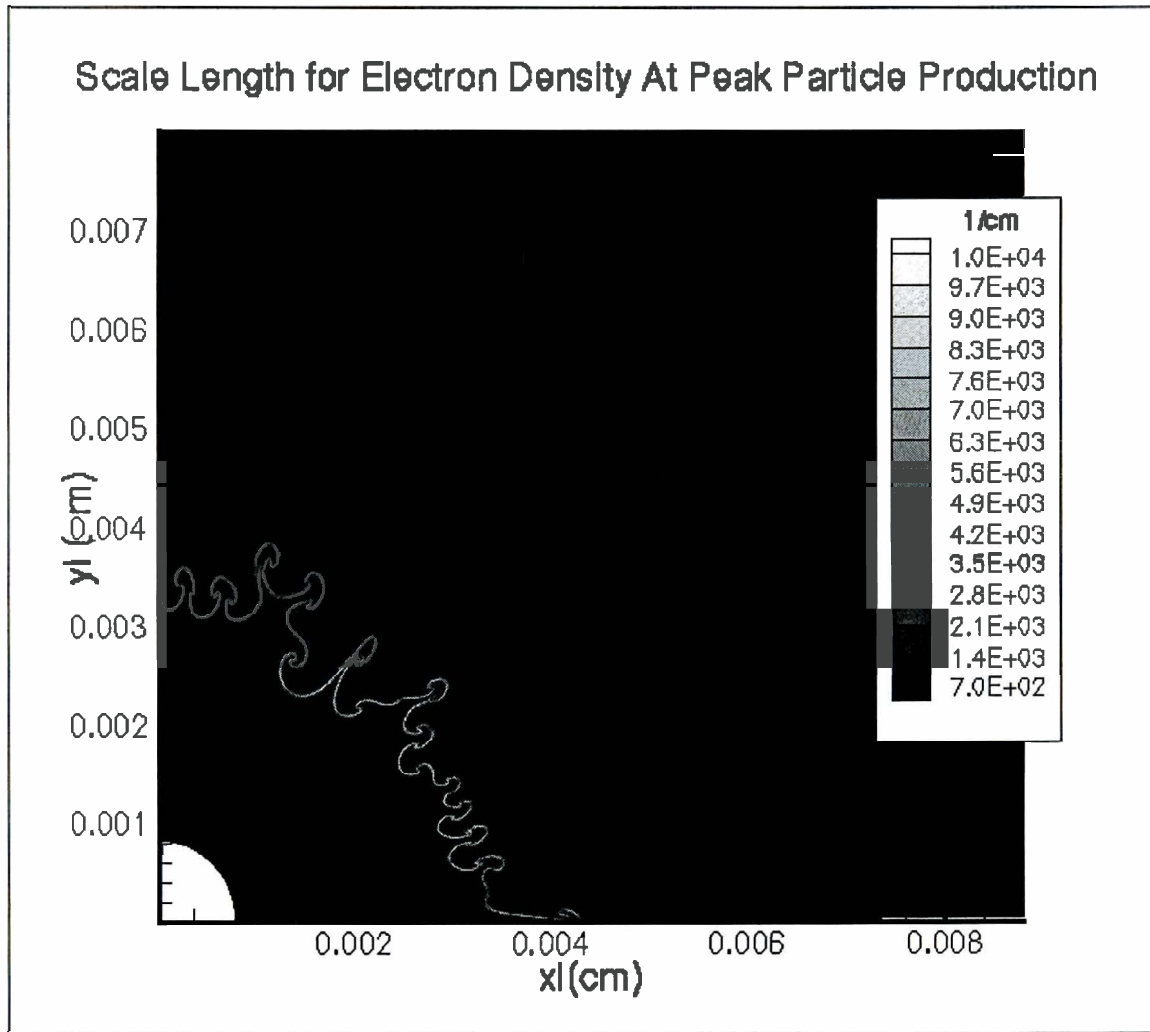


Figure 9: This contour plot shows the “scale length” for temperature gradients, or the approximate distance over which particles are subjected to magnetic fields caused by temperature gradients. Notice that the temperature change is gradual compared to the “quick” changes in density across the shell interface, so the scale lengths for temperature gradients are larger than those of density gradients.

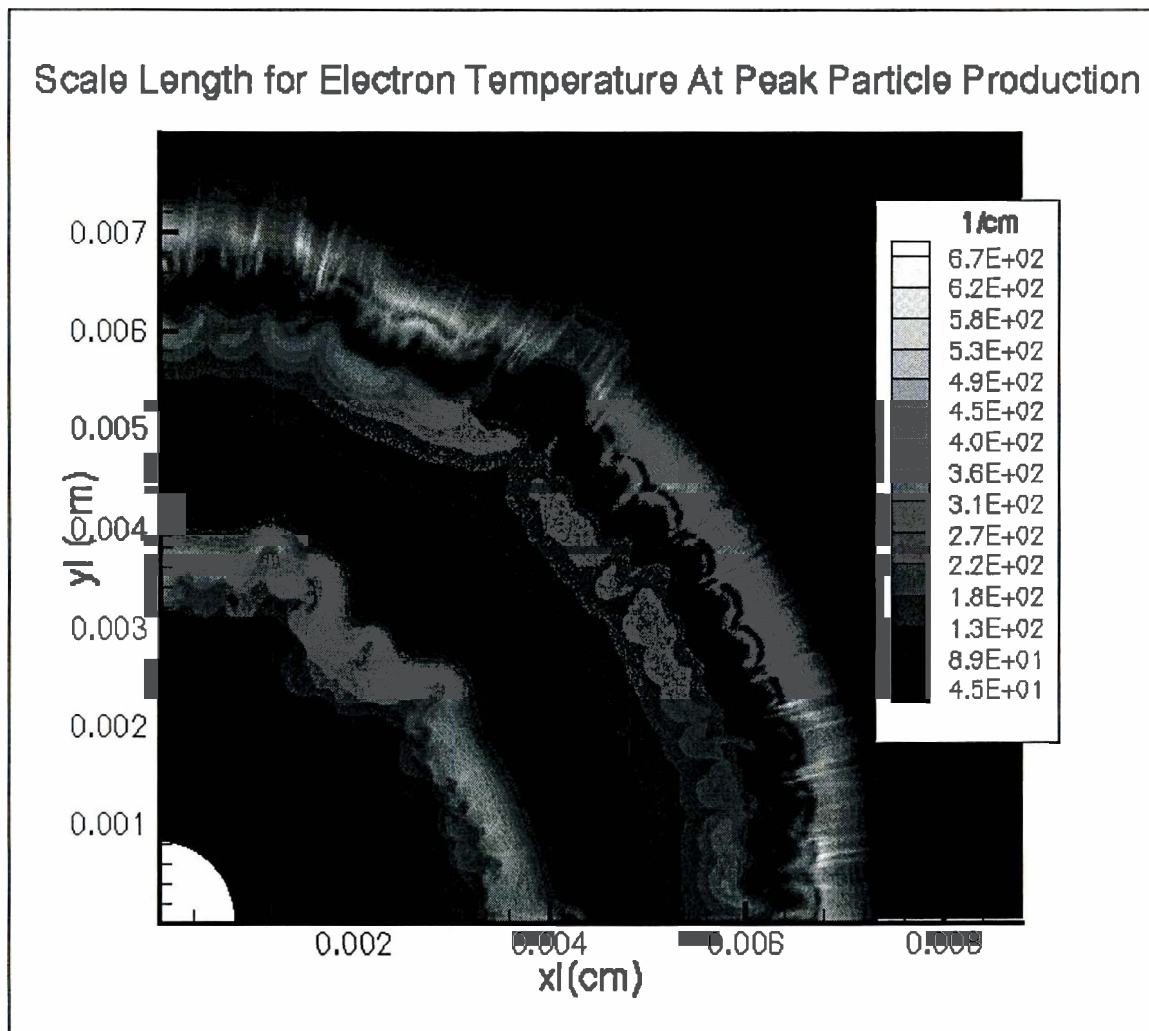


Figure 10: This contour plot shows the deflection for 14.5 MeV protons as a function of magnetic field strength and scale length. Particles in these implosions are subject to fields of magnitudes between 500 KiloGauss and 5 MegaGauss, over distances of between 2 and 4 microns, so that section of the graph has been highlighted.

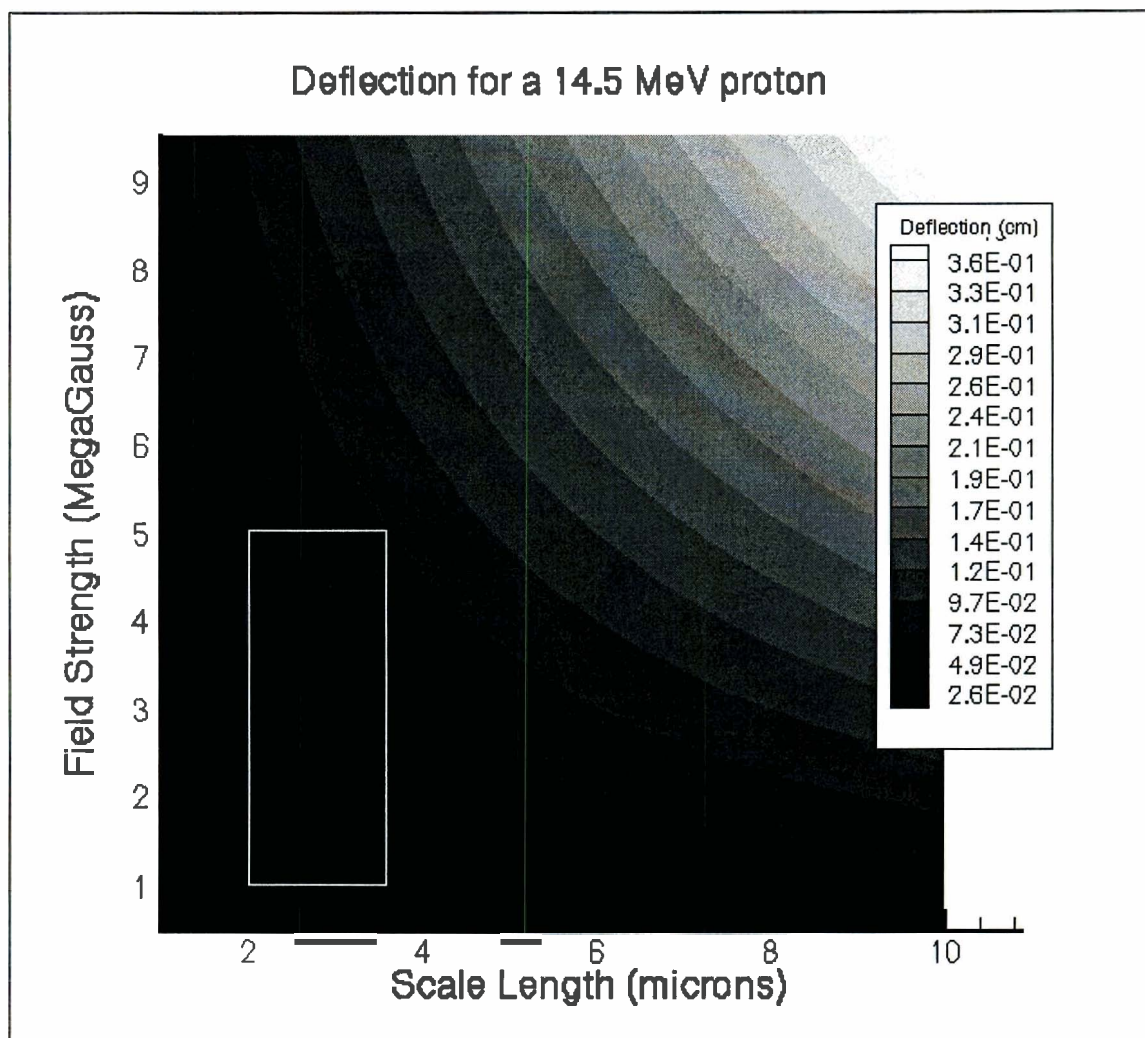
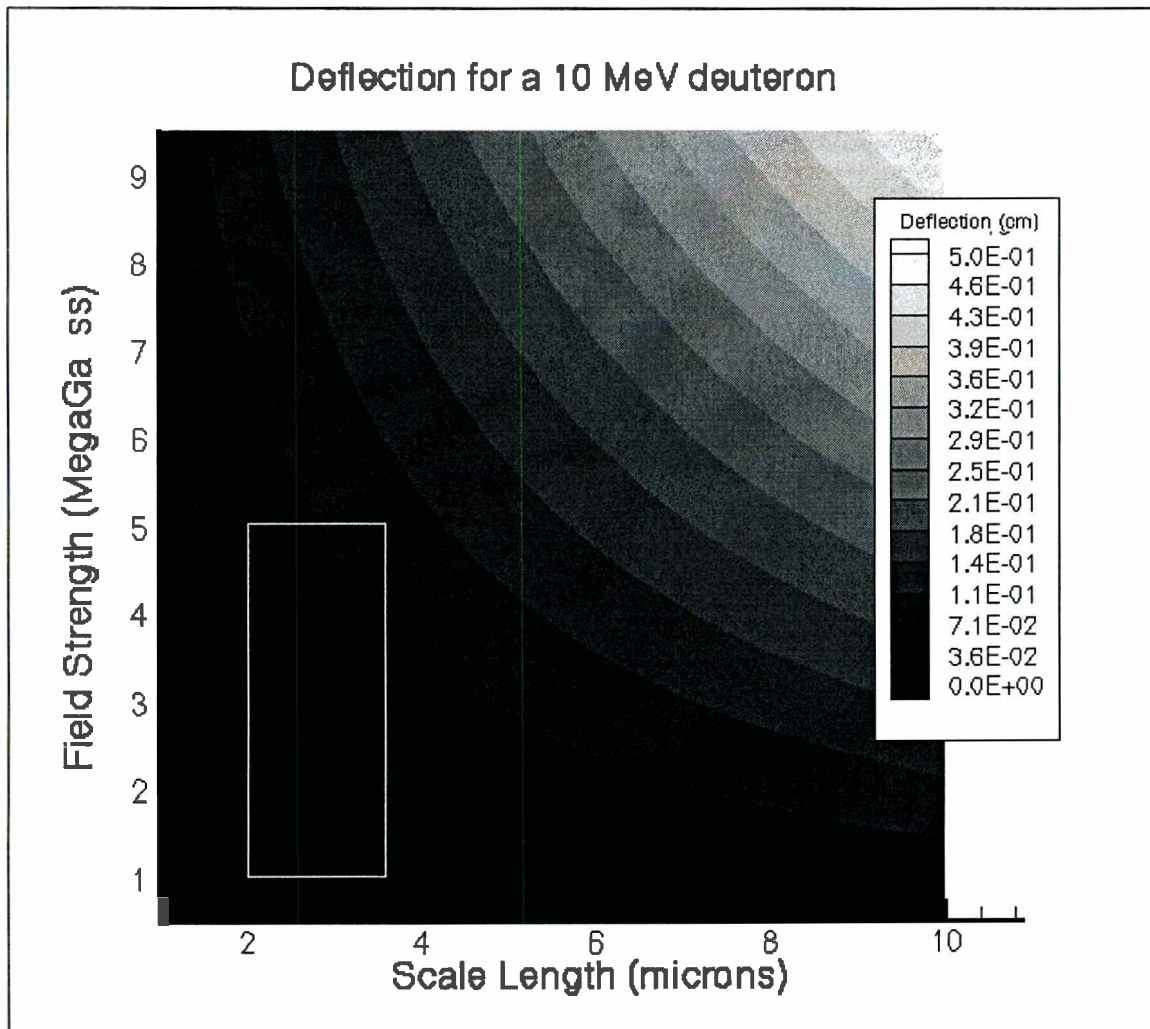


Figure 11: This contour plot shows the deflection for 10 MeV deuterons as a function of magnetic field strength and scale length. Particles in these implosions are subject to fields of magnitudes between 500 KiloGauss and 5 MegaGauss, over distances of between 2 and 4 microns, so that section of the graph has been highlighted.



**Improvement of Self-Organization and Selective Reflection Quality in
Lyotropic Crystalline Polysaccharide Films**

Christine Balonek

**Improvement of Self-Organization and Selective Reflection Quality in
Lyotropic Liquid Crystalline Polysaccharide Films**

Christine M. Balonek
Byron-Bergen High School
Bergen, NY

Advisor Mr. Kenneth L. Marshall
Research Engineer

Laboratory for Laser Energetics
University of Rochester
Rochester, NY

1. Introduction

3-Chloro and phenyl cellulose tricarbaniates (CTCs) have been used in combination with photopolymerizable acrylate hosts to create lyotropic cholesteric liquid crystal gels that are then polymerized using UV light into permanently aligned films that exhibit selective reflection of certain wavelengths of light. These liquid crystal films present an inexpensive and easily producible product that can be used as circular polarizers, in color filters, laser protection glasses, and document security devices. Improvement of the films in these experiments has resulted in the reduction of viscosity and the enhanced quality of selective reflection in the liquid crystal films. Lower viscosity allows for easier formation of liquid crystal phases, thus stronger selective reflection. Lower MW CTCs have been found to lower the viscosity of samples and allow phases to align more rapidly to demonstrate selective reflection. Also, using a non-reactive diluent with an acetate group or functionality has been demonstrated to reduce the viscosity of samples, lower the temperature at which selective reflection occurs, and lengthen the pitch of the liquid crystals causing a wider color range of selective reflection to be obtained. Finally, it was found that the wavelength of selective reflection can be adjusted with the variance of the sample temperature before polymerization.

Improvement of Self-Organization and Selective Reflection Quality in Lyotropic Liquid Crystalline Polysaccharide Films

Summary

Liquid crystal films have many potential uses from color filters to laser protection glasses. They have the ability to reflect (selective reflection) and polarize certain wavelengths of light. Previously, solid films were costly and time consuming to produce. In my research, inexpensive cellulose and solvent host materials were used to synthesize films produced in hours rather than days. These films had improved selective reflection in which the wavelengths of light can be adjusted.

a. Liquid Crystals and Selective Reflection

Liquid crystals exist as a mesophase between the crystalline and isotropic states of matter, possessing characteristics of both. Liquid crystals are semisolids, showing characteristics of liquids, but also exhibiting optical properties that are characteristic of crystals, such as birefringence, double refraction, and scattering.

Three examples of liquid crystal structures are nematic, smectic, and cholesteric (see Figure 1). Nematic liquid crystals possess the least amount of order out of the three classes. They are ordered in one dimension with the molecules lined up parallel to each other, but with the ability to slide past one another. Smectic liquid crystals on the other hand are the most highly ordered with the molecules arranged parallel to one another and in layers one molecule thick. The molecules of cholesteric liquid crystals are arranged in a helical fashion and are the type of liquid crystal most commonly used to create films with selective reflection.

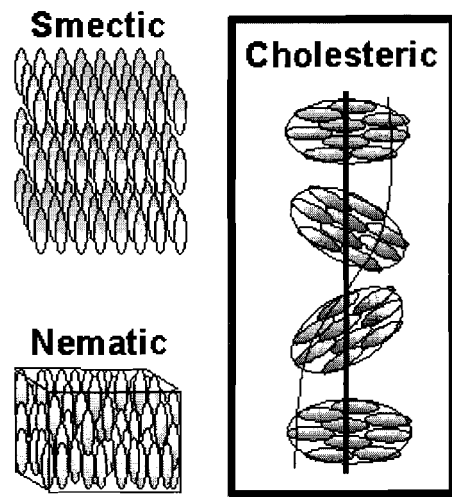


Figure 1: Three types of liquid crystal structures

Selective reflection is an optical property unique to liquid crystal systems. Specifically, selective reflection is obtained from the helical structure of cholesteric liquid crystals. The wavelength of light that is reflected depends upon the pitch length of the helical liquid crystal molecules and their average refractive index. The pitch length is the distance it takes for the helix to rotate 360°. Wavelengths of light, λ , that satisfy the relationship $\lambda = \bar{n} p$, where \bar{n} is the average refractive index and p is the pitch length, are reflected by the sample (see Figure 2). Thus shorter pitch lengths of the helix are required to reflect shorter wavelengths of light (violet and blue).

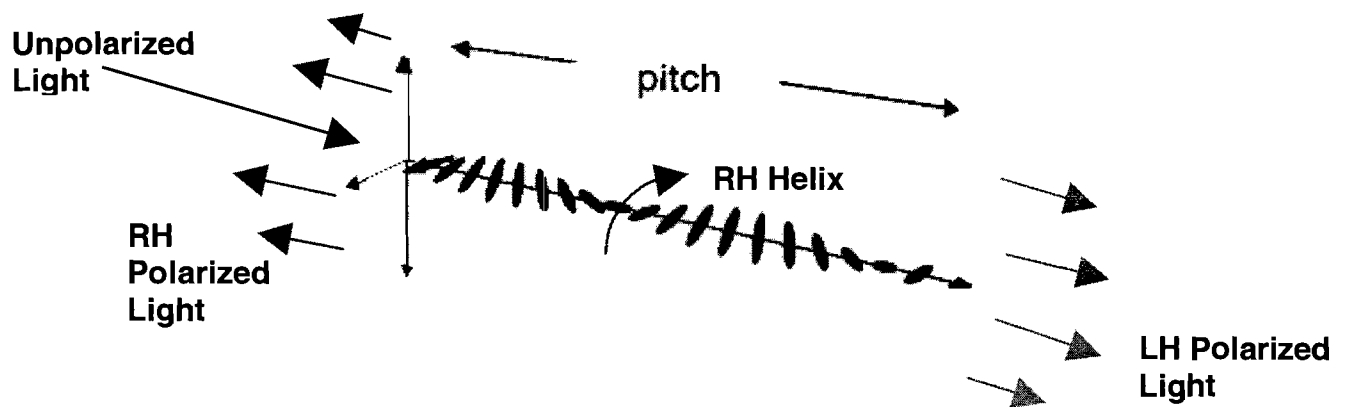


Figure 2: The helix structure of the cholesteric liquid crystals used in this work allows samples to polarize light into right-handed and left-handed light, depending upon the handedness of the helix. In this example, unpolarized light strikes a right-handed helix, which transmits left-handed light and reflects right-handed light.

One application of cholesteric liquid crystals is perfect circular polarizers, since unpolarized light passing through cholesteric liquid crystal samples is polarized into a single-handedness of light depending upon the helicity of the sample. For example, cholesteric liquid crystals are used as circular polarizers for laser systems such as OMEGA during laser shots. OMEGA is currently the world's largest laser, housed in the Laboratory for Laser Energetics, used for various types of research including achieving

the goal of fusion. Current monomer liquid crystal polarizers are fluid-filled glass cells that are time consuming to produce and use. These polarizers could one day be replaced with low-cost films that are easy to produce and that are either free-standing or that require only a single substrate for support. Liquid crystal mixtures can be adjusted to reflect certain wavelengths of light and then made into photopolymerized films in which the molecules of the film become linked creating a solid selectively reflective film, rather than using the fluid-filled cells.

Lyotropic liquid crystals can be used to try to create strong selectively reflective films that exhibit many advantages over their thermotropic liquid crystal counterparts. Lyotropic liquid crystals experience phase changes with changes in both the solute concentration and temperature of the sample, unlike thermotropic liquid crystals that only exhibit such changes with variations in temperature. This gives more control and opportunity to adjust the selective reflection in lyotropic liquid crystal films. Lyotropic liquid crystals can also be dissolved into various solvent hosts that are photochemically reactive, commonly available, and very inexpensive. Whereas, the available thermotropic liquid crystal films are already mixed in solvent hosts and pre-polymerized, which limits the opportunities to adjust the selective reflection and causes them to be expensive.

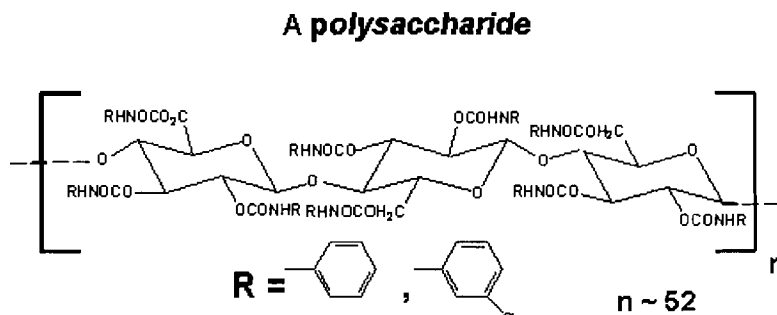
Cholesteric liquid crystals are created from cellulose tricarbaniates (also called urethanes) that are dissolved in suitable photopolymerizable hosts (i.e., an acrylate) and crosslinked to obtain temperature-insensitive, robust films that show selective reflection. Cellulose tricarbaniates (CTCs) are polysaccharides with either benzene or cyclohexane substituents

that contain a halogen (F, Cl, Br) or other aliphatic or aromatic groups (see Figure 3). Cellulose is a desirable starting material

because it is derived from plants and thus extremely

low-cost and plentiful. Cellulose must first go through several processes before it can be used to synthesize liquid crystals. The process of degradation lowers the MW of cellulose acetate from more than one million to optimally 100,000 or less, saponification removes the acetate group from cellulose molecules, and urethane formation attaches a urethane R group to cellulose molecules forming both phenyl and 3-chloro phenyl CTCs.³

The following experiments worked toward the goal of producing strong selective reflection in polymerized films by improving high quality spontaneous molecular alignment at room temperature. To achieve this, lower molecular weight distributions of CTCs and host materials with lower viscosities were used. It is also desirable to be able to tune the selective reflection maximum over a broad range of



Cellulose Tricarbaniate (a urethane)

Figure 3: The structure of one segment of a CTC molecule used to create liquid crystals.

wavelengths by adjusting the host chemistry and composition and the temperature of the sample prior to crosslinking. Previously, lyotropic cholesteric liquid crystal formulations took from 48 hours to several weeks at elevated temperatures before demonstrating any molecular alignment and selective reflection, as described by Muller, Zentel, and Keller¹. More recent research² with phenyl and 3-Chloro phenyl CTCs reduced the time requirement to 15 minutes at 50°C. However, this process is still not practical or efficient.

With further development of liquid crystals with selective reflection, polymerized films have much potential for optical applications. These films have the capacity to be used for liquid crystal displays (i.e., computer screens and watches), modulators, document security, polarization rotators, and polarizing pigments. Films made using CTC-based liquid crystals can also be used in color filters, notch filters, and laser protection glasses since their selective reflection properties allow them to stop certain wavelengths of light and transmit all others.

2. Experimental

Nearly all lyotropic cholesteric liquid crystal films in this project were made using one basic process. Both phenyl and 3-Chloro phenyl CTCs were used as the starting material. CTCs were first added to a liquid host of acrylate and diacrylate reactive monomers, usually 2-ethoxyethyl acrylate and di(ethylene glycol) dimethacrylate. The starting formulation for liquid crystal samples consisted of 45 wt-% CTCs combined with 45 wt-% 2-ethoxyethyl acrylate and 10 wt-% di(ethylene glycol)

dimethacrylate. The sample was then heated at 50°C for one hour to allow the CTCs to dissolve into the host and form a homogenous liquid crystal gel. Next, the sample was knife-cast onto a glass microscope slide and polymerized with UV light at a wavelength of 365 nm in combination with Lucirin TPO photoinitiator in a process called crosslinking to achieve a selectively reflective CTC liquid crystal film with an average thickness of 25 μm .

a. Molecular Weight

1) High MW

Initially, research² using CTCs with molecular weights of 244K and above was repeated. In many cases, the CTCs simply did not dissolve into the acrylate hosts; samples that were created in the original formulation and heated to 50°C on a hot plate for one hour were grainy with a milky appearance. Adding a non-reactive diluent with an acetate group (i.e. ethyl acetate or amyl acetate), heating at a higher temperature (60°C), and heating for upwards of 24 hours yielded no improvement in dissolving the cellulose CTCs. Previous research² and samples of CTCs (MW 244K) in the original formulation were heated until dissolved (about five days), knife cast onto a glass slide, and then heated for a minimum additional 15 minutes at 50°C to show selective reflection with an optical density of only about 0.14 at about 400 nm (see Figure 4). Such high MW caused samples to become extremely viscous, which prevents the liquid crystal phases from aligning easily and showing selective reflection. Extremely high MW also caused the difficulty in initially dissolving the CTC molecules because they were so large. Such high viscosity, difficulty in creating samples, long time for selective reflection to occur, and low optical density levels make these previous samples undesirable.

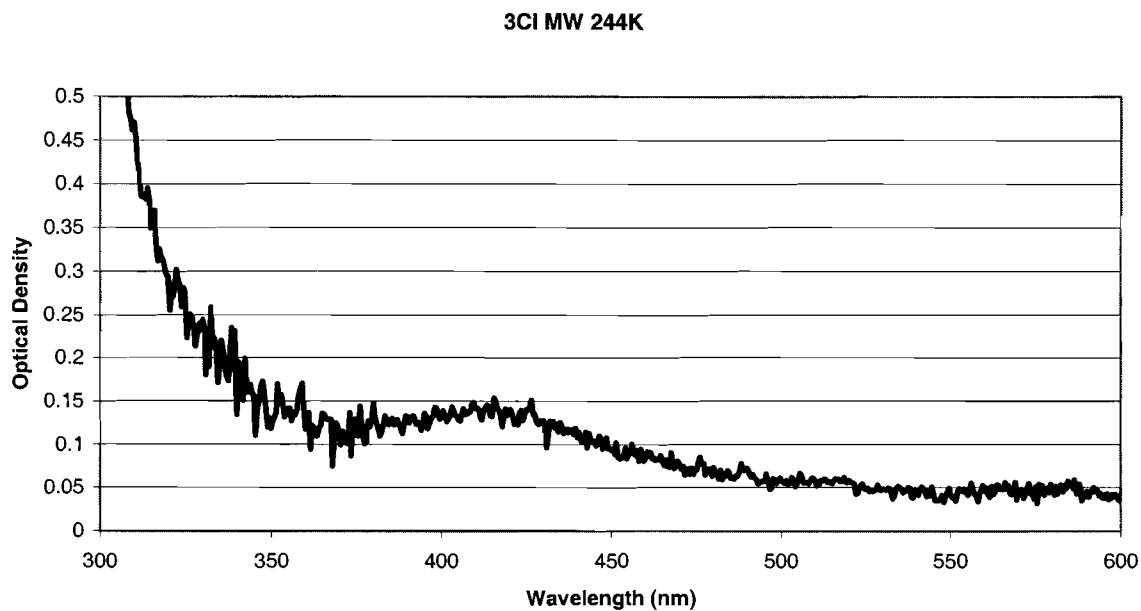


Figure 4: Optical density of a polymerized 3-Chloro phenyl CTC (MW 244K) film viewed in absorption mode in a spectrophotometer

2) Low MW

Lower molecular weight CTCs were therefore used. Longer degradations were performed on the original cellulose materials, ranging from 6 to 36 hours, yielding cellulose CTCs with MWs that were measured to range from 37,080 to 129,000. First, lower MW cellulose CTCs were observed to have greatly reduced sample viscosity by a factor of about 50 compared with that of high MW cellulose CTC samples. Reduced system viscosity alone provided numerous advantages. It made the samples easier to knife cast onto glass slides. It also made it easier to shear samples by moving the glass slide and coverslip against one another to align samples in the liquid crystal phase.

Lower molecular weight cellulose CTCs were also found to have the advantage of dissolving into the host material much more rapidly than higher MW material. CTC samples with molecular weights of 129K and 85K were prepared in the

starting formulation and were fully dissolved into a homogeneous mixture after being heated for only one hour at 50°C compared with five days.

Slides of 3-Chloro phenyl cellulose CTC MW 129K produced selective reflection instantaneously upon knife casting at room temperature. The samples of cellulose CTC MW 129K also had an optical density of 0.32 (see Figure 5), more than double that of the cellulose CTC MW 244K. The rapid alignment is due to reduced viscosity and because the smaller molecules move more readily in the sample to align properly than do larger, bulkier molecules of higher molecular weights.

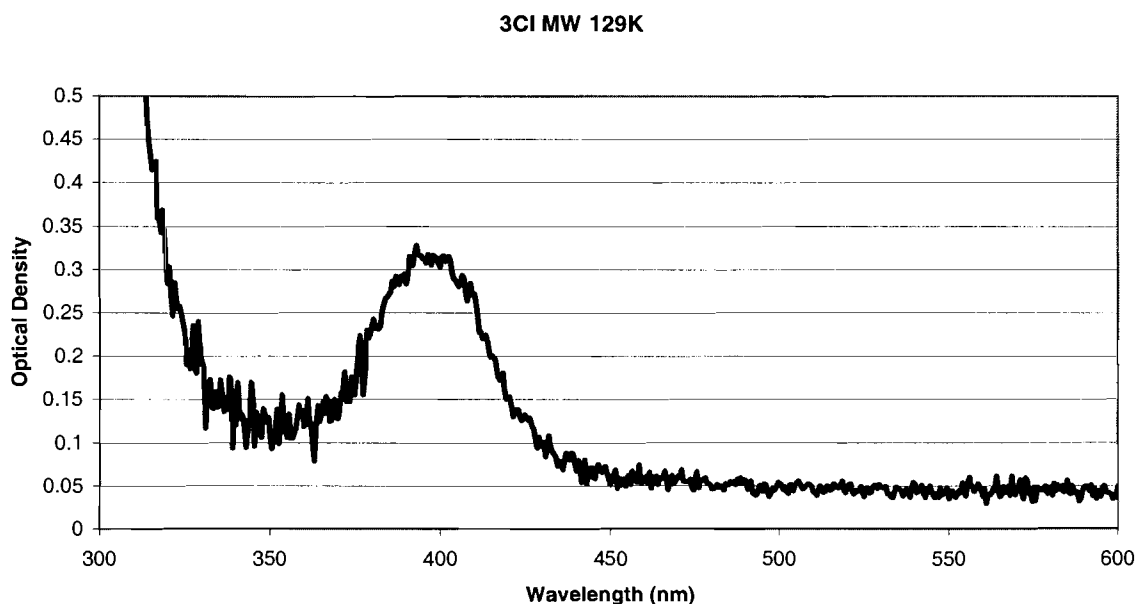


Figure 5: Optical density of a polymerized 3-Chloro phenyl CTC (MW 129K) film viewed in absorption mode in a spectrophotometer

b. Addition of non-reactive diluents

Additional improvements were found when acetate-containing, non-reactive diluents are added to low MW CTC and host mixtures. Amyl acetate and ethyl acetate were the two non-reactive diluents used. Both are isotropic materials and do not

chemically react with the hosts or the CTCs of the liquid crystal mixtures. Rather, the diluents affect the physical characteristics of the samples.

First, the acetate-containing non-reactive diluents were found to greatly reduce the viscosity of CTC samples. The structures of the molecules of amyl and ethyl acetate are not very rod-like and thus have a very low ordering capability when added to mixtures, contributing to the disorder of the liquid crystal molecules within the samples. With greater molecular disorder, the viscosity is reduced and the casting of films is made easier. Lowering the viscosity of extremely viscous samples also allows the liquid crystal phases to align more easily, thus producing selective reflection.

Secondly, when a non-reactive diluent was added to a sample, I observed that the onset color temperature of the sample was reduced to room temperature and that the spectrum of reflected colors was widened. Without the acetate-containing non-reactive diluents, I found samples to be colorless at room temperature (samples exhibit selective reflection only at elevated temperatures from about 52 – 70°C with color reflection only ranging from violet to green). However, upon adding a diluent, violet selective reflection is observed at room temperature. For example, a sample was created consisting of 60 wt-% 3-Chloro phenyl CTC (MW 53K), 35 wt-% 2-ethoxyethyl acrylate, and 5 wt-% di(ethylene glycol) dimethacrylate. This sample showed no color at room temperature, only blue selective reflection from 66 – 74°C. When 59.25µl of amyl acetate was added to the 0.1g sample, the color onset temperature was lowered and violet selective reflection was observed at room temperature. With continued addition of an acetate-containing non-reactive diluent, the initial onset color at room temperature is shifted from violet, across the visible spectrum, to red. For example, a 0.1g sample of 3-

Chloro phenyl CTC (MW 129K) was prepared in the starting formulation with 26 μ l of additional amyl acetate and exhibited red selective reflection at room temperature. (Refer to Figure 6 and Figure 7).

Comparison of selective reflection temperatures in 3CI polymerized films with and without amyl acetate				
Film composition \rightarrow	3CI MW 129K	3CI MW 129K with ~10 wt-% amyl acetate	3CI MW 85K	3CI MW 85K with ~10 wt-% amyl acetate
Selective reflection color \downarrow				
violet	50°C	38°C	40°C	-°C
blue	60	40	-	-
teal	60	45	-	-
green	65	50	50	25
red	65	50	-	-
clears	70	60	60	30

Figure 6: 3CI polymerized films were created in the original formulation, using molecular weights of 129K and 85K. Four films were created, two without amyl acetate and two with ~10 wt-% amyl acetate. The addition of ~10 wt-% amyl acetate reduced the color onset temperature in each case.

Comparison of Wavelengths of Light Reflected With and Without Amyl Acetate in 3CI MW 129K

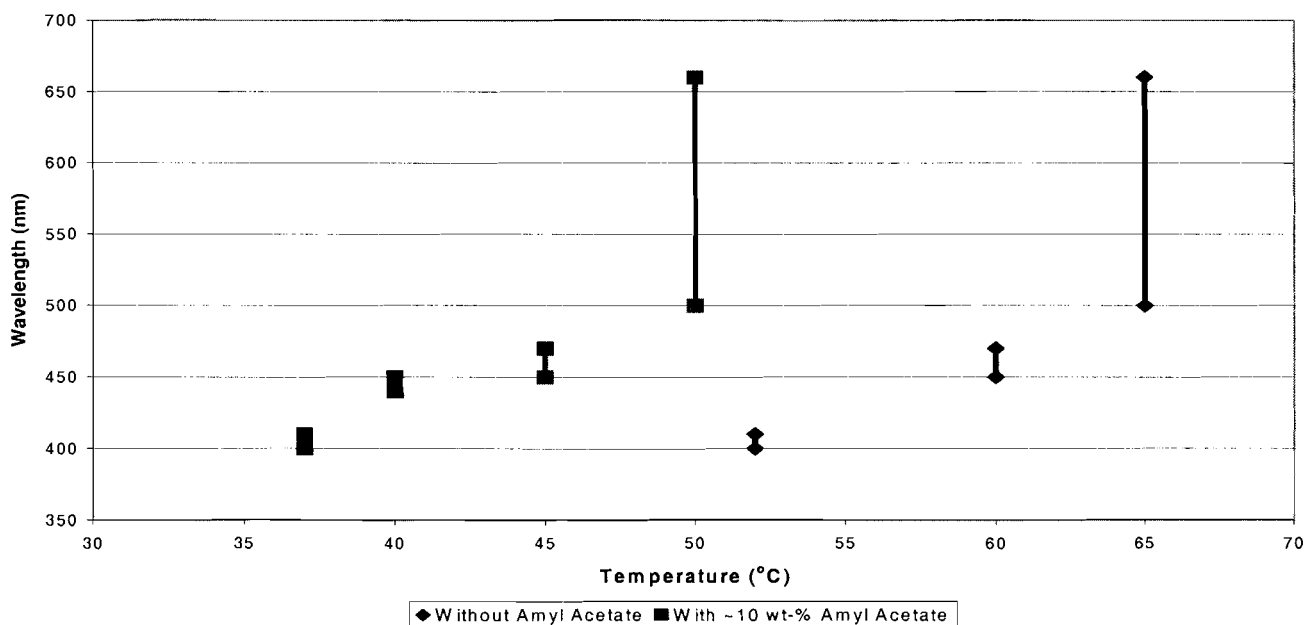


Figure 7: The observed wavelength ranges of reflected light are shown at their respective measured temperatures. As shown by the graph, with the addition of ~10 wt-% amyl acetate the onset temperature for selective reflection is reduced by about 25°C.

These changes in the selective reflection of 3-Chloro phenyl CTC samples are understood to be a result of the low ordering capability of the isotropic diluents. The diluents add to the disorder of mixtures, depressing the liquid crystal phase transition temperature of the whole mixture, thus lowering the color onset temperature to room temperature.

Secondly, amyl and ethyl acetate are slightly more polar than the acrylate hosts of liquid crystal samples are, which broadens the selective reflection color range by elongating the helix.

3. Conclusion

I found that the selective reflection of lyotropic cholesteric liquid crystal films could be greatly improved by using low MW CTCs. The lower MW CTCs dissolve much more readily than high MW CTCs that were previously used and resulted in samples with a much lower viscosity. These results allow films to be created easier and in a matter of hours rather than days. The low MW CTC samples also showed stronger selective reflection than the higher MW samples. Selective reflection was found to occur instantaneously rather than over a period of up to several weeks. Lower viscosity in host systems also allows liquid crystals to align more rapidly and enhance the quality of selective reflection.

In addition, adding non-reactive diluents to low molecular weight cellulose CTC mixtures, the selective reflection obtained in liquid crystal films was greatly increased and it was possible to adjust its wavelength of reflection. Non-reactive diluents

added to liquid crystal mixtures lowered the selective reflection onset temperature, broadened the color temperature range, and further reduced the overall system viscosity. These effects are thought to be caused by the lengthening of the helical pitch of the liquid crystal molecules by the diluents.

By adjusting CTC MW, the host composition, and the amount of acetate-containing non-reactive diluents in the liquid crystals it is possible to adjust the selective reflection properties. Liquid crystal films can be photopolymerized to create solid films. These films have numerous applications in laser systems as inexpensive circular polarizers, as document security devices, polarizing pigments, modulators, polarization rotators, liquid crystal displays, color filters, notch filters, and laser protection glasses.

References:

1. M. Muller, R. Zentel, and H. Keller, *Adv. Mater.* 1997, 9, pp 159-162
2. K. L. Marshall and D. Mott, unpublished results
3. Oliver, Gloria. Improvements in the Strength of Visible Selective Reflection in Lyotropic Liquid Crystals Made from Cellulose Urethanes. LLE High School Summer Research Program, summer, 2000.

Plasma Energy Measurement with an Open-Cell Metal Foam

David Dingeldine

Plasma Energy Measurement with an Open Cell Metal Foam

David J. Dingeldine

Advisor: James P. Knauer

Laboratory for Laser Energetics
University of Rochester

Summer High School Research Program
2002

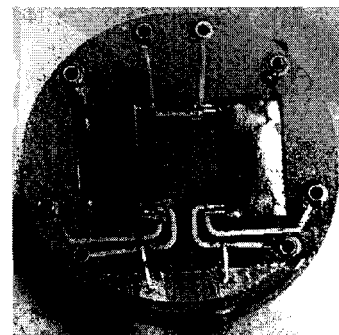
Abstract:

Metal foams were researched to possibly replace current tantalum calorimeter foils. Different foam properties were characterized using SEM scans and spectrophotometer readings. Fluffy gold was also developed to possibly be coated on current foils or foams to improve UV absorption and reflectance properties. Fluffy gold samples were also characterized using SEM scans and spectrophotometer readings.

Performing routine maintenance of the plasma calorimeters in the OMEGA laser system can often be a tedious task. A new mounting system for the window assembly utilizing magnets was developed. The use of magnets allows for the calorimeter window to easily be aligned to the calorimeter foils and reinstalled in the OMEGA target chamber. Ultra bright LED's which produced 5,500 mcd each were interfaced with Labview computer software to bench test the calorimeter system. This allows for a complete test of a calorimeter before installation.

Introduction to Plasma Calorimeters:

The plasma calorimeters used in OMEGA serve the main function of recording how much plasma energy is expelled during the irradiation phase of laser fusion. The calorimeter uses two 25 μm thick Tantalum foils to absorb energy. One foil is exposed to all energy while the other is only exposed to light, this allows for plasma energy to be determined (all energy – light



energy = plasma energy). A small Quartz window that transmits only light energy is

placed in front of one of the foils. A small reference pad is unexposed to any energy and is used as a zero temperature reference for data collection.

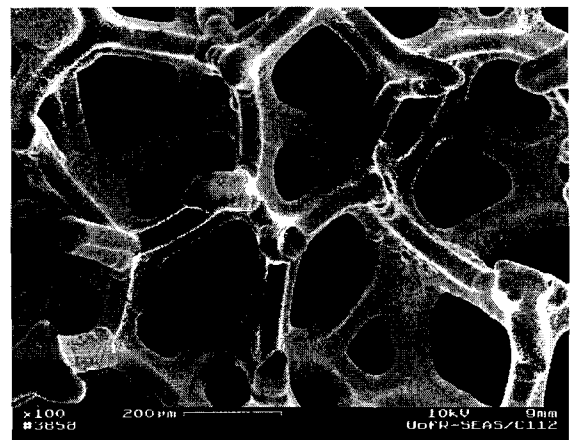
When energy is absorbed into the calorimeter foils they heat up. This change in temperature is read by small thermocouples located at different points on the foils and reference pad. Very sensitive and precise thermocouples are used so small changes in heat intensity over small amounts of time can be read and analyzed.

The main physical property that we were interested in improving was the reflectance characteristics of the Tantalum foils on the calorimeters. The metal foam would theoretically have a much lower reflectance than the tantalum foil, thus decreasing the sensitivity of the measurement to scattered laser radiation. Each tantalum foil reflects a unique amount of energy (depending on the amount of imperfections on the foil itself), the less energy that is reflected means more energy gets absorbed into the foil and read.

Foam Absorber Testing:

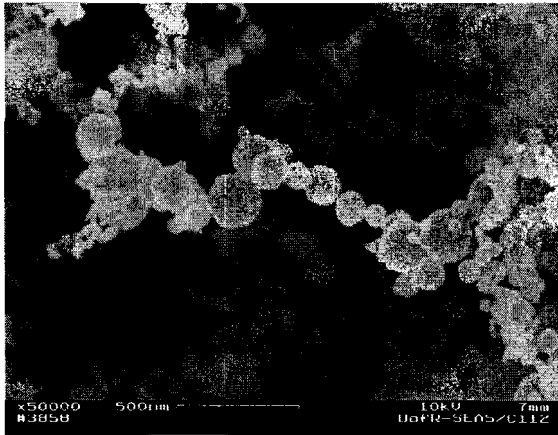
One aspect of my work was testing different foam materials to possibly replace the current tantalum foils on the calorimeters. Two instruments were used to determine characteristics of metal foams and Au smoke (fluffy gold). A scanning electron microscope (SEM) was used to investigate the structures of the materials, as well as take different size dimensions of the pores on the metal foam and the spherical diameters of the fluffy gold. A Spectrophotometer was used to test reflectance as well as transmission properties of the materials.

Nickel foam with 100 pores per inch (PPI) was tested to replace the Ta foils with metal foam. At 350 nm the foam had a reflectance of 9.8%, about half of the original Ta foil. One of the worries with a open cell foam would be that a large amount of light would simply pass through the foam. Spectrophotometer scans showed that only 0.15% of light passed through the foam at 350 nm. The image to the right shows the SEM scan of



nickel foam. The foam had very large pores with diameters between 450 to 500 μm . The structure of the foam was uniform over the whole surface.

Fluffy gold showed the lowest reflectance of all measured materials. Fluffy



gold was made in house, and intended as a coating for the current Ta foils or alternate metal foams to improve reflectance characteristics. Fluffy gold excelled in the area of reflectance, with only 2.5% of light reflected at 350 nm. SEM scans showed an interesting spherical shape to the deposited fluffy gold. The photo on the left was also

taken with the SEM and shows the ultra-small spheres with diameters ranging from approximately 250 nm to 25 nm. The downside to the fluffy gold was how easy it was to remove from the surface it was deposited on. It was agreed that the fragile material would not fare well in OMEGA bay conditions, due to the fact that simple handling of the foam would remove it from its surface.

Calorimeter Window Mount Redesign:

The amount of time a scientist or technician spends in the laser bay is crucial. The less time spent adjusting instruments means the less time that the laser system could get contaminated. One issue with the plasma calorimeters that had to be remedied was the way that the UV window was attached to the target bay mount.



The current mount uses tiny pins to line up and hold in the window mount. These pins (shown in photograph above) are also used to hold the calorimeter to the base. The main issue, besides tedious removal and installation, was the amount that dimensions could vary. The distance from the UV window to the calorimeter face could vary as much as 0.2 inches.

After investigating several different designs, I decided that the use of

magnets would be the best solution. Small high intensity magnets replaced the pins and showed excellent results. The magnets eliminated the ability for the window to calorimeter distance to vary. The magnets also snapped the window into proper orientation, and due to the fact that three magnets were used, the window could only be placed one way. Time spent installing the window assembly to the calorimeter was greatly reduced. One thing that still needs to be investigated with the use of the magnets is stray magnetic fields that might be leaking into the bay.

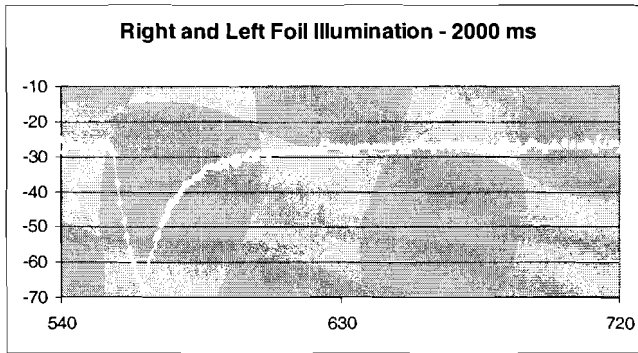
Ultra-bright LED Lab Testing System

The LED testing system was developed to recreate OMEGA style data collection curves on the calorimeters to ensure proper working order of a complete system while still in a lab setting. This would allow one to double check the calorimeters instead of having to install them in the laser bay and then find out they are not functioning correctly. Labview programs were developed along with electrical hardware to create accurate pulse widths and frequencies. Pulse widths and frequencies could be varied to test different data curves. A 4 LED array was set up so each foil could be tested independently (2 LED's per foil) or both at the same time. This would allow inconsistencies between foils to be found and compensated for. The LED's used are rated at 5,500 mcd each and are the first to be able to recreate an OMEGA style data curve.

Two electronic boxes were created to control the LED's. One was specifically designed to help the LED's interface with the computer, using an FET to trip a nine volt power source and light the LED's. This unit needed to be build due to the fact that the power output from the Labview interface was too low to light the LED's at full power. Another box was also created to switch between the LED's in the 4 LED array. It used two switches set up as an OR gate to chose between LED's.

Data Modeling:

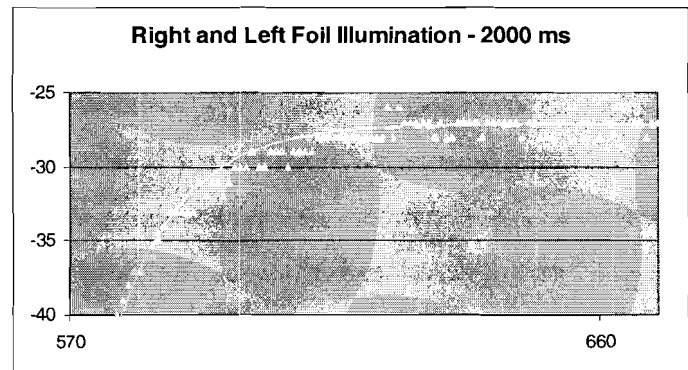
The calorimeter foil is modeled as a capacitor to better understand data. When the test data was collected in the Labview programs, it often had many inconsistencies due to equipment limitations. Modeling data curves allows them to be smoothed using mathematical equations. The equation also determines many variables so



the data can also be checked for consistency and accuracy. These models were created in Microsoft Excel.

The graph to the left shows a typical data output graphed in Microsoft

Excel. The triangular dots are actual data points and the line is the mathematical model. The rising slope of the graph indicates the calorimeter foils “charging” with energy, while the decay of the slope shows the foils “releasing” the energy as they are no longer exposed to light. The foils charge and release energy much like that of a capacitor, and that is why we model it as such. The graph to the right better depicts how the mathematical formula “averages” data to give a smoother curve.



Conclusion:

The use of magnets to hold in the calorimeter window assembly proved to make removing and reassembling the calorimeter housing a lot easier. Microcellular metal foams are a better alternative to the current tantalum foils. Laboratory testing the calorimeters using ultrabright LED’s created curves much like those seen in OMEGA. A capacitor model was used to average out data collected from laboratory testing as well as determine different variables to ensure test accuracy.

**Analyzing the Structure of Shell Modulations Around Peak
Compression of Spherical Implosions**

Sonya Dumanis

***Analyzing the Structure of Shell Modulations Around Peak Compression of Spherical Implosions**

Sonya Dumanis
Advisor: V.A. Smalyuk

LABORATORY FOR LASER ENERGETICS
University of Rochester
250 East River Road
Rochester, NY 14623

Abstract

Programs were created to analyze the structure of shell modulations at peak compression of spherical implosions. Measurements of the modulations were taken by using absorption of titanium-doped layers placed at distances 1,5,7, and 9 μm from the inner surface of 20 μm -thick plastic CH shells filled with 18 atm of D^3He gas. These nonuniformities were measured using ratios of monochromatic target core images taken inside and outside the titanium 1s-2p absorption spectral regions. The results show that the peak-compression, time-integrated areal-density modulations are higher at the inner shell surface, unstable during the deceleration phase of implosion, with the modulation level of $59 \pm 14\%$. The nonuniformities are lower in the central part of the shell, having a modulation level of $18 \pm 5\%$. The outer surface of the shell, unstable during the acceleration phase of the implosion, has a modulation level of $52 \pm 20\%$.

*This report has been adapted from "Radial Structure of Shell Modulations Near Peak Compression of Spherical Targets" by V.A. Smalyuk, S.B. Dumanis, F.J. Marshall, J.A. Delettrez, D.D. Meyerhofer, T.C. Sangster, and B. Yaakobi, submitted to Physics of Plasmas

Introduction

In direct-drive inertial confinement fusion, the type attempted at the Laboratory for Laser Energetics (LLE), the deuterium and tritium react to produce neutrons, helium, and excess energy as byproducts. The goal of LLE is to find a way to gain as much excess energy output as possible through the fusion process. LLE achieves this by using laser-driven inertial confinement fusion when the laser heats and compresses spherical targets filled with deuterium and tritium. As the target shell implodes from the force of the laser, the shell compresses the core (using Newton's third law) forcing the deuterium and tritium to react. If there are instabilities and modulations in the target shell, then the fusion reaction won't be as efficient as possible. In fact, one of the greatest factors limiting target performance in spherical implosions is the growth of shell perturbations. This is why assessing the structure of the shell modulations near peak compression is necessary.

One can determine the shell structure during peak compression by placing diagnostic titanium-doped layers inside the shell. At around peak compression when the maximum density and temperature occur, the compressed core and inner surfaces produce strong x-ray emissions which can be used as a backlighter to probe the outer, colder shell.¹ The x rays can be imaged through the titanium-doped layers and captured by a GMXI camera. These images can be used to assess what is going on inside the core.

Initially, the nonuniformities come from target imperfections and the irradiation from the laser. These perturbations grow at the outer shell during the laser-driven part of the experiment due to the Rayleigh-Taylor instability and convergent Bell-Plesset effects. During the acceleration of the shell, these perturbations feed through the shell seeding the

Raleigh-Taylor instability on the inner surface. The modulations on the outer shell are not of great concern because they become stable when the laser is turned off. What is of great concern are the modulations caused on the inner surface. As the shell starts to decelerate, the perturbations on the inner surface of the shell now become the subject of Rayleigh-Taylor instability. As a result, the modulations from the inner shell can penetrate deep, causing the shell and the fuel to mix.² This mixing inhibits the achievement of high compression and high temperature necessary to sustain an efficient fuel burn.

Present shell-integrity measurements have been made using imaging at photon energies in and out of the sensitive (1s-2p) titanium absorption regions. The images captured out of the 1s-2p absorption region (energies not absorbed by the shell) provide the spatial shape of the core, while core images taken in the 1s-2p absorption region (energies highly absorbed by the shell's titanium) contain information about the structure of the shell areal-density modulations in the titanium doped layer. Computer programs were written to filter out the background noise from the images and to calculate the optical depth modulations of the target shell.

Earlier experiments were limited,^{1,3} because the results only measured the perturbations at the shell inner surface. The titanium-doped layers placed at the central and outer parts of the shell were not sufficiently sensitive to detect the instabilities and modulations. That is because previous images were taken at energies around the titanium K-edge. This particular experiment extends the idea of differential imaging into the much more sensitive titanium 1s-2p region. Thus, the titanium in the layer can absorb not only above 4.966 keV (which is what the previous K edge experiments did) but also in the 1s-2p absorption region with the photon energies of ~4.5-4.7 keV. The mass absorption rate

at any absorption line in the titanium 1s-2p spectral region is about one order of magnitude higher than at photon energies above the K edge. This means that the differential imaging can be extended to the central and outer parts of the shell where the compression and the modulations are smaller. For the first time, measurements of the compressed shell modulation structure were conducted.

Experimental Conditions

Figure 1(a) shows the schematic representation of the target shell. The shell is a sphere with a $\sim 450\ \mu\text{m}$ initial radius filled with 18 atm D^3He gas. The target shell is made of a 20- μm -thick plastic CH. The titanium-doped layers are placed at the distances of 1, 5, 7, and 9 μm from the inner surface of the shell. The thick solid lines in figure 1(b) represent those layers. Figure 1(b) also shows the profile of what the target looks like around peak compression. The thick line represents the mass density and the thin line represents the electron temperature vs. the radius. Those two profiles were calculated using the 1-D code LILAC.⁴ One can see that the 1 μm layer is where there is high temperature and high density; this represents the inner part of the shell. The 9 μm layer, where there is low temperature and low density, represents the outer part of the shell. The 5 and 7 μm layers represent the central part of the shell. Each of the layers was 1 μm thick. These titanium-doped layers absorbed the x rays which were then used to analyze the density shell modulations at the inner, central, and outer parts of the surface.

Each of these targets with the titanium-doped layers was imploded by 351 nm laser light using the 60-beam OMEGA laser system⁵ with a 1-ns square pulse shape at a total energy of $\sim 23\ \text{kJ}$. All the shots were taken with laser beams smoothed by distributed phase plates (DPP's)⁶; 1-THz, two-dimensional smoothing by spectral dispersion (2-d

SSD)⁷; and polarization smoothing (PS)⁸ using birefringent wedges. The average beam-to-beam imbalance was ~3%.

A monochromatic x-ray imager known as the GMXI⁹ camera captured the core images. One channel of the GMXI recorded monochromatic images at ~4.60 keV (in the titanium 1s-2p absorption region) and another channel was set up at ~4.87 keV (outside the titanium absorption region). The core images were taken at two different channels. Figure 2 shows the images that were captured after Wiener filtering¹⁰. There is a lot of background noise due to light during the implosion. Therefore, it was necessary to write programs using Wiener filtering to filter out all of this extra noise.

The principle of the Wiener filter program was to use a noise level constructed from the differences in the two images (one in the 1s-2p region and one not) in the shot 26633 without titanium. Taking this and the measured GMXI modulation transfer function (MTF), one was able to assess what the exact noise level in each image was. For more details of the image processing one can see References 1,3, and 10.

To get a better idea of where exactly the images were taken, one can look at Figure 3(a). The spectral intensity vs. the energy $S_{\text{meas}}(E)$ is shown by the thin solid line (for shot 26625). The first channel of the GMXI camera was set up in the 1s-2p absorption region at the dashed spectral response. The second channel was set up at the dotted spectral response.

After filtering out those two images, the shell optical depth (OD) was calculated. A program was written that took the natural logarithm of the ratio of intensities of the two images at photon energies in the 1s-2p region, below the K edge (weakly absorbing by the shell), $I_{<K}(r)$, $\delta[\text{OD}(r)] = \delta\{\ln[I_{1s-2p}(r)/I_{<K}(r)]\}$. In Figure 3(a), the thick solid line

represents the estimated continuum level $S_{\text{con}}(E)$ of core x rays used to calculate the average titanium optical depth, $OD = \ln[S_{\text{con}}(E)/S_{\text{meas}}(E)]$ at a photon energy of $E = 4.6$ keV. The average titanium optical depth, OD, is used to determine the relative optical depth modulations (which are approximately the relative areal-density modulations), $\delta[OD(r)]/OD = \delta[\rho R(r)]/\rho R$, to compare levels of the modulations in the different areas of the shell.

This measured spectrum in Figure 3(a) is used to also calculate the spatial variations in the images due to the small variations of the spectral response across the horizontal axis of the images. A program was written so that the resulting correction function for each shot used the corresponding spectra. Why is there a correction factor? Look for example at the central part of an image of Fig. 2, which is set up at 4.6 keV. When it goes through the camera, it is reflected in the GMXI multilayer mirror at an angle of 5.88 ± 0.01 degrees. The x rays that originated from the vertical line at $100 \mu\text{m}$ off the image center are reflected from the mirror at a slightly different angle of 5.91 ± 0.01 degrees, corresponding to a photon energy of 4.58 keV. The program takes into account the different angles at which the light hits the camera and then corrects the image accordingly. For the images at the 1s-2p absorption channel, the resulting correction function is proportional to the convolution of the measured spectrum, $S_{\text{meas}}(E)$ with the spectral response function $R_{1s-2p}(E)$.

Figure 3(b) shows the correction functions for the shot 26625 in (dashed line) and out of (dotted line) the 1s-2p-absorption channel. For each Wiener-filter image the x-ray intensity was divided by the corresponding correction function to compensate for these spatial variations.

Experimental Results

Figure 4 shows the images of the optical depth modulations in the titanium-doped layers offset by 1,5,7, and 9 μm . The more bumpy and darker the image is, the more instabilities and modulations are occurring at that area. Figure 5(a) presents the power per mode spectra of these modulations as functions of spatial frequency. The modulation levels are highest at the spatial frequency of $\sim 20\text{mm}^{-1}$ which corresponds to the wavelength of $\sim 50\mu\text{m}$. It was determined that the absolute values of the optical depth modulations decrease monotonically from 0.30 ± 0.06 at the inner surface as shown by the solid line in Figure 5(b). The relative areal-density modulations are $59\pm 14\%$, $18\pm 5\%$, $26\pm 10\%$, and $52\pm 20\%$, in the layers offset by 1,5,7, and 9 μm respectively, as shown by the dashed line in Figure 5(b). This implies that the modulations and the instabilities are the highest at the inner part of the shell (where the 1 μm titanium-doped layer was located). As expected, the modulations decrease at the central part of the shell (in the 5 and 7 μm layers) and increase again at the outer part of the shell (at the 9 μm layer). Recall that the modulations that occur at the outer part of the shell are due to the perturbations that grow when the laser is hitting the target, and the shell is about to implode. When the laser is turned off, however, the perturbations stop growing and stabilize. So these measured modulations are not of that great concern. What is of concern is the high modulation level due to the Raleigh-Taylor instability that is occurring at the inner shell surface, The areal-density modulations are dominated by these nonuniformities.

In the future, the time-integrated measurements of modulations will be extended to time-resolved measurements, using the same titanium 1s-2p absorption

technique. In addition, data will be analyzed not only for titanium-doped filters but for other ones such as argon. This way, scientists will be able to get a clearer picture of what exactly occurs inside the target shell.

Conclusion

For the first time, the structure of the inner, the central, and the outer parts of the shell could be analyzed. Instabilities and nonuniformities were measured using titanium-doped layers placed at the 1,5,7 and 9 μm points from the shell inner surface. The shell modulations were obtained using the ratio of images in and out of the titanium 1s-2p absorption region and various other programs. The inner part of the shell had more modulations (~59%) than any other part of the shell. The outer surface had a high modulation level of ~52%, but its contribution to the modulations in the whole shell is small due to the fact that these instabilities stabilize once the laser is turned off. The central part of the shell was the most uniform.

Acknowledgements

First and foremost, I would like to acknowledge Vladimir Smalyuk for his time and effort in helping me with my programs and analysis. I am also grateful to Dr. Craxton for inviting me into the program and allowing me to be part of the Laser Lab research that goes on at LLE. Also, I would like to thank Fred Marshall and Reuben Epstein for the data that they sent me when I need to use it. Thank You.

-
- ¹ B. Yaakobi, *et al.*, Phys. Plasma 7, 3723 (2000).
² S. P. Regan, *et al.*, Phys. Rev. Lett. 89, 085003-1 (2002)
⁴ J. Delettrez, *et al.*, Phys. Rev. A 36, 3926 (1987).
⁵ T.R. Boehly, *et al.*, Opt. Commun. 133, 495 (1997)
⁶ Y. Lin, *et al.*, Opt. Lett. 20, 764 (1995)
⁷ S.P. Regan, *et al.*, Opt. Soc. Am. B 17, 1483 (2000)
⁸ T.R. Boehly, *et al.*, Appl. Phys. 85, 3444 (1999)
⁹ F.J. Marshall, *et al.*, Phys. Rev. A 36, 3926 (1987)
¹⁰ V. A. Smalyuk, *et al.*, Rev. Sci. Instrum. 72, 635 (2001)

FIGURES

Figure 1

(a) Schematic of spherical targets with diagnostic titanium-doped (2% by atom) layers offset by 1, 5, 7, and 9 μm of pure CH from the inner surface. (b) *LILAC*-simulated profiles of target density and temperature at peak compression of the implosion. The locations of titanium-doped layers are shown by the gray areas.

Figure 2

(a) Measured time-integrated spectrum $S_{\text{meas}}(E)$ as a function of photon energy for shot 26625 (thin solid line). Estimated continuum level $S_{\text{con}}(E)$ as a function of photon energy (thick solid line). The instrumental spectral responses as functions of photon energy of GMXI channels inside [$R_{1s-2p}(E)$, dashed line] and outside of [$R_{<K}(E)$, dotted line] the titanium $1s-2p$ absorption region. (b) The spatial correction functions as a function of distance in the vertical axis for images inside (dashed line) and outside (dotted line) the titanium $1s-2p$ absorption region.

Figure 3

Wiener-filtered core images around peak compression at energies inside (~ 4.60 keV, upper row of images) and outside (~ 4.87 keV, lower row of images) the titanium $1s-2p$ absorption spectral region for shots with 1- μm - (shot 26625), 5- μm - (shot 26630), 7- μm -

(shot 26631), and 9- μm -offset (shot 26632) titanium-doped layers, and for the shot without titanium (26633).

Figure 4

Optical-depth modulation images at peak compression for shots with 1- μm - (shot 26625), 5- μm - (shot 26630), 7- μm - (shot 26631), and 9- μm -offset (shot 26632) titanium-doped layers integrated over ~ 200 ps of x-ray emission.

Figure 5

(a) Power per mode as a function of spatial frequency of relative areal-density modulations at peak compression for shots with 1-, 5-, 7-, and 9- μm -offset titanium-doped layers. (b) Peak compression optical-depth modulation σ_{rms} (solid line) and relative areal-density modulation σ_{rms} (dashed line) as a function of the layer offset.

Figure 1

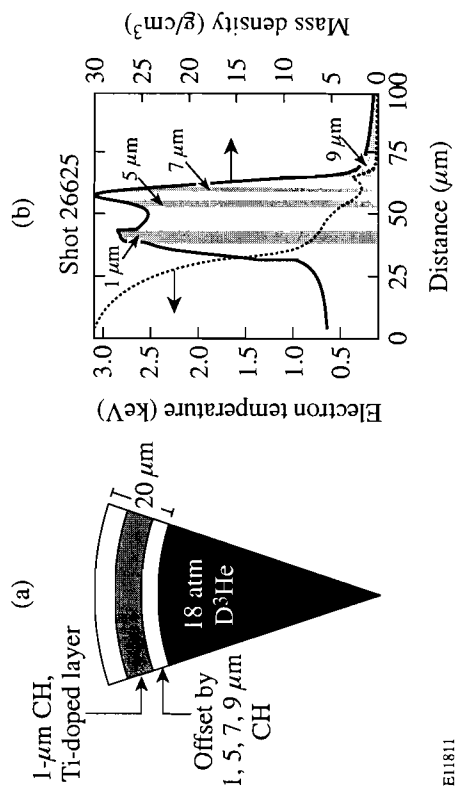
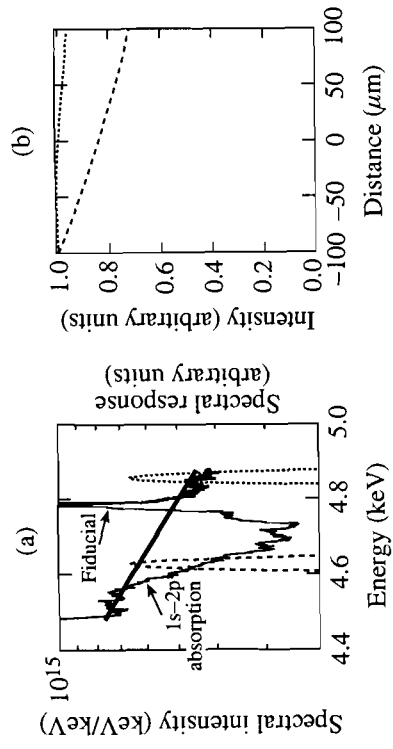


Figure 2



E11813

Figure 3

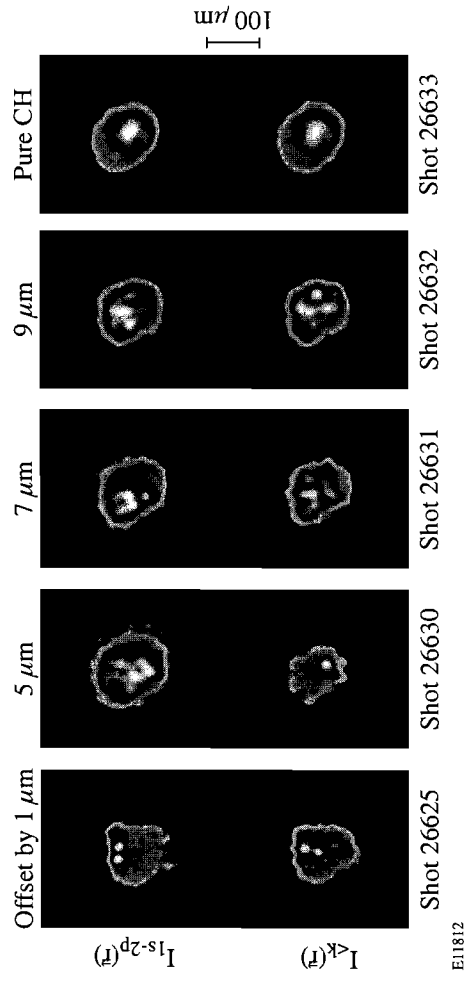


Figure 4

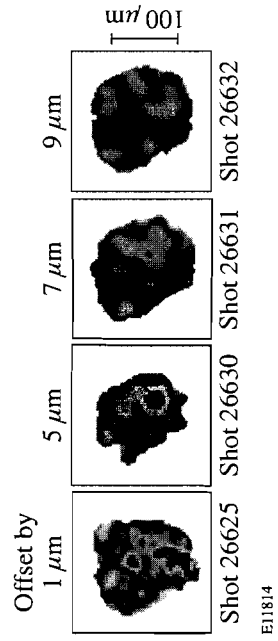
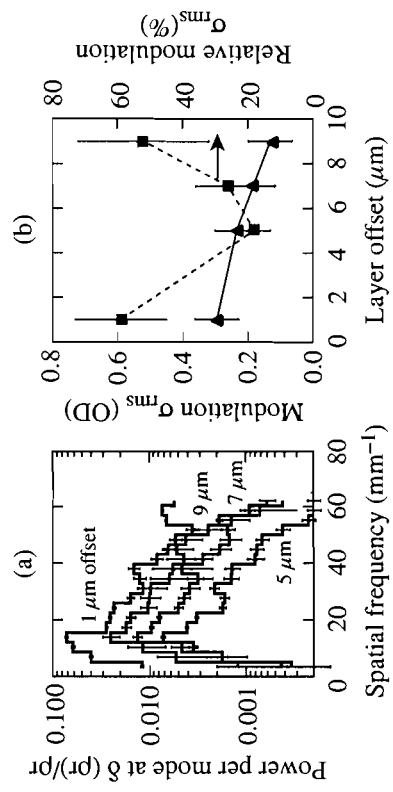


Figure 5



E11815

Secondary Electrons from X-Ray Photocathodes

Sid Ghosh

Secondary Electrons from X-Ray Photocathodes

S. Ghosh

Advisor: Dr. P.A. Jaanimagi

University of Rochester
LABORATORY FOR LASER ENERGETICS
250 East River Road
Rochester, NY 14623-1299

ABSTRACT

Streak cameras are used to study the x-rays that are emitted from Inertial Confinement Fusion (ICF) targets as they implode. These cameras operate by using a photocathode to convert the x-ray flux to a secondary electron current. Secondary electrons are then focused onto a phosphor screen using the streak tube electron optics, and finally recorded using a charged coupled device (CCD) camera. The pulse height distributions for the number of secondary electrons per each absorbed x-ray event in the photocathode can be traced from the CCD data. Several photocathode materials were tested for their secondary electron number distributions by using a DC x-ray source and a slow ramp to uniformly illuminate the streak camera. The data was analyzed by generating histograms of the values of CCD superpixels that integrated the recorded signal in the pixels surrounding an x-ray event. The distribution for the number of secondary electrons produced per each absorbed x-ray event can then be derived by using the distribution for the number of CCD electrons recorded per single streak tube electron.

1. INTRODUCTION

X-ray streak cameras are used at the Laboratory for Laser Energetics (LLE) to serve as a diagnostic tool in inertial confinement fusion (ICF) experiments. The uniformity of a target's implosion can be studied by analyzing the x-ray emission that it produces. This is an important factor in determining the success of direct drive experiments in which the target needs to be

uniformly compressed.¹ The characterization of the x-ray diagnostics is important to the ICF program because it allows for better measurement and detection capabilities. By understanding the properties that govern the operation of the streak camera components, the system performance can be improved upon for greater accuracy.²

The PJx streak camera, built at LLE, was used for this work. The basic components of the streak camera system include the photocathode, streak tube and the CCD camera that is used to read the image into the computer. The streak tube operates on the principle of the photoelectric effect. X-ray photons create high-energy primary electrons, which in turn produce low energy secondary electrons. The secondary electrons are emitted from the photocathode surface and then focused through the streak tube. The streak tube consists of an electron optic system that relays an image of the photocathode to a phosphor screen. The PJx uses a quadrupole doublet lens for optimal focusing capabilities. The tube also includes a deflection system to sweep the electron beam across the screen (see Fig. 1). The light from the phosphor is fiber coupled to the CCD camera for maximum transfer efficiency. The PJx streak camera incorporates a Spectral Instruments 800 Series CCD Array Scientific Imaging Camera.³ The x-ray source used in this experimentation was built by a previous summer student. It is a large area source; the x-ray flux is produced by 4 keV electrons bombarding a gold anode.⁴

The major component of the CCD camera is the CCD chip which contains a 2-dimensional pixel array to receive the incident light. This light is allowed to accumulate as charge in the wells of the pixels. The charge produced is proportional to the integral of the light intensity during the exposure time. Collected charge is then transferred to an output amplifier. This creates a measurable voltage signal proportional to the charge. The voltage is sent through an analog to digital converter, which converts the signal to Analog to Digital Units (ADUs). This

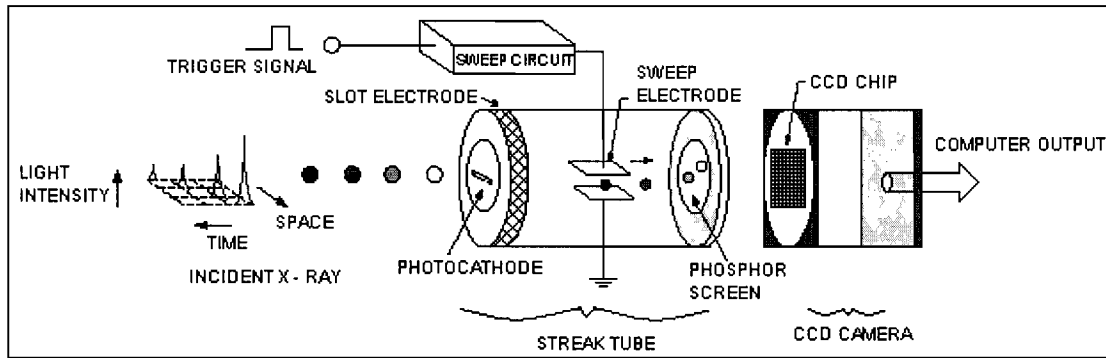


Fig. 1. Incident light is collected on the photocathode with respect to space and then swept across the phosphor screen of the streak tube in time.

output is then sent to the computer, where the image is displayed in terms of ADUs.

Various photocathode materials create different number distributions of streak tube secondary electrons. A method requiring several steps has been used to find the number of secondary electrons produced per single x-ray event. Streak data must first be generated using the DC x-ray source and a slow (0.5 s) streak ramp. The flux levels are kept sufficiently low so that individual absorbed x-rays are recorded as isolated events; less than 5% of the CCD pixels are illuminated in any one frame. The data is background subtracted and compiled into superpixel histograms. The superpixels integrate the energy in the pixels surrounding a given event. The histograms from multiple streak images are then summed together in order to improve the signal to noise ratio (SNR). Each histogram is the sum of the distributions of ADU values produced for 0 - n electron events. In order to derive the secondary electron number distributions, the ADU distributions for zero and single electron events needed to be found first.

2. CCD CALIBRATION

The CCD camera must first be calibrated in order to take accurate measurements of the secondary electron output. The background noise level, system gain (CCD electrons/ ADU) as well as the linearity of the A/D need to be measured. These values will determine the authenticity of the collected data.

Noise in the CCD can be attributed to several factors. The biggest contribution to the background is the read noise from the A/D digitization process. The read noise should be Gaussian distributed. A second source of background noise is from dark current, which is thermally generated charge that accumulates in the CCD wells during exposure times. Noise created by dark current is Poisson distributed. To avoid the accumulation of dark charge, the CCD camera is thermoelectrically cooled to a temperature of $-40\text{ }^{\circ}\text{C}$, where the dark charge is almost negligible. Another source of noise is from cosmic ray hits. These hits produce very large pixel values that can be easily eliminated during the data analysis.

In Fig. 2, we present the resulting histogram from the subtraction of a pair of background frames. This data is well fit by a Gaussian distribution centered about a value of 0 ADUs, with a standard deviation (σ) of 7.95 ADUs (or 8.67 CCD electrons). This σ value is relatively small, so it indicates that our CCD camera is a good detector with low noise. The data collected here is for a readout speed of 200 kHz in the camera.

Poisson statistics describes the distribution for the number of photons incident upon a unit of area per a unit of time. When photons are absorbed in the CCD array, the resulting CCD electrons are also Poisson distributed. Using the principle that under Poisson statistics the variance is equal to the mean of the data, we can find the gain of the system and verify its linearity. A green LED light source was used to uniformly illuminate the CCD array for the data collection. The variance was calculated from the subtraction of a pair of data frames, while the mean signal was found by subtracting a background frame from a data frame. The exposure levels were varied by adjusting the duration of the LED pulse. Figure 3 shows the plot of the variance vs. mean and the straight line fit to the data.

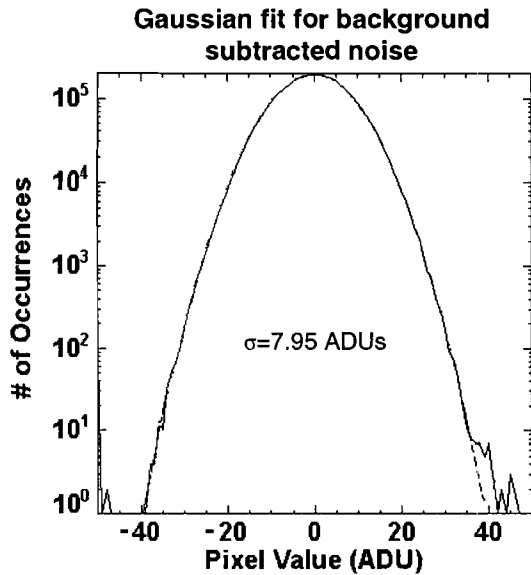


Fig. 2. Background subtracted frames produce a Gaussian distribution.

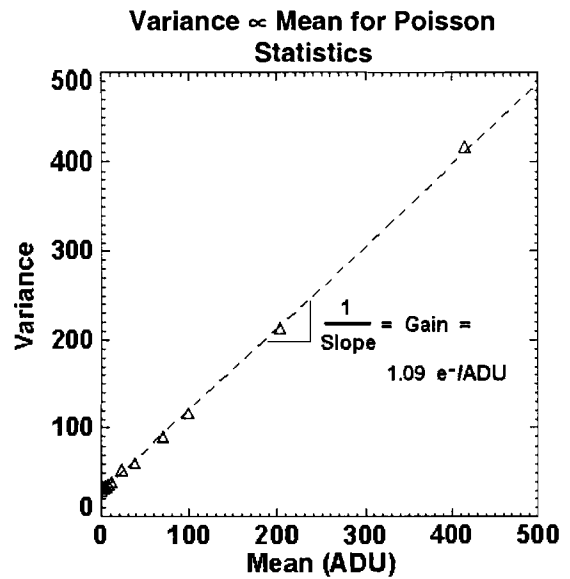


Fig. 3. Variance vs. Mean data produces a linear relationship.

To find the linear relationship for the data, a least squared fit was used, where:

$$(x_i, y_i) \quad y = a_0 + a_1x$$

$$\chi^2 = \sum (a_0 + a_1x_i - y_i)^2 = \min. \quad (1)$$

The inverse of the slope for the line in this plot is equal to the CCD gain, which was found to be 1.09 CCD electrons per ADU.

3. STREAK IMAGES

Typical streak images are presented in Fig. 4, where each spot represents an absorbed x-ray event. The range of spot intensities and sizes corresponds to the distribution of the number of CCD electrons generated per single streak tube electron convolved with the number distribution of secondary electrons produced per absorbed x-ray. The spots are sparsely scattered throughout the image, so single events can be analyzed.

As is illustrated in Fig. 5, the 1x1, or normal pixel size does not capture the entire recorded signal from an event. The phosphorescence from a single electron event, even if it is centered on a single pixel, will generally be distributed among many pixels. Multiple secondary

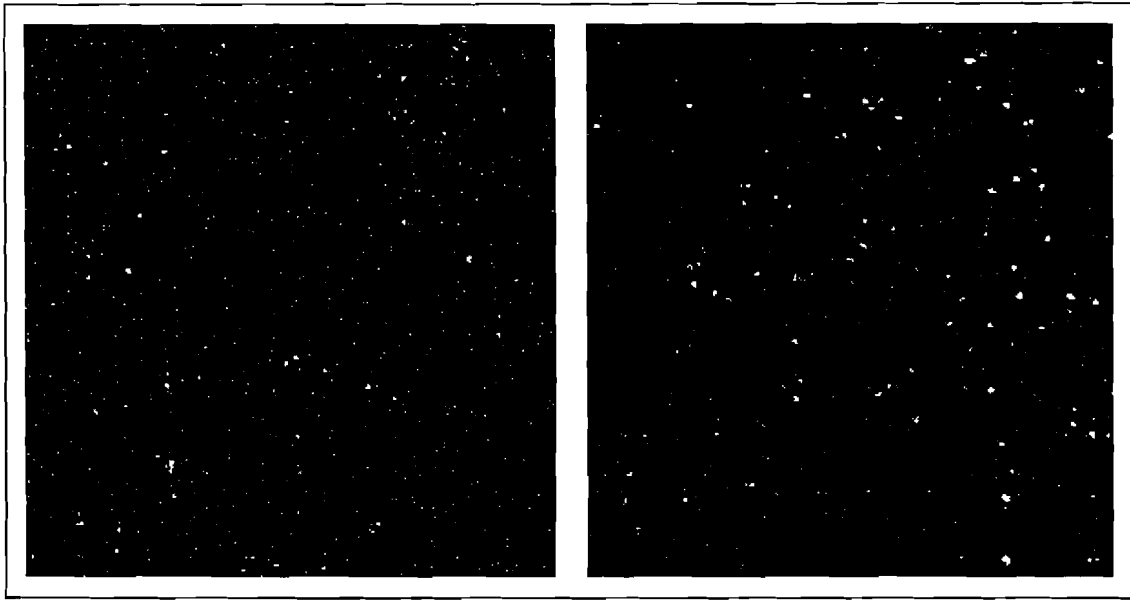


Fig. 4. The image on the left shows the secondary electron distribution from the Gold photocathode, while the image on the right shows the Potassium Bromide photocathode. The spots indicate secondary electron events. Both images are background subtracted and taken from streak tube operations of -25 kV. They are both 400×400 pixels of the CCD array in size.

electron events will spread their signal even further since the individual electrons will be imaged to different points on the phosphor screen, (dependent on their initial position and velocity vector at the photocathode). To ensure that the entire signal from a given event is integrated, superpixels centered about a local maximum pixel are created. The different superpixel sizes that were implemented in this study included 3×3 , 5×5 , 7×7 and 9×9 superpixels.

4. PHOTOCATHODE MATERIALS

Several photocathode materials were experimented with to find their secondary electron number distribution per absorbed x-ray event. Metals in addition to insulators were tested. The metals included aluminum, gold and beryllium. Aluminum was used because it forms an aluminum oxide layer rather quickly, and therefore a stable material for use as a photocathode. Gold was used because of its stability and x-ray absorption characteristics. Beryllium was tested simply because it was a material that was available at the time of experimentation. The insulators included potassium bromide (KBr) and “fluffy” KBr. KBr is a commonly used photocathode material with higher quantum efficiency and a narrower secondary electron energy distribution

than metal photocathodes. The fluffy type of the photocathode is produced by coating the material in an Argon atmosphere. The resultant coating has a lower density and higher quantum efficiency than standard KBr. Data was collected at streak tube potentials of -15 kV as well as -25 kV. This will affect the gain for recording single electron

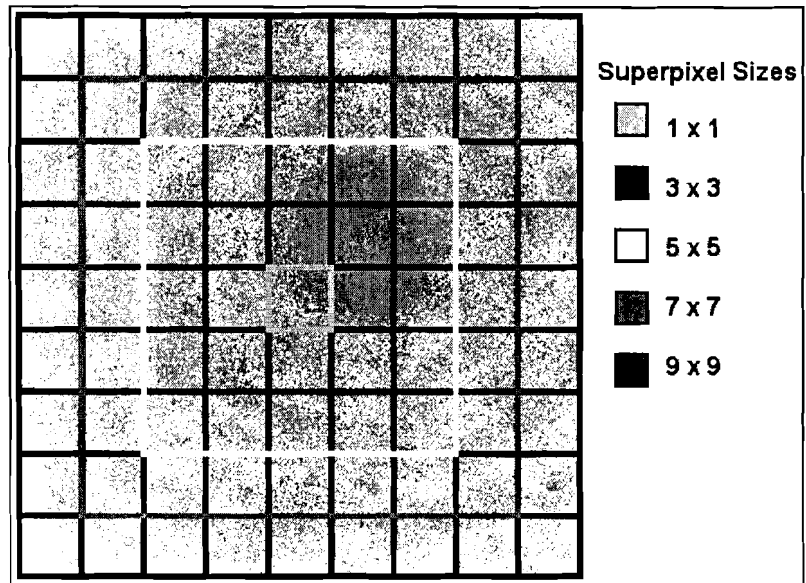


Fig. 5. Superpixels are created about a peak value (not the center of the distribution), and integrate the ADU values for the pixels surrounding the center.

events but should not affect the secondary electron number distribution. The following photocathodes and conditions were used for experimentation:

Material:	Thickness:	Streak tube Potential:
Potassium Bromide (KBr)	1500 angstroms (Å)	-15 kV
Aluminum (Al)	2000 Å	-15 kV
Fluffy KBr	-	-15 kV
Gold (Au)	300 Å	-15 kV
Fluffy KBr	-	-25 kV
Au	300 Å	-25 kV
KBr	1500 Å	-15 kV, inverse
KBr	1500 Å	-25 kV, inverse
Beryllium (Be)	12.7 microns (μ)	-15 kV, inverse
Be	12.7 μ	-25 kV, inverse

The inverse mode operation of the streak camera produces a tighter focus of the electron beam in the time direction. The distribution for recording single electron events was generated using an aluminum photocathode illuminated with a mercury light source. The mercury source produces

ultraviolet radiation that is much lower in energy than x-rays, thus allowing for the release of single photoelectrons from the photocathode.

5. SUPERPIXEL HISTOGRAMS

The superpixel histograms were generated by first ordering the pixel values in the background subtracted image from maximum to minimum. Starting with the maximum pixel value and proceeding down to a threshold value of 5 ADU, the superpixel value is calculated as the sum of the 3x3 to 9x9 neighboring pixels. The original pixel values are then replaced with a random value selected from a Gaussian distribution with $\sigma = 7.95$ ADU, (see Fig.2). This allows us to avoid multiple counting of events. Since the data is sparse, the superpixel histograms are dominated by the N=0 electron component, i.e. background which we may define as D0. The N=1 electron component is added as the D1 distribution convolved with the background, D0. The N=2 electron component is added as the D2 (= D1 convolved with D1) distribution convolved with the background, D0, and so on for the N>2 electron components. As the superpixel size increases, a greater amount of energy is integrated and therefore the range of the data values in

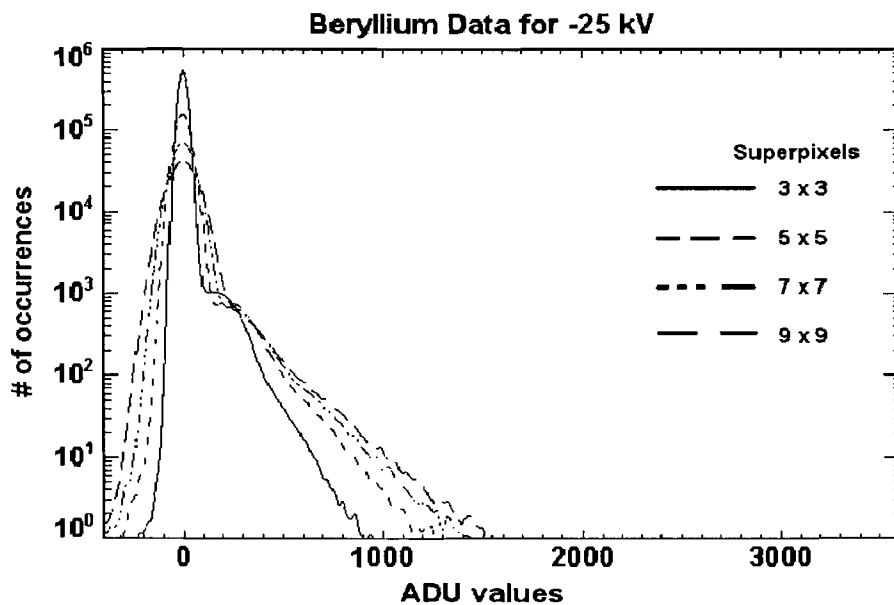


Fig. 6. Be data demonstrates visible signal on wing.

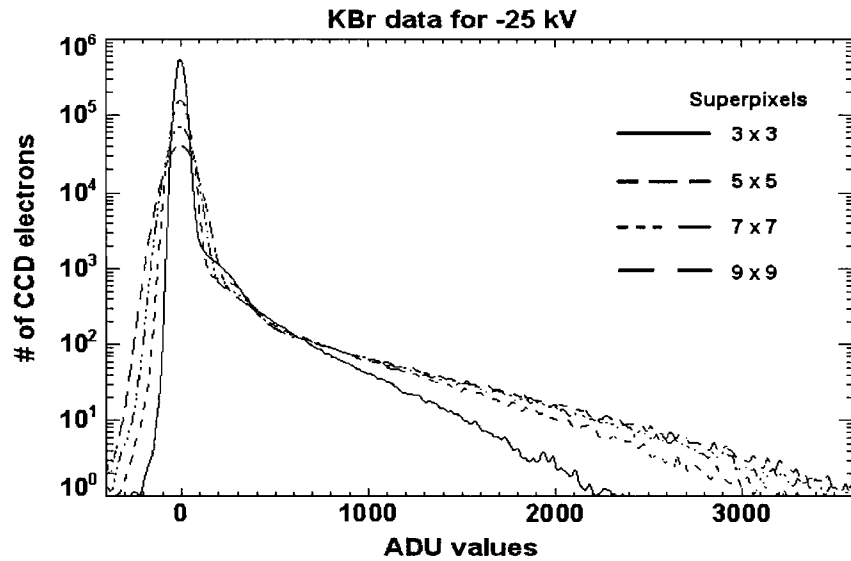


Fig. 7. KBr data extends out much farther, because the KBr photocathode produces a greater number of secondary electron events

ADUs increases as well. Also, the σ for the background Gaussian (D0) varies with the square root of the number of pixels in the superpixel. The histograms of the Be dataset are given in Fig. 6. The KBr data (Fig. 7) has a wing that extends out much farther than in the Be histogram. This is indicative of the fact that the signal is present through the N=15 secondary electron component. The shelf (near 200 ADU) that can be seen for the 3x3 superpixel in the Be and KBr histograms shows that the single electron event distribution is centered somewhere in that region, but is not clearly visible because of the large background signal.

6. QUANTUM EFFICIENCY AND TRANSMISSION

Another consideration in finding the number of secondary electrons produced can be made by calculating the quantum efficiency and transmission of the photocathode. Quantum efficiency is the probability that an electron will be released from a photocathode and is equal to the ratio of the number of electrons produced to the number of incident photons. It is proportional to the energy absorbed in the photocathode. Transmission represents the photons that go through the

photocathode without being absorbed. The transmission for a photocathode can be calculated through the formula:

$$Transmission = \frac{I_T}{I_O} = e^{(-\mu\rho x)} \quad (2)$$

where μ is equal to the mass absorption coefficient, ρ is the density and x is the effective secondary escape depth of the photocathode.⁵ Absorption can be represented by 1-Transmission. Therefore the ratio of quantum efficiency to the absorption is equal to the number of secondary electrons produced.

$$\#Secondary\ Electrons = \frac{Quantum\ Efficiency}{1 - Transmission} \quad (3)$$

The plots for the transmission and quantum efficiency for 1500 Å KBr were found. (see Fig. 8)

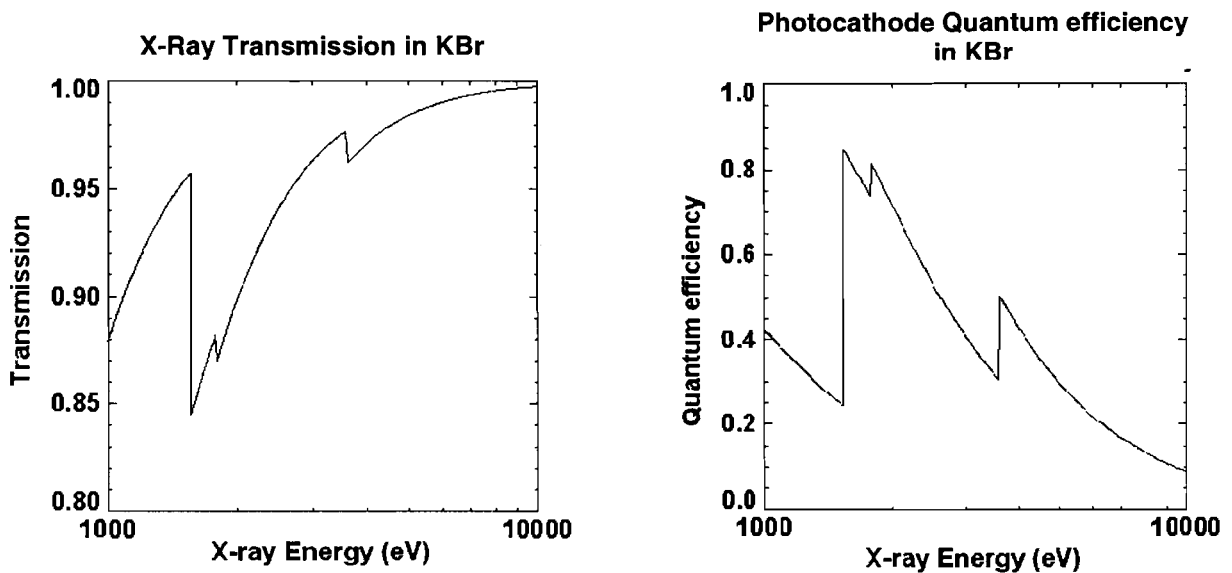


Fig. 8. X-Ray transmission and quantum efficiency plots for KBr (1500 Å).

The upper bound for our x-ray energy is set by the 4 keV electrons bombarding the gold anode in our x-ray source. The lower bound is 1 keV obtained from the transmission plot for Beryllium. In the range of 1-4 keV, the expected secondary electron production for KBr is approximately 3.5 to 14. These numbers however, do not correspond to the results we received for secondary electron

production. This may be due to the aging of the KBr photocathode; its response will degrade when exposed to atmospheric conditions. Since the calculations are made for an ideal situation, the discrepancy between the calculated results and the experimental results may be attributed to the degradation of the photocathode.

7. DATA ANALYSIS

In the superpixel histograms the data is in the form of:

$$\text{Signal} \otimes \text{Background} = \text{Data}. \quad (4)$$

where \otimes denotes convolution. To find the signal, the background must be deconvolved from the data. This can be done through a Fast Fourier Transform (FFT). If the FFT is taken for the signal, background and the data, then the signal times the background should equal the data. The deconvolution can then be made through a division in Fourier space. When this procedure was applied to the data however, erroneous results were produced. The signal is lost in the noise

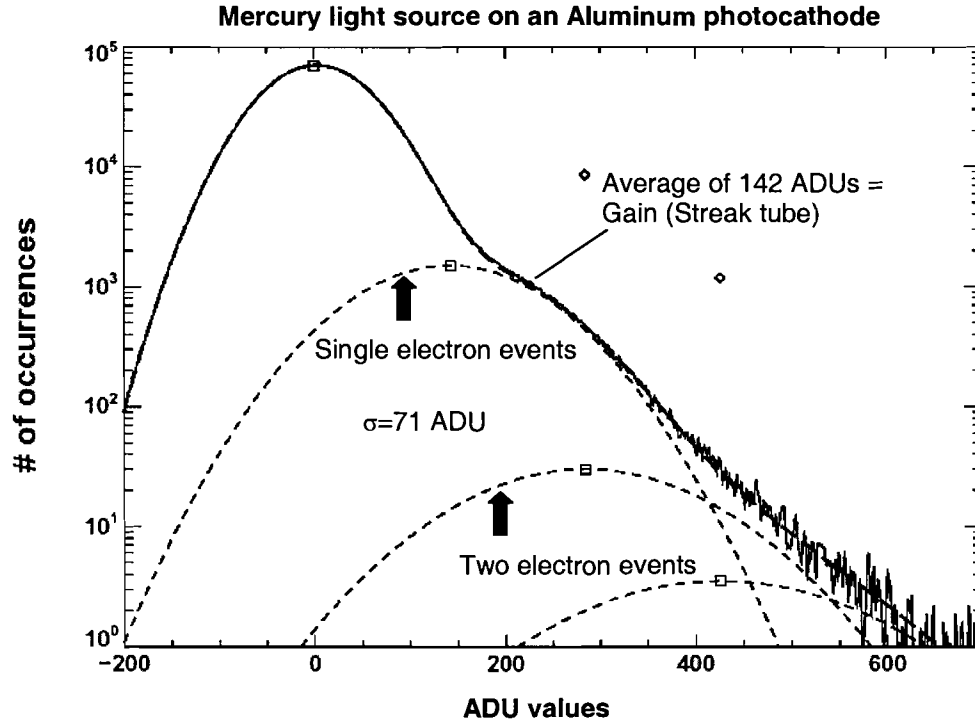


Fig. 9. The single electron event distribution is shown for the UV data. An average value of 142 ADUs is found signifying streak tube gain.

because the zero electron component is so much larger than any of the secondary electron components. Therefore the alternative process used was to find the single photoelectron distribution from the UV data and then apply the average found to predict the centers for multiple secondary electron events. The distribution for single electron events was found (see Fig. 9) from the Aluminum data taken with the mercury light source. The single photoelectron distribution is well fit by a Gaussian centered about an average of 142 ADUs, and a σ of 71 ADU. This signifies the gain for the streak tube, and states that on average, 142 ADUs are produced per streak tube electron (or 1 photoelectron). The ADU values can then be converted to CCD electrons by the gain of the CCD camera. Now we can predict 284 ADUs will be produced for 2 electron events, 426 ADUs for 3 electron events and so on. The ADUs per single electron event has now given the centers for the distributions in the other superpixel histograms. In order to find the signal, the amplitudes for the distributions at each electron event location can be subtracted from the data to

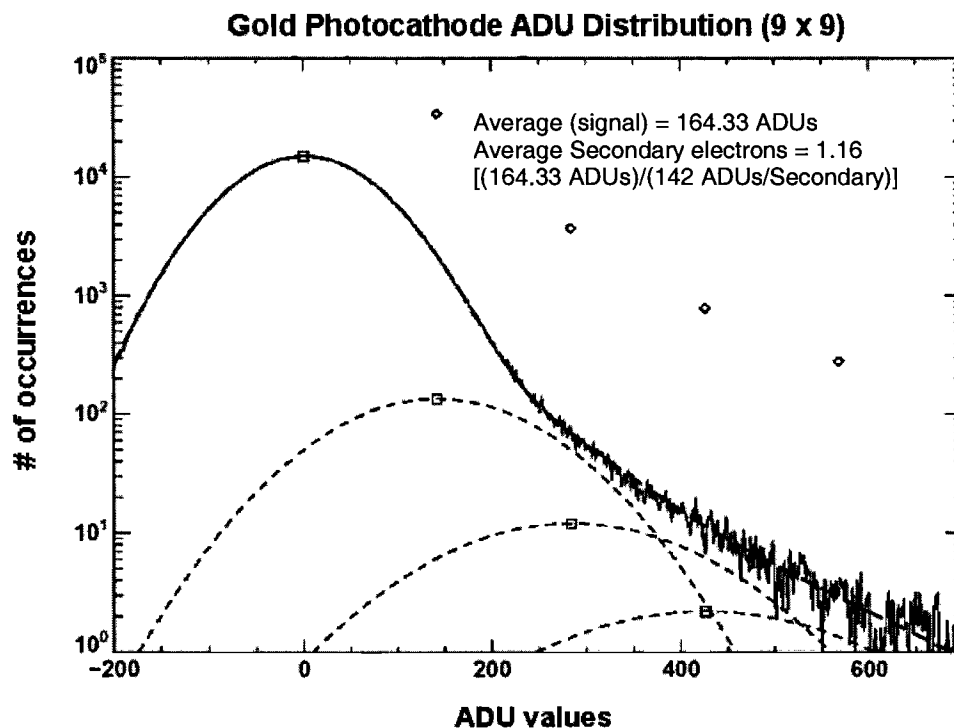


Fig. 10. The average of the gold data signal is found to be 162.62 ADUs. Applying the streak tube gain, the average secondary electrons produced is 1.16. The probability of 1 : 2 : 3 : 4 electron events is 0.877 : 0.095 : 0.020 : 0.007. The relative probability is shown as \diamond in the figure.

drive the residual (difference between the signal and the data) to 0. The secondary electron event distributions were found through four events for the 9x9 superpixel size of the gold photocathode. (see Fig. 10) When the background is removed from the gold data and only the signal composed of the multiple secondary electron events is left, an average signal of 164.33 ADUs with a signal to noise ratio (SNR) of 1.33 is obtained. Dividing out the streak tube gain allows us to find that the average secondary electron production per x-ray event in the gold photocathode is 1.16. The same process is applied to the 9x9 superpixel information in KBr. The primary difference is that KBr produces up through 15 secondary electron events, as was predicted from the elongated wing. (see Fig. 11)

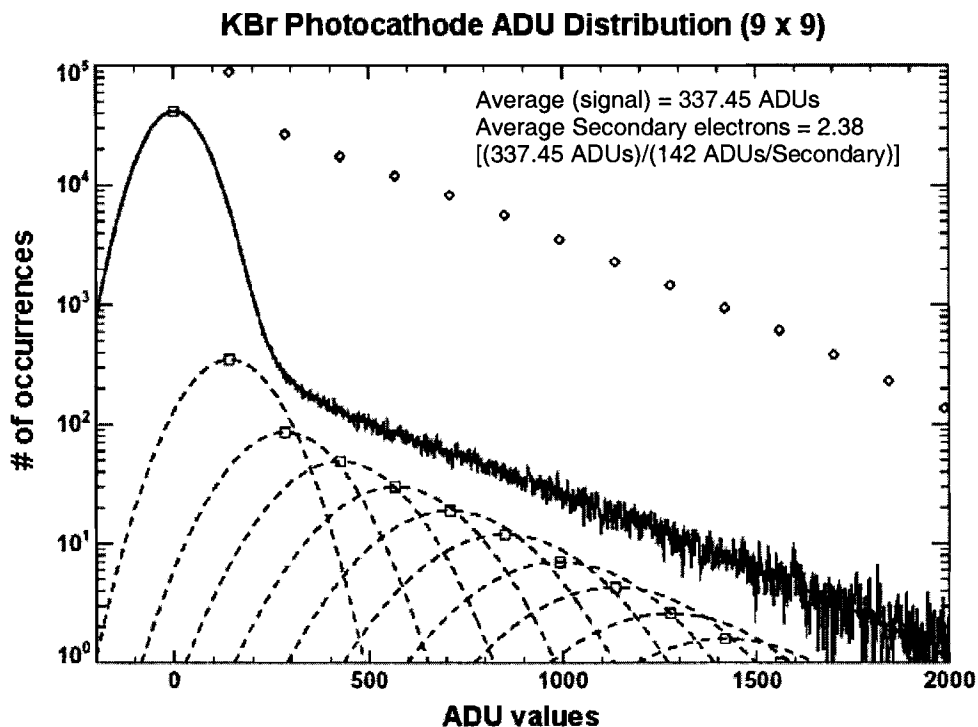


Fig. 11. The average secondary electron production in KBr is found to be 2.38. The signal extends through 15 electron events. The probability of 1 : 2 : 3 : ... events is 0.527 : 0.158 : 0.104 : ..., decreasing approximately by 0.68 for additional electrons.

For the KBr data, the average signal is found to be 337.45 ADUs with an SNR of 1.04, making the average secondary electron production per x-ray event 2.38.

8. DISCUSSION

After finding the single photoelectron distribution in ADUs per streak tube electron, the signal for the superpixel data was deconvolved. The photoelectron information allows us to correlate quantitatively the CCD data to the electron current in the streak tube. For single electron events, the σ is 71 ADU, which happens to equal half the streak tube gain for an SNR of 2.0. The generation of multiple secondary electrons per x-ray event degrades the SNR. Furthermore the secondary electron number distribution per x-ray event was measured for the Gold and KBr photocathodes, but the photoelectron information can be extended to find the distributions for the other photocathodes as well. The main significance of this finding, however, is that now measurements of the secondary electron distribution in CCD electrons will allow for the absolute calibration of the x-ray streak camera. With the Gold and KBr photocathodes as examples, we can now trace the CCD electron distribution all the way back to the absorbed x-rays because the secondary electron distribution per x-ray event has been found.

For future experimentation, we can work on finding the quantum efficiency for the photocathode from the secondary electron distribution. This can be done through the use of a monochromatic x-ray source, which will deliver only one energy and not a range as was used in this experimentation (1-4 keV). This will allow us to monitor the photocathode and the streak camera system and maintain the best diagnostics.

9. ACKNOWLEDGEMENTS

I would like to thank Dr. R. Stephen Craxton for giving me the opportunity to participate in this program. It has truly been an incredible experience for me. Next I would like to thank Mr. Robert Boni for the help he provided me during the first week of the program and later on as well. I would also like to thank Mr. Steven Noyes for taking the time to coat the photocathode materials that were used in the experimentation. Most of all I would like to thank my advisor, Dr. Paul

Jaanimagi for all the time and help he provided me in this project. Without his patience and many clarifications, this work would not have been possible for me.

10. REFERENCES

1. R.L. McCrory et al., “Omega ICF Experiments and Preparation for Direct-Drive Ignition on NIF”, Nucl.Fusion, 41, 1413 (2001).
2. W.R. Donaldson, R. Boni, R.L. Keck and P.A. Jaanimagi, “A self-calibrating multichannel streak camera for inertial confinement fusion applications,” in the *Review of Scientific Instruments*, Vol. 73, pg. 2606, July 2002.
3. “800 Series Camera System User’s Manual,” Spectral Instruments Inc., Tucson, Arizona, 2000.
4. A. Campanella, “Large Area, Low Voltage X-Ray Source,” LLE Summer Program, 2000.
5. B.L. Henke, J.P. Knauer and K. Premaratne, J. Appl. Phys. 52, 1509, 1981.

Computer-Controlled Neutron Diagnostics

Kyle Gibney

COMPUTER CONTROLLED NEUTRON DIAGNOSTICS

K. Gibney

Advised by Dr. Christian Stoeckl

LABORATORY FOR LASER ENERGETICS

University of Rochester

250 East River Road

Rochester, NY 14623

ABSTRACT

In order to upgrade current neutron diagnostic software, and solve problems found within that software, a replacement program has been built using Java. This application is designed to acquire data from FASTBUS time-to-digital converters and export it to a file to be analyzed at a subsequent time. Data is produced using the MEDUSA neutron diagnostic system which is designed to record arrival times of individual neutrons that are emitted in inertial confinement fusion experiments. Neutrons are allowed to pass through an opening in the wall of the target area and strike scintillator detectors housed in a separate building approximately 19 meters away. The signals produced by the scintillators are sent to CAMAC discriminators and stored as encoded data in the FASTBUS TDC's. Former versions of this data acquisition program, written in Visual Basic, have become outdated and incompatible with current versions of the

language. They have also depended on single pieces of hardware that can no longer be purchased, so it was vital to construct a program that could still function on external hardware if the internal card were to become unusable. These problems have been successfully remedied, and the program has been improved internally to allow for easy modification and real time updates of hardware status and the data acquisition process.

INTRODUCTION

The University of Rochester's Laboratory for Laser Energetics (LLE) attempts laser driven inertial confinement fusion (ICF) in which deuterium and tritium are compressed to high density and high temperature. As a result of the fusion of these two isotopes an intermediate particle is formed that immediately breaks down into an alpha particle and a neutron. By studying the released neutrons the burning fuel region can be characterized and primary and secondary yields can be measured.

The neutron diagnostic system at LLE, known as MEDUSA (Multi-Element Detector Using a Scintillator Array), depends on software developed in-house to acquire data from hardware specially made for high energy physics applications. Neutrons strike scintillators on MEDUSA that send signals through CAMAC (Computer Automated Measurement and Control) discriminators and end up being stored as encoded data in FASTBUS time-to-digital converters. This data acquisition software, originally written in Visual Basic 4.0, has been heavily updated since the introduction of MEDUSA to the laboratory in 1998 to be used with Visual Basic 5.0, and though it can still get its job

done, it has become obsolete and extremely difficult to maintain. Therefore, a major overhaul was warranted. Knowing the rate at which technology changes, it goes without saying that there have been several other languages introduced in the time that has elapsed, and many of these are much better suited for this type of application than Visual Basic.

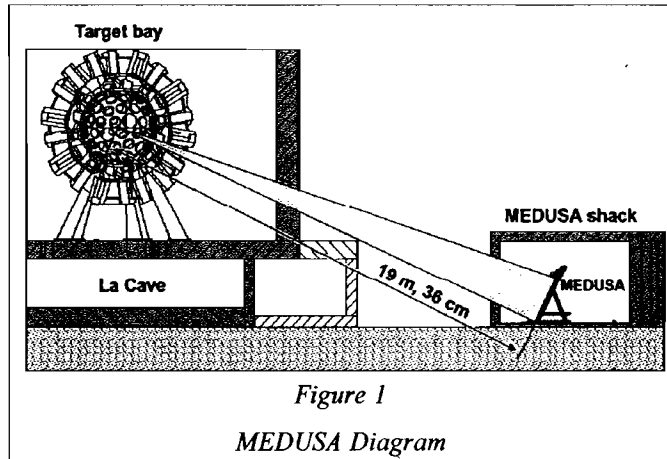
One of these emerging languages is Java. Introduced in 1995 under the name OAK, Java has become one of the most widely used development tools for new projects in recent years. Developers have grasped Java for good reason. It introduced many built-in features that were until then left up to the programmer to implement. Among these are multi-threading (parallel processing), portability, garbage collection, and automatic memory allocation. So, since Java has many features that could be utilized in this type of application, it was the logical choice for the language of the replacement program.

MEDUSA NEUTRON TIME-OF-FLIGHT ARRAY

The MEDUSA neutron diagnostic system consists of 824 specially made photomultiplier/plastic scintillator detectors that are used to measure fast neutron spectra from laser driven ICF experiments.

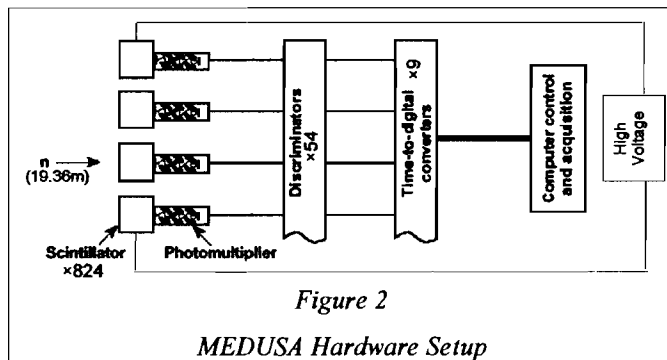
MEDUSA is located in a small building roughly 19 meters from the center of the target chamber. The wall around the target chamber has an opening designed to allow neutrons to pass through and strike the scintillator detectors on MEDUSA. The detectors consist of scintillating plastic connected to a photomultiplier tube. Neutrons hit the

scintillating plastic causing protons to be elastically scattered. The protons then pass through the plastic causing photons to be emitted and hit the photomultiplier tube. The photomultiplier tube is designed to turn a small light signal



into an electrical signal by taking advantage of the photoelectric effect, in which light hitting a surface causes electrons to be ejected. A sequence of electrodes arranged at increasing voltage provides an amplifier, which turns this initially small current into a measurable pulse of charge that can be recorded.

The scintillators themselves are powered using a programmable LeCroy 1458 High Voltage system connected to a personal computer using a serial



interface (RS-232). The hardware connected to the scintillator array is made up of five CAMAC crates holding 54 LeCroy 4413 discriminators along with a single FASTBUS crate holding nine LeCroy 1877 time-to-digital converters (TDC's). The signal produced by a photomultiplier is sent through a CAMAC 16-channel discriminator with a threshold set to 200 mV and then transferred to a FASTBUS TDC where it is encoded by a Monolithic Time Digitizer, which is an 8-channel, 16-bit dynamic range TDC circuit. At

this point, after the signals have been digitized, they are ready to be read using the data acquisition program.

PROGRAM FUNCTION AND USER INTERFACE

The MEDUSA data acquisition program is meant to read the data from the FASTBUS crate and export it into a file that will be analyzed by a data analysis program. When the program is loaded it automatically checks the hardware that is needed (CAMAC, FASTBUS, HV) and alerts the user if any problems are encountered, such as a CAMAC crate being turned off, or a discriminator module not functioning correctly. Following the hardware check the program remains idle, listening to messages from the OMEGA broadcast server which tells the program at what stage the shot process is in. If the program receives a message it recognizes as a cue, a task will be started that corresponds with that message. For example, a message of "POSTSHOT" would cause the program to begin reading data from the FASTBUS TDC modules and make a file containing this data, or a message of "CHARGE" would cause the the program to perform a precautionary hardware check to ensure that all crates and modules are still in working condition. This means that the program is fully automated and requires absolutely no user input. Following acquisition, data is printed to a file on the local disk and/or UNIX server that matches the format required by the analysis program and the acquisition application returns to an idle state.

The graphical user interface (GUI) was made to be as user-friendly and

intuitive as possible.

Although the program is designed to require no user input, aside from being able to select the preferred save path and auto-acquire options, it was still crucial to

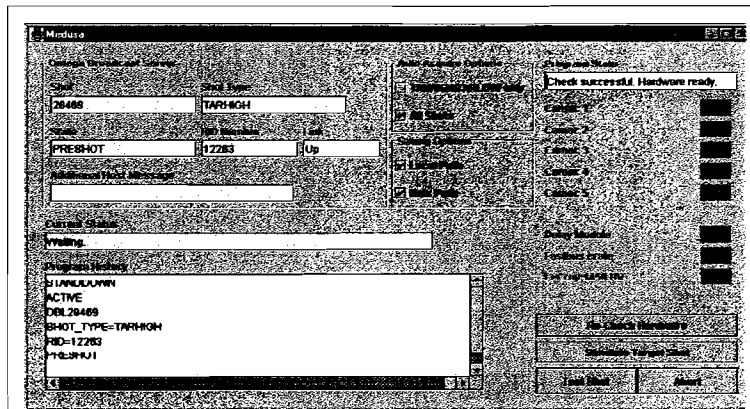


Figure 3

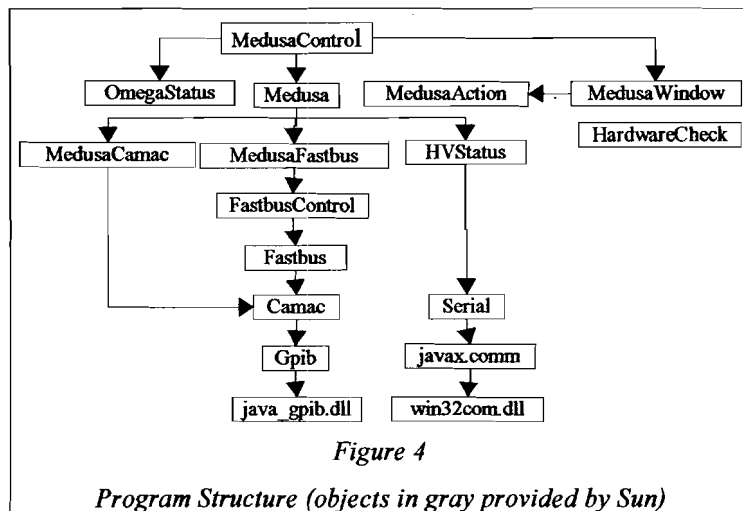
MEDUSA User Interface

try and make interacting with the program as effortless as possible. It was important to display information about each shot, program history, and hardware status in places on the window that made viewing easy and understandable. The user interface was not drastically changed from the previous Visual Basic version mainly to prevent an unnecessary retraining of all operators. Because there are many people that need to understand how to operate the program, and most of them are comfortable with the Visual Basic interface, it seemed logical to keep the interface as similar as possible.

PROGRAM STRUCTURE

One of the big advantages Java brought was the ability to design the program in layers. Layering the classes in Java allows for reusable code and easy modification when it is necessary. Classes written for the data acquisition program can be easily reused as they are in another program that will need similar functions. Easy modification is also important in a program that will need to be maintained by others following completion.

Code needs to be as readable as possible to allow for modification, and again the layering becomes beneficial because classes can be altered independently of the modules above and below, meaning



that a slight change in one class will not cause major problems in others around it. Because this program is written in three different languages it is important that it is adequately documented. The majority is done in Java, but the functions needed to control GPIB (General Purpose Interface Bus) needed to be done using the Java Native Interface and C, and assembly microcode was used to control the FASTBUS embedded microcontroller.

ADVANTAGES

The MEDUSA data acquisition program, completed in Java, has many advantages that were not found in the Visual Basic version, and it has many possibilities for future use. The updated program takes advantage of multi-threading, so long-running tasks are able to run simultaneously with the user interface with no obvious effect on performance being seen the user. This allows users to see updates in real-time, as tasks are being processed in the background. Within the program updates were made to the error reporting process. If problems are found with hardware, or a save path is non-existent, an

explanatory message is given to the user so the problem can be solved quickly. If a problem with hardware is found, data acquisition is canceled until the errors have been resolved.

One of the major problems with the Visual Basic version of MEDUSA was compatibility. Visual Basic is not backward compatible, so recent versions of Visual Basic (VB 6, VB .NET) are not compatible with the version that MEDUSA was originally written in. Java does not have this problem, so updates to the language are generally well received and easily adaptable.

Another large problem was hardware dependency. One of the goals of the program from the beginning was to avoid being dependent on a single piece of hardware. These devices can no longer be purchased because companies have stopped manufacturing them due to lack of demand, so it is very important that the program can be easily told to utilize different pieces of hardware. If one were to break, it is vital that there is a backup that can be used as a replacement, instead of having no secondary option and having no way to acquire data at that point.

FUTURE USES

The program is not only designed for use on MEDUSA at LLE, but also possibly on the newly added 1020 Array. The hardware setup for this new detector is very similar to that of MEDUSA, so modifying the program to take data from this device should be fairly simple. Java is also a National Ignition Facility (NIF) approved language,

so if they have a similar setup the data acquisition program could be utilized there as well, again with minimal modification, after the completion of the NIF in 2008.

CONCLUSION

The development of the replacement program has been successful. The program is currently being used in place of the Visual Basic program while being debugged for errors. This switch to Java has brought many advantages that have made further development of the program much easier, and has made possible porting the program to be used with other systems. The 1020 Array and possibly NIF applications are now options that have been opened up by the development of this new program. Also, most issues found within the previous version were successfully remedied, including hardware dependency and compatibility problems.

ACKNOWLEDGMENTS

I would like to thank Dr. Stephen Craxton, director of the Summer High School research program at LLE for giving me this wonderful opportunity and allowing me to work here the summer of 2002. I would also especially like to thank Dr. Christian Stoeckl and Dr. Vladimir Glebov for their amazing patience and willingness to assist me with whatever I asked of them. There is no question that the completion of this project would have been impossible without their explanations and hints.

A Ray-Tracing Model for Cryogenic Target Uniformity Characterization

Sharon Jin

A Ray-Tracing Model for Cryogenic Target Uniformity Characterization

Sharon Jin

Advisor: Dr. Stephen Craxton

Laboratory for Laser Energetics

University of Rochester

Summer High School Research Program

2002

Abstract

The Laboratory for Laser Energetics attempts to create fusion energy by irradiating a fuel capsule with many laser beams. In trying to achieve high energy gain, the fuel must be uniformly compressed to high density. Thus, the fuel capsule design is a thin plastic shell containing a thick layer of cryogenic Deuterium-Tritium (DT) fuel. One primary source of laser-fusion target performance degradation is a non-uniform inner surface on the dense fuel ice layer. Target characterization, therefore, uses shadowgraphy to produce within the periphery of the target image a virtual bright ring, a critical indication of variations in thickness of the fuel ice. A computer model, *Pegasus*, was built to trace light rays through an ideal target. It maps the outgoing intensity, taking into account Fresnel losses, polarization of light, ice absorption, and divergence of light path. In addition, the model sums up contributions from multiple light beams to allow finite F-numbers for both the light source and collection optics. Simulations of cryogenic and surrogate targets, when compared with experimental data, show agreement in intensity levels as well as in virtual bright ring position. This computer model aims to provide further insight into the best position of the focal plane, ideal combinations of light source and collection optics F-numbers, and effects of scattering on intensity.

1. Introduction

The ultimate goal of Inertial Confinement Fusion (ICF) research at the Laboratory for Laser Energetics (LLE) is to reap a high energy gain from fusion reactions with the OMEGA laser. In direct drive ICF, multiple, intense laser beams illuminate a spherical target pellet and compress it to extremely high plasma densities and temperatures [1].

By design, cryogenic targets are able to deliver a high concentration of fusion fuel. Cryogenic targets generally have a thin plastic (CH) shell, about $3\mu\text{m}$, enveloping a thick, dense layer of Deuterium (D_2) or Deuterium-Tritium (DT) fuel, about $100\mu\text{m}$, chilled to 20K (see Fig. 1) [2,3].

The inner ice layer is formed by infrared radiation in D_2 and beta heating in DT [4]. These methods currently make the layer uniform to $3\mu\text{m}$ [5]. In order to achieve high energy gain, it is desirable to have uniformity to $1\mu\text{m}$, because any non-uniformity will grow exponentially under implosion conditions and decrease target performance.

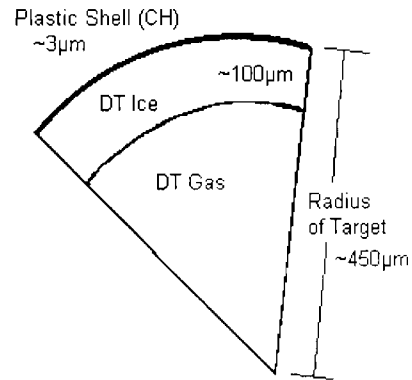
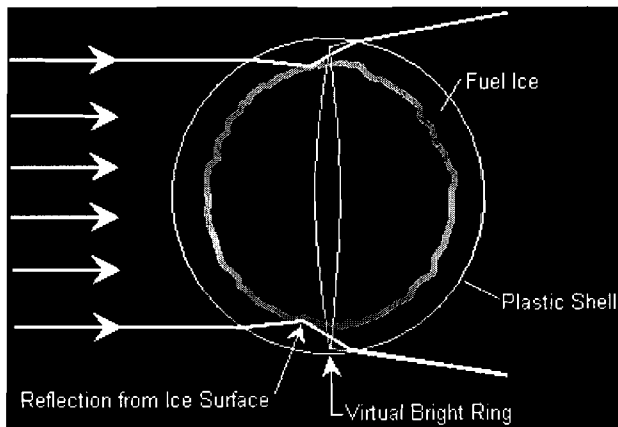


Fig. 1: Cross section of the cryogenic targets at LLE showing target component layers.

2. Shadowgraphy

Shadowgraphic analysis is a technique that characterizes inner ice surface non-



uniformities [4,6,7]. When a single collimated light source is shined on the target, the parallel light rays refract at the plastic shell and a few rays by total

Fig. 2: Experimental shadowgraphic analysis. Virtual bright ring shows inner ice uniformity.

internal reflection bounce off the inner ice surface as shown in Fig. 2. When these few rays are projected back to a focal plane, a virtual bright ring is formed. Deviations of this ring from a perfect circle as well as ring intensity give an accurate picture of the uniformity of the inner ice surface.

3. Ray Tracing Model *Pegasus*

This project involved writing a computer code, *Pegasus*, to model the experimental shadowgraphic system. *Pegasus* traces light rays through an ideal target and provides information on the position and intensity of the expected virtual bright ring. *Pegasus* can operate under two modes. One, it traces light rays from a single parallel light source. This portion of the code is based on an earlier ray tracing code [8]. Two, it incorporates multiple light beams from different directions in an effort to imitate real life conditions. The goal is to create a final intensity plot that will match up with experimental readouts from shadowgraphic analysis.

3.1 Modeling ray paths in single beam ray tracing

The foundation of this project is using Snell's Law to trace the paths of light rays. First, the vectors which represent the light rays are defined, and thereafter, the position and direction of rays on the light path are calculated using vector algebra. The code starts with the desired number of rays from the light source plane with even intervals of height (see Fig. 3). These rays are each given a starting point and a direction. With this, the rays are then traced through every interface on the cryogenic target. The first surface is the thin plastic (CH) shell. Because light rays refract going from one medium to another medium of different density, Snell's Law must be used at this interface to find the new direction of the ray:

$$n_1 \sin \theta_i = n_2 \sin \theta_r$$

where θ_i is the angle of incidence, n_1 is the index of refraction for the first material, θ_r is the angle of refraction, n_2 and is the index for the second material. The index of refraction for the

first material, air in this case, is 1.00 and the index of refraction for the second material (plastic) is 1.59. The same principle is applied at each interface.

The code starts out with a large number of rays, but along the way, rays that do not fall into one of three predefined groups are terminated and therefore the graph only shows final intensity readouts for these three groups. At each successive interface, the code determines whether or not the ray intersects the next interface. The definition of each group is as follows:

- Group A rays must travel through all 6 interfaces: air-plastic, plastic-ice, ice-vapor, vapor-ice, ice-plastic, and plastic-air.
- Group B rays must reflect off the inner ice surface and follow this route: air-plastic, plastic-ice, reflect off inner ice surface, ice-plastic, plastic-air.
- Group C rays do not intersect the target at all and therefore do not use Snell's Law.

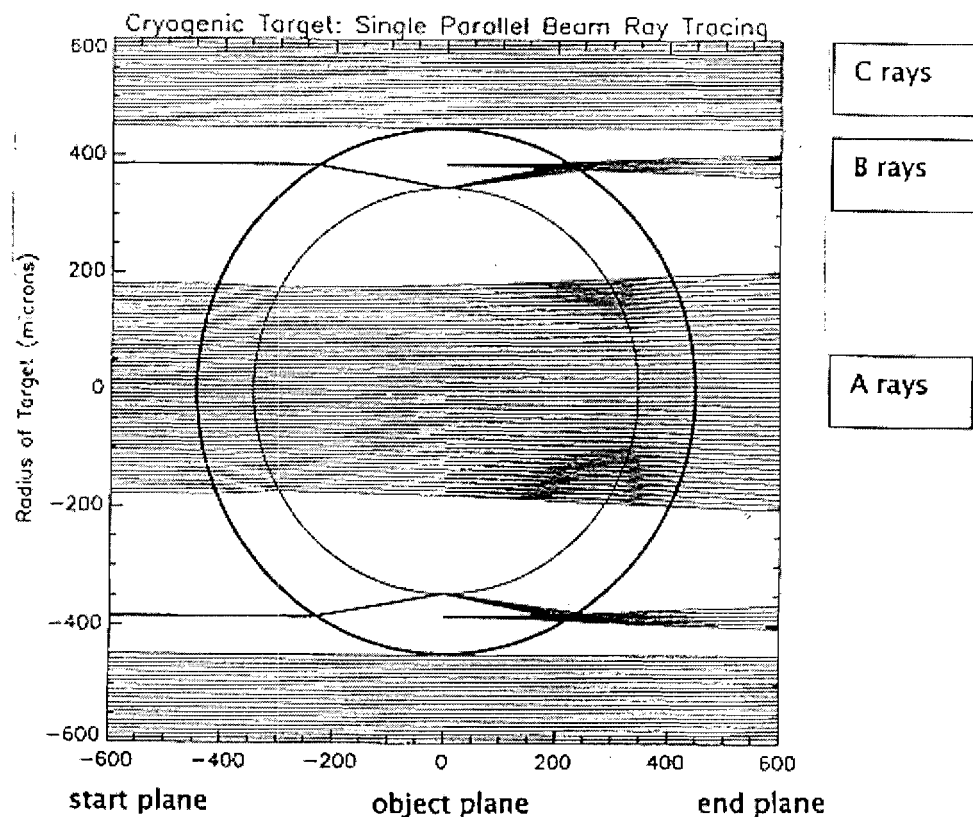


Fig. 3: Light rays are traced using Snell's Law through a cryogenic target of diameter $449\mu\text{m}$. The axes represent distance in microns. The indices of refraction used for the interfaces were: air(1.00), plastic(1.59), ice(1.13), vapor(1.00). The object plane was placed at $0\mu\text{m}$.

If a ray does not intersect the next interface, then it is tagged and the code aborts tracing its ray path. After each intersection with an interface, light rays have a new position vector and direction vector. Thus, the light rays are traced from a starting plane to an end plane then projected back to an object plane where intensity will be plotted.

3.2 Factors in calculating final intensity

Three major factors were considered in calculating final intensity. They are: Fresnel losses, ice absorption, and divergence of light path.

The Fresnel formulae are based on the physical phenomenon that when light travels from one medium to another of different refractive index, a portion of the light is transmitted while the rest is reflected back. The equations are as follows:

$$\text{Transmittance in p polarization} \quad T_p = \frac{2n_1 \cos \theta_i}{n_2 \cos \theta_i + n_1 \cos \theta_t}$$

$$\text{Transmittance in s polarization} \quad T_s = \frac{2n_1 \cos \theta_i}{n_1 \cos \theta_i + n_2 \cos \theta_t}$$

$$\text{Reflection in p polarization} \quad R_p = \frac{n_2 \cos \theta_i - n_1 \cos \theta_t}{n_2 \cos \theta_i + n_1 \cos \theta_t}$$

$$\text{Reflection in s polarization} \quad R_s = \frac{n_1 \cos \theta_i - n_2 \cos \theta_t}{n_1 \cos \theta_i + n_2 \cos \theta_t}$$

For the simulations shown in this report, the polarization was taken to be the average (A) of the p and s polarizations. The intensities after adjusting for Fresnel losses (where I_i is the initial intensity) are given as:

$$\text{Intensity after transmittance in p} \quad I_{Tp} = (n_2/n_1)(T_p)^2 I_i$$

$$\text{Intensity after transmittance in s} \quad I_{Ts} = (n_2/n_1)(T_s)^2 I_i$$

$$\text{Intensity after reflectance in p} \quad I_{Rp} = (R_p)^2 I_i$$

$$\text{Intensity after reflectance in s} \quad I_{Rs} = (R_s)^2 I_i$$

In the experimental readouts of a cryogenic target, it was observed that the A rays, particularly those passing through the center of the target without much refraction, ended up

with an intensity reduced to about 85% of the original intensities. This was accounted for by Fresnel losses.

Finally, intensity is defined as energy per area of space. The last major contributor to the final intensity plot accounted for by *Pegasus* is the divergence of the light path. The object plane is defined as a reference grid onto which light rays will be projected to map the final intensity. For each ray, the intensity is adjusted by the equation given below:

$$I_{\text{final}} = I_{\text{initial}} (\text{Area}_{\text{in}} / \text{Area}_{\text{out}})$$

where Area_{in} is taken to be the area between two neighboring rays at the starting plane and Area_{out} is taken to be the area between two neighboring rays at the object plane.

3.3 Diffuse illumination: multiple beams

In assuming a diffuse illumination, the source is represented as a large number of cylinders, pointed with various angles spread uniformly within the range of light defined by the initial f-number (F_{in}). Light rays start from the source of illumination, but not all are collected by the end optic system. Only the light rays that fall within a set maximum collection angle contribute to the final intensity. The angles are given by the f-number of the illumination source and light collecting optic system:

$$\theta_{\text{inmax}} = \tan^{-1}(\frac{1}{2} F_{\text{in}})$$

$$\theta_{\text{outmax}} = \tan^{-1}(\frac{1}{2} F_{\text{out}})$$

This means the starting light rays must have angles to the propagation direction less than θ_{inmax} to be traced through the target, and ending light rays must have angles less than θ_{outmax} to be collected.

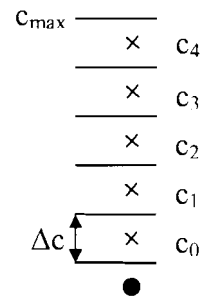
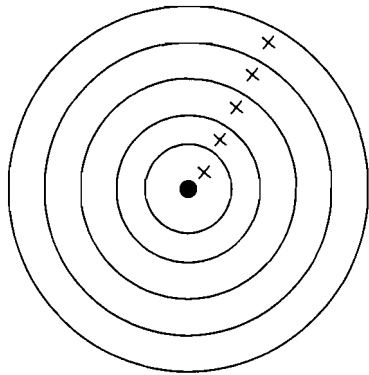
To account for the fact that the cylinders are spread uniformly in the input direction plane, the plane is divided into rings (see Fig. 4). The defining input direction for each ring is:

$$\Delta c = c_{\text{max}} / (\text{number of rings})$$

$$c_i = (1 + \frac{1}{2}) \Delta c$$

Each ring is assigned an energy: $E = (2c_i \Delta c) / c_{\text{max}}$, where Total Energy = 1. This gives the appropriate weight to each ring.

Fig. 4: Representation of diffuse light source as a series of cylinders of light, designated as weighted rings.



Each ring cylinder is divided into wedges and light rays from each wedge are traced through the target as in the single beam mode. To make the final intensity independent of the number of wedges, the initial intensity of each ray in the wedge was set to 1/(number of wedges).

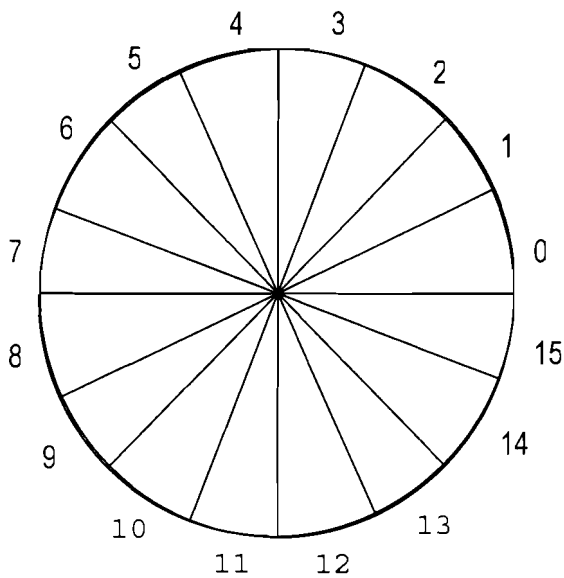


Fig. 5: A view of the incoming beam from the target center.

For $i = 0 \dots (\text{number of wedges}) - 1$
 $\Delta\theta = 2\pi / (\text{number of wedges})$
 $\theta_{\text{wedge}(i)} = i (\Delta\theta)$

The angle of each wedge is used to assign a direction to each ray in the starting plane of the incoming beam.

Tracing light rays using a large number of rings and wedges results in an intensity graph that accurately reflects the conditions of experimental shadowgraphic analysis.

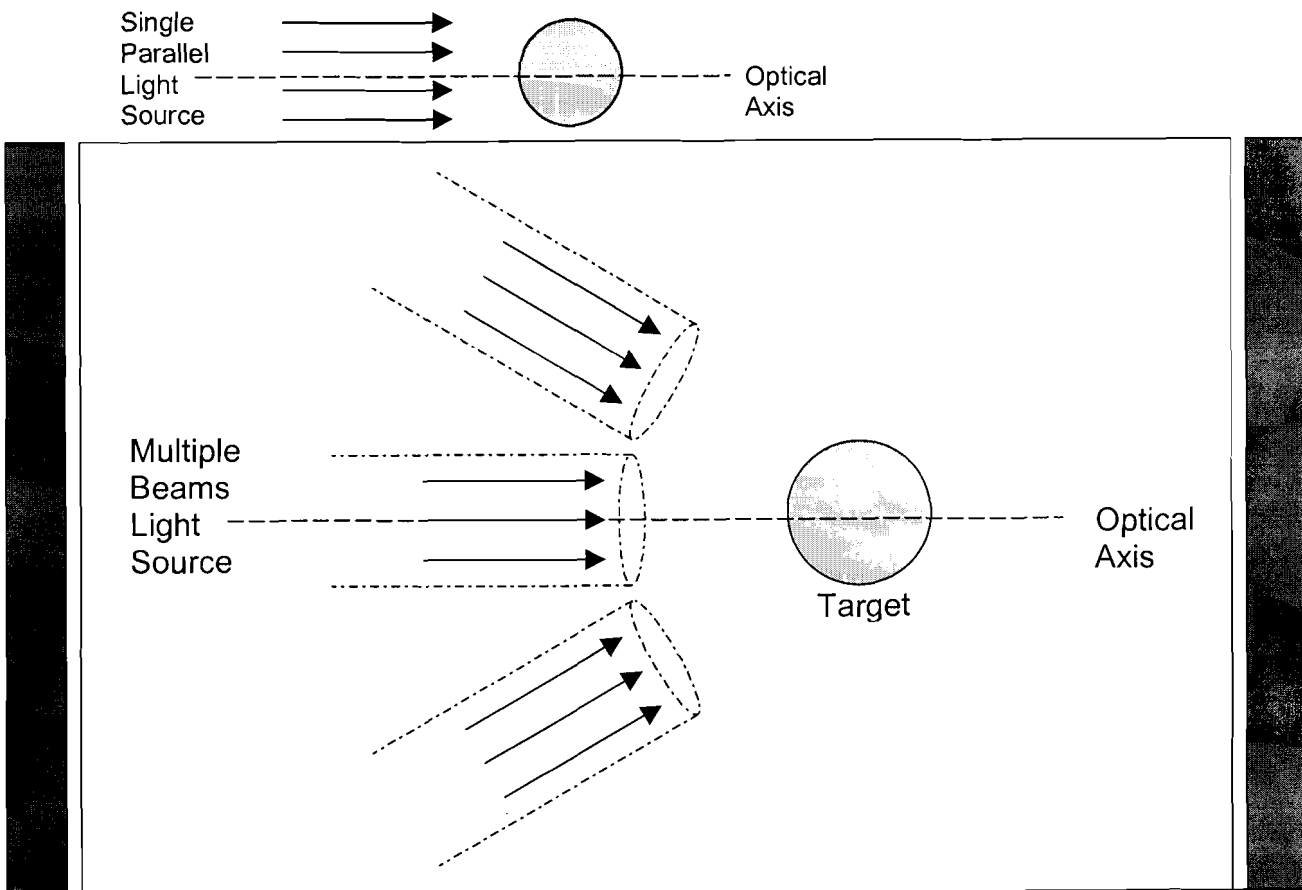


Fig. 6: *Pegasus* runs under two modes: single beam and multiple beam light tracing. Multiple beam light tracing is designed to closely resemble the experimental setup by the simulation of light from multiple directions.

3.4 Caustic Analysis

Caustic analysis specifically looks at the light rays that reflect off the inner ice surface and form the virtual bright ring. In this particular one dimensional, single beam trace of a cryogenic target, the caustic was located between 20 and 40 microns from the center vertical axis.

It is impossible experimentally to know where the focal plane is located to an accuracy of $20\mu\text{m}$. A small shift in the focal plane can result in a relatively large difference in intensity. In practice, the position of the focal plane can easily be varied when comparing with experimental data.

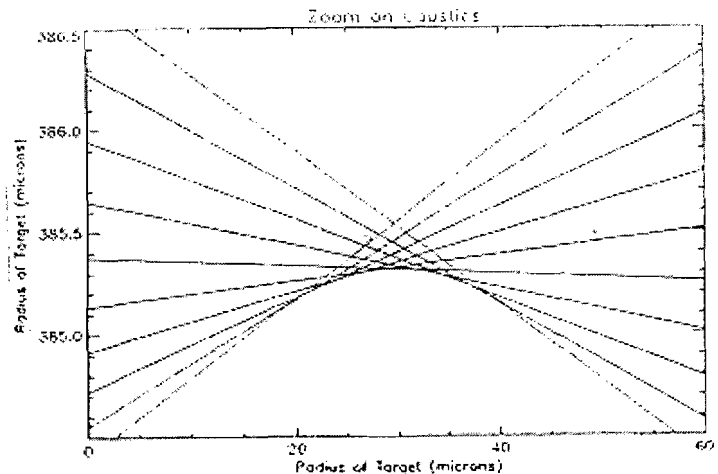


Fig. 7: Zoom of a portion of Fig. 3, where light rays converge when projected back to an object plane.

When running *Pegasus* initially, the focal plane was located at $0\mu\text{m}$ on the horizontal axis. Adjustment of the focal plane position used by *Pegasus* would then be necessary after comparison with experimental data.

Because one of the major factors of final intensity is divergence of the light path, the location of the focal plane near a caustic, where light rays are very close together, can produce a very bright virtual ring. However, in real life, the ring is prevented from being infinitely bright by diffraction.

3.5 Intensity Comparisons

Cryogenic

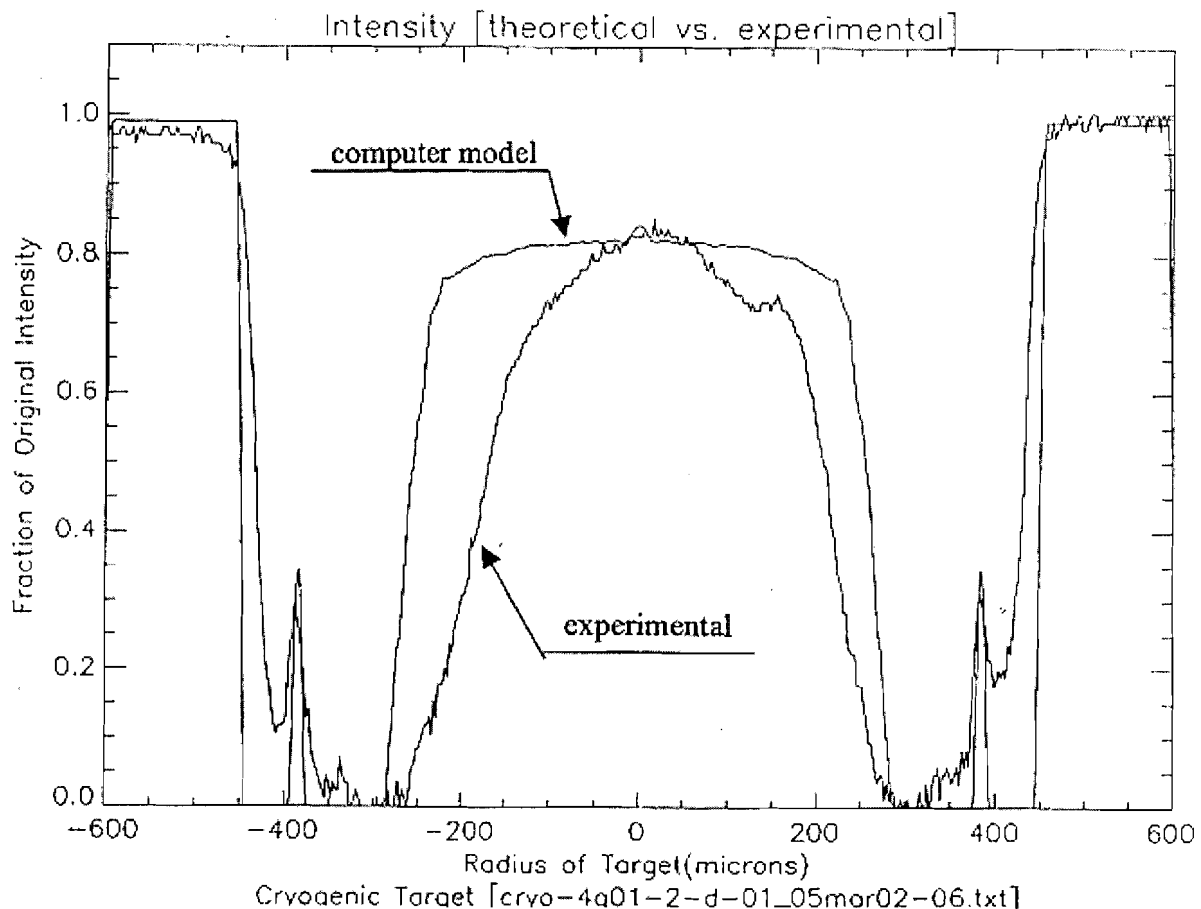


Fig. 8: An intensity comparison of the cryogenic target in Fig. 3. Final intensities are from experimental data and as modeled by *Pegasus*. The focal plane was located to $-150\mu\text{m}$. F_{in} was taken to be 5 and F_{out} 12.

The intensity calculated by the modeling program *Pegasus* was superimposed onto intensity readouts from experimental shadowgraphic analysis, after scaling and interpolating onto a 1200-point reference grid (see Fig. 8). Here, the intensity was plotted for a cryogenic target of diameter 499 μ m. The center matches very well with the model, which had no absorption by the ice. The bright ring is observed at a radius of 380 μ m in both the computer model and experimental results. Because of caustic regions, the position of the focal plane has the greatest impact on the bright ring intensity. Placing the focal plane at -150 μ m brings model intensities close to experimental levels. The effects of scattering were not evaluated by *Pegasus* in these sets of simulations, which may account for the thinner experimental profile of A rays, and experimental intensity readings outside the 3 groups of rays this simulation analyzed.

Surrogate 1

Cryogenic targets are difficult to handle because of the fact that they must be kept chilled at 20K. In order to develop the characterization system more conveniently, representations are produced as surrogate targets. The surrogate target here is a thick plastic shell of a 650 μ m radius and about 190 μ m thickness. Light rays that form the bright ring in shadowgrams reflect off the inner surface of the plastic shell instead of the inner surface of the ice layer in cryogenic targets.

In Fig. 9, absorption by the thick plastic shell was taken in consideration by *Pegasus* and its effect is seen in the low center intensity. The bright ring is again modeled at the correct position. The width difference in the middle may be due to an experimental uncertainty in the F# actually used to collect the light.

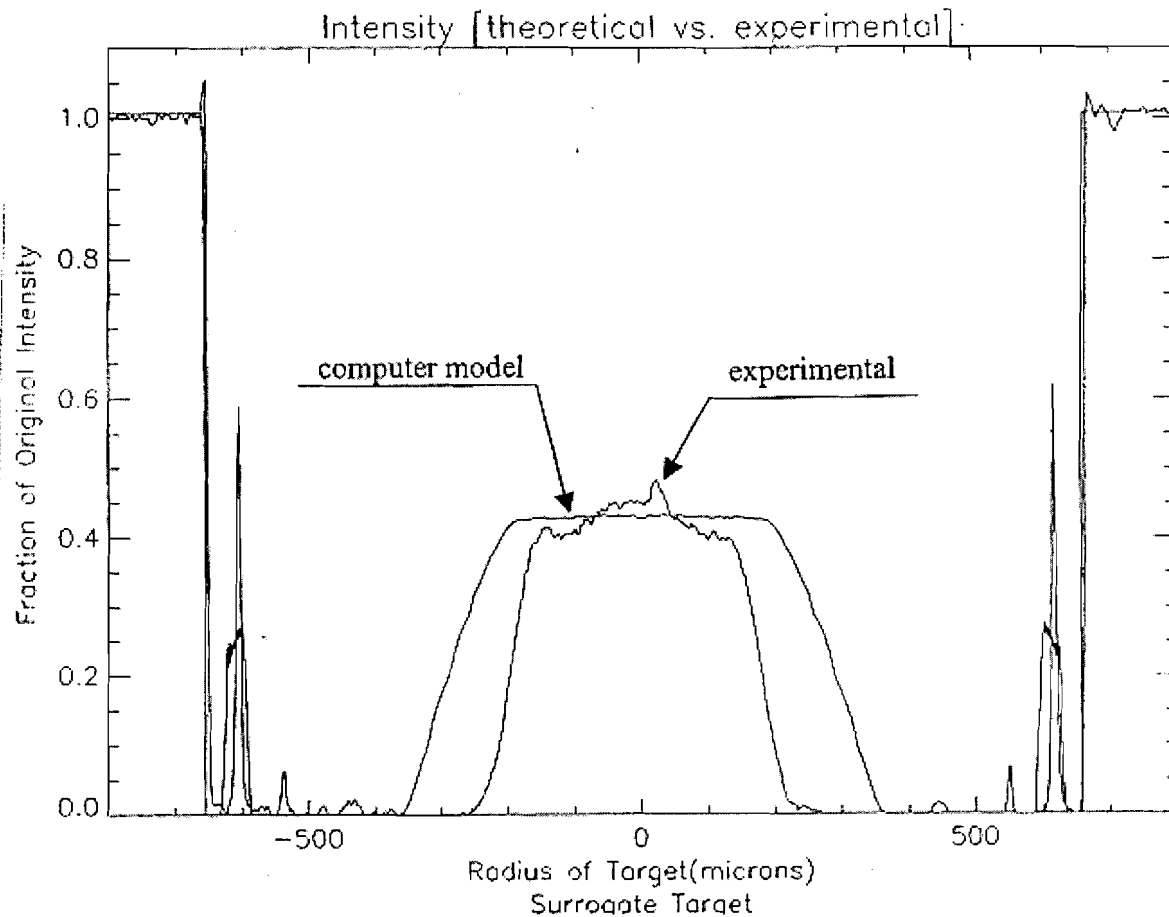


Fig. 9: An intensity comparison of a surrogate target. Final intensities are from experimental data and as modeled by *Pegasus*. The focal plane was located to $24\mu\text{m}$. F_{in} was taken to be 2.45 and F_{out} 5.

The same surrogate target, under a different viewing system, produces a somewhat different intensity plot. The main difference between the two intensity plots is the F numbers, which sheds light on the large impact of the experimental setup on intensity data.

Surrogate 2

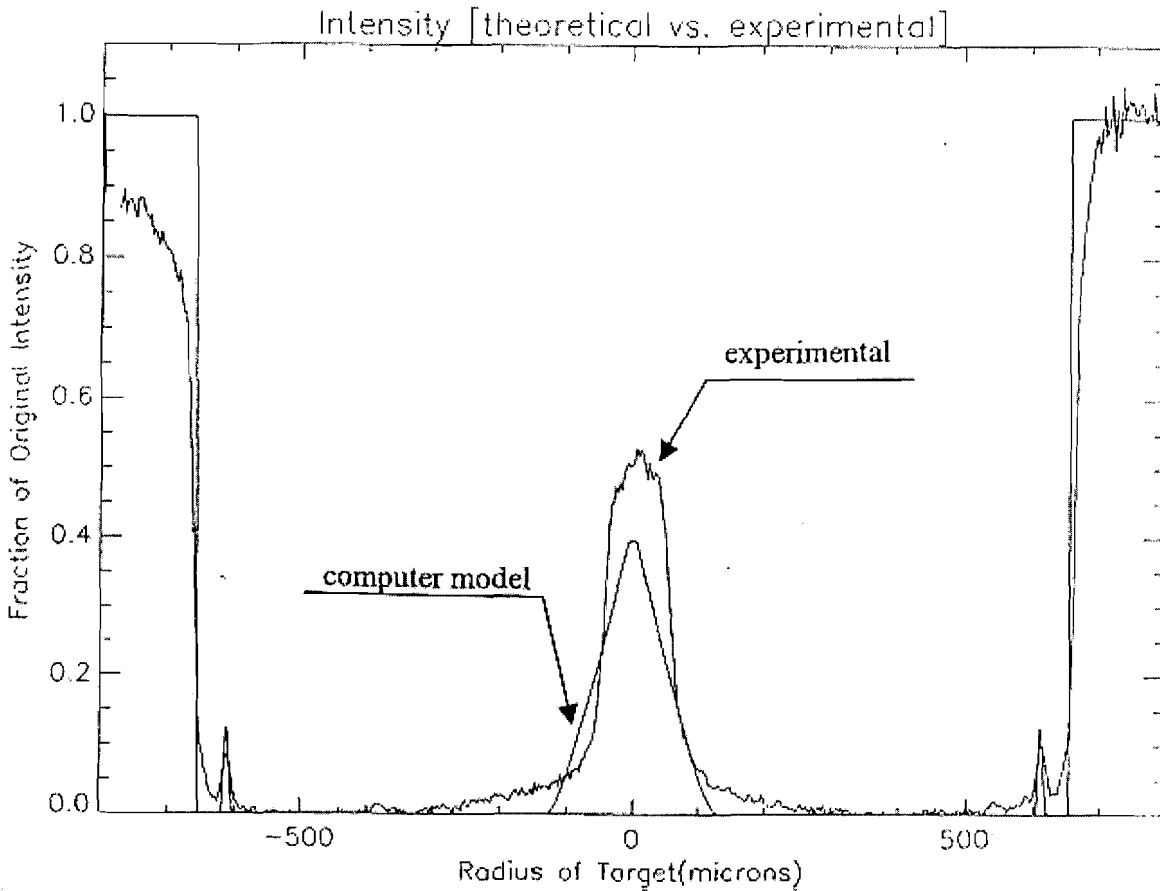


Fig. 10: An intensity comparison of the same surrogate target in Fig. 9 but under a different viewing system. Final intensities are from experimental data and as modeled by *Pegasus*. The focal plane was located to $-100\mu\text{m}$. F_{in} was taken to be 15 and F_{out} 15.

In this case, the central portion is much thinner, probably because the collection optics had a larger F-number, or smaller angle through which rays were collected. *Pegasus* again correctly positioned the bright ring. The small level of experimental intensity readings in regions between the three groups modeled by *Pegasus* could be due to scattering of light rays, which presently is not accounted for by the computer model.

A comparison between Fig. 9 and Fig. 10 shows the tradeoff between a high F number and a low F number. Low F number has the advantage of a strong signal. High F number has the advantage of fewer rays collected and thus a narrower signal making it easier to accurately locate where the inner bright ring radius is.

5. Conclusions

A light tracing computer model *Pegasus* has been built to characterize cryogenic target uniformity. The OMEGA laser at LLE requires a highly uniform fuel layer surface, because non-uniformities will grow exponentially under Inertial Confinement Fusion and drastically reduce target performance. The code *Pegasus* has successfully modeled the paths of light rays from diffuse illumination through targets. Each layer in the cryogenic target has its respective index of refraction and this program follows the paths of 3 major groups of rays – A, B, and C – as they refract and reflect their way through. The B rays are the select few that reflect off the inner fuel layer surface. Where the B rays are projected back to meet the focal plane, a virtual bright ring is observed within the periphery of the target image in shadowgraphic analysis. It is the position, continuity, and intensity of this virtual bright ring that are analyzed to determine the uniformity of the inner ice surface.

By representing the uniform light source as rings and wedges, *Pegasus* traces each light ray through a target and then projects the light rays to an object plane where the intensity is plotted. The modeled intensity, when superimposed and compared with the experimental intensities, has shown strong agreement in intensity levels and position of virtual bright ring. The position of the focal plane has been shown to greatly affect bright ring intensities. This program is flexible so that input variables, such as thickness and index of refraction of each layer, collection optic F-number, and focal plane position, can be manipulated for modeling of future designs of Inertial Confinement Fusion targets.

Acknowledgements

I would like to thank Dr. Stephen Craxton for giving me the opportunity to participate in the High School Summer Research program at the University of Rochester Laboratory for Laser Energetics, and for all the work he spent making the program so successful. I would also like to thank Dr. Craxton for working patiently with me for many hours and helping me through the project. A special thanks to all the other students in this program for the good times, and for becoming such important friends, especially my cubicle buddies! This has been one summer I will never forget.

References

- [1] Craxton, R.S., Robert L. McCrory, and John M. Soures, *Scientific American*, Volume 225, pp. 68–79, “Progress in Laser Fusion (August 1986).”
- [2] Laboratory for Laser Energy Report LLE-02422, October 2001, Section 2.3, “Target Physics.”
- [3] Stoeckl et al., *LLE Review*, Volume 90, pp.49–56, January–March 2002, “First Results from Cryogenic Target Implosions on OMEGA.”
- [4] Bittner, D.N., et al., “Forming Uniform HD Layers in Shells Using Infrared Radiation,” *Fusion Technology*, Volume 35, March 1999, pp. 244–249.
- [5] Laboratory for Laser Energy Report LLE-02422, October 2001, Section 2.9, “Cryogenic Target Handling System.”
- [6] Sater, J., et al., General Atomics Report GA-A23240, FY99 ICF Annual Report, 5.1.2., “Shadowgraphy and Spherical Capsules.”
- [7] July 2001 Progress Report on the Laboratory for Laser Energetics Inertial Confinement Fusion Program Activities
- [8] Turner, Amy, “Ray Tracing Through the Liquid Crystal Point Diffraction Interferometer,” 1998 Summer High School Research Program at the University of Rochester’s Laboratory for Laser Energetics.

**Rayleigh–Taylor Growth Rates for Arbitrary Density Profiles
Calculated with a Variational Method**

Jue Liao

Rayleigh-Taylor growth rates for arbitrary density profiles calculated with a variational method

Jue Liao
Brighton High School

Advised by Dr. R. Epstein

University of Rochester
Laboratory for Laser Energetics (LLE)
2002 Summer High School Research Program

Abstract: The Rayleigh-Taylor instability exists at the interface of two fluids with different densities when the acceleration is pointing from the light fluid to the heavy one. It produces important effects in inertial confinement fusion (ICF). In order to understand more about the Rayleigh-Taylor instability, it is helpful to calculate the rates at which the perturbations grow at the interface. Assuming that the fluids are incompressible, using a variational method gives approximate growth rates for different density profiles. Growth rates are obtained using this method in a Fortran program and are compared with exact results calculated by integrating the Rayleigh equation in another Fortran program. The variational method is shown to be effective in solving for linear growth rates of the Rayleigh-Taylor instability.

I. INTRODUCTION:

If one looks up in a dictionary, he will find the word "instability" being defined as "the quality or condition of being erratic or undependable." The physical concept of the Rayleigh-Taylor instability is a kind of instability as well. It exists at the interface of two fluids with different densities when the acceleration is pointing from the light fluid to the heavy fluid. It exists in everyday life, as illustrated in the example between oil and water.

In Fig.1, we have oil, the light fluid, on top of water, the heavy fluid. The perturbations exist at the interface. They are under the condition in which gravity pulls

down, which is equivalent to the fluid being accelerated upward. In Fig.2, we still have

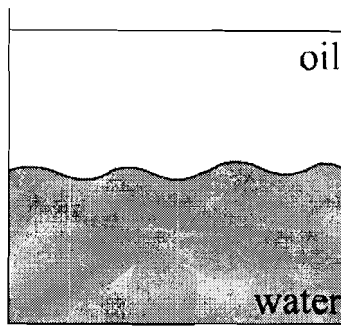


Fig.1

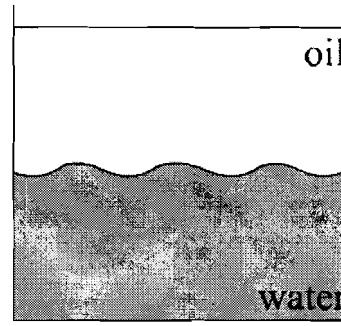


Fig.2

With gravity pulling down, which is equivalent to the fluid being accelerated upward, the state of oil on top of water is stable. The perturbations oscillate.

water on top of oil with perturbations existing. The condition does not change much, because this is a stable state. The perturbations oscillate.

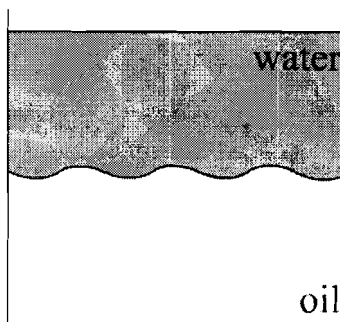


Fig.3

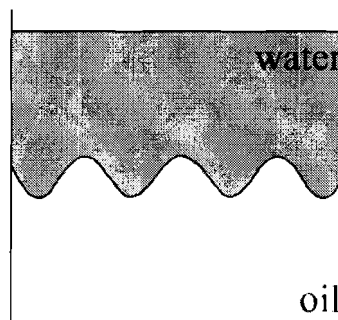


Fig.4

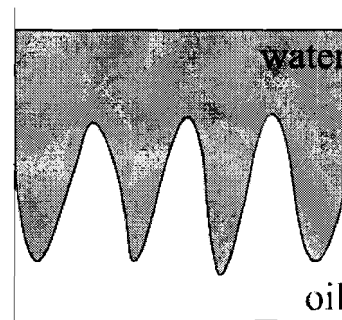


Fig.5

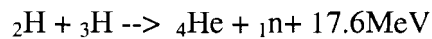
With gravity pulling down, meaning the acceleration going up, the state of water on top of oil is unstable. The perturbations grow exponentially with respect to time.

However, in Fig.3, water, the heavy fluid, is now on top of oil, the light fluid. With acceleration going up, it becomes unstable. The perturbations will not oscillate; rather, they will grow exponentially with respect to time. From Fig.3, Fig.4, to Fig.5, the perturbations have grown from little ripples to huge bubbles and spikes. Eventually, the perturbations will grow big enough that they will bring down the heavy fluid to exchange places with the light fluid. The water and oil will switch places and this unstable state will become a stable state as in Fig.1 and Fig.2 again. The unstable state described from Fig.3 to Fig.5 is called the Rayleigh-Taylor instability.

In the cases where I am going to solve for growth rates, the linear approximation is assumed to apply. The amplitudes of the perturbations are small compared to the wavelengths of the perturbations. In addition, ripples are assumed to vary sinusoidally across a planar interface.

II. IMPORTANCE:

The Rayleigh-Taylor instability is important to Inertial Confinement Fusion. The fusion process is a nuclear reaction, which scientists hope to apply to the generation of energy. In this reaction, deuterium and tritium, two isotopes of hydrogen, react to produce one helium nucleus, one neutron, and 17.6MeV energy:



Two requirements for the fusion process are high temperature and high pressure. Scientists at the Laboratory for Laser Energetics shine laser beams onto a fuel target to help to create these two conditions.

Fig.6 shows a representative target. It consists of a thin plastic shell, a layer of deuterium and tritium ice fuel, and the core of deuterium and tritium gas fuel. When the laser begins to shine on the surface of the target, the plastic shell ablates. Vaporizing plastic accelerates outwardly, and this outward acceleration creates an inward acceleration, according to Newton's Third Law. In this acceleration phase, the interface becomes unstable due to the density difference between the ablated plastic shell and the plastic shell, with acceleration pointing from the expanding plastic vapor, the light fluid, to the solid plastic shell, the heavy fluid. The Rayleigh-Taylor instability exists here.

When the target is compressed small enough to create relatively high pressure inside the core, the target enters its deceleration phase. Reversing the direction of the acceleration, the interface between the ablated plastic shell vapor and the plastic shell becomes stable while the interface between the deuterium and tritium ice fuel and deuterium and tritium gas fuel becomes unstable. The Rayleigh-Taylor instability causes

the perturbations to grow at this interface. When the perturbations grow, they will bring the deuterium and tritium ice fuel, which is relatively cool, into the deuterium and tritium

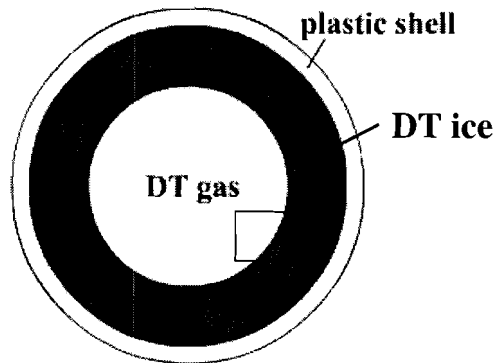


Fig.6: A target consists of a thin plastic shell, deuterium and tritium ice fuel, and deuterium and tritium gas fuel. During the acceleration phase, the Rayleigh-Taylor instability exists at the interface between the ablating plastic shell and the solid plastic shell. During the deceleration phase, it exists between the deuterium and tritium ice fuel and the deuterium and tritium gas fuel.

gas fuel to cool down the inner core. As a result, the high temperature requirement may not be met, and the fusion process may then not take place. In order to avoid this, scientists study the Rayleigh-Taylor instability, hoping to control the perturbations so that they will not grow big enough to ruin the fusion process. Thus, knowing the growth rates becomes important.

III. SOLUTIONS:

1. Exact Integration:

In order to solve for the exact growth rates, we use the Rayleigh equation:

$$d/dz(\rho dw/dz) - \rho k^2 w + (k^2 g/\gamma^2)(d\rho/dz)w = 0.$$

The Rayleigh equation is obtained from the physical theories of Newton's Second Law and the Conservation of Mass.¹ In addition, boundary conditions are imposed, i.e. $dw/dz = \pm kw$, which imposes exponentially decaying behavior at the left and right boundaries of the problem, respectively, where $d\rho/dz = 0$. This equation works for incompressible

fluids in a planar geometry. The variable z represents the position along the direction of acceleration, normal to the fluid interface, and ρ is the mass density at that point z . The constant k is the wave number; it equals to 2π divided by the wavelength (λ) of the perturbation. g is the acceleration of the fluids. The $w(z)$ function and the parameter γ are the two things to be solved for. $w(z)$ is the distribution of the z component of the perturbation velocity with respect to the z coordinate, and γ is the growth rate, which describes how fast the perturbations grow. For this equation, the assumed time dependence of the perturbation consists of a growth factor of $e^{\gamma t}$. The linear approximation applies to the perturbations to be solved for.

The Rayleigh equation is one example of a Liouville equation. According to the Sturm-Liouville Theory, for every eigenvalue, there will be an eigenfunction that satisfies the equation. In the Rayleigh equation, $w(z)$ is the eigenfunction and the dimensionless quantity $\Gamma = \gamma^2/kg$ is the eigenvalue. Another useful quantity in the mathematical manipulation is the dimensionless distance coordinate $x = kz$. Among all the possible eigenvalues and their corresponding eigenfunctions, my goal is to focus on the largest eigenvalue and the corresponding eigenfunction. That means there are many different possible perturbation velocity distributions in an unstable state, but the most important one is the one with the biggest growth rate. Since it grows the fastest, it has the biggest potential to destroy a fusion implosion. Therefore, we are looking for the largest value for Γ .

The shooting method is used in the exact integration for different density profiles. Boundary conditions are supplied for the problem. After guessing Γ , $w(z)$ is evaluated, and the eigenfunction is checked to see if it satisfies the boundary conditions. If they are not satisfied, the calculation is iterated, adjusting the eigenvalue and repeating the integration. This sequence is repeated until the boundary conditions are satisfied, indicating that the right eigenvalue and its corresponding eigenfunction have been found.

This exact integration of the Rayleigh equation works well for almost any density profile if the boundary conditions are provided. But if the boundary conditions cannot be easily defined, or if many iterations would be too time-consuming, what should

we do? In these situations, scientists will choose an approximate method over an exact integration.

2. The variational method:

The variational method is a standard approximate method. The goal for my project is to test this method to see if it works well with several density profiles that are Rayleigh-Taylor unstable. For this method, we guess a trial function for the eigenfunction $w(z)$ first. The trial function I used for w is $w = e^{-|x-x_0|}$ as has been suggested by Mikaelian.² The density scale length is used here as an estimate of its center. The density scale length L equals $\rho/(dp/dz)$. A common rule is that this density scale length is a minimum where the eigenfunction will be centered. This rule is used to estimate x_0 , the center of the trial eigenfunction. This function decays exponentially far from $x = x_0$, and no further boundary condition is imposed. If this trial function is a good choice, then *no* further iteration is required to obtain a good estimate of the growth rate. Once a proper trial function is chosen, there is no need to maximize or minimize any quantity. This is one very good thing about this implementation of the variational method. According to the "calculus of variations," the eigenvalue, Γ , is accurate to second order with respect to variations in the trial function about the exact eigenfunction. For the two density profiles that are shown below, the variational method works well. It provides good approximations.

IV. RESULTS:

1. Ramp density profile:

The ramp density profile jumps from one density to another over a spatial interval. The Atwood number is a quantity used to describe a density profile. It is the quotient of the difference between the two densities divided by the sum of these two densities. In the example shown in Fig.7, the ramp density profile jumps from 1 to 9 as x

changes from -0.2 to 0.2. This gives us a profile with an Atwood number equal to 0.8 and a dimensionless ramp length equal to 0.4. Under the same boundary conditions as imposed before, the graphs are plotted from $x = -3$ to 3.

In Fig.7, we show the graph obtained using the exact integration of the Rayleigh equation. The dashed line represents the density profile. The solid line is the eigenfunction, $w(z)$. The Fortran program generates the eigenvalue $\Gamma = 0.754$ using the shooting method. In Fig.8, the graph is obtained using the variational method and the solid line is the trial function $e^{-|x-x_0|}$. The inverse of the scale length peaks where the density profile begins to jump, which is shown by the dotted line. The eigenfunction is centered at its peak, which is around $x = -0.2$. Γ is evaluated to be 0.753. This gives a -0.77% percent error in the eigenvalue. By moving the center of the eigenfunction x_0 , it is found that the eigenvalue is not very sensitive to the changes. Fig.9 gives a comparison between the trial function and directly integrated result for the eigenfunction $w(z)$. The solid line is obtained by using the exact integration, and the dashed line is the trial function used in the variational method. The graph for the exact integration tends to have a round peak and the one for the variational method has a sharp peak. But overall, they are very close to each other.

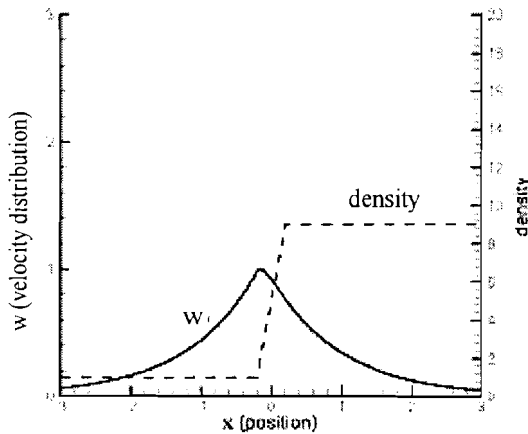


Fig.7: Exact integration for the ramp density profile.

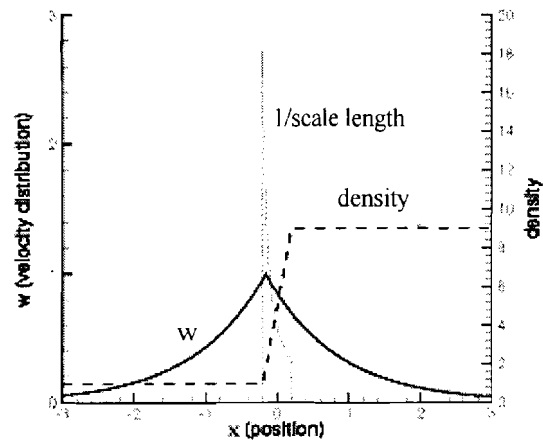


Fig.8: The variational method for the ramp density profile with one over scale length plotted to find the center of the eigenfunction.

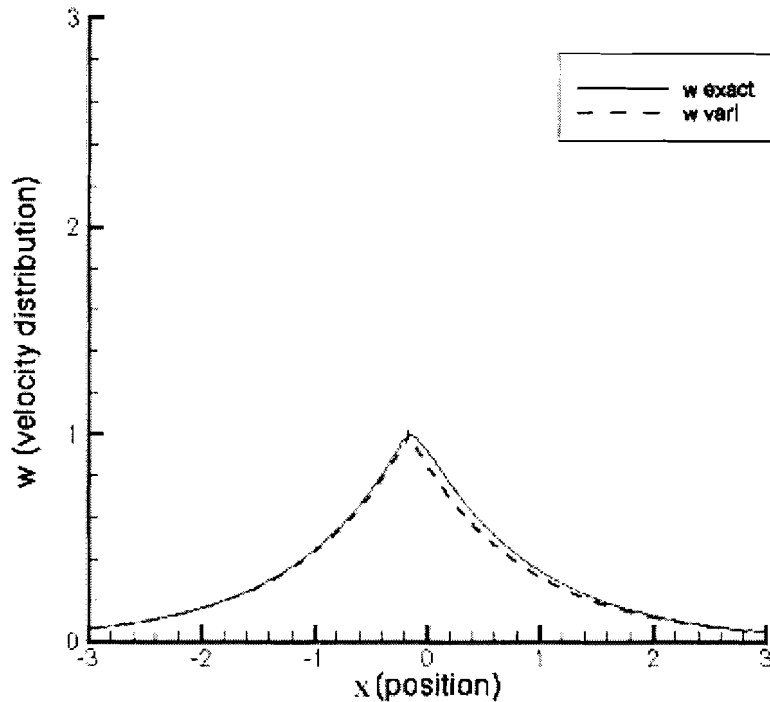


Fig. 9: Comparison between the real function and the trial function for the velocity distribution for the ramp density profile. The solid line is obtained by using the exact integration and the dashed line is the trial function used in the variational method. The graph for the exact integration tends to have a round peak and the one for the trial function has a sharp peak. But overall, they are very close to each other. The error in the eigenfunction yielded for this density profile is -0.77% .

2. Exponentially growing density profile:

One other interesting density profile is the exponentially growing density profile. The density changes exponentially with respect to position within an interval. One thing that makes this density profile interesting is that the density scale length indication of the trial function center does not work because the density scale length is a constant over the interval where the density changes. So, the question comes up, where should we center the trial function? Should it be somewhere near where the density starts to jump, or in the center of the jumping interval, or at the end where the density stops

changing?

The density profile shown jumps from density one which is 1, to density two, which is 9, over the x interval -0.2 to 0.2. This gives a density profile with 0.8 Atwood number and 0.4 ramp length. The graphs are plotted from x = -3 to 3.

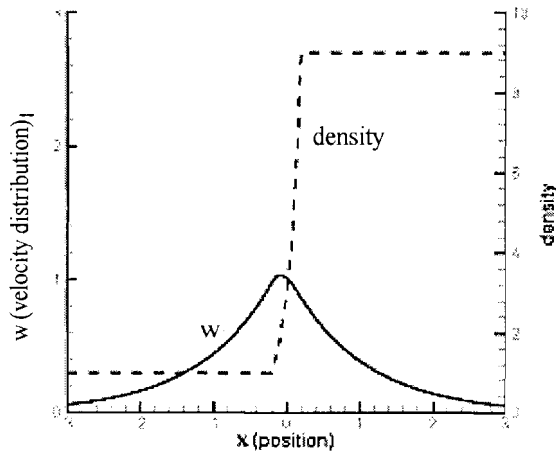


Fig.10: Exact integration for the exponentially growing density profile.

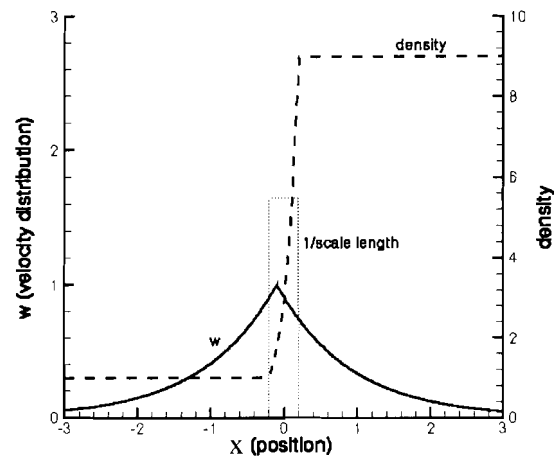


Fig.11: The variational method for the exponentially growing density profile showing the constant value of one over the density scale length over the entire width of the exponential density ramp.

In Fig.10, the dashed line represents the density profile. The solid line is the eigenfunction w. The program calculates the eigenvalue $\Gamma = 0.750$ by iteration.

In Fig.11, for the same exponentially growing density profile shown as the dashed line, the solid line is the trial function $e^{-|x-x_0|}$ for the eigenfunction. The interesting thing about this density profile is that the scale length is a constant over the interval

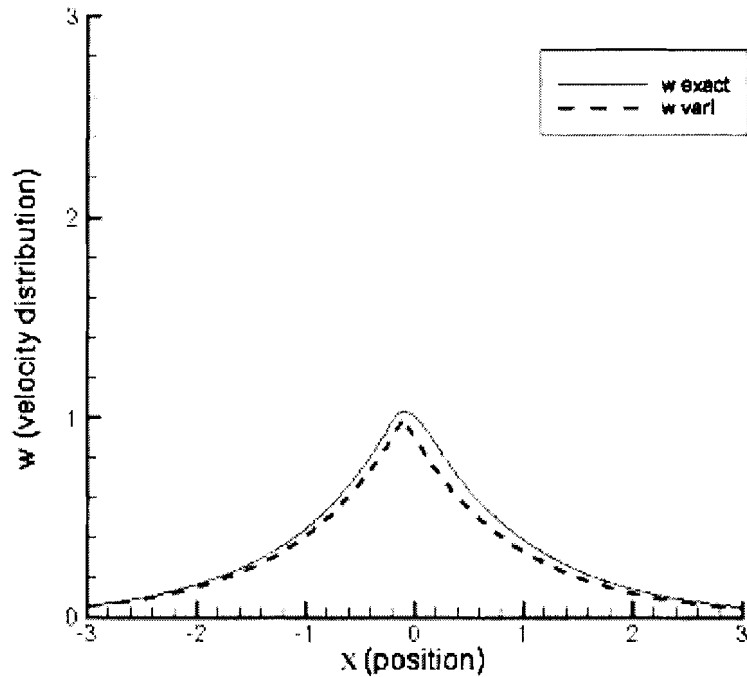


Fig.12: Comparison between the real function and the trial function for the velocity perturbation for the exponentially growing density profile. This density profile yields an error of -2.67% .

where the density changes, so its minimum cannot be used as an indication of the eigenfunction center. As seen in the graph, the one-over-scale-length plot is a constant over the interval -0.2 to 0.2 . By moving the center to get the maximum eigenvalue, it is shown that the center is near the middle of the density jump interval. So in this case, it is near the position $x = 0$. The approximate eigenvalue equals 0.730 . It gives an error of -2.67% in the value of Γ . The eigenvalue is not very sensitive to the center of the eigenfunction. Fig.12 compares the two eigenfunctions, the result of the direct integration and the approximate trial function obtained from the variational method. The solid line is the exact solution and the dashed line is the approximate solution. The two curves are close to each other.

V. ACCURACY:

1. Comparison between three approximate methods:

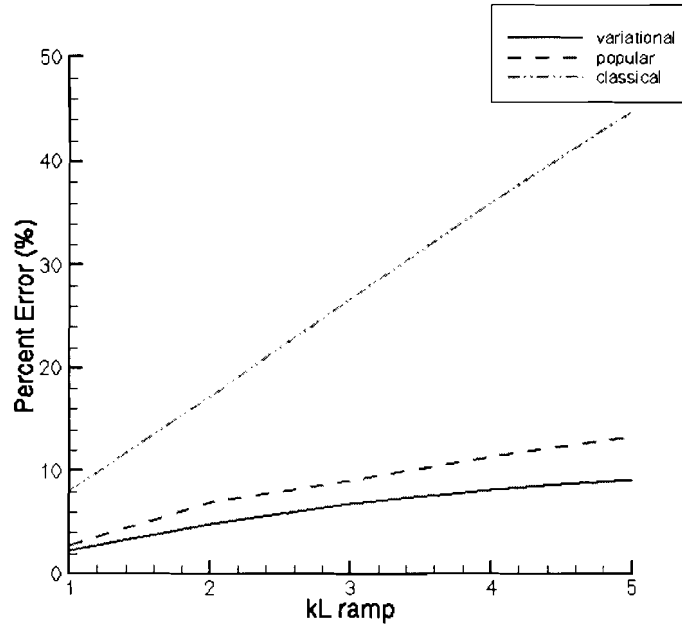


Fig. 13: The accuracy comparison between three different approximate methods is shown for the case of the linear density ramp with an Atwood number equal to 0.8 and a width L . The variational method has the least percent error, compared to the popular formula ($\gamma^2 = Akg/(1+AkL)$) and the classical formula ($\gamma^2 = Akg$).

There is not just one approximate method for calculating the Rayleigh-Taylor instability growth rate. One popular formula $\gamma^2 = Akg/(1+AkL)$ is commonly used by scientists.³ Another is the classical formula $\gamma^2 = Akg$. Fig.13 is generated for comparison among the variational method, the popular formula, and the classical formula by calculating the exact solution for each kL . The data are collected for the case of a linear density ramp with an Atwood number of 0.8 and a width L . The variational method is shown to be effective. The accuracy depends a lot on the density profile. When smaller Atwood numbers, such as 0.2, are used for a linear density ramp profile, the scale-length indication for the trial function center seems to not work as well. The best center of the eigenfunction does not occur at the minimum of the density scale length.

2. Growth factor and growth rate accuracy:

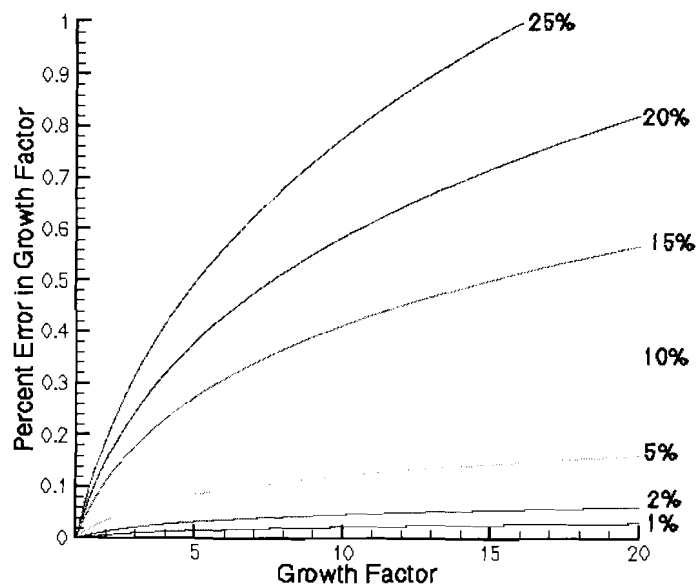


Fig.14: Growth factor accuracy is plotted for various values of the growth rate uncertainty, such as 1%, 2%, 5% and so on. The conversion between the growth rate accuracy and the growth factor accuracy can be obtained from the graph.

Fig.14 is a graph of the growth factor accuracy. It is plotted for various values of the growth rate uncertainty, such as 1%, 2%, 5%, and so on. The conversion between the growth factors and the growth rates is obtained through the following equation:

$$\text{Growth factor} = e^{\gamma t} \quad (\gamma \text{ being the growth rate})$$

One interesting growth factor for the NIF would be 10 and the accuracy of the growth factor should be 10%.⁴ From the graph, which converts the accuracy in the growth factor into the accuracy in the growth rate, this point lies mostly near the 5% line. 5% accuracy in the growth rate is satisfied from the tests I did in my program using the variational method, so the variational method is shown to be acceptable for at least these cases.

VI. CONCLUSION:

The results of the project indicate that the variational method is an acceptable method for approximating the growth rates for the Rayleigh-Taylor instability. While the percent error is largely dependent on the properties of the density profiles being solved for, Fig.13 shows that the variational method yields lower errors in the determination of the growth rate than either the popular or classical method for at least the case shown. For the linear ramp density profile, the trial eigenfunction centers on around where the density starts to change. For the exponentially growing density profile, the center is shown to be somewhere near the center of the density ramp. The indication of the eigenfunction center using the point of minimum scale length does not work well when the Atwood number is too small.

VII. REFERENCES:

1. S. Chandrasekhar, *Hydrodynamic and Hydromagnetic Stability* (Dover Publications, Inc., New York, 1961).
2. K. O. Mikaelian, Phys. Rev. A **33**, 1216 (1985).
3. R. Betti, V. N. Goncharov, R. L. McCrory, and C. P. Verdon, Phys. Plasmas **5**, 1446 (1998).
4. V. Goncharov, private communication.

ACKNOWLEDGEMENT:

I would like to thank my advisor, Dr. Reuben Epstein for his help in both understanding and completing my project. I would also like to acknowledge other members of the staff such as Dr. Craxton for accepting me into this program, Dr. P.B. Radha and Dr. Valeri Goncharov for helping me with my questions. And finally, I would like to thank all the other high school participants for making this summer enjoyable.

**Characterization of the Absorption Spectrum of Deuterium for
Infrared Wavelengths**

Christopher Moody

Summer Research Project:
Characterization of the Absorption Spectrum of Deuterium Ice
Christopher Moody

Introduction

The primary goal of the research undertaken at the Laboratory for Laser Energetics is to achieve fusion reactions with the highest energy yield possible. A high energy yield is achieved from an OMEGA target implosion experiment when the target sphere is compressed uniformly by the OMEGA laser. Therefore LLE scientists strive to achieve the most uniform compression of the target that is possible. In order to compress uniformly, both the shell of the target and the distribution of the deuterium fuel within must be as uniform as possible. When deuterium gas is used as a fuel, the gas fills the sphere in a uniform manner owing to the random motion of gas particles. However, the target type of choice for fusion experiments in OMEGA is a target shell containing a uniform thickness of deuterium ice. Deuterium ice is a more desirable fusion fuel than deuterium gas because the solid form is more dense, allowing a greater quantity of deuterium molecules to fit within the target. However when the target contains solid deuterium, the process of ensuring target uniformity is considerably more complex.

Owing to the effect of gravity during the process of freezing, the deuterium ice layers are naturally non-uniform. To obtain the desired high degree of uniformity, the layers are smoothed by bathing the target in infrared from an optical parametric oscillator (OPO) laser. Owing to the excitation of the deuterium molecules by the infrared, energy from the OPO laser is absorbed by the ice as heat. Areas in the target with high ice thickness become hot and the deuterium melts, forms a gas, and is redeposited in the cooler, lower thickness areas of ice deposition. This process is continued until there exists a dynamic equilibrium within the target sphere between boiling and deposition that creates a uniform layer of ice within the sphere.

The process of creating a target shell containing deuterium ice begins in the same

manner as for a deuterium gas target. The target is placed within pressure and temperature specific conditions that facilitate the diffusion of deuterium gas through the permeable wall of a target shell until the desired quantity of fuel has entered the shell and it is rendered impermeable to continued diffusion. When the goal of the target fabrication process is to produce a deuterium ice target, the aforementioned shell is exposed to extremely cold temperatures in a controlled environment that causes the deuterium within to slowly freeze and form the layer of ice on the inside surface of the spherical target shell.

The OPO laser is tunable and the wavelength of the infrared used is between 2.9 and 3.4 micrometers. These wavelengths are used because they most closely match the frequency at which the deuterium molecule vibrates. The infrared is absorbed with the greatest efficiency at these wavelengths.

Experiment

The goal of the project was to characterize the absorption spectrum of deuterium ice. Specifically, we wish to know how the absorption varies with the infrared wavelength. The target smoothing process can be made more deterministic if it is known what wavelength of infrared is best absorbed by the deuterium ice. The ice could be smoothed to a greater degree of uniformity and perhaps at a faster rate. To determine how well deuterium ice absorbs infrared wavelengths, an apparatus was specially created. A cylindrical cell one centimeter deep with a radius of one centimeter was created to hold a controlled amount of deuterium gas supplied by an external source. The cell's walls are composed of a heat conducting metal. The bottom and top of the cylindrical cell were made of thin polyimide which does not significantly absorb the wavelengths of infrared radiation used for our test. The cell is housed within a cylindrical, airtight chamber to permit the creation of a vacuum. The presence of a vacuum allows the chamber to be cooled below the freezing point of deuterium to around 16 Kelvin. A small heating coil is attached by heat conductive metal to the cell. This allows the temperature within the

cell to be manipulated from around 16 Kelvin to 25 Kelvin. This range of temperatures allows for the deuterium in the cell to be heated or cooled to obtain the solid, liquid, or gaseous form. By manually adjusting the current passing through the heating coil the deuterium could be slowly frozen to obtain visually uniform ice, devoid of cracks or major light-scattering imperfections. The uniformity of the ice in the cell was visually confirmed by the use of a video camera that could view the cell through a window in the chamber surrounding the cell. An optical parametric oscillator laser was shined through the cell which contained, at various times, solid, liquid, or gaseous deuterium. The OPO laser is tunable to a range of wavelengths, with a wavelength resolution of .01 micrometers. Figure 1 gives a picture of the apparatus and Figure 2 gives a diagram of the optical path through the apparatus.

To determine how much of the infrared radiation was absorbed by the phase of deuterium in the cell, optical elements were placed before and after the cell in the path of the laser. These optical elements reflect a known proportion of the infrared to InSb photodiodes. The infrared which is reflected onto the photodiode generates a current which we measured and recorded. By comparing the measured amperage from both photodiodes, we could determine how much of the infrared was absorbed by the deuterium.

We applied Beer's Law to determine how much of the infrared radiation was absorbed by the deuterium. For our project, Beer's law is written as $I_{\text{tr}} = I_0 \exp(-al)$. I_0 is the amperage measured by the photodiode placed before the cell in the optical path. I_{tr} is the amperage measured by the photodiode placed after the cell in the optical path. The absorption coefficient is denoted by the term "a". The length of the optical path is denoted by the term "l". "a" is the unknown term we are trying to determine. By using the amperage data we collected, the absorption coefficient for a given wavelength can be determined. These values can be applied to the target smoothing process to make it more deterministic. The wavelength found to have the greatest absorption coefficient would be

the best wavelength to use in the target smoothing process.

Our current data is not statistically significant, as an insufficient number of accurate trials have been performed up to this point. However, our preliminary findings as illustrated by figure 3, a graph of absorption of infrared radiation by deuterium solid and liquid phases, indicate that the deuterium ice best absorbs an infrared wavelength of 3.16 microns. Further trials will hopefully establish the validity of this result.

Conclusion

The project is not yet finished. The process of determining the absorption coefficients is incomplete. In the future, a broader range of the infrared spectrum will be characterized by the determination of the absorption coefficients at more wavelength values. The addition of a feedback loop will increase the power and wavelength stability of the OPO laser. More trials will be performed to increase the statistical significance of our results. The accuracy of the tunable wavelengths of the OPO laser will be verified by measurement with a spectrometer. These steps will ensure that the absorption coefficient values obtained are accurate. If the project is completed successfully, LLE scientists will be able to smooth deuterium ice targets for fusion experiments with greater efficiency.

Acknowledgments

I would like to thank several individuals who made my participation in the Summer research program a positive and successful experience. Firstly I would like to thank the University of Rochester in general and the Laser Energetics lab and the Target Fabrication department in particular. Especially helpful were Dr. Harding and Roger Gram who guided me through my research project.

Figure 1: This is a picture of the apparatus used to cool the deuterium ice in the cell to around 16 Kelvin. Note the video camera above the chamber and the laser fiber below it. Note that a chopper was used to compensate for background noise.

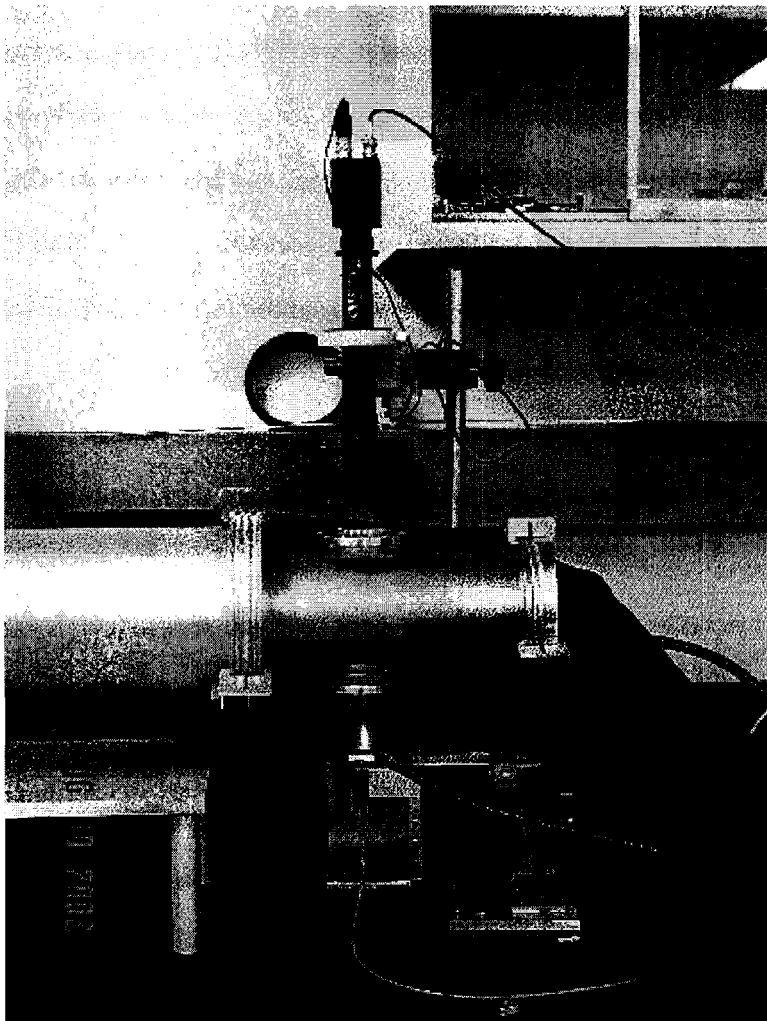


Figure 2 : A diagram of the optical path of the apparatus. Note the position of the InSb photodiodes before and after the deuterium cell in the optical path. Visible light was beamed into the optical path to permit the use of a video camera.

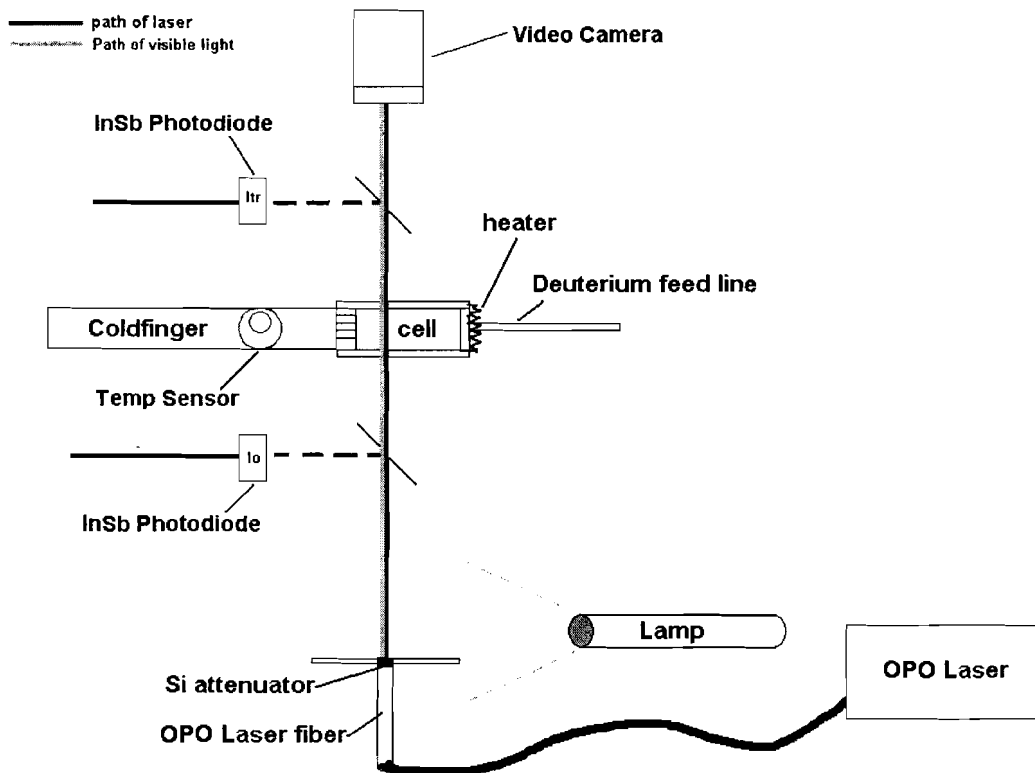
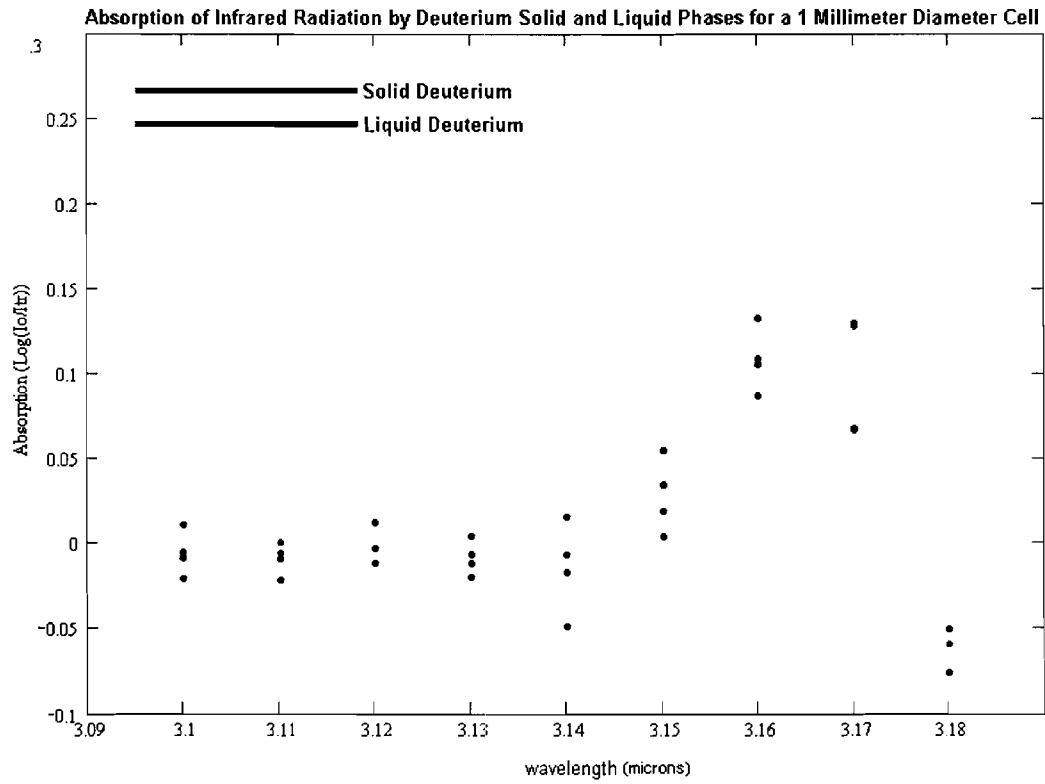


Figure 3: A graph of the absorbance of infrared radiation of deuterium ice and liquid phases. Note that the wavelength of greatest absorbance is 3.16 microns



Multiple-Tripler Broad-Bandwidth Frequency Conversion for Laser Fusion

Phoebe Rounds

Phoebe Rounds

**Multiple-Tripler Broad-Bandwidth Frequency Conversion
for Laser Fusion**

Phoebe Rounds

Irondequoit High School
Rochester, NY

Advisor: Dr. R. S. Craxton,
Senior Scientist

Laboratory for Laser Energetics
University of Rochester
Rochester, NY

Multiple-Tripler Broad-Bandwidth Frequency Conversion for Laser Fusion

Summary:

Many researchers worldwide are using high-power lasers to obtain the conditions necessary for nuclear fusion. Such laser systems include crystals, known as doublers and triplers, which convert infrared beams to the higher-frequency ultraviolet beams necessary for fusion. I developed a systematic method for generating new designs which use additional crystals to significantly increase the bandwidth and thus the smoothness of the laser beams.

Multiple-Tripler Broad-Bandwidth Frequency Conversion for Laser Fusion

1. Background

Many researchers worldwide are investigating laser-induced inertial confinement fusion (ICF) as a possible energy source [1,2]. Laser-fusion researchers garner from intensely focused laser beams enough power to induce deuterium and tritium fusion in small, spherical pellets with plastic shells and deuterium and tritium cores. The high-intensity power directed on a pellet ionizes the atoms of the pellet's shell into a plasma; this plasma, as it is heated, separates from the pellet and ablates outward. Complementing the force of the plasma accelerating outward, in accordance with Newton's Third Law, is an opposite force which drives the pellet inward upon itself, so much so that its radius is decreased by as many as fifty times [1]. The dramatic implosion of the pellet generates the high-density, high-temperature environment necessary for the fusion of the pellet's deuterium and tritium and the accompanying release of an energetic neutron. Researchers hope that eventually laser-induced ICF will reach an ignition state, a state at which more energy is released by the fusion process than that used to produce the high-temperature, high-density conditions necessary for ICF.

One site of ICF research is the Laboratory for Laser Energetics (LLE) at the University of Rochester. The OMEGA laser system at LLE employs 60 ultraviolet beams directed on a pellet from all sides [3]. While these 60 beams overlap as they hit the pellet, their incidence on the pellet remains somewhat nonuniform. Many researchers

are working to minimize this nonuniformity and thus maximize the effectiveness of target implosions. My work involved amending one portion of the OMEGA laser system—the frequency conversion portion—to increase uniformity. My work is applicable to other laser systems in need of increased uniformity, among them the National Ignition Facility (NIF) laser, which is currently under construction in Livermore, California [2].

1.1. Frequency conversion

The neodymium-doped glass lasers used on OMEGA and included in the NIF design emit beams in the infrared range. Infrared beams, however, are ineffective in ICF because only a small fraction of their energy is actually absorbed by fuel pellets and, furthermore, much of the absorbed energy is diverted to “suprathermal” electrons which move through the plasma and heat the fuel before it is compressed [1, 2]. Thus, all neodymium-doped glass ICF laser systems employ some method of frequency conversion to generate from IR frequencies the UV frequencies better suited for target implosions. The problem of infrared beams' ineffectiveness is conveniently solved on the OMEGA laser system with potassium dihydrogen phosphate (KDP) crystals, which, when correctly oriented to an incoming beam, triple its frequency. KDP crystals are appropriate for OMEGA's frequency conversion process because they convert relatively broad bandwidths of IR frequencies to the UV. Generation of the third harmonic frequency (see Fig. 1), which is used for the OMEGA system, involves at least two KDP crystals, a “doubler” and at least one “tripler.” The doubler crystal splits the incoming laser beam into components polarized along each of the crystals' two axes, the ordinary

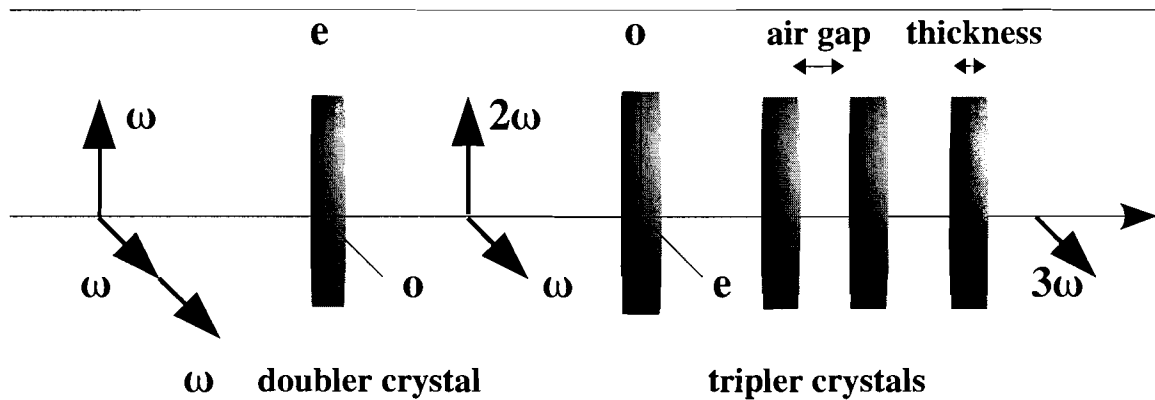


Figure 1. Third-harmonic frequency generation with doubler and tripler crystals. Three IR photons (ω) polarized in two directions enter the doubler, and two combine to form a green photon (2ω) with twice an IR photon's frequency. The green photon and the remaining IR photon enter the tripler and combine to form a UV photon (3ω) with three times an IR photon's frequency. The air gaps between the triplers, the thicknesses of the triplers, and the tilts of the triplers affect the efficiency of this conversion at various incoming frequencies.

(o) axis and the extraordinary (e) axis [4]. When the beam is polarized at 35° to the doubler's o axis, there are two o -polarized photons for each e -polarized photon at the original frequency. One o -polarized photon and the e -polarized photon combine into one green second-harmonic photon polarized in the e direction. The tripler crystal(s) combine the green photon and the remaining IR o -polarized photon into one e -polarized ultraviolet photon with three times the frequency and energy of one of the three IR photons [4].

1.2. Broadband frequency conversion on OMEGA

The original frequency-conversion-crystal design for OMEGA involved only one tripler crystal. The design converted efficiently (near 80%), but it only converted for a small range of wavelengths—about 5 \AA —surrounding the wavelength to which it was tuned (see dotted line on Fig. 2). Wavelengths too far from the tuning

wavelength of the tripler did not convert to the UV efficiently because they were not phase-matched: that is, the driving force for the UV wave did not move in phase with the UV wave [5]. Broader conversion bandwidth than afforded by the one tripler was required for Smoothing by Spectral Dispersion (SSD) [6], a technique used for the creation of smoothly focused laser beams. Eimerl et al. [7] suggested that a second tripler could increase the bandwidth of wavelengths efficiently converted, since two triplers could be tuned to wavelengths on either side of the central wavelengths and thus convert, together, a wider range of wavelengths than that converted by one tripler. Oskoui [5] wrote a program which calculated dual-tripler conversion and with his

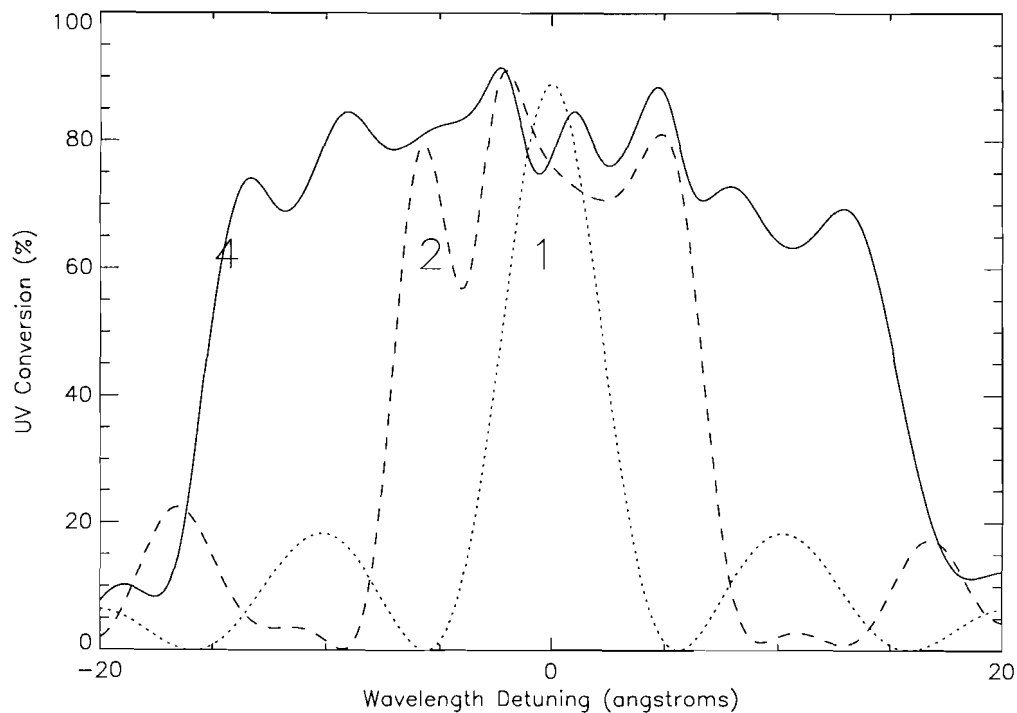


Figure 2. UV conversion as a function of IR laser wavelength at laser beam intensity of 1.5 GW/cm^2 for three frequency-conversion-tripler designs: OMEGA's original one-tripler design (dotted line), the two-tripler design as implemented on OMEGA (dashed line), and my four-tripler design (solid line). Bandwidth of the 1-tripler design is 5 \AA ; that of the 2-tripler design, 14 \AA ; that of the 4-tripler design, 30 \AA .

program developed an optimized solution to the two-tripler problem. His design, subsequently implemented on OMEGA with slight modifications, converted about 14 Å of IR bandwidth with efficiency almost equivalent to that of the single tripler and sustained over a broad range of wavelengths (see dashed line on Fig. 2) [5]. Experimental results matched his program's conversion predictions very closely [8]. A similar broadband two-tripler design was developed for the NIF laser [9].

1.3. Project goal

Because broader bandwidth on OMEGA is still desired, it was wondered if additional triplers could broaden OMEGA's bandwidth yet again. Designs with more than two triplers had not been explored prior to this project. I modified Oskoui's code to accommodate multiple-tripler designs and then developed a systematic method for creating broadband designs for any number of triplers. This method involves the optimization of tripler thicknesses, tilts, and spacings. I used this method to generate designs for three, four, and five triplers, designs which significantly broaden the conversion bandwidth on OMEGA. Whereas the original one-tripler design and OMEGA's current two-tripler design convert 5 and 14 Å, respectively, my four-tripler design converts 30 Å with no loss in conversion efficiency (see solid line on Fig. 2).

2. Methodology

The program in the PV-Wave language which simulates multiple-tripler designs is based upon the frequency-conversion equations. These differential equations

$$\frac{dE_1}{dz} = -\frac{1}{2} \gamma_1 E_1 - iK_1 E_3 E_2^* \exp(-i\Delta k \cdot z) \quad (1)$$

$$\frac{dE_2}{dz} = -\frac{1}{2} \gamma_2 E_2 - iK_2 E_3 E_1^* \exp(-i\Delta k \cdot z) \quad (2)$$

$$\frac{dE_3}{dz} = -\frac{1}{2} \gamma_3 E_3 - iK_3 E_1 E_2 \exp(i\Delta k \cdot z) \quad (3)$$

Frequency-conversion equations.

track the growth of the electric fields ($E_1 - E_3$) of the three different frequencies as the waves travel in the z direction through the crystals [4, 10]. Each equation's main term (e.g., $-iK_3 E_1 E_2$) describes the growth of the corresponding electric field; each K term is the growth coefficient for the corresponding electric field. The presence of the electric fields or the complex conjugates of the electric fields (e.g. E_2^*) of other waves in each wave's equation demonstrates the interdependence of the three waves. The intensity of an electric field is proportional to the square of the amplitude of the electric field. The air gap between each tripler and the preceding tripler determines the initial direction of electric field growth in the complex plane. The phase term ($-i\Delta k z$) describes the relative phase of the three waves. The Δk term is determined from the angle detuning and wavelength detuning of a tripler. Δk is linearly proportional to both angle detuning and wavelength detuning, so tuning a crystal to a certain wavelength involves tilting it to a corresponding angle. The conversion factor is 166 μrad of tilt per 1.0 \AA of IR wavelength. Each equation also includes an absorption term (γ), though this term is of little import in the approximately 1 cm-thick crystals I used. The program uses the

Halfstep-Wholestep approximation method (calculation of the slope at a point, calculation of a “halfstep” point between the original point and the intended second point, calculation of the slope at the halfstep point, then calculation of the second point) to trace the electric fields' growth through the crystals. Three categories of variables—crystals' tilts, thicknesses, and separations—are involved in the optimization process. Because many variables are involved with even a modest number of crystals (eleven variables for four triplers, for instance), it was necessary to experiment with many setups to arrive at the multiple-tripler designs.

3. Results

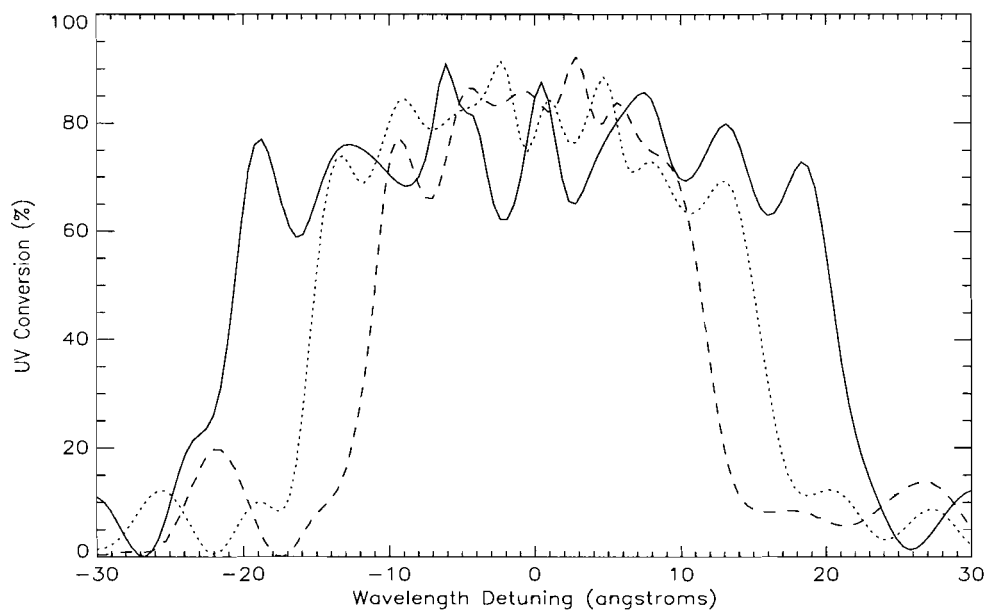


Figure 3. Baseline 3- (dashed line), 4- (dotted line), and 5-tripler (solid line) designs at an input intensity of 1.5 GW/cm^2 . Bandwidth increases with each additional tripler.

I developed designs with broad bandwidth and consistently high conversion efficiency for three, four, and five triplers (see Fig. 3 and Table 1). The four-tripler design more than doubles the bandwidth of OMEGA's current two-tripler design, and the five-tripler design more than triples it. Both the three- and four-tripler designs have conversion efficiency across the bandwidth more consistent than that of the two-tripler design (see Fig. 2 and Fig. 3).

Table 1. Characteristics of baseline designs for 1-5 triplers at 1.5 GW/cm² input intensity. The 1-tripler design was originally used on OMEGA. The 2-tripler design is the current OMEGA design. Detuning refers to tilt in μrad from the angle at which a crystal is phase-matched. Separation refers to the air gap between a given tripler and the previous tripler. Mean conversion refers to the mean conversion above half-maximum. In all designs the doubler crystal has a thickness of 12.2 mm and a detuning of 0 μrad .

	1-tripler design	2-tripler design	3-tripler design	4-tripler design	5-tripler design
1st tripler thickness detuning	12.2 mm 0 μrad	12.2 mm 620 μrad	10.0 mm 1350 μrad	10.0 mm 2250 μrad	10.0 mm 3000 μrad
2nd tripler thickness detuning separation	-----	8.0 mm -380 μrad 1.00 cm	8.0 mm 0 μrad 0.90 cm	9.0 mm 900 μrad 0.75 cm	9.0 mm 1450 μrad 0.9 cm
3rd tripler thickness detuning separation	-----	-----	9.0 mm -1350 μrad 1.00 cm	9.0 mm -450 μrad 0.90 cm	9.0 mm 0 μrad 0.8 cm
4th tripler thickness detuning separation	-----	-----	-----	9.0 mm -1800 μrad 0.90 cm	9.0 mm -1250 μrad 0.8 cm
5th tripler thickness detuning separation	-----	-----	-----	-----	9.0 mm -2650 μrad 0.9 cm
Bandwidth at half-maximum	4.9 Å	13.7 Å	22.6 Å	30.3 Å	41.4 Å
Mean conversion	67.8 %	71.3 %	77.0 %	75.3 %	72.3 %

To create an efficient design, it is necessary to understand how the multiple-tripler conversion process functions; this process will be explained in terms of the three-tripler design but applies to designs for any number of triplers.

3.1. Three-tripler design

Any multiple-tripler frequency-conversion curve arises from the individual frequency-conversion curves of the triplers involved. Each tripler in a given design has its own frequency-conversion pattern similar to that of the tripler in OMEGA's original one-tripler design (see the dotted lines on Fig. 4). Such a single-tripler curve is symmetrical and centered at the wavelength to which it is tuned. The curve's height and

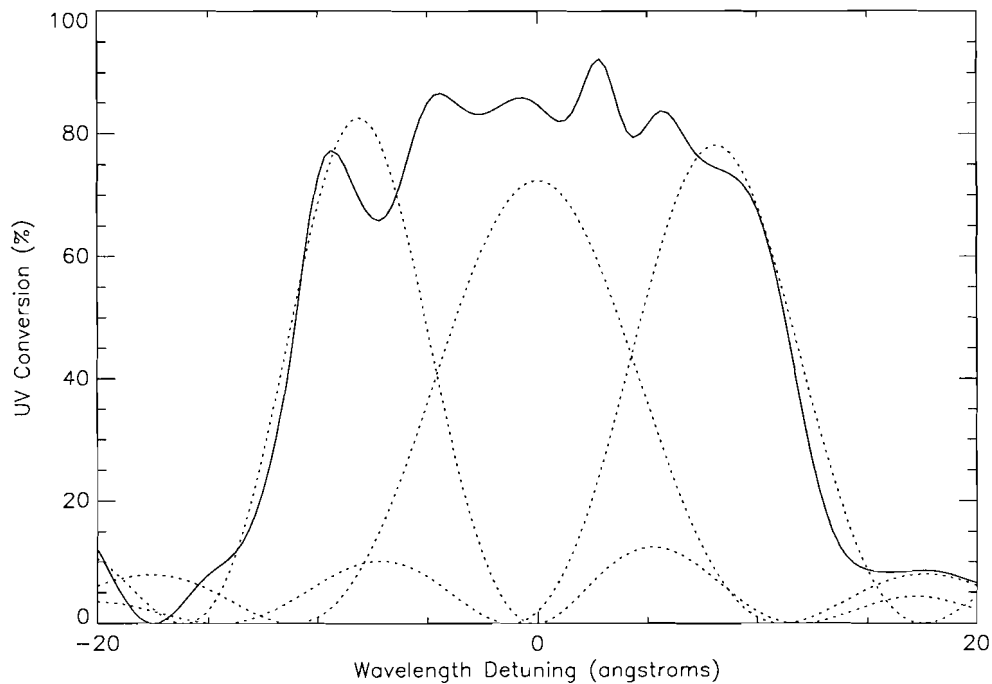


Figure 4. Three single-tripler curves (dotted lines) which combine constructively and destructively, as determined by phase, to create the baseline 3-tripler conversion curve (solid line; see Table 1). Input intensity is the usual 1.5 GW/cm^2 .

length are determined for a given incoming-laser-beam intensity by the tripler's thickness: thicker triplers yield taller, narrower conversion curves. Each tripler in a design converts to varying degrees the wavelengths in the neighborhood of the wavelength to which it is tuned. Tripler parameters determine whether the conversion achieved by a given tripler at a specific wavelength is increased or decreased by the next triplers in a design. A tripler-by-tripler plot such as Figure 5 demonstrates that each tripler is primarily responsible only for the conversion of the wavelengths near that to which it is tuned. However, such a plot demonstrates that later triplers can significantly influence conversion at wavelengths nearer to the tuning wavelengths of earlier triplers.

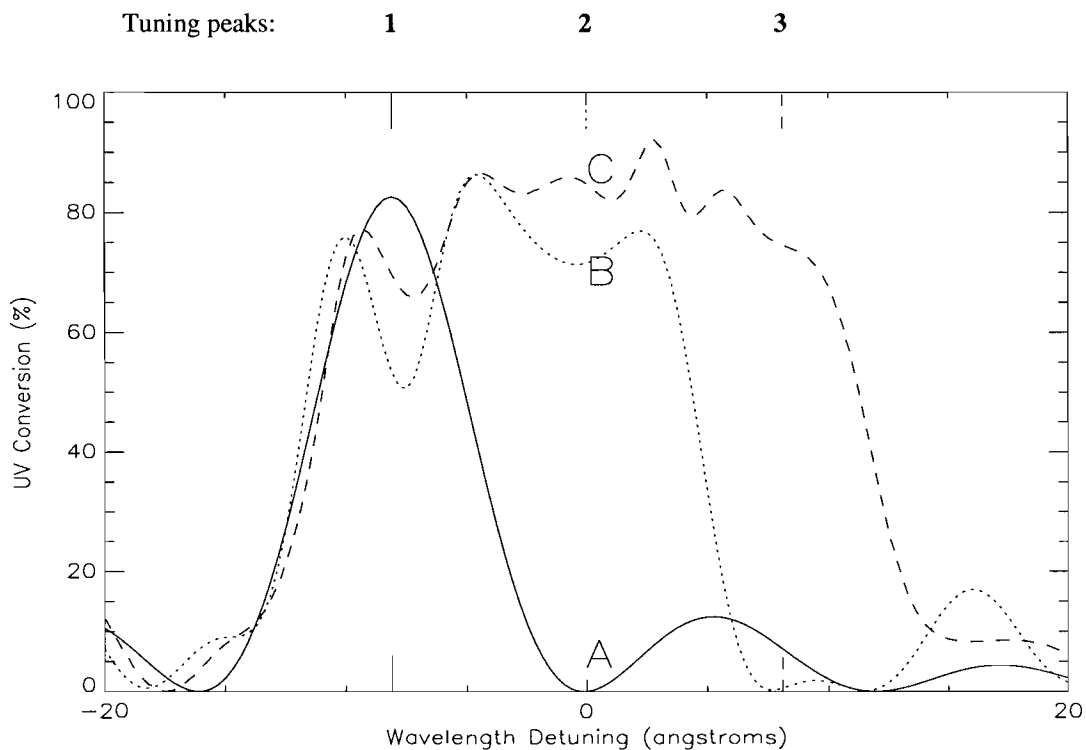


Figure 5. Tripler-by-tripler buildup of baseline 3-tripler curve. The solid line represents conversion after the beam has traveled through the 1st tripler; the dotted line, after it has traveled through the 2nd tripler; and the dashed line, after it has traveled through the 3rd tripler. Small notches represent tuning peak locations for the 1st, 2nd, and 3rd triplers. Electric field growth from point A to point C is shown in Fig. 6.

Figure 5 reveals that the second tripler is tuned almost exactly to the zero of the first tripler's curve and that the third tripler is tuned near the zero of the combined curve of the first and second triplers. The technique of tuning a tripler to the zero of the previous combined conversion curve is often successful. The final conversion at this zero wavelength is attained solely by the additional triplers. It is important to note that the optimum tuning for additional triplers is not necessarily exactly at the zeroes of previous curves. Because of the complicated phase interactions of the triplers at all wavelengths, the tuning which provides optimum conversion at a certain wavelength may not serve well wavelengths on one or the other side of this wavelength.

A plot of the UV electric field in the complex plane provides an enlightening view of conversion curve generation (see Fig. 6). Figure 6 shows the growth through three tripler crystals of the UV electric field generated from the IR

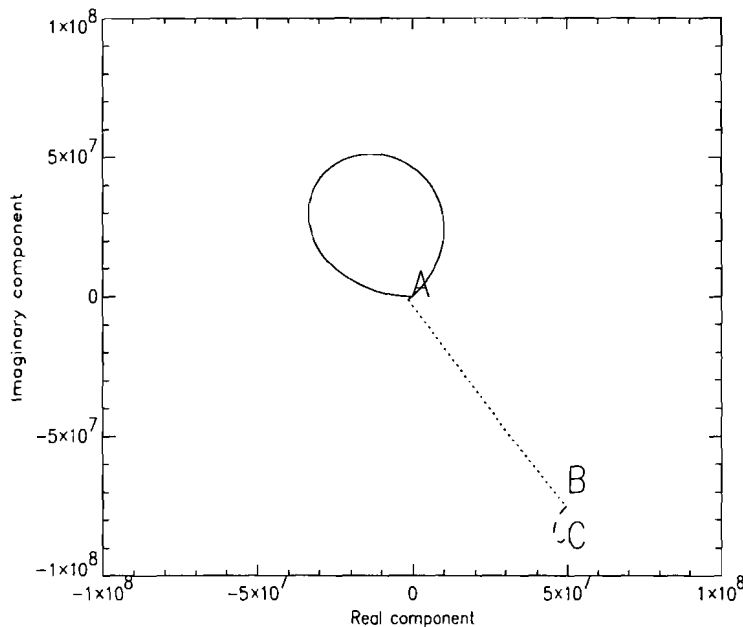


Figure 6. Growth of the UV electric field (plotted in the complex plane) generated from the central IR wavelength as waves travel through the baseline three-tripler design at an input intensity of 1.5 GW/cm^2 . The solid line represents the path through the 1st tripler (to A); the dotted line, the path through the 2nd tripler (A to B), and the dashed line, the path through the 3rd tripler (B to C). At this wavelength most growth occurs in the 2nd tripler, which is tuned to this wavelength, a wavelength very near a zero in the 1st tripler's conversion curve.

central wavelength. The electric field's curve as the waves travel through the first tripler returns nearly to zero (point A). Because the second tripler is tuned to the selected wavelength, its waves are in phase and thus the UV electric field grows in a straight line (see A to B on Fig. 5 and Fig. 6). It can be seen that the third tripler influences conversion at this wavelength little, since its tuning wavelength is far from the wavelength in question (see B to C on Fig. 5 and Fig. 6).

The air gap between any two triplers in a multiple-tripler design determines the relative phase of the waves entering the second of the two triplers and must be adjusted so that conversion increases at as many wavelengths as possible with the addition of the second tripler.

3.2. Tripler detuning

Optimum detunings of the triplers are essential to the success of a multiple-tripler design. Triplers tuned too far from one another (see Fig. 7) do not achieve high enough conversion at intermediate wavelengths to create an acceptable conversion curve. If triplers are tuned too closely to one another, the resulting conversion curve is also poor, in this case because there is so much interference that adjusting the tripler spacings cannot satisfactorily minimize the pronounced modulations (see Fig. 8).

Figure 7. As Fig. 4 but with 3 triplers widely detuned (detuning of the 1st tripler is 2000 μrad ; that of the 2nd tripler is 0 μrad ; and that of the 3rd tripler is -2000 μrad). The separation between the 2nd and 3rd triplers has been adjusted to 2.0 cm to optimize conversion with these detunings. The conversion is low in regions between triplers.

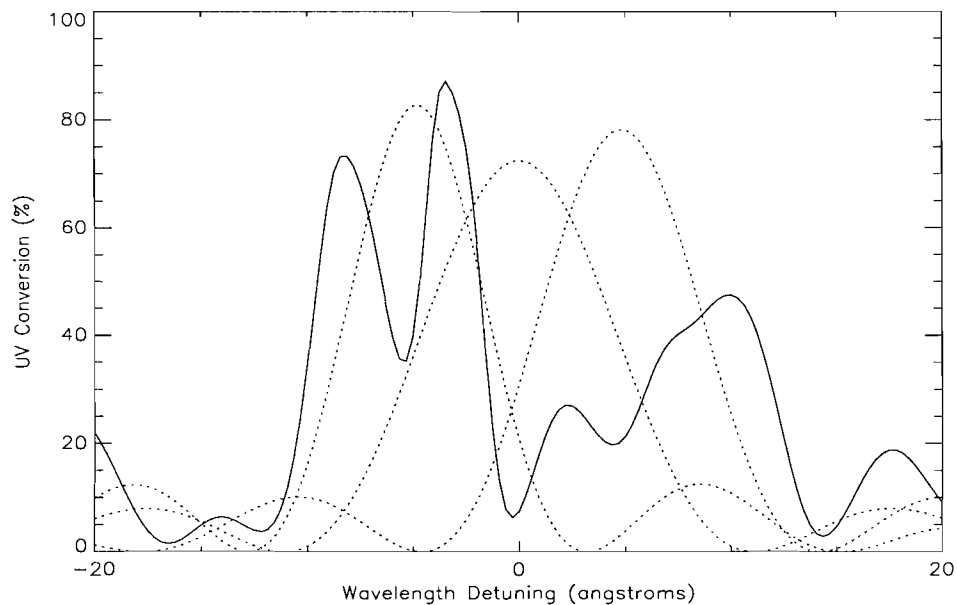
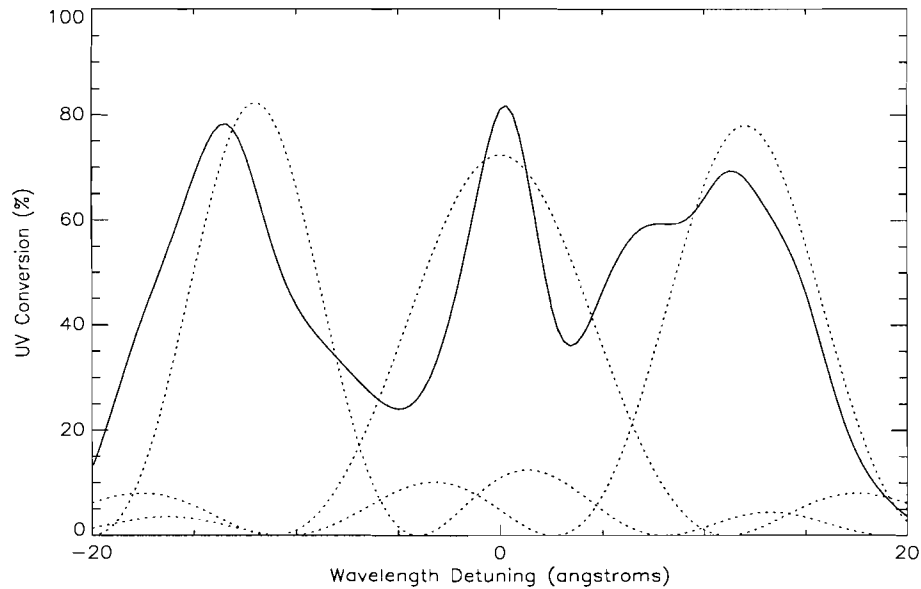


Figure 8. As Fig. 4 but with 3 triplers narrowly detuned (detuning of the 1st tripler is 800 μrad ; that of the 2nd, 0 μrad ; that of the 3rd, -800 μrad). Extreme modulations persist due to unavoidable destructive interference.

3.3. Tripler thickness

The thickness of the triplers in a design must be set appropriately. Figure 9 shows the dependence on the third-tripler thickness for the otherwise-optimized three-tripler-design conditions. The 11-mm length effects better conversion at wavelengths near the tuning wavelengths of the third tripler but decreases conversion in the central part of the bandwidth. The 7-mm length produces an unwanted dip on the left side of the curve and also converts weakly on the right side. Thus, the 9-mm thickness produces the best overall performance. Triplers thicker than 11 mm induce profound modulations and isolated peaks rather than uninterrupted regions of high efficiency.

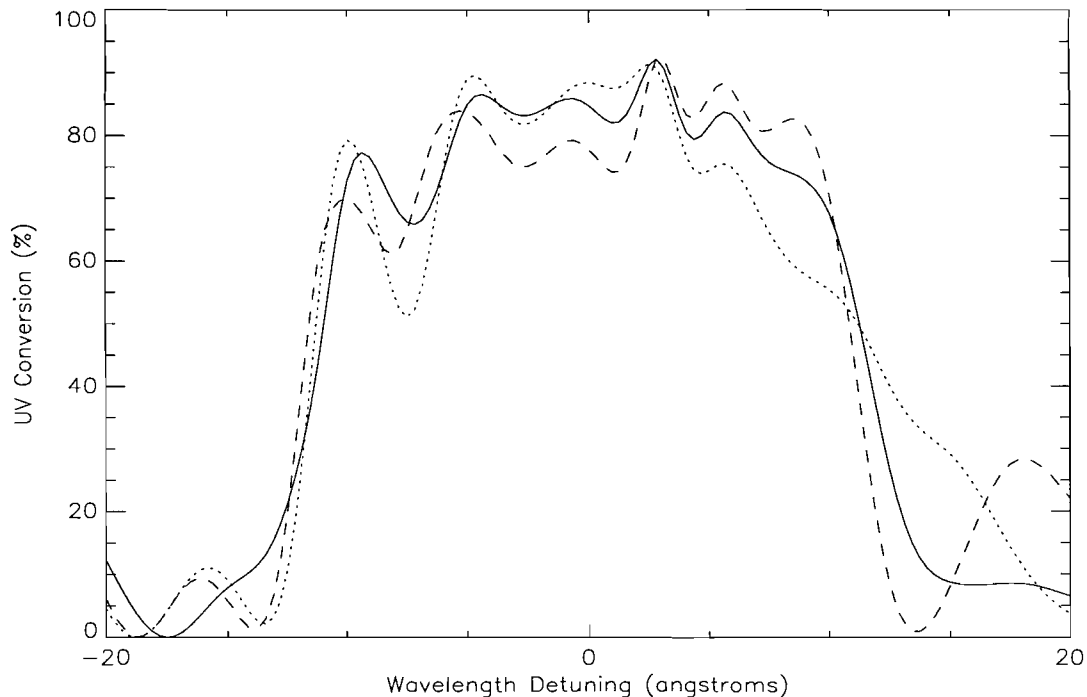


Figure 9. Baseline 3-tripler design (solid line; see Fig. 4) compared with 3-tripler designs with different thicknesses of the 3rd tripler. For the dashed line, the thickness of the 3rd tripler is 11 mm; for the dotted line, it is 7 mm.

All designs have been optimized at an input intensity of 1.5 GW/cm²; however, it can be shown from Equations 1-3 that any design can be scaled for any intensity by multiplication of the tripler lengths by the square root of the reciprocal of the ratio of intensities and the detuning angles by the square root of the ratio of intensities. Thus, my designs could be applied to any high-intensity laser.

3.4. Performance at lower intensities

I initially optimized my conversion curves exclusively for an input intensity of 1.5 GW/cm². However, intensities vary throughout OMEGA laser pulses; 1.5 GW/cm² is OMEGA's peak operating intensity but not the only operating intensity of interest. Early in the implosion broad bandwidth is required in the small-signal input intensity regime, which includes intensities as low as 0.1 GW/cm². Therefore, I investigated the viability of my designs at a range of lower intensities. The four-tripler design performs particularly well over a wide range of intensities, maintaining an impressive bandwidth of 29 Å at small-signal intensity (0.1 GW/cm²) and symmetry at all intensities of interest. The three- and five-tripler designs also retain broad bandwidth at small-signal intensity.

3.5. Designs which include OMEGA's current triplers

One question of particular interest to OMEGA researchers is whether multiple-tripler designs exist which incorporate the existing tripler crystals. Investigation

showed that broad-bandwidth three- and four-tripler designs including OMEGA's current triplers are possible. Though both designs contain more modulation than their optimized counterparts, they achieve bandwidths—18.6 and 26.3 Å, respectively—significantly broader than OMEGA's current bandwidth of 14 Å. Their mean conversions are, in fact, slightly higher than that of OMEGA's current design.

4. Conclusions

In investigating multiple-tripler designs, I developed a systematic method for creating a design for any number of triplers. The method involves choosing triplers thick enough that individual conversion is strong but not so thick that the combined curve degrades. It also involves tuning each successive tripler near the zero of the curve produced by the preceding triplers and adjusting tripler separations so that constructive interference is emphasized. My research led to the creation of three-, four- and five-tripler designs which facilitate broad-bandwidth, high-efficiency frequency conversion. These designs broaden the current conversion bandwidth, achieved with two triplers, by a factor of two or three. The multiple-tripler designs I created could be implemented on the OMEGA laser system or on any other high-power laser system which requires smooth laser beams.

5. Acknowledgments

I would like to thank Dr. R. S. Craxton for allowing me to participate in the High School Summer Program at the Laboratory for Laser Energetics. I would also like

to thank him for the innumerable hours and unending enthusiasm which he has devoted to this project. As well, I would like to thank all of the participants in the High School Summer Research Program for their help with this project.

6. References

1. R. S. Craxton, R. L. McCrory, J. M. Soures, "Progress in Laser Fusion," *Scientific American*, vol. 255, p. 5, Aug. 1986.
2. J. Lindl, "Development of the Indirect-Drive Approach to Inertial Confinement Fusion and the Target Physics Basis for Ignition and Gain," *Physics of Plasmas*, vol. 2, no. 11, Nov. 1995.
3. T. R. Boehly, D. L. Brown, R. S. Craxton, R. L. Keck, J. P. Knauer, J. H. Kelly, T. J. Kessler, S. A. Kumpan, S. J. Loucks, S. A. Letzring, F. J. Marshall, R. L. McCrory, S. F. B. Morse, W. Seka, J. M. Soures, C. P. Verdon, "Initial Performance Results of the OMEGA Laser System," *Optics Communications*, vol. 133, pp. 495-506, Jan. 1997.
4. R. S. Craxton, "High Efficiency Frequency Tripling Schemes for High-Power Nd:Glass Lasers," *IEEE Journal of Quantum Electronics*, vol. QE-17, no. 9, p. 1780, Sept. 1981.
5. S. Oskoui, "Broad-Bandwidth Frequency Conversion," *1996 Summer Research Program for High School Juniors at the University of Rochester's Laboratory for Laser Energetics*, Laboratory for Laser Energetics Report No. 277, NTIS document No. DOE/SF/19460-173 (1996).
6. S. Skupsky, R. W. Short, T. Kessler, R. S. Craxton, S. Letzring, J. M. Soures,

- “Improved Laser-Beam Uniformity Using the Angular Dispersion of Frequency-Modulated Light,” *Journal of Applied Physics*, vol. 66, 1989.
7. D. Eimerl, J. M. Auerbach, C. E. Barker, D. Milam, P. W. Milonni, “Multicrystal Designs for Efficient Third-Harmonic Generation,” *Optics Letters*, vol. 22, no. 16, p. 1208, Aug. 1997.
8. A. Babushkin, R. S. Craxton, S. Oskoui, M. J. Guardalben, R. L. Keck, W. Seka, “Demonstration of the Dual-Tripler Scheme for Increased-Bandwidth Third-Harmonic Generation,” *Optics Letters*, vol. 23, no. 12, p. 927, Jun. 1998.
9. A. Babushkin, R. S. Craxton, S. Oskoui, M. J. Guardalben, R. L. Keck, W. Seka, “Demonstration of Dual-Tripler, Broadband Third-Harmonic Generation and Implications for OMEGA and the NIF,” Society of Photo-Optical Instrumentation Engineers reprint, vol. 3492, 1999.
10. R. S. Craxton, S. D. Jacobs, J. E. Rizzo, R. Boni, “Basic Properties of KDP Related to the Frequency Conversion of 1 μm Laser Radiation,” *IEEE Journal of Quantum Electronics*, vol. QE-17, no. 9, Sept. 1981.

2-D Pulsed Laser Beam Modeling Using PROP

Gurshawn Singh

2-D Pulsed-Laser Beam Modeling Using PROP

Gurshawn Singh
Rush-Henrietta Senior High School
Advisor: Dr. John A. Marozas

Laboratory for Laser Energetics
University of Rochester
250 East River Rd.
Rochester, NY 14623-1299

1. Abstract

Many complexities of laser propagation can be eased by the use of PROP to model a laser. PROP is a computational tool that was created at the Lawrence Livermore National Laboratories [1]. This code can be specified to create different types of lasers with different beam fluences and different pulse shapes. As it is implemented at the University of Rochester LLE, it will allow scientists to propagate any laser, any distance, with the use of hardware such as lenses, rod amplifiers, slab amplifiers, spatial filters, and active mirrors. Since PROP can model 2-D effects on lasers, many effects such as diffraction, aberrations, small-scale self-focusing, 2-D gain and saturation can be accounted for. PROP is also flexible as it takes user input data and analyzes it, creating a profile from that data. Using the features of PROP, a rod amplifier spatial filter chain was modeled to demonstrate many of its functions and capabilities. PROP will replace the current 1-D code at LLE creating new possibilities of diagnosing laser-induced damage and accurately modeling the 60-beam laser chain at OMEGA.

2. Introduction

The laser propagation program, PROP, was introduced to the Laboratory for Laser Energetics at the University of Rochester for its capabilities to model laser propagation itself including two dimensional effects. The current laser modeling program, Rainbow does not have the capabilities to model two-dimensional effects. Using PROP will allow the scientists at the Laboratory for Laser Energetics to take into account the two-dimensional effects such as diffraction, small-scale self-focusing, two-dimensional gain, and saturation. The modeling of these effects will lead to further investigation and inquiry upon the harm that they can cause to the high-powered laser system. PROP also has the capability to model the one-dimensional effects and the components such as rod amplifiers, slab amplifiers, spatial filters, aberrations and deformable mirrors. Along with these individual components, a Rod Amplifier Spatial Filter chain typical of that in OMEGA was created using PROP to demonstrate its abilities.

The knowledge of each component is vital while using PROP. Each component has several parameters specific to the modeling of that component. By understanding these parameters, and the significance of each, the programming of PROP is quite simple. In the following paragraphs are brief descriptions of some of the main components and effects for understanding the small scale model of OMEGA that was modeled in PROP. Among these are spatial filters, amplifiers, and aberrations.

An aberration is an effect that comes from the propagation of a laser through space. It is basically an unavoidable and unwanted consequence of propagation, affecting

the two main components of a beam: the phase and the intensity. When the beam is propagated, the aberration causes the phase front to distort. The phase front is focused locally into regions of high intensity and low intensity. With this modulated intensity, the beam must be focused so the high intensity peaks don't cause any laser damage.

The spatial filter's purpose is to remove any high spatial frequency components, such as those caused by an aberration. The beam first goes through a lens, where all high and low frequency waves are focused into a pinhole. When the laser goes through the pinhole, the higher frequencies on the edges of the profile are blocked, allowing the center portion of the beam to maintain its path as it is magnified in the second lens. The end result of the beam is a much smoother profile.

There are two main types of amplifiers, rod amplifiers and slab amplifiers. Slab amplification is a simple linear process. As the beam goes through the slab, ions in the slab stimulate the beam, creating a higher intensity end result. Rod amplifiers amplify the beam without a uniform gain profile. The rod has flash lamps on either side of it that keep the ions inside the rod stimulated. Therefore, the ions closer to the lamps are more energized than those in the middle of the rod. So when the beam goes through the rod, the edges of the rod have a higher intensity. This creates the inconsistency on the gain profile.

3. Using PROP

Using special syntax, one is able to direct PROP to model whatever is needed within the program. This input into PROP is done so using a *.txt file, usually made with Microsoft Notepad. In this notepad document, the parameters of the components and

features needed to be set can be specified. The basic format of this text-based document is similar to any other basic programming structure. At the top, the heading consists of the title, sizes of the plots, and other global factors. From there, the beam injection and temporal calculations are described. The strength, intensity, fluence, and shape are all detailed in this area. The next part describes the physical components of the laser that is being modeled, for example the amplifiers and filters. Different features of the program for user preference can be activated in these sections. These are all detailed in the user manual.

PROP can be run by the user specifying each parameter in the script, or PROP can be run by input files. The previous paragraph explained the specifying of parameters in a script. The use of input files has its benefits, as it's more user friendly. There are input files that were made specifying the beam injection, pulse shape, and 2-D profiles. Each component has a separate input file, either in the binary format (more efficient and consumes less storage) or the ASCII format (text based and much simpler than binary). Although the input files are quite complex, the user has more freedom to change parameters according to their need rather than relying on PROP's intrinsic functions and settings.

4. MATLAB and Input files

Input files were created using MATLAB, a mathematical programming environment. For each component/effect in PROP (amplifiers, aberrations, beam profiles), a program using MATLAB was created. Each program is directed to generate an input file. These input files take user input data, and using the functions programmed

in the script, they generate the entire input file. The user only has to specify in PROP that the input file exists, so the desired effects can be modeled through the input file.

The MATLAB program, PropPulseGen, was created in order to create the pulse specified by the user. MATLAB was programmed to read the functional form of the pulse:

$$pulse = e^{-\ln(2)*(2*(t-t_0)/tfwhm)^{SG}} \quad \text{EQ. 4.1}$$

The user specifies the reference in time (t_0), the full-width-half-max (tfwhm), and the supergaussian index (SG) of the pulse needed. With this data, MATLAB calculates the pulse, shows a graph of the pulse, and creates an input file. The input file is then moved to the PROP directory and the script is changed in PROP, so PROP is aware that there is an input file it must read. Once that is done, PROP will create a beam with the pulse that was specified in the MATLAB program.

The PropGainProfile generates an input file of small signal gain profiles of OMEGA amplifiers for PROP. There are different stages of rod amplifiers in OMEGA with different aperture radii. The A and B amplifiers have a 64 mm diameter aperture, the C stage amplifiers have 90 mm diameter aperture, the stage-D amplifiers also have 90 mm diameter aperture, and the E and F stages use disk amplifiers (disk amplifiers have a constant value of the stored energy per unit volume E_{stored}). The small signal gain (SSG) of an amplifier is defined by the expression [2]:

$$SSG = e^{\{\alpha*L*E_{stored}\}} \quad \text{EQ. 4.2}$$

The user specifies the alpha (α), which is a constant that depends on the laser material. The OMEGA system uses doped phosphate laser glass, so the alpha constant is $0.2120 \text{ cm}^2/\text{J}$. The L stands for pumped length of laser glass, and equals 30.5 cm for all OMEGA amplifiers. For each amplifier stage, the Estored value is different, and is given by a specific functional form. Once the small signal gain value is calculated, the MATLAB script plots the data on a graph, and then creates an input file. The user can make sure the data is correct with the graph provided, and from there decide whether to go on and use the input file in PROP.

PropBeamGen generates the beam energy input file. This script uses the functional forms of a square beam (eq. 4.3) and a round beam (eq. 4.4), depending on the

$$Beam = e^{-\ln(2)(2X / xfwhm)^{SG}} e^{-\ln(2)(2Y / yfwhm)^{SG}} \quad \text{EQ.4.3}$$

$$Beam = e^{-\ln(2)(2R / dfwhm)^{SG}} \quad \text{EQ. 4.4}$$

user's preferences, and creates a beam intensity profile. Each beam profile is specific to the full width half max of the x (xfwhm) and y (yfwhm) values of the square beam and the diametrical (dfwhm) value of the round beam.

Through input files, PROP can model a pulse profile, two-dimensional gain profiles, two-dimensional aberration profiles, and two-dimensional apodization files. Once the MATLAB program for these programs runs, an input file is generated. These input files are compliant with PROP, in that they follow the format that PROP can read the file in, ultimately producing the expected effects. These files are made in either the binary (*.bin) or ASCII (*.dat) formats. They should then be transferred to the correct

directory where the PROP script resides. The PROP script must be altered so that PROP will expect these input files.

5. Rod Amplifier Spatial Filter Chain

Using PROP, a chain of components, similar to those in OMEGA, was created. As in OMEGA, the beam in PROP was aberrated, and then propagated through a spatial filter, rod amplifier, and spatial filter again. This chain was modeled through the input files created by a MATLAB script. The script was used to create a pulse, a beam, and a

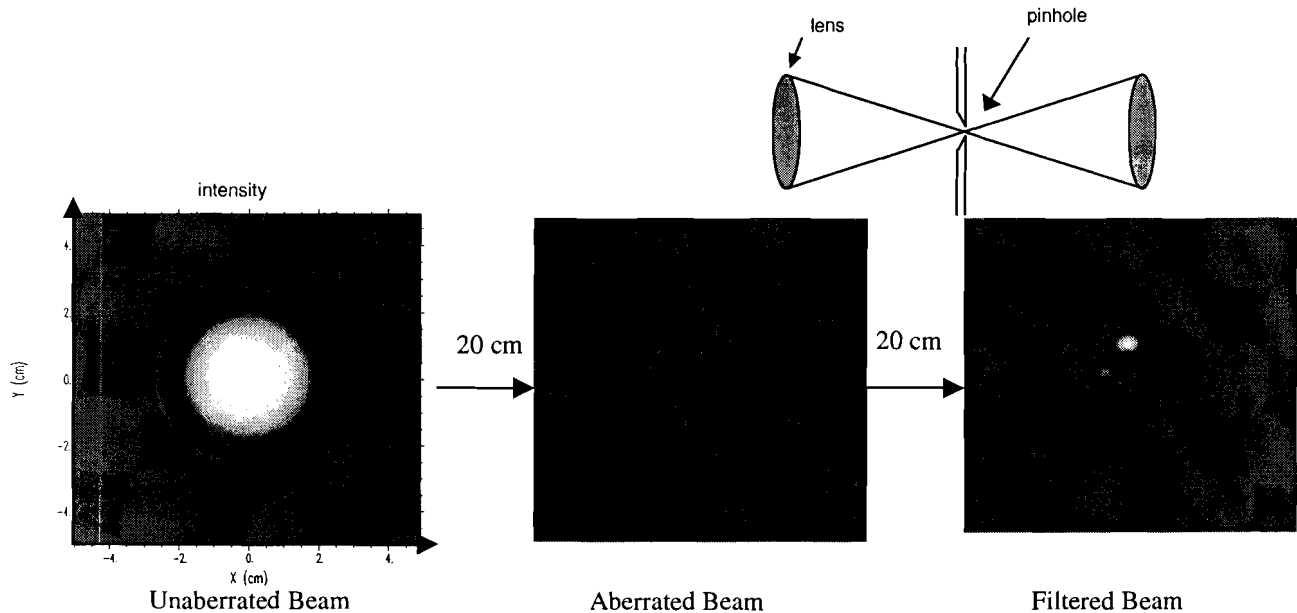


FIGURE 5.1

gain profile. The aberration, amplifiers, and filters were all created using PROP's intrinsic functions. The distances between these components were taken into consideration, so this model is quite accurate.

The output files in PROP display graphics and graphs, with information about the beam. The first graphic of fig. 5.1 is the original beam, before any propagation or altering. The beam is then propagated 20 centimeters, and aberration through the air

occurs. Higher intensity and lower intensity areas can be seen on the beam. By focusing the beam through a lens and cutting off this high frequency

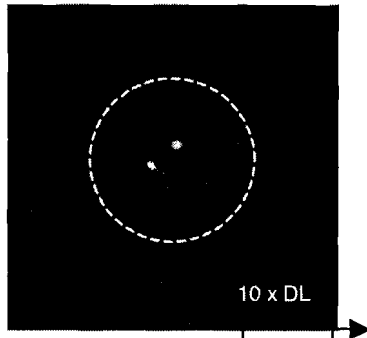


FIGURE 5.2

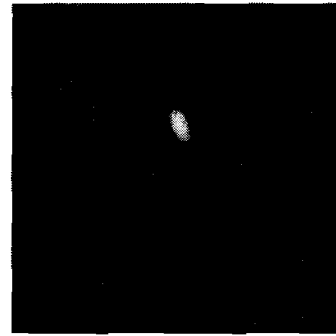


FIGURE 5.3

through the pinhole, we get a much cleaner and smoother beam. The beam at the pinhole would resemble figure 5.2. Since the beam is extremely small it is then enlarged with another lens and the product is the filtered beam as in the last graphic in figure 5.1.

Then, the filtered beam is propagated through a rod amplifier, creating distortion on the beam, so then we put it through another spatial filter. The spatial filter is the last component, so the outcoming beam is the end result (fig. 5.3).

6. Conclusion

PROP has become a useful tool for scientists at LLE. Many 2-D effects on OMEGA can be accounted for with PROP such as diffraction, aberrations, small scale self-focusing, 2-D gain and saturation effects. Also, hardware such as amplifiers and spatial filters were accurately modeled. These features allow scientists to diagnose laser

induced damage. Currently, PROP is heavily relied on to model intensity modulations on the new LLE EP program.

7. Acknowledgements

I would like to thank my advisor, Dr. John A. Marozas, who made himself readily available when I needed any type of help. He took numerous hours out of his day just to help me and make sure I was on track. Also, Dr. Jack Kelly took time out of his busy schedule to answer any question I had. Lastly, I would like to thank Dr. R.S. Craxton for putting together the program and everyone at LLE including all the students for making the program an awesome experience.

8. References

1. Sacks et al. "The PROP92 Fourier Beam Propagation Code," LLNL Annual Report
2. Siegman, Anthony E. Lasers. 1996.

**Characterization of Multilayer Diffractors for Framed
Monochromatic Imaging**

Archana Venkataraman

Characterization of Multilayer Diffractors for Framed Monochromatic Imaging

Archana Venkataraman
University of Rochester, Laboratory for Laser Energetics
2002 Summer High School Program

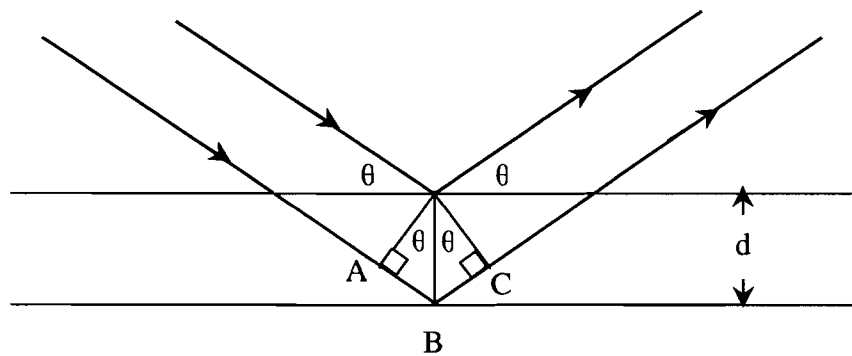
INTRODUCTION

The OMEGA laser facility¹ at the University of Rochester's Laboratory for Laser Energetics is used to explore the conditions needed for sustaining thermonuclear fusion reactions². X rays emitted by the laser-generated plasma can be imaged, providing information about the state of the plasma, i.e. temperature and density. Framing cameras allow the x-ray emission to be resolved in time and, when used in combination with mirrors and filters, to image the emission in narrow energy bands³.

In this work, two WB₄C (tungsten boron carbide) multilayers⁴ are characterized at several x-ray energies by finding the efficiency (reflectivity) of each one as a function of angle. A Gaussian analysis of this data yields values of the peak reflectivity and the energy resolution [full width at half maximum (FWHM)]. Analysis of multiple energies allows for inference of the atomic layer spacing d . The multilayers which have nominal layer spacings of 26 Å and 37 Å are found to have reflectivities of ~40 to ~70 % and ~32 to ~89 % respectively and narrow energy resolutions of 1.5 to 2.1 % and 1.8 to 3.7 % respectively. Both are functions of energy. When used in conjunction with framing cameras on the OMEGA laser, they will provide time-resolved, narrow energy band (monochromatic) images of the laser-plasma x-ray emission.

EXPERIMENTS

This project entails the calibration of two such WB_4C multilayer diffractors with approximate $2d$ atomic layer spacings of 26 and 37 Å to be used in the study of laser fusion plasmas. There are three properties of each multilayer that must be determined. The first is the layer spacing d , the second is the reflectivity as a function of energy, and the third is the energy resolution. This is accomplished by measuring x rays diffracted from the multilayer as a function of angle for three emission lines using a Si PIN detector⁵. By finding the angle of maximum reflectivity, or Bragg angle, these characteristics can be determined by using the following derivation⁶:



$$\text{Path difference} = AB + BC = d \sin \theta + d \sin \theta$$

If the path difference is an integral number of wavelengths the outgoing waves interfere constructively, hence

$$n\lambda = 2d \sin \theta, \quad (1)$$

where λ is the wavelength, d is the layer spacing, and θ is the angle the ray makes with the tangent to the surface.

(a) BEAM COLLIMATION AND ALIGNMENT

The x-ray source must be collimated to observe the desired diffraction. The collimator consists of two slits, aligned optically using a telescope, restricting the x-ray emission to a narrow beam. The entrance aperture (dimensions 0.175 mm x 1mm) is positioned 1650 mm away from the exit aperture (dimensions 0.1 mm x 1.2 mm). The detector is positioned an additional 263 mm away from the exit aperture. Figure 1 below illustrates the final calculations of the beam size. The distance x is found using Eq. (2), $Y3$ is then found using Eq. (3), and then the angle α from Eq. (4).

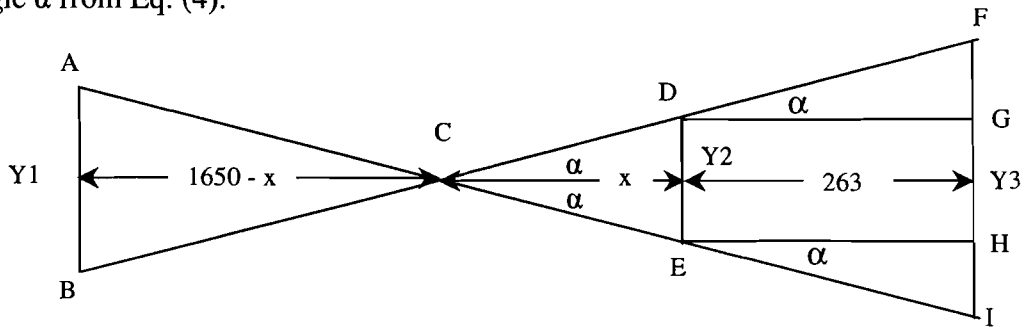


Fig. 1. Diagram of the Collimator setup followed by the calculations for the spatial and angular width of the beam

$$\frac{Y1}{1650 - x} = \frac{Y2}{x} \quad (2)$$

$$\frac{Y2}{x} = \frac{Y3}{x + 263} \quad (3)$$

$$\alpha = \tan^{-1} \left(\frac{0.5(Y3)}{x + 263} \right) \quad (4)$$

When solved using the known dimensions for the slits, the beam size is found to be 0.144 mm x 1.55 mm, making the angular width along the narrower dimension equal to 0.0096°.

Optimum beam alignment consists of the diffractor being positioned parallel to the line of sight and midway through the x-ray beam with respect to the horizontal plane. The observed

beam flux (count rate) is determined with respect to the following four values: the vertical (z) position of the detector, the horizontal (y) position of the detector, the angular orientation of the diffractor, and the horizontal (y) position of the diffractor. The adjustments are done using two concentric stepper-motor driven rotary stages mounted on a linear stage. Each step of the rotary motors equals 0.01° , and each step of the linear motor equals $2.54\mu\text{m}$. Figure 2(a-e) below illustrate the steps of the alignment process.

Figure 2. X-ray detector alignment.

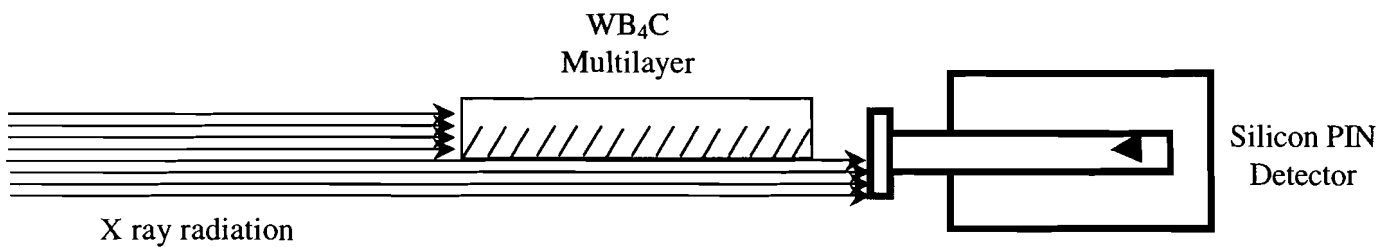


Fig. 2(a). Alignment goal is to have diffractor parallel to beam and in its center.

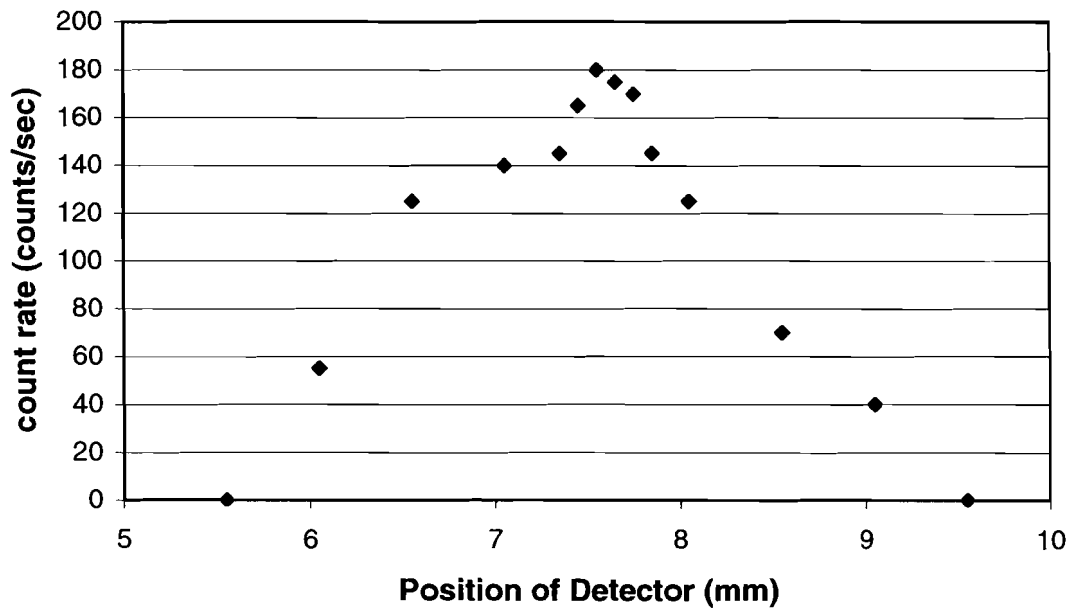


Fig. 2(b). Count rate as a function of detector vertical position.

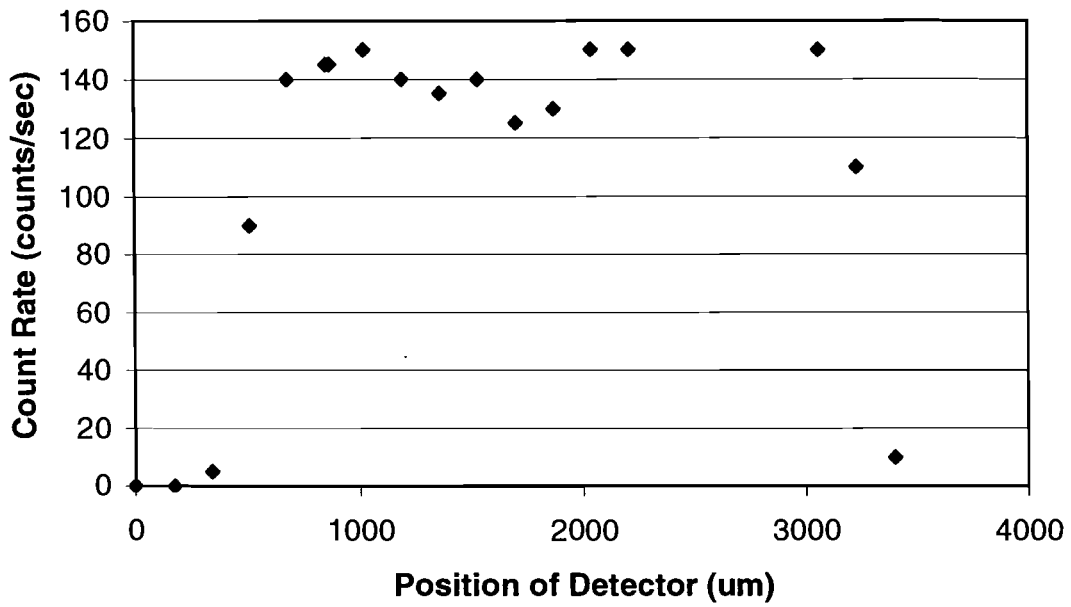


Fig. 2(c). Count rate as a function of detector horizontal position.

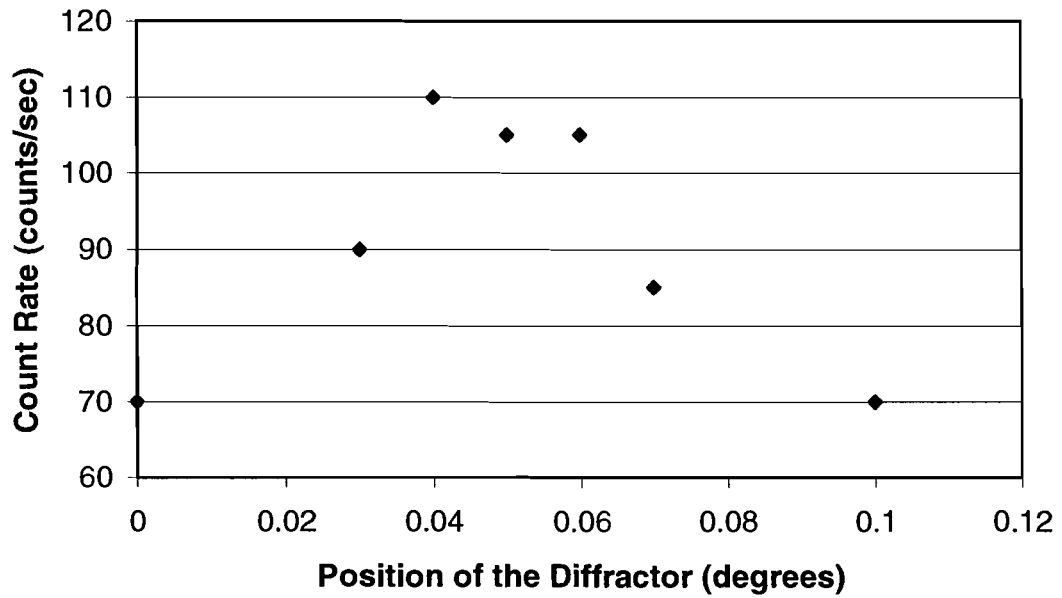


Fig. 2(d). Count rate as a function of diffractor angular position. A maximum rate indicates that diffractor is parallel to the beam

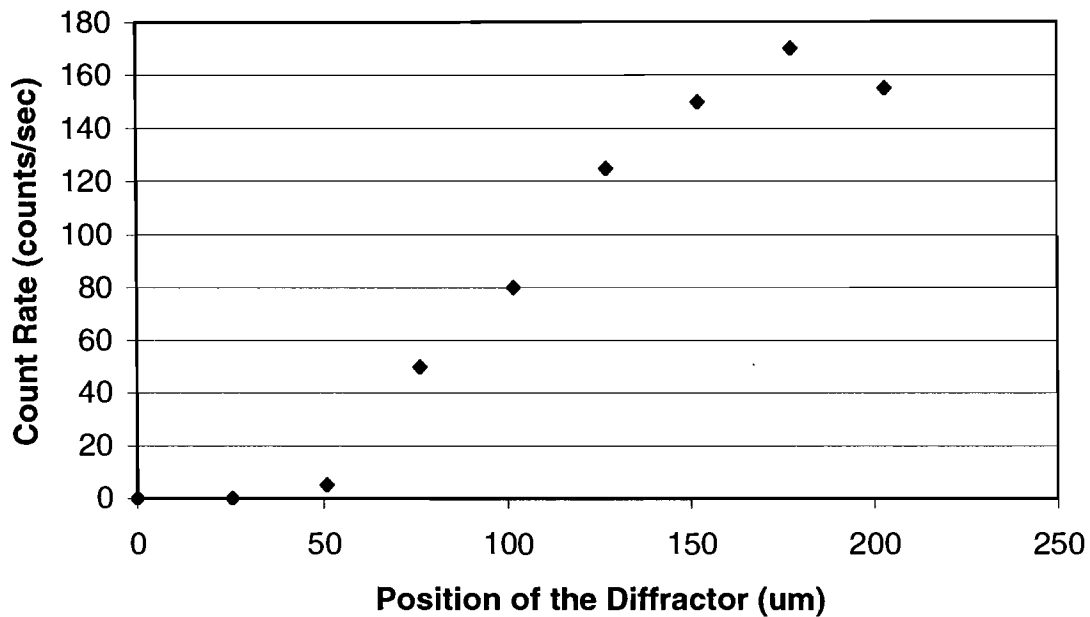


Fig. 2(e). Count rate as a function of diffractor horizontal position.

(b) THE X-RAY SOURCE

The source generates x rays by focusing an electron beam on a metal target⁷. By choosing the target material, different output spectra can be produced. An initial measurement of the undiffracted spectrum is taken for each target as well as subsequent readings periodically throughout the experiment. This allows for the determination of the x-ray photon flux to serve as a reference for measuring the reflectivity. Sample spectra readings for Ti, Cu and Si targets are shown in Figs. 3(a-c).

Fig 3 (a-c): Plots of undiffracted x-ray source spectra as measured by the Si PIN detector.

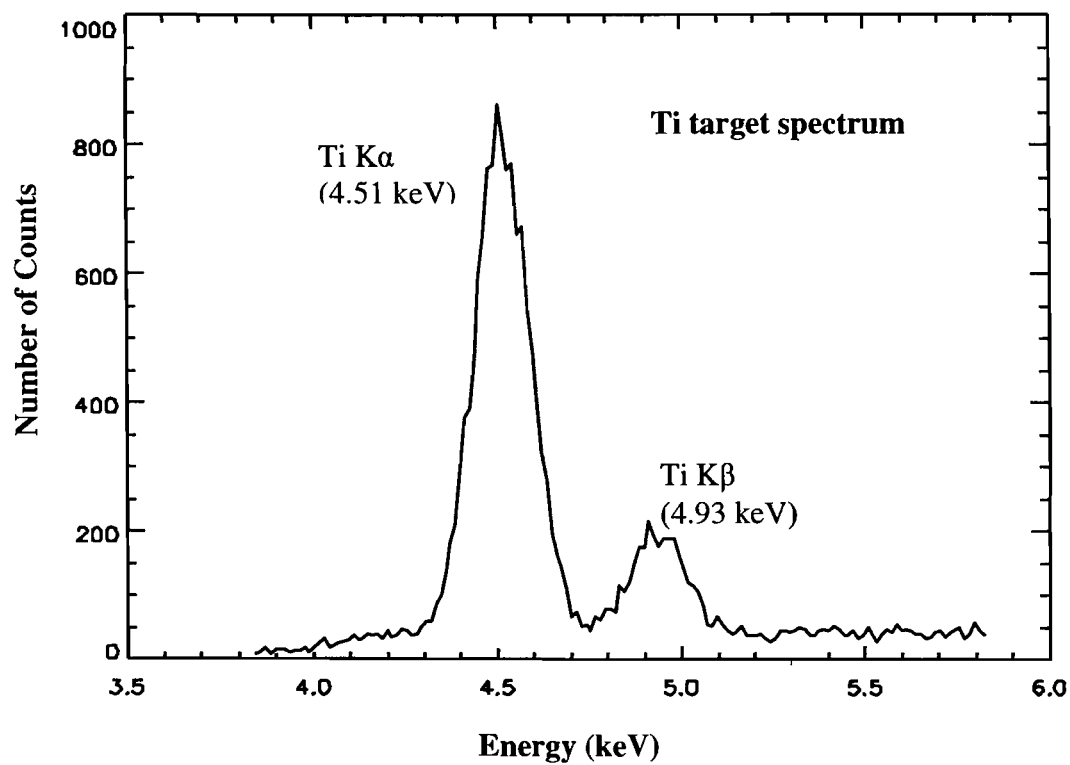


Fig. 3(a)

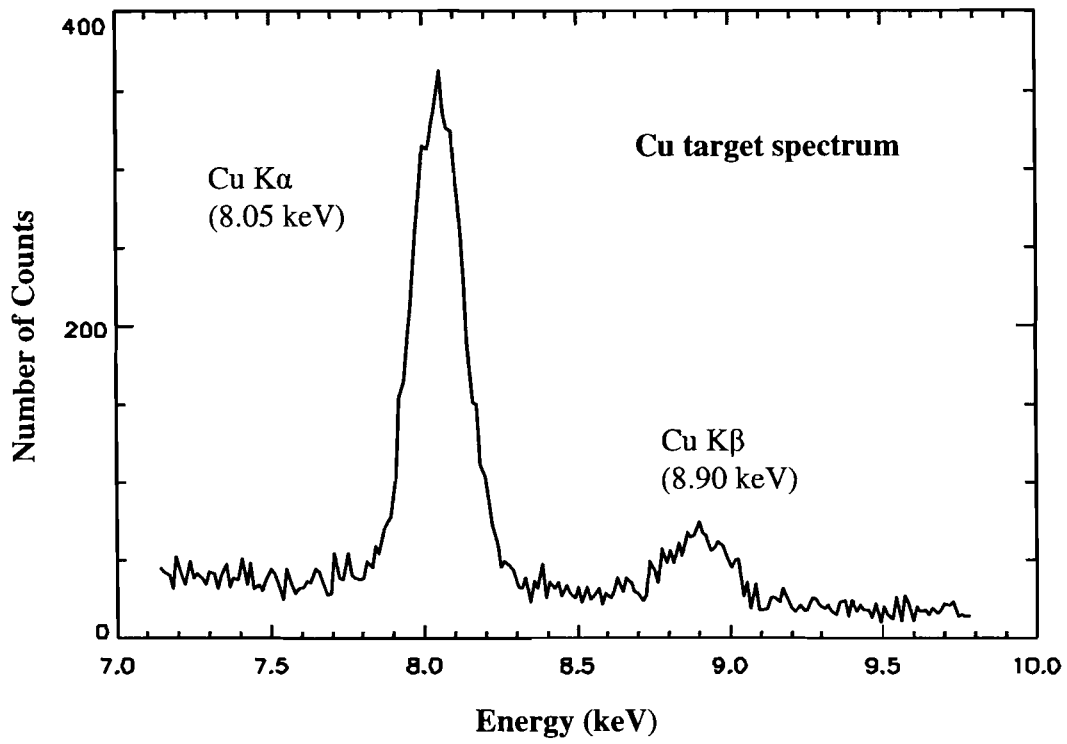


Fig. 3(b)

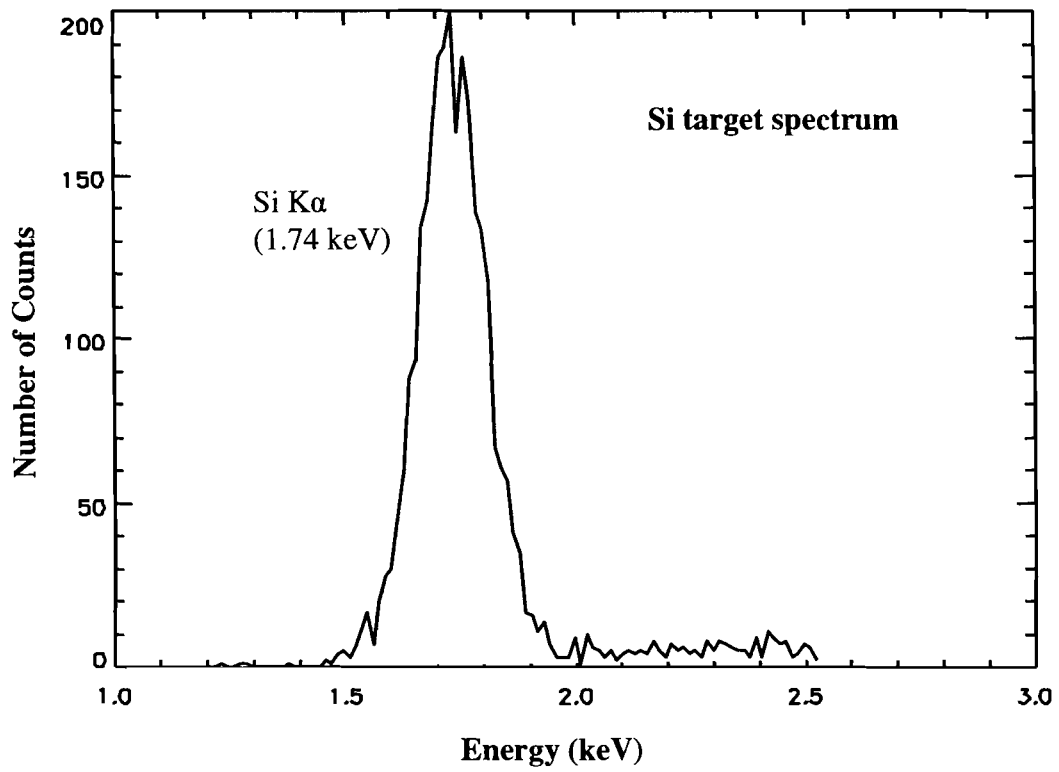


Fig. 3(c)

(c) DIFFRACTION MEASUREMENTS

In order to measure the x-ray diffraction properties of the multilayer, a scan about the Bragg angle is performed. The stepper motors are used to rotate both the multilayer and the Si PIN detector in order to locate the optimum angle of diffraction as defined by Bragg's law. The first multilayer has a nominal d spacing of 25.9 Å and is tested using the Ti K α , Ti K β , and Cu K α line emission. The second multilayer has a nominal d spacing of 37.3 Å and is tested using Si K α , Ti K α , and Cu K α line emission. Figure 4 illustrates this procedure, and Figs. 5(a,b) show the diffracted peaks for each line of the first and second multilayer.

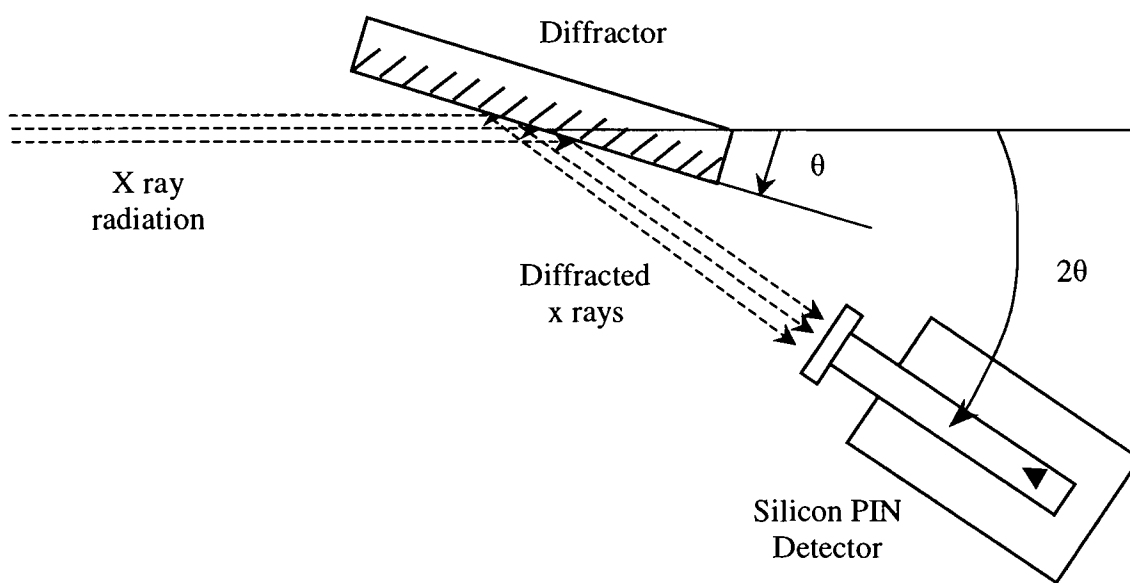


Fig. 4. Diagram of x-ray diffraction apparatus. The diffractor is positioned at an angle θ , and the detector at an angle 2θ , both of which are changed in fixed increments in order to complete the scan. Spectral data readings to check for beam fluctuations are also taken periodically throughout the procedure.

Fig. 5. Plots of each diffracted line (shown combined in this figure) at the specified angle as taken using the Si PIN detector while using both the first multilayer (a) and the second multilayer (b). The number of counts is plotted as a function of energy, but is not proportional to the reflectivity since each line measurement is taken under different conditions relative to the source.

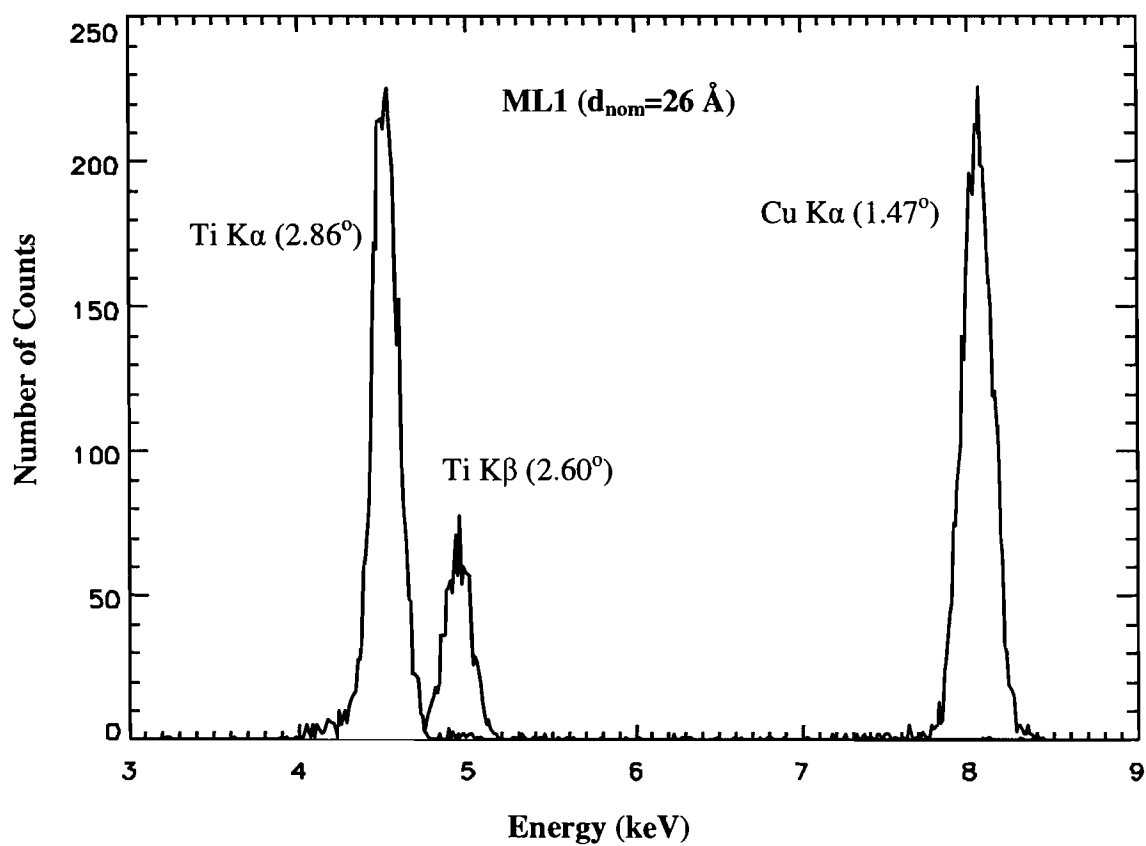


Fig. 5(a)

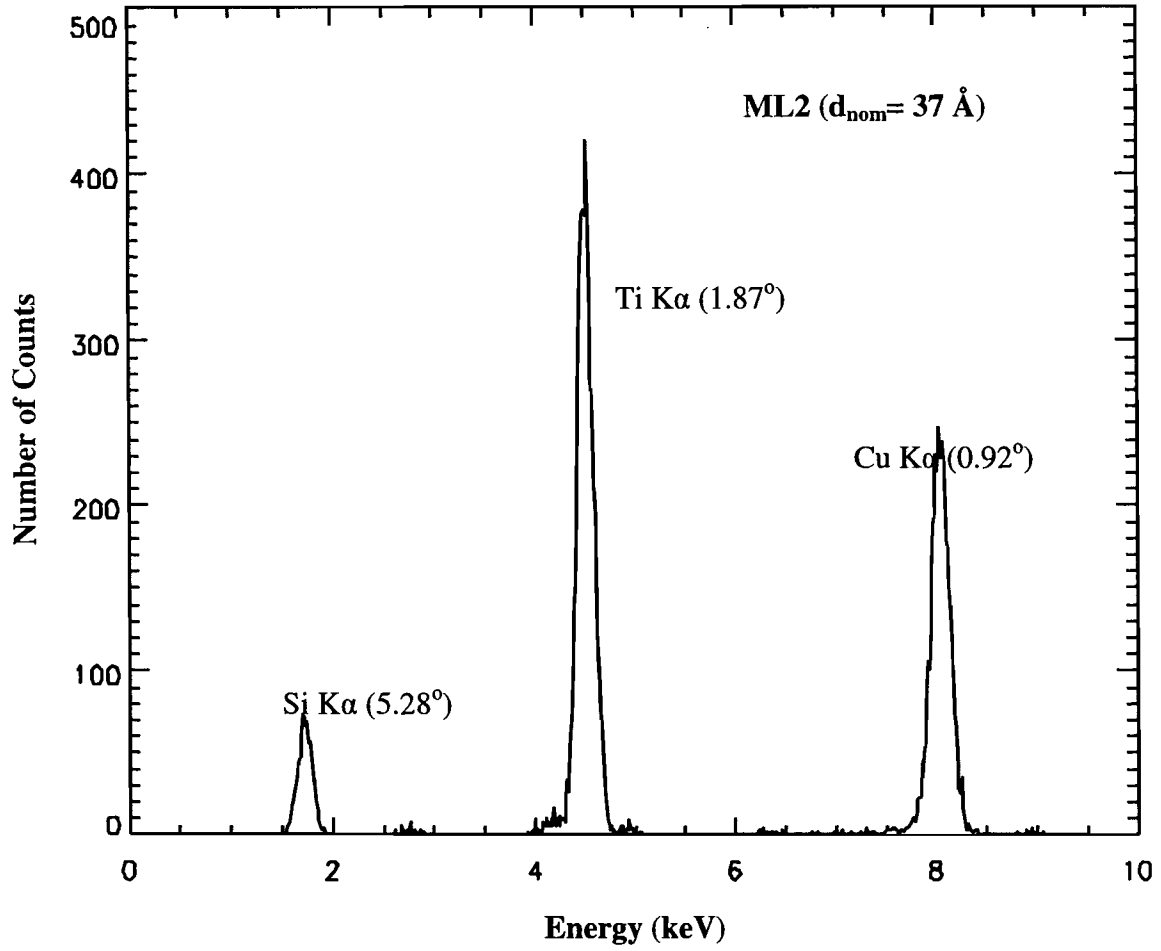


Fig. 5(b)

RESULTS

The line and spectral readings of figs. 3 and 5 taken by the detector displayed the results in terms of counts per bin where each bin corresponds to a mean photon energy. The energy axis scaling factor is calibrated using an Fe⁵⁵ source⁸ and fitted to a Gaussian distribution as follows⁹:

$$f(x) = \frac{1}{\sqrt{2\pi} \sigma} e^{-\frac{(x-x_m)^2}{2\sigma^2}} \quad (5)$$

where x is the angular position, and x_m is the position of the peak, and σ is the standard deviation in degrees. The optimization is done using the CURVEFIT program in PV Wave^{10,11}.

The reflectivity at a given x-ray line energy is determined by dividing the diffracted x-ray count rate by the undiffracted count rate from the same line. The x-ray source rate is monitored periodically to establish its rate as a function of time. The reflectivity is then plotted as a function of angle, and another Gaussian fit is applied in order to determine the angle at which there is a maximum reflectivity.

The integrated reflectivity R_{int} is taken to be the area under the fitted Gaussian and is given by:

$$R_{int} = R_p \sigma \sqrt{\pi}, \quad (6)$$

where R_{int} is in units of degrees, R_p is the peak reflectivity, and σ is the standard deviation. The FWHM of each Gaussian is equal to 2.35σ . Table 1 and Fig. 6 summarize the results gathered when plotting this final result to obtain the maximum angle and reflectivity.

	(a)	(b)	(c)	(d)	(e)	(f)	(g)	(h)	(i)	(j)
Multilayer	Line	Energy (keV)	λ (Å)	θ_B (deg)	R_p	R_{int} (deg)	FWHM (deg)	b_k	error θ_B (deg)	$\frac{\Delta E}{E}$
1	Ti K α	4.51	2.75	2.860	0.395	0.0132	0.044	0.042	0.00215	0.015
	Ti K β	4.93	2.51	2.603	0.427	0.0159	0.050	0.061	0.00194	0.019
	Cu K α	8.05	1.54	1.475	0.690	0.0160	0.031	0.037	0.00104	0.021
2	Si K α	1.74	7.13	5.292	0.323	0.0237	0.097	0.038	0.00460	0.018
	Ti K α	4.51	2.75	1.888	0.542	0.0230	0.056	0.035	0.00310	0.030
	Cu K α	8.05	1.54	0.911	0.888	0.0223	0.033	0.029	0.00052	0.037

Table 1: Measured Properties of WB₄C Multilayer Diffractors. (a) Line name, (b) Line energy in keV, (c) Line wavelength in Å, (d) Bragg angle in degrees, (e) Peak reflectivity, (f) Integrated reflectivity in degrees, (g) Full Width at Half Maximum in degrees, (h) Constant background of reflectivity curve, (i) One standard deviation of the Bragg angle, (j) Energy Resolution.

Fig 6: Measured diffraction efficiency (reflectivity). WB₄C multilayer # 1 (a-c), and WB₄C multilayer # 2 (d-f).

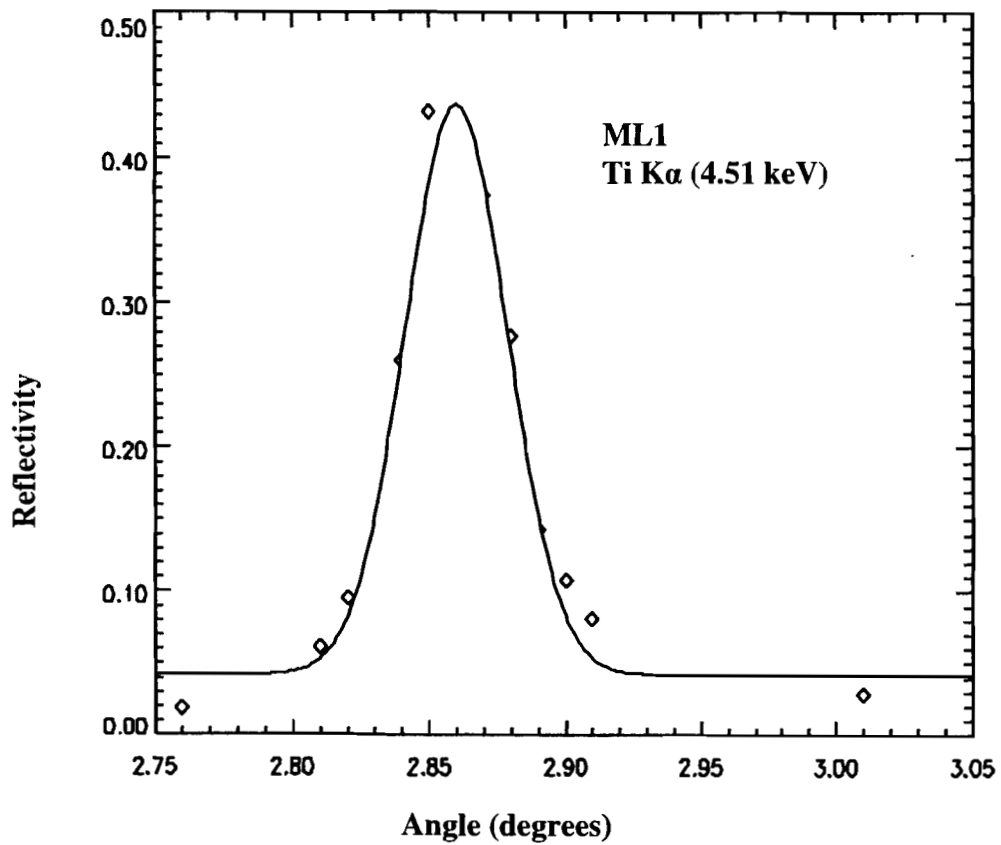


Fig. 6(a)

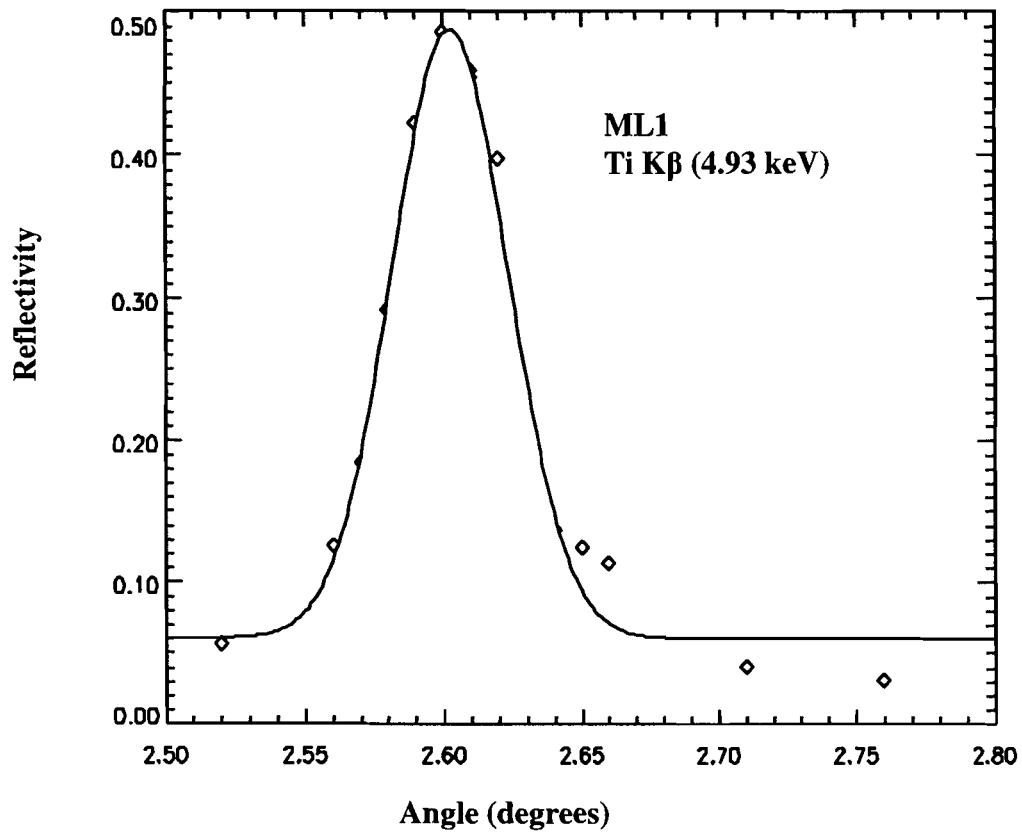


Fig. 6(b)

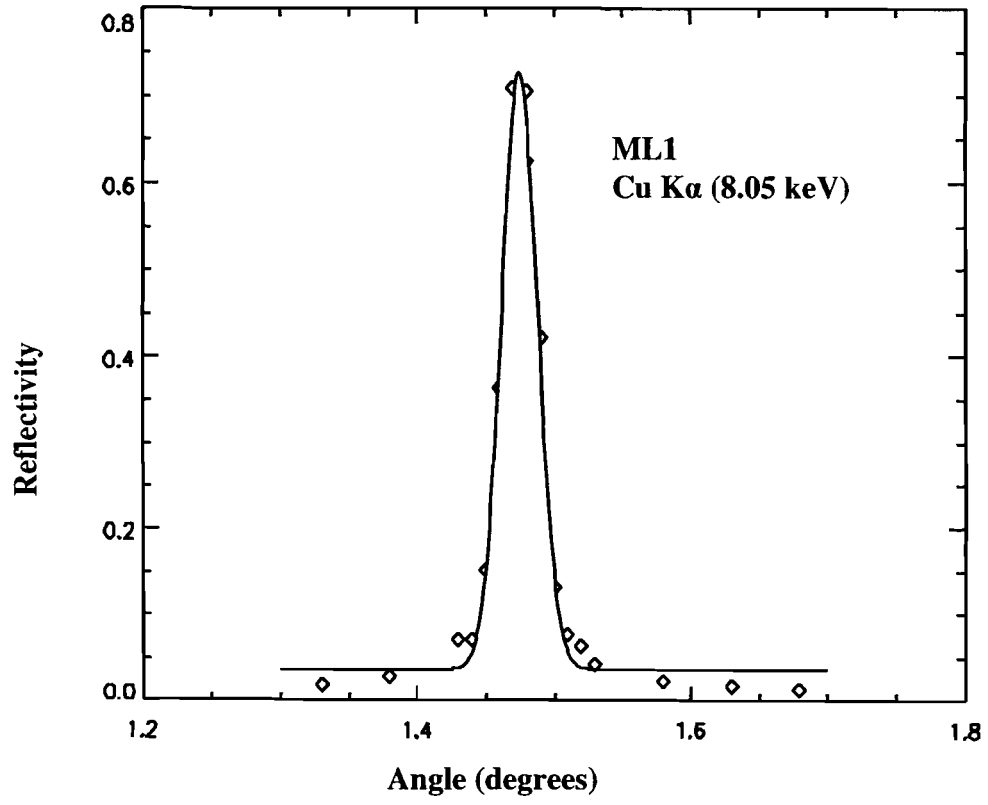


Fig. 6(c)

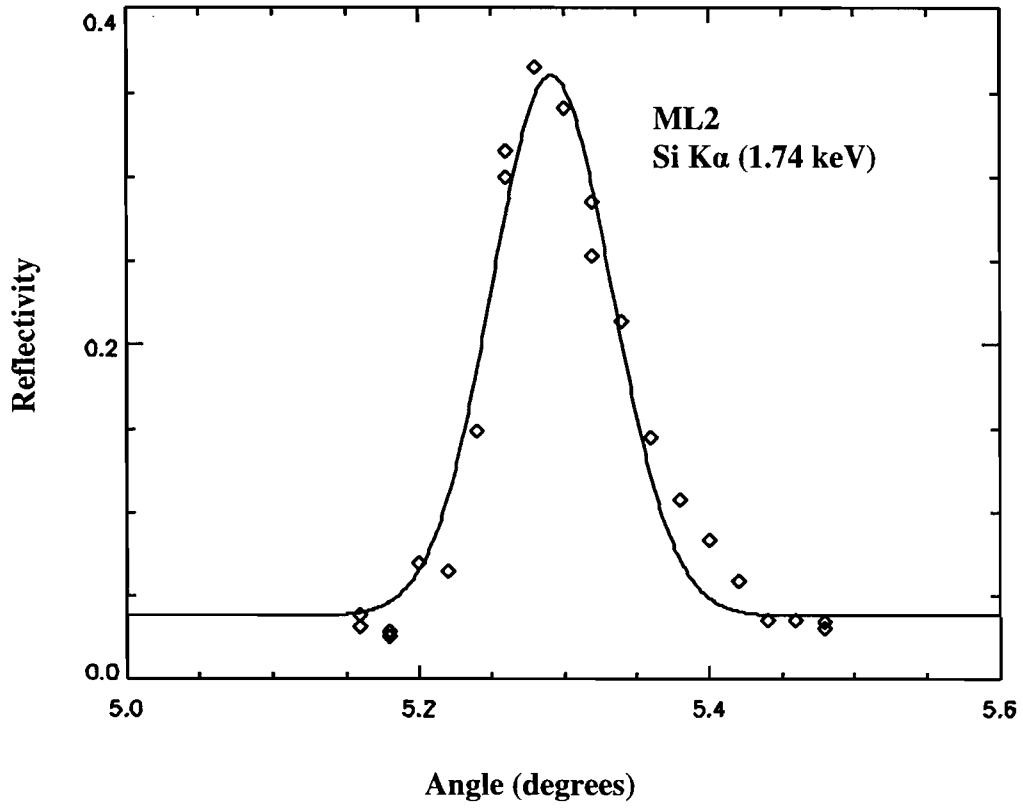


Fig. 6(d)

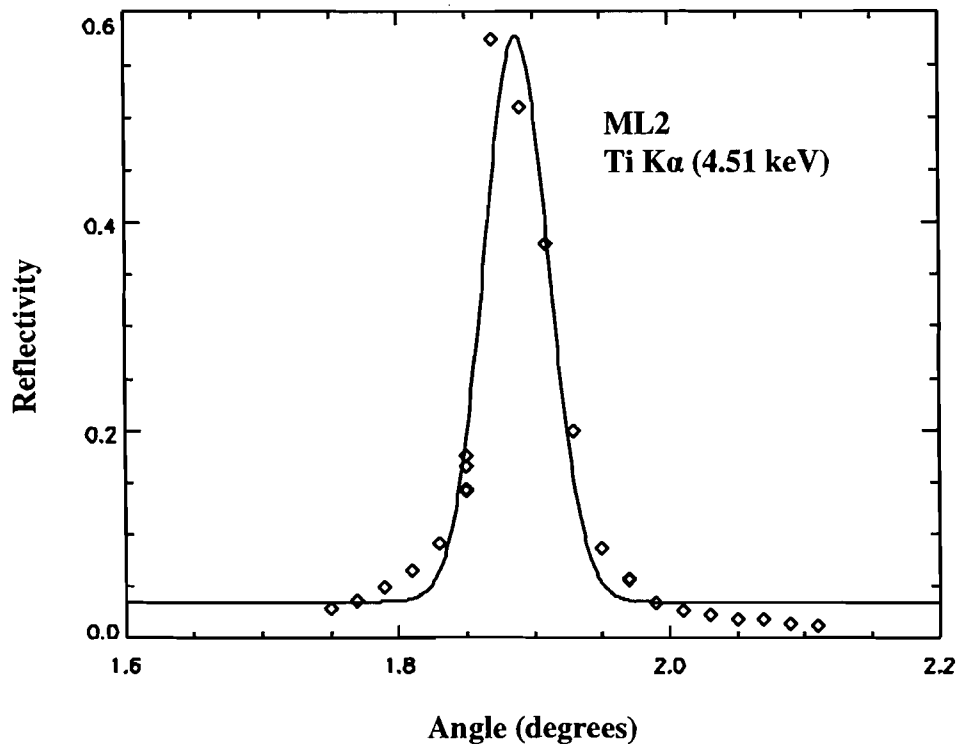


Fig. 6(e)

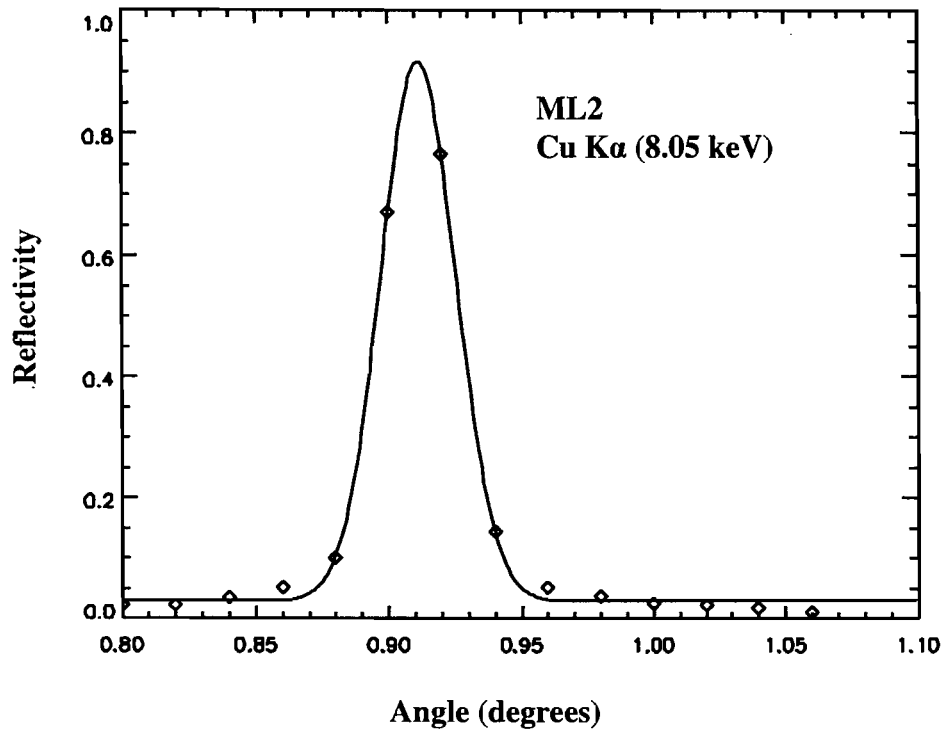


Fig. 6(f)

To solve for the d spacing of each multilayer, the diffraction from more than one x ray line must be measured in order to eliminate error in the zero position. This is accomplished by solving the following equation for two or more diffracted lines:

$$\lambda_i = 2d \sin(\theta_i + \theta_0) \quad (7)$$

where λ_i is the corresponding wavelength for each trial, θ_i is the measured angle of peak reflectivity, and θ_0 is the zero offset. The solution to equation 7 is obtained implicitly through graphical analysis. Equation 7 can be rewritten as follows:

$$\theta_0 = \sin^{-1}\left(\frac{\lambda_i}{2d}\right) - \theta_i \quad (8)$$

The error on the best-fit value of the angle of peak reflectivity has been determined by the following prescription given in Lampton et al¹². It is as follows: Normalize χ^2 to be equal to 1 per degree of freedom ν ,

$$\frac{\chi^2}{\nu} = 1 = \frac{1}{\nu} \sum_{i=1}^n (f(a_i) - y_i)^2 w^2, \quad (9)$$

where $f(a_i)$ is a Gaussian fit to the observed values of reflectivity y_i , and w is chosen to make $\frac{\chi^2}{\nu} = 1$. Then select a value of the peak angle that increases χ^2 by 4.7 (appropriate for fitting four important parameters). The difference in peak angle from χ^2 minimum is an estimate of the uncertainty. Including the standard deviation fails to yield an intersection point for all three lines of each trial, indicating that there may have been additional, unaccounted errors. Alternatively, the positioning error should be no less than one step of the rotary motors (0.01°). Estimates of the error are shown in Fig 7.

Fig 7 (a-b): Implicit graphical solution to solve for the d spacing and angle offset of the first (a) and second (b) multilayer while incorporating an error of $\pm 0.01^\circ$.

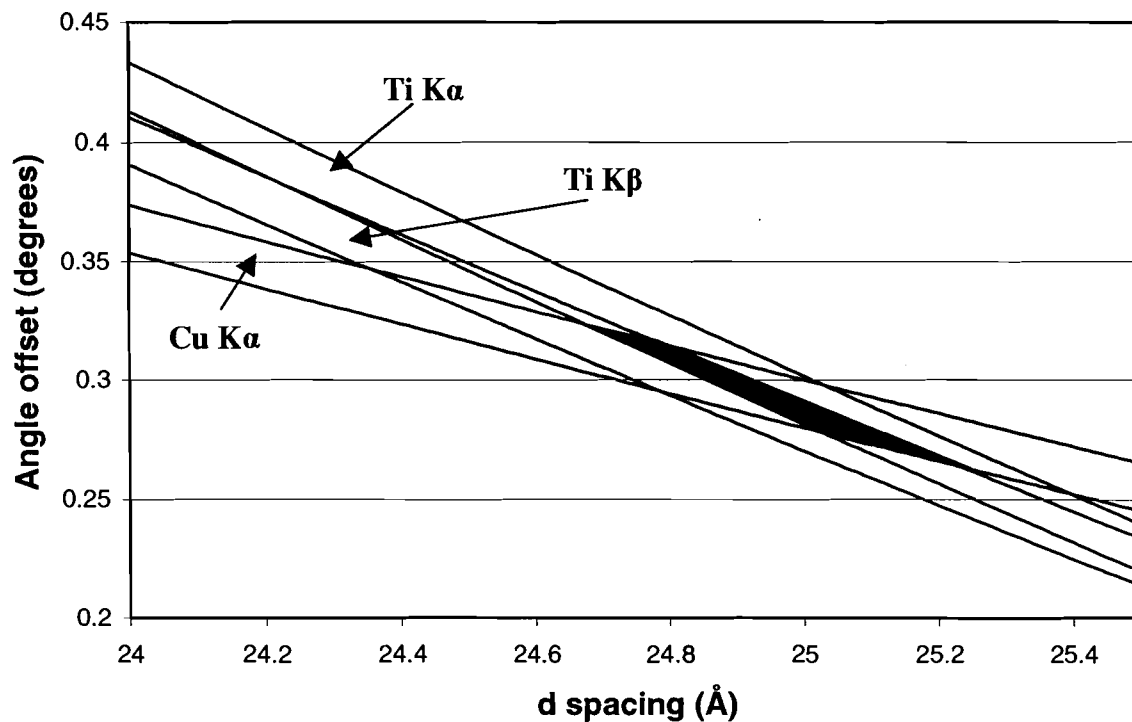


Fig. 7(a). Angle offset as a function of d spacing for the first multilayer

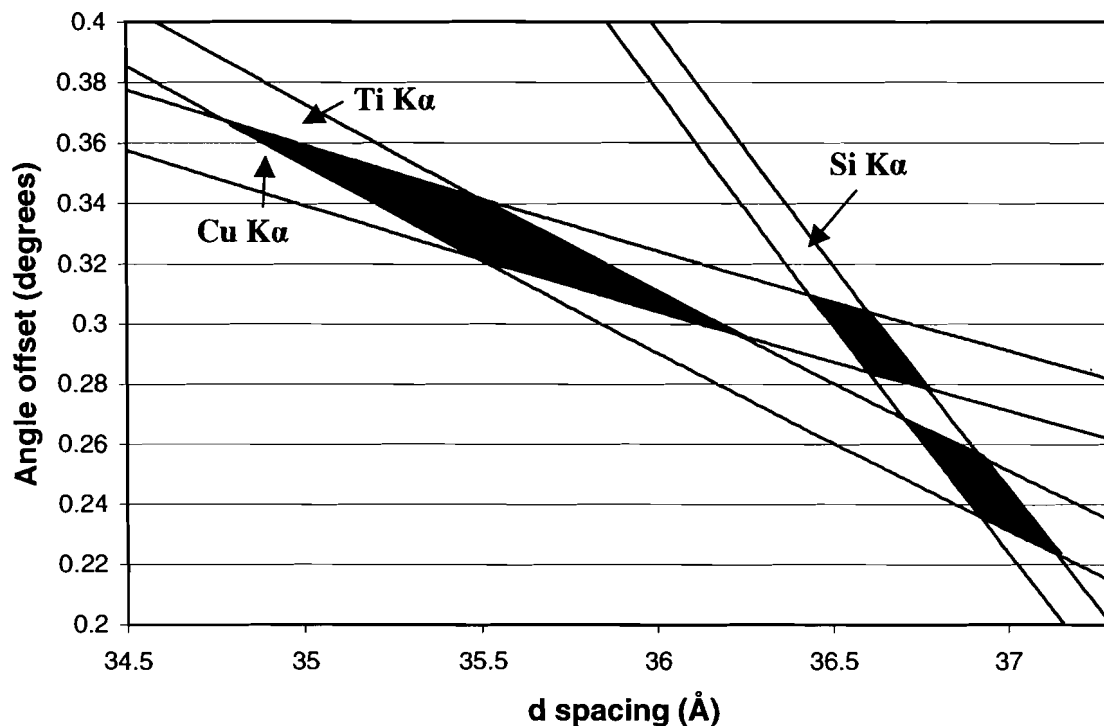


Fig. 7(b). Angle offset as a function of d spacing for the second multilayer

In Fig. 7(a), the intersection of the error bands for the three lines indicates the range of values for the d spacing and angle offset. Statistical analysis of the data yields a value of $24.95 \pm 0.3 \text{ \AA}$ for the value of the d spacing for multilayer 1 (the midpoint of the banded region plus or minus half the length of the region). Figure 7(b) fails to yield an intersection for the three lines. Statistical analysis of the three intersections yield a value for the d spacing of $36.3 \pm 0.74 \text{ \AA}$ for multilayer 2 (the average of the intersections plus or minus half the range of values within all three intersections).

The peak reflectivity of the multilayer diffractors is found to depend upon the energy of the diffracted line. This can be seen in Fig. 8 below.

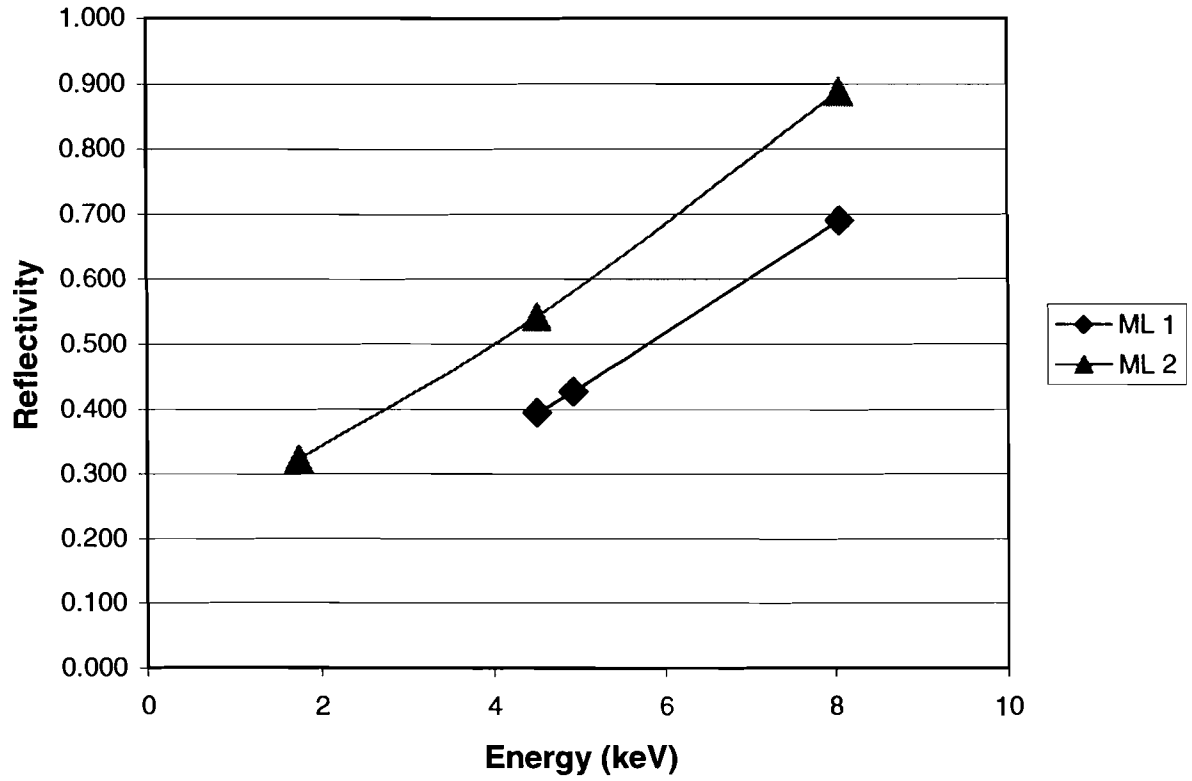


Fig. 8. Peak reflectivity as a function of energy for each multilayer

The energy response of the multilayer is defined to be $\frac{\Delta E}{E}$. Differentiating Eq. (1), and using the identity $E = hc/\lambda$, where h is Planck's constant and c is the speed of light, yields the equation

$$\frac{\Delta E}{E} = \frac{\Delta \lambda}{\lambda} = \cot(\theta)\Delta\theta, \tag{10}$$

where θ is the Bragg angle and $\Delta\theta$ is equal to the full width at half maximum. Applying the equation to the results is shown in Fig. 9.

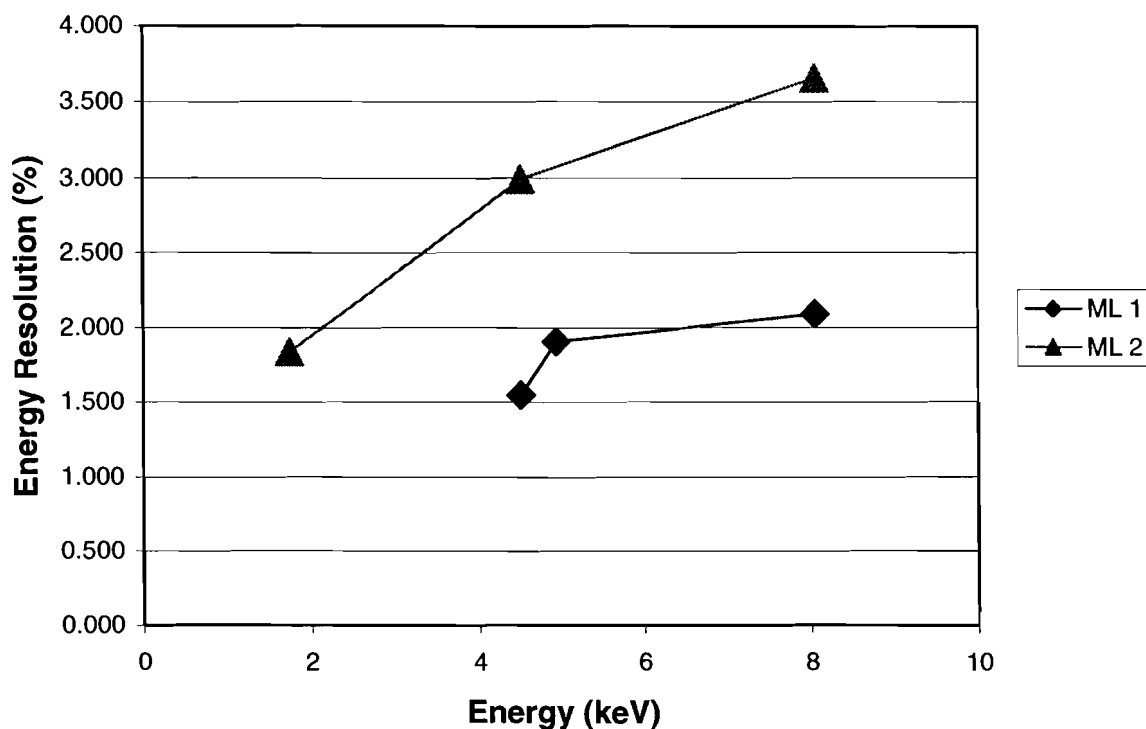


Fig 9. Energy Resolution as a function of energy for each multilayer

CONCLUSIONS

The WB_4C multilayer diffractors have been characterized as a function of x-ray energy by measuring their reflectivity as a function of angle using a Si PIN detector. Optimization using Gaussian curve fitting allows determination of the peak reflectivity as well as the energy resolution [full width at half maximum (FWHM)]. The multilayer spacing d is determined using Bragg's Law and the simultaneous analysis of multiple diffracted lines.

The first multilayer ($d = 24.95 \pm 0.3 \text{ \AA}$) had a reflectivity of 40 to 70 % and an energy resolution of 1.5 to 2.1 %. The second multilayer ($d = 36.3 \pm 0.74 \text{ \AA}$) had a reflectivity of 32 to 89 % and an energy resolution of 1.8 to 3.7 %. The observed and calculated data can accurately be used as a foundation for further work with x-ray imaging using these multilayer diffractors.

Acknowledgements

I would like to acknowledge the support of the staff at the Laboratory for Laser Energetics of the University of Rochester. I would especially like to thank Dr. Frederic J. Marshall for his guidance and Robert Forties for his assistance in the completion of my project. I would also like to thank Dr. Stephen Craxton for allowing me to participate in this research program.

References

1. T.R. Boehly, D.L. Brown, R.S. Craxton et al., *Opt. Commun.* 133, 495 (1997).
2. Ahlstrom, H.G. Physics of Laser Fusion Vol. II: Diagnostics of Experiments on Laser Fusion Targets at LLNL. (Lawrence Livermore Laboratory, University of California, Livermore, CA, 1982), pp.2-9.
3. F. Ze, R.L. Kauffman, J.D. Kilkenny et al. *Rev. Sci. Instrum.* 63, 5125 (1992).
4. OSMIC, Inc. Auburn Hills, MI 48326.
5. AMPTEC, Inc. 6 DeAngelo Drive. Bedford, MA 01730
6. Cullity, B. D. Elements of X-Ray Diffraction. (Addison-Wesley Publishing Company, Inc., Reading, MA, 1956), pp. 78-103.
7. Cullity, *ibid.*, pp. 17-23.
8. Knoll, Glenn F. Radiation Detection and Measurement. (John Wiley & Sons, New York, 1989), pp. 17-18.
9. Young, Hugh D. Statistical Treatment of Experimental Data. (McGraw-Hill Book Company, Inc., New York, 1962), pp. 64-76.
10. Visual Numerics, Inc. Houston, TX 77042.
11. Bevington, Philip. Data Reduction and Error Analysis for the Physical Sciences. (Mc Graw-Hill, New York, 1969)
12. M. Lampton, B. Margon, S. Bowyer. *Astrophysical Journal*. 208, 181 (1976).

**Noncollinear Phase Matching in Optical Parametric
Chirped-Pulse Amplification**

Joy Yuan

Noncollinear Phase Matching in Optical Parametric Chirped Pulse Amplification

Summary

Optical parametric chirped pulse amplification (OPCPA) is a method used to generate high-powered laser pulses. In this process, energy from a “pump” pulse is used to amplify a signal “seed” pulse. A computer program based on an analytical model was written and used to demonstrate the influence of noncollinearity, a condition in which the pump and seed are not parallel, and crystal tilt on the signal seed pulse. The investigations showed that maximum signal amplification is achieved when the crystal is slightly detuned.

1. Introduction

Energy is required to do work, and therefore is essential to the sustenance of life.

With the energy supplies of the last century rapidly draining away, scientists seek new sources of energy to power the advanced technologies that make modern human civilization possible. One possible avenue is fusion power. Scientists at the University of Rochester Laboratory for Laser Energetics (LLE) hope to make fusion power a viable energy source. The fusion of nuclei can generate a massive amount of energy. Certain conditions, however, must be met if fusion is to occur. High temperatures give the nuclei energy to overcome the strong nuclear forces that exist between them, and high densities increase the probability that the nuclei will collide. At LLE, these conditions are met by inertial confinement fusion (ICF). A fuel pellet, approximately 1 mm in diameter, holding deuterium and tritium isotopes, is uniformly irradiated by 60 amplified laser beams¹. The lasers cause the outer shell of the pellet to vaporize and ablate, or become explosively torn free at a tremendous force. According to Newton's Third Law, an equal and opposite force is directed into the pellet, creating the high temperatures and densities needed for fusion to occur. When the nuclei of the tritium and deuterium isotopes fuse, energy is given off as alpha particles and neutrons. Some of this energy is deposited in unreacted fuel, allowing the fusion reaction to continue and more energy to be generated as a result. This phenomenon is called ignition. Researchers hope to maximize the energy yield from implosions.

Increasing the power of the laser can help maximize the energy yielded in the fusion reaction. Scientists at LLE are designing a new petawatt laser system, which will allow them to amplify a low-energy signal seed pulse, while maximizing its bandwidth. Optical parametric chirped pulse amplification (OPCPA) is a method which can produce the high-power laser pulses needed, and is being considered for the next generation of laser systems at LLE.

Numerous variables influence the effectiveness of signal seed amplification in the OPCPA process. Although a collinear interaction between the pump and the signal seed has been analyzed in great detail, scientists have discovered that the amplified signal seed pulse can be extracted more easily from the process if the seed is not collinear with the pump. A computer program based on an analytical model is written and used here to calculate the effect of noncollinearity on the intensity and spectrum of the amplified signal seed pulse. This model illustrates that the crystal must be tilted in order for maximum amplification to occur. By calculating the total intensity integrated over time for a range of crystal tilts, I was able to calculate the crystal tilt that will maximize the total energy of the signal pulse. I was able to prove that this angle was slightly less than the angle needed to achieve the degenerate phase-matching condition. The model also simulates the parametric fluorescence that is generated simultaneously as the pump passes through the crystal.

2. OPCPA generates a short, high-intensity laser pulse

OPCPA can begin by stretching a Gaussian-shaped signal seed pulse in time, as shown in Fig. 1. Diffraction gratings stretch the pulse by bending different frequencies at different angles. As a result the individual frequencies become separated creating a chirped signal seed pulse. According to the conservation of energy, the total energy of the stretched pulse remains unchanged. Since the energy is stretched over a longer period in time, the pulse power at a specific time is reduced. The stretched signal seed and a pump pulse are then sent into the optical parametric amplifier (OPA). The OPA used is a lithium triborate (LBO) crystal. This crystal has two indices of refraction, a property known as birefringence. Because it has different

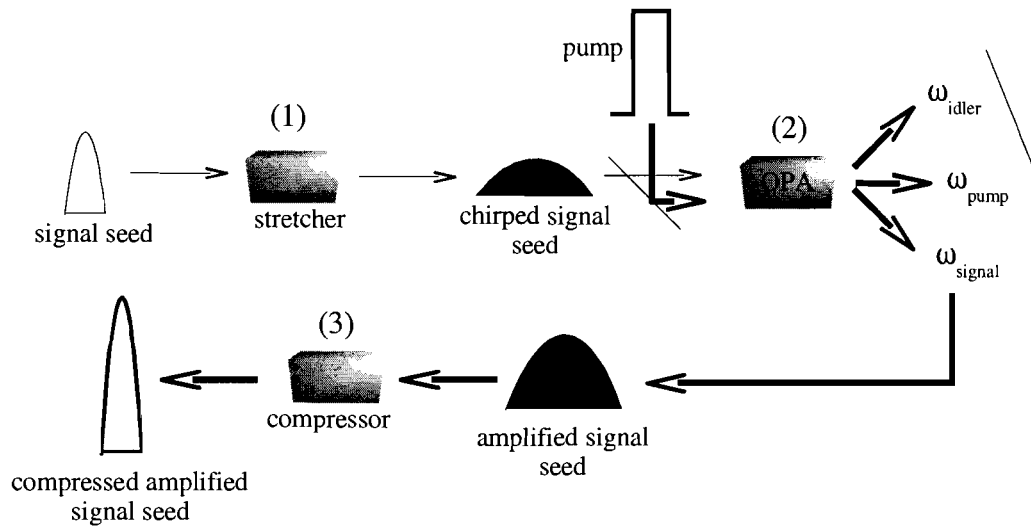


Figure 1. A graphical illustration of optical parametric chirped pulse amplification (OPCPA). (1) A Gaussian-shaped signal seed pulse is stretched into a chirped pulse. (2) The stretched seed and a pump are sent into an optical parametric amplifier (OPA). The OPA allow the signal and pump to interact, creating an idler pulse and allowing for the amplification of the signal. The OPA used consisted of lithium triborate (LBO). (3) The amplified signal is compressed into a short, high-intensity pulse, whereas the pump and idler are blocked from further use.

indices of refraction, light will travel at different speeds as it passes through the crystal from different directions.

When two pulses pass through the crystal, energy from the pulses excite the molecules within the crystal. Because of the nonlinear properties of the crystal molecules, the energy is reradiated as idler pulses. Amplification of the signal pulse is only possible when there exists an idler. My simulations assumed a small signal regime. In this type of interaction, the relative energy of the signal to the pump is low enough that any change in pump energy is considered negligible. Therefore, a small signal regime assumes that the energy of the pump remains undepleted, even though energy is being lost to the seed. OPA follows Equation 1 for the small signal regime. In reality, the changing pump energy affects how much energy is transferred to the signal seed.

$$E_{\text{signal}}(z) = \left[E_{\text{signal}}(0) \left(\cosh gz - \frac{i\Delta k}{2g} \sinh gz \right) + \frac{\kappa_{\text{signal}}}{g} E_{\text{idler}}^*(0) \sinh gz \right] e^{i\Delta k z/2}$$

$$\kappa_{\text{signal}} = \frac{8\pi i \omega_{\text{signal}}^2 d E_{\text{pump}}}{\kappa_{\text{signal}} c^2}$$

$$g = \left[\kappa_{\text{signal}} \kappa_{\text{idler}}^* - (\Delta k/2)^2 \right]^{1/2}$$

$$E_{\text{idler}}(z) = \left[E_{\text{idler}}(0) \left(\cosh gz - \frac{i\Delta k}{2g} \sinh gz \right) + \frac{\kappa_{\text{idler}}}{g} E_{\text{signal}}^*(0) \sinh gz \right] e^{i\Delta k z/2}$$

$$\kappa_{\text{idler}} = \frac{8\pi i \omega_{\text{idler}}^2 d E_{\text{pump}}}{\kappa_{\text{idler}} c^2}$$

Equation 1. The undepleted pump approximation was used to calculate parametric intensities. E represents the electric field. The intensity of a pulse can be determined from $|E|^2$. Because we assumed a small signal regime, the energy of the pump remained constant. z represents the distance the pulse passes through the crystal. Because we want to calculate the intensity at the end of the crystal, z represents the length of the crystal, or 25 mm. Notice that when Δk equals zero, the intensity of the signal and idler are maximized.

In a related situation, the reradiated energy is used to generate fluorescence at a wide range of wavelengths and at numerous angles, depending on the phase-matching conditions within the crystal. Fluorescence results from interactions with photons, acting as signal pulses.

As a result of this energy exchange process, a third pulse is generated called the idler pulse. In a type I interaction, both the signal and the idler are ordinary waves, and the pump is an extraordinary wave. The electric field of an ordinary wave is perpendicular to the crystal's optic axis; therefore, the indices of refraction of the two ordinary waves, the signal and the idler, are not dependent on the angle at which they propagate through the crystal. The electric field of an extraordinary wave has a component along the optic axis; therefore, the index of refraction of an extraordinary wave, such as the pump, can vary depending on the angle of propagation of the pump in relation to the optic axis.

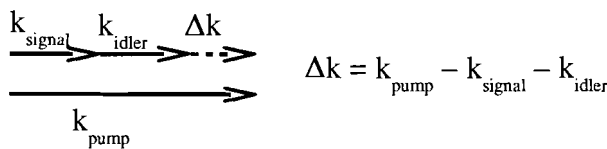
After the three pulses pass through the crystal, the amplified signal seed pulse is compressed into a short, high-intensity pulse. Compressors, like stretchers, involve diffraction gratings; however, the diffraction gratings in a compressor bend the frequencies of a chirped

pulse so that the frequencies become mixed once again. While the pump and idler are blocked from further use, the compressed amplified signal is sent toward the target. The fluorescence that is generated can affect the spectrum of the amplified signal seed pulse, thereby decreasing the pulse contrast ratio and exacerbating the prepulses in the compressed signal.

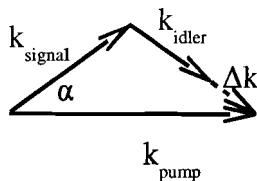
3. Energy transfer differs in collinear and noncollinear interactions

In a collinear interaction, the signal seed and the pump are sent into the crystal at the same angle; as a result, the idler pulse generated is parallel to both the signal and pump. Because the signal and the idler have the same direction of propagation and the same polarization, it is difficult to separate the signal seed pulse, which will later be compressed, from the unwanted idler. By sending the signal seed at an angle to the pump, this issue is eliminated, because in a noncollinear interaction the signal and idler propagate at different angles through the crystal. In a noncollinear interaction, Δk can be derived based on the geometry of a triangle.

Collinear Interaction



Noncollinear Interaction



(Eq. 2)
$$\Delta k = k_{\text{signal}}^2 + k_{\text{pump}}^2 - 2k_{\text{signal}}k_{\text{pump}}\cos(\alpha) - k_{\text{idler}}^2$$

Figure 2. In a collinear interaction, the k -vectors of the signal, idler, and pump are parallel to one another. In a noncollinear interaction, the k vectors form a triangle. α represents the angle of noncollinearity between the signal and the pump. When the endpoint of k_{idler} and the endpoint of k_{pump} coincide, so that Δk equals 0, energy transfer is maximized. The equation for Δk in a noncollinear interaction was derived from the law of cosines.

An expression derived from the law of cosines (Eq. 2) shows that Δk depends on the angle between the signal and the pump in a noncollinear interaction. Because the Δk expression differs between collinear and noncollinear interactions, energy transfer must differ between them as well.

4. How the spectrum and intensity of a pulse can be changed

4a. Wavelength

Because the signal seed is a chirped pulse, it contains a range of wavelengths that are uniquely spaced out in time. As the wavelength of the signal changes, the wavelength of the generated idler must vary, and the k-vector mismatch, or Δk , must change as well. Consequently, for the range of wavelengths in a chirped signal pulse, there must exist a corresponding range of values for Δk . The relationship between Δk and wavelength of the signal pulse is approximately parabolic, and the minimum Δk value occurs at or near the central wavelength of the signal seed pulse. The spread of Δk values and the wavelength(s) for which Δk equals zero will determine the spectrum of the amplified signal seed pulse. The signal used in these investigation was a 200 fs Gaussian seed pulse, stretched in time to 1 ns, with a central wavelength of 1054 nm.

4b. Angle of Noncollinearity

When the angle between the pump and the signal increases, the Δk associated with all wavelengths will increase (see Eq. 2). As seen in Fig. 3, the entire plot of Δk , as a function of wavelength, will be pulled downward and the spectrum of the signal pulse will be changed. When the Δk plot is tangent to the x-axis, there exists one signal wavelength for which Δk equals zero (see Figure 3a). When this condition exists, the signal is said to be degenerate. This

configuration correlates to a single peak intensity in the Gaussian-shaped signal pulse spectrum. When the Δk plot is pulled below the x-axis, by increasing the angle of noncollinearity, there exist two wavelengths for which Δk equals zero, corresponding to two peak intensities (see Figure 3b). As the angle of noncollinearity continues to increase, the two intensity peaks will be pulled farther apart².

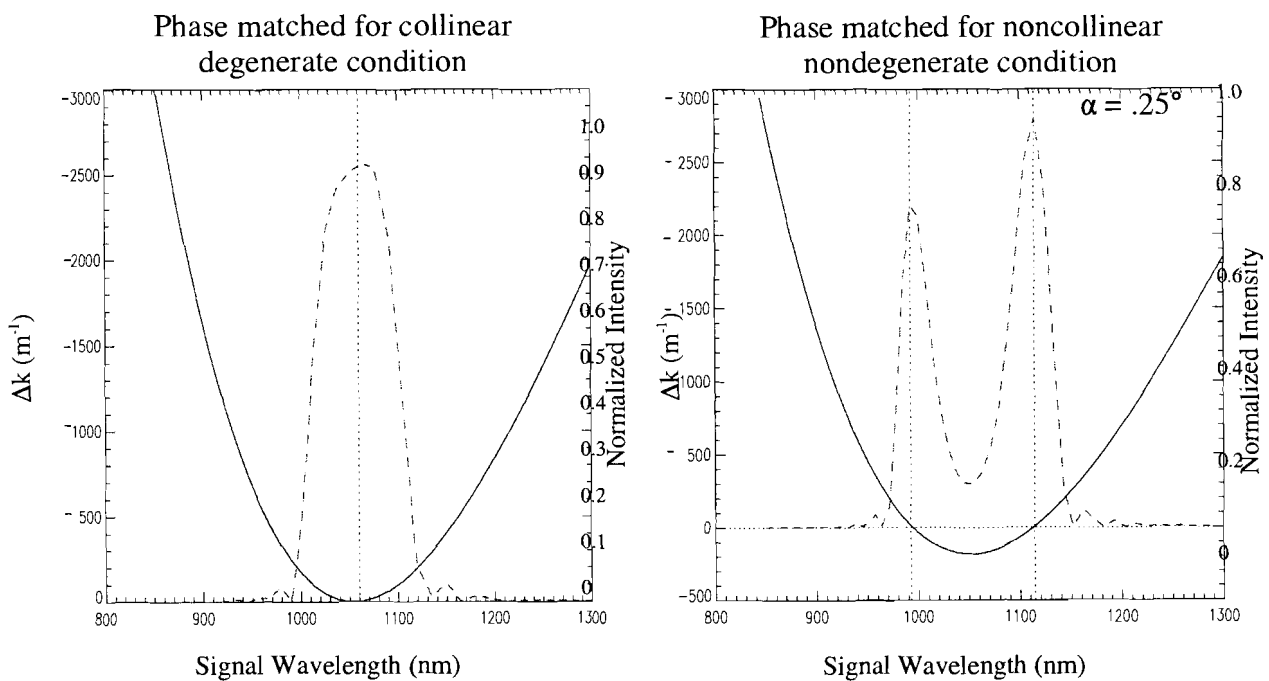
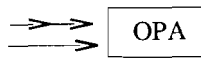


Figure 3a.

Figure 3b.



In these diagrams, the solid curve illustrates Δk and the dashed line represents the normalized intensity. When the angle between the signal and the pump (α) is increased from the collinear ($\alpha = 0$) degenerate (wavelength of signal = 1054 nm) condition to an angle of noncollinearity of $.25^\circ$, while keeping the crystal tilt constant, the entire plot of Δk is pulled downward, such that there now exist two locations where Δk equals zero, or two intensity peaks.

Phase matched for noncollinear slightly-nondegenerate condition by tilting crystal

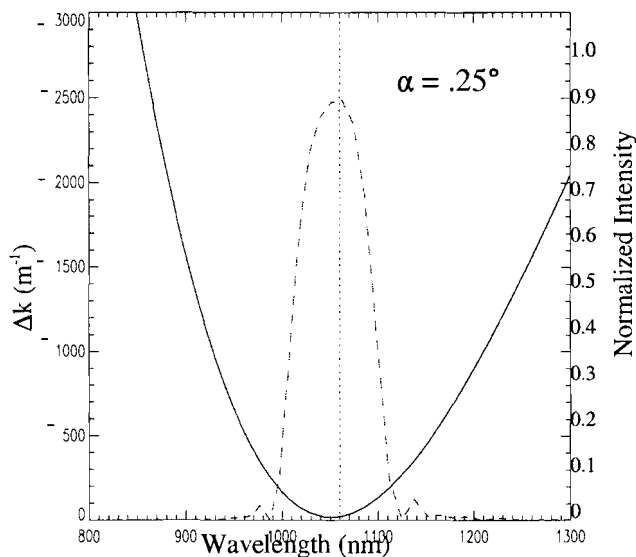


Figure 3c. When the crystal tilt is increased slightly, while maintaining the angle of noncollinearity constant (compare to Fig. 3b), the Δk plot is pulled upward, forcing the two intensity peaks back together. Phase-matching to achieve the nearly-degenerate condition can be achieved by tilting the crystal ($\sim .215$ radians). The noncollinear phase-matching angle was calculated by finding a crystal tilt value which brings about a Δk of zero for a specific angle of noncollinearity and a given central wavelength.

4c. Crystal tilt

The spectrum of the output signal pulse can also be changed by tilting the crystal. Increasing the crystal tilt increases the angle between the pump and the optic axis. Because the pump pulse is an extraordinary wave, its index of refraction will change as the crystal tilt is altered. In an LBO crystal, as the crystal tilt increases, the pump index of refraction decreases. Since the index of refraction is proportional to k , when the pump index of refraction decreases, k_{pump} decreases as well. According to Eq. 2, when k_{pump} decreases, all values of Δk decrease; therefore, increasing the crystal tilt will pull the entire plot of Δk upwards. The spectrum of the signal pulse is important to consider when choosing the tilt of the crystal, because it influences the compressibility of the amplified signal seed pulse.

Another important characteristic of the pulse is its total intensity. It is desired to maximize the total intensity of the signal seed pulse. The total energy corresponds to the sum of

all the energies attained from each wavelength in the chirped signal pulse. The total energy corresponds to the total area beneath each of the intensity curves seen in Figure 3, and can be calculated by analytically integrating the intensity over a range of wavelengths. By calculating the total intensity integrated over wavelength for a range of crystal tilts, one can calculate the crystal tilt that will maximize the total energy of the signal pulse. I discovered that the angle needed to achieve maximum total intensity is slightly less than the angle needed to achieve the degenerate phase-matching condition (illustrated by dotted lines in Fig. 4). As the crystal tilt decreases, the Δk plot is pulled downward and the two intensity peaks of maximum amplification in the pulse spectrum are pulled apart. This is important because it allows scientists to calculate the angle needed to maximize signal amplification.

Since maximum total intensity is achieved for a slightly nondegenerate phase-matching angle, there exist two wavelengths for which maximum amplification occurs. This development gives rise to two intensity peaks in the pulse spectrum. To some extent, the separation of the two intensity peaks results in a relatively wide bandwidth but a low contrast ratio in the compressed pulse.

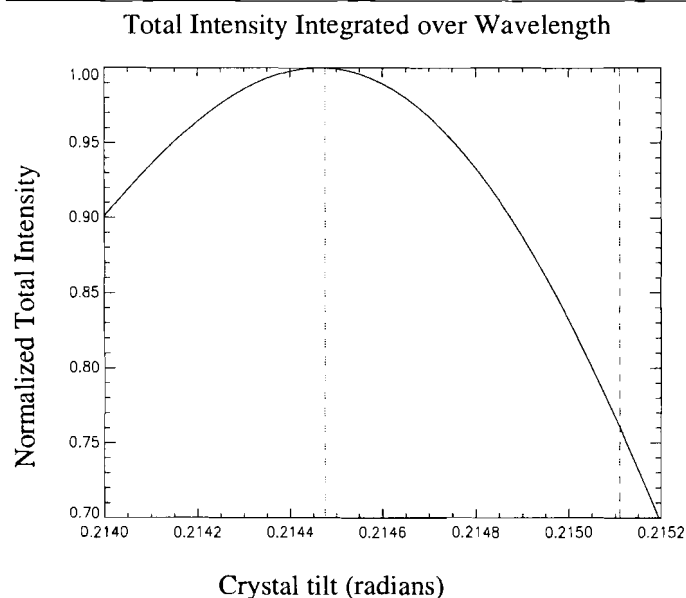


Figure 4. This graph shows the relationship of total intensity integrated over wavelength as a function of crystal tilt. It is clear that the angle needed to achieve maximum total intensity (left dotted line) is slightly less than the angle needed to achieve the degenerate phase-matching condition (right dotted line). When the crystal tilt decreases the two intensity peaks of maximum amplification are pulled apart; consequently, when the crystal tilt is slightly detuned from the degenerate phase-matching angle, the two intensity peaks separate, and maximum total intensity is achieved because the spectral bandwidth is enhanced.

5. Fluorescence

When the pump passes through the crystal, signal and idler pulses are generated spontaneously at a wide range of wavelengths and at numerous angles. The intensity distribution of parametric fluorescence depends on the phase-matching conditions, analyzed before, within the crystal. Fluorescence development is similar to that involving the amplification of the seed by the pump. A notable difference between the two processes is that while the signal seed has a limited bandwidth and a single chosen angle of noncollinearity, fluorescence is generated at all wavelengths and at numerous angles of noncollinearity. Many aspects of the fluorescence intensity distribution, such as the number of fluorescence intensity peaks, are determined by the tilt of the crystal³.

Each point (Fig. 5) corresponds to a value of maximum intensity; therefore, the total intensity for a specific angle of noncollinearity can be calculated by summing up all the intensities across a horizontal region. When the slope approaches zero, more intensities are being summed together; consequently, maximum total intensity occurs where horizontal tangents take place. With regards to the wavelengths left of the dotted line, for some values of crystal tilt (e.g. 13.5°), there exist two locations where the slope approaches zero, or two total intensity peaks (Fig. 5b). Whereas for other values of crystal tilt (e.g. 11.5°) there exists only one location where the slope approaches zero, or one total intensity peak (Fig. 5c).

Many patterns can be drawn from the plot in Figure 5a. For the wavelengths used for the signal seed pulse, there are specific wavelengths and angles of noncollinearity for which Δk equals zero and the intensity is peaked. Intensity peaks for a specific arrangement of wavelength and angle of noncollinearity can be achieved by changing the tilt of the crystal. The total intensity for a specific angle of noncollinearity can be calculated by summing up all the

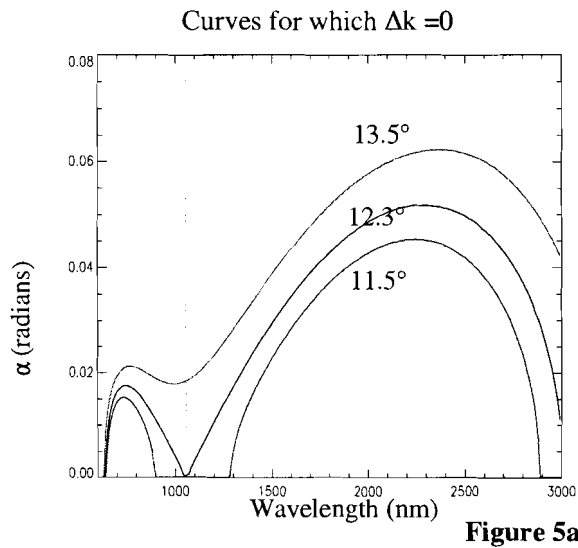
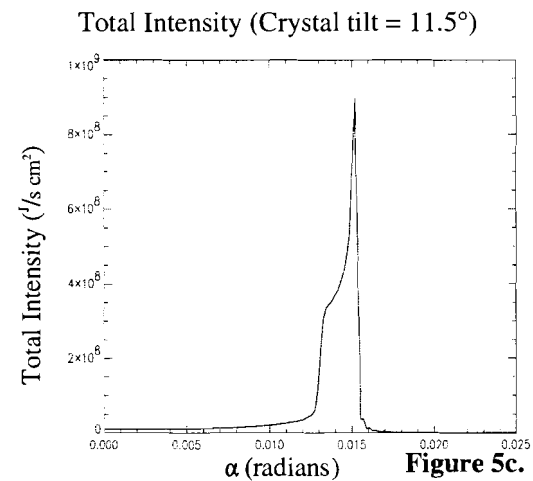
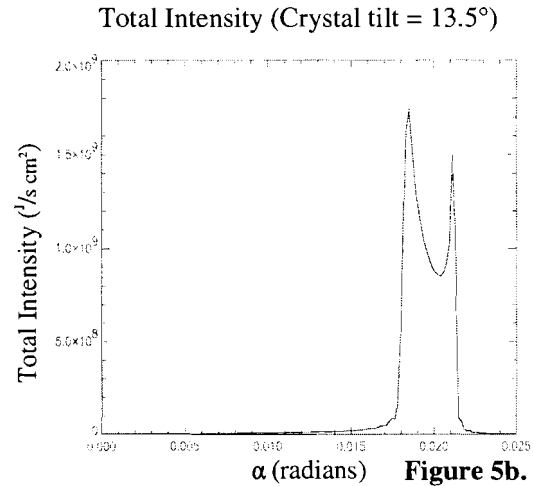


Figure 5. These are curves for which Δk equals zero or the intensity is maximized for various values of crystal tilt (Fig. 5a). Each point in Fig. 5a corresponds to a value of maximum intensity. The central plot represents the Δk curves for the collinear degenerate phase-matching angle (12.3°). The other two plots depict arbitrary crystal tilts (11.5° and 13.5°). Each point in Fig. 5a holds a value of maximum intensity. If the intensities of each crystal tilt plot were calculated and summed as a function of the angle of noncollinearity (α), the graphs on the right would result. Notice that for some values of crystal tilt, there exists two peaks of maximum total intensity (Fig. 5b); whereas, other angles only have one (Fig. 5c)



intensities along a specific angle of noncollinearity, or α . Maximum total intensities occur at turning points, in the curves of Fig. 5a, where more intensities are being summed together. The number of fluorescence intensity peaks, as well as the angle of noncollinearity at which they occur, are determined by the tilt of the crystal (Figure 5b and 5c).

Fluorescence is generated in all directions from the pump pulse. Since the signal and idler are ordinary waves, Δk depends on the angle of noncollinearity. Assuming that the fluorescence patterns seen before apply to all directions within the crystal, the fluorescence image as captured by a camera at the end of the crystal would appear to be a series of concentric

circles (Fig. 6). The radius of each circle corresponds to the angle of noncollinearity, and the number of maximum total intensity rings and the angle(s) of noncollinearity at which they occur, are determined by the tilt of the crystal. Fig. 6 illustrate the images of the the signal and idler if taken by a camera at the end of the crystal. The two white rings, best seen in the signal represent the two intensity peaks seen before (Fig. 5b).

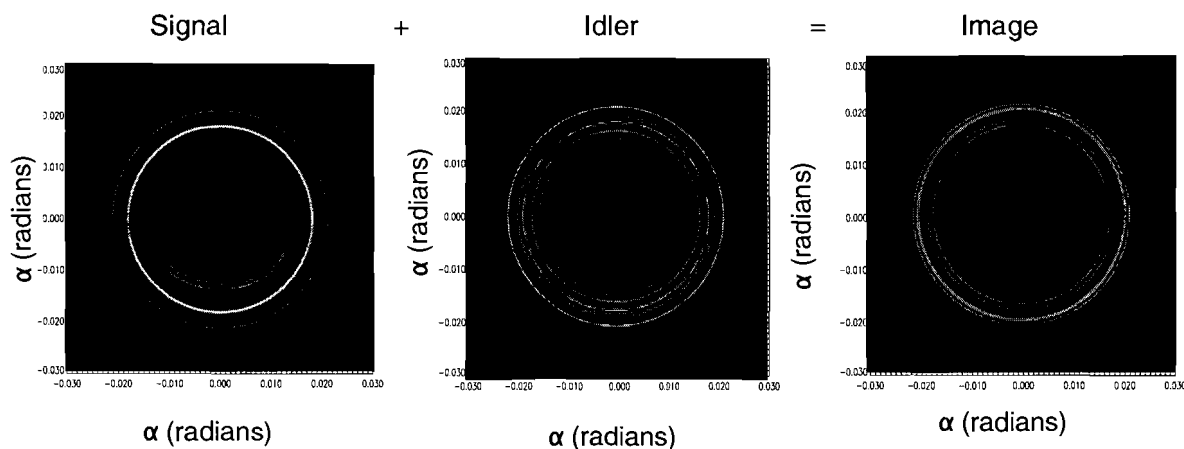


Figure 6. These are the images of the signal and idler if taken by a camera at the end of the crystal. Notice the two rings of maximum total intensity which correspond to the two total intensity peaks seen before for this particular crystal tilt (13.5°). The actual image seen at the end of the crystal is a combination of the signal and idler and has characteristics of both.

Fluorescence plays a significant role in the formation of an amplified signal seed pulse. When the angle of noncollinearity between the signal and the pump of the generated fluorescence is the same as the chosen angle between the signal seed and the pump, energy from the fluorescence amplifies the energy of the signal seed. The amplified signal pulse is raised upon a pedestal of energy obtained from the fluorescence. The spectrum of the amplified signal pulse is such that the contrast ratio of the compressed amplified signal is decreased and any prepulses are exacerbated. Scientists hope to manipulate the tilt of the crystal and the angle of noncollinearity, such that the contrast ratio is maximized. When the laser beam hits the target, the prepulses preheat the fuel pellet and change the initial conditions for when the actual pulse

hits the target. If the prepulses are too high and the contrast ratio is too low, the effectiveness of the hit can be compromised. It is hoped to get experimental results to confirm my predictions in Fig. 6 as this will help improve our understanding of fluorescence.

6. Future Work

Future work in this field entails writing a numerical model to show how fluorescence affects the amplified signal seed pulse. Studies can be performed to investigate the effect of fluorescence on signal pulse bandwidth, and to find the conditions needed to minimize the pre-pulse level in the compressed OPCPA pulse. Increased accuracy can be achieved by not assuming a small signal regime. Since the pump energy decreases as it transfers energy to the signal and idler, the amount of energy transferred will also decline. It would be interesting to see how these patterns might change if the energy of the pump was limited. Specifically, it would be interesting to see how the optimum tilt predicted in Section 4c will compare to the optimum tilt in a large signal regime.

7. Conclusion

My research concentrates on the Δk term, a heretofore unappreciated but essential factor, involved in laser amplification, which will in turn allow us to model and better understand and predict the conditions needed for fusion to occur. Likewise, my research concerning OPCPA will give insight to the University of Rochester Laboratory for Laser Energetics as it plans on building a more powerful and efficient laser system. I calculated the influence of noncollinearity and crystal tilt on the spectrum and intensity of a signal seed pulse. The program indicated how

these factors influenced Δk . These investigations showed that maximum signal was achieved when the crystal was slightly detuned. The crystal tilt needed to achieve optimum amplification was calculated for the small signal regime. The program also predicted the parametric fluorescence patterns that would be generated. By comparing my results with experiments to be carried out on fluorescence, my research will help to improve our understanding of OPCPA. These findings allow us to further investigate the conditions necessary for creating a short pulse with high energy and low prepulses, necessary for laser fusion to occur.

Acknowledgments

I would like to express my sincere appreciation to my advisor, Mark Guardalben, for his patience and guidance during my investigations. I would also like to thank Dr. Stephen Craxton for giving me this opportunity to participate in the High School Research program at the LLE, as well as all the other participants who have helped me endure through my frustrations and have celebrated with me in our successes.

References

- (1) R. Stephen Craxton, Robert L. McCrory, and John M. Soures. "Progress in Laser Fusion." *Scientific American* 255, 68-79 (1986).
- (2) Matthew J. Shelton, and David P. West. "Degenerate noncollinear emission from a type I collinear parametric oscillator." *Optics Express*, Vol. 9, No. 1, 16-23 (2001).
- (3) A. Berzanskis, W. Chinaglia, L. A. Lugiato, K.-H. Feller, and P. Di Trapani. "Spatial structures in optical parametric amplification." *Physical Review A*, Vol. 60, No. 2, 1626-1635 (1999).